VICTORIA UNIVERSITY OF WELLINGTON

DOCTORAL THESIS

Aminophosphine Reduction Mechanisms and the Synthesis of Indium Phosphide Nanomaterials

---

Author:
Geoffry LAUFERSKY

Supervisor:
Prof. Thomas NANN

A thesis submitted in fulfillment of the requirements for the degree of Doctor of Philosophy

in the

Nannomaterials Research Group
School of Chemical and Physical Sciences

August 6, 2019

Victoria University of Wellington

Abstract

Faculty of Chemistry
School of Chemical and Physical Sciences

Aminophosphine Reduction Mechanisms and the Synthesis of Indium Phosphide Nanomaterials

by Geoffry LAUFERSKY

Indium phosphide (InP) nanomaterials are attractive for countless technological applications due to their well-placed band gap energies. The quantum confinement of these semiconductors can give rise to size-dependent absorption and emission features throughout the entire visible spectrum. Therefore, InP materials can be employed as low-toxicity fluorophores that can be implemented in high value avenues such as biological probes, lighting applications, and lasing technologies. However, large scale development of these quantum dots (QDs) has been stymied by the lack of affordable and safe phosphorus precursors. Syntheses have largely been restricted to the use of dangerous chemicals such as tris(trimethylsilyl)phosphine ($(TMS)_3P$), which is costly and highly sensitive to oxygen and water. Recently, less-hazardous tris(dialkylamino)phosphines have been introduced to produce InP QDs on par with those utilizing $(TMS)_3P$. However, a poor understanding of the reaction mechanics has resulted in difficulties tuning and optimizing this method.

In this work, density functional theory (DFT) is used to identify the mechanism of this aminophosphine precursor conversion. This understanding is then implemented to design an improved InP QD synthesis, allowing for the production of high-quality materials outside of glovebox conditions. Time is spent understanding the impact of different precursor salts on the reaction mechanisms and discerning their subsequent effects on nanoparticle size and quality. The motivation of this work is to formulate safer and less technical indium phosphide quantum dot syntheses to foster non-specialist and industrial implementation of these materials.

Acknowledgements

Arriving at this crowning moment in my research career would not have been possible without the help of countless people along the way. The ever-present trust and support of Prof. Thomas Nann over the last several (6?!) years were fundamental to my development as a researcher. You nurtured my creativity and fostered my confidence in my work, and being your student has shown me that excellence doesn't have to come at the expense of kindness or sincerity. It has been an honor to be a part of your group and I happily look forward to our future collaborations.

Similarly, the contributions of Dr. Renee Goreham and my groupmates, past and present, cannot be overlooked, as their feedback and creativity constantly helped me to refine my work and frequently provided new inspiration from unexpected places. A special thank you also goes to Dr. Matthias Lein for introducing me to computational chemistry – my thesis would be half as full and twice as boring without your patience in answering my silly questions and your assistance while I was beginning with this new field. I also would like to thank Prof. Geoffrey Strouse for getting me started with research and instilling me with a love of quantum dots and nanoscience.

A huge shoutout goes to my mentor-turned-bestie, Megan Crump *née* Muroski. You pushed me to do better, to have standards, and to get sh*t done. Thank you for getting me a job that one time, and for frequently letting me crash on your couch/spare bed, and for providing me with so much delicious food (and booze). But most importantly, thank you for the late night porch chats, the dog walking chats, and the video chats. Your companionship and advice over the last near-decade have made this journey so much easier and I very much look forward to having a real job so I can afford to visit more often.

And finally, the love and support of my friends and family have allowed me to grow and become the mostly functioning adult that I am today. A big thank you to my Wellington whānau — James, Josh, Dom, Rebecca, Hannah, SAJ, and many many others — that have made my stay in New Zealand so welcome and cherished. Thank you for the Orphan's Christmases, the BYOs, the weekends away, and everything in between that brought joy and eased my stress in this process. Thank you to my partner Andrew, for listening to me rant, making me eat when I get hangry, and for putting up with my socks on the floor. You have helped me to slow down and have provided a bit of stability in my life. I am so grateful to my family – Mom, Dad, Geramie, Haley, Amanda, Mia, and Graylon – for all the love and understanding you've shown me over the years, even when I moved to the other side of the world. Your constant encouragement and support have made it possible for me to become who I am today.

Love y'all, mean it.

Curriculum Vitae

Education

- Doctor of Philosophy in Chemistry, Victoria University of Wellington, 2019
  (anticipated)
- Bachelor of Science in Chemistry, Florida State University, 2012
- Bachelor of Science in Mathematics, Florida State University, 2012

Publications

- **Laufersky, G.**, & Nann, T. (2019). "1.01 - Physical chemistry of nanoparticle syntheses." In D. L. Andrews, R. H. Lipson, & T. Nann (Eds.), *Comprehensive Nanoscience and Nanotechnology (Second Edition)* (pp. 1-16). Oxford: Academic Press.
- Ayupova, D., Dobhal, G., **Laufersky, G.**, Nann, T., & Goreham, R. V. (2019). "An in vitro investigation of cytotoxic effects of InP/Zns quantum dots with different surface chemistries." *Nanomaterials*, 9(2), 135.
- Dobhal, G., Ayupova, D., **Laufersky, G.**, Ayed, Z., Nann, T., & Goreham, R. (2018). "Cadmium-free quantum dots as fluorescent labels for exosomes." *Sensors*, 18(10), 3308.
- **Laufersky, G.**, Bradley, S., Frécaut, E., Lein, M., & Nann, T. (2018). "Unraveling aminophosphine redox mechanisms for glovebox-free InP quantum dot syntheses." *Nanoscale*, 10(18), 8752-8762.
- Elmas, S., Beelders, W., Bradley, S. J., Kroon, R., **Laufersky, G.**, Andersson, M., & Nann, T. (2017). "Platinum terpyridine metallopolymer electrode as cost-effective replacement for bulk platinum catalysts in oxygen reduction reaction and hydrogen evolution reaction." *ACS Sustainable Chemistry & Engineering*, 5(11), 10206-10214.
- Bradley, S. J., Kroon, R., **Laufersky, G.**, Röding, M., Goreham, R. V., Gschneidtner, T., ..., Nann, T. (2017). "Heterogeneity in the fluorescence of graphene and graphene oxide quantum dots." *Microchimica Acta*, 184(3), 871-878.
- Dewi, M.R., **Laufersky, G.**, & Nann, T. (2015). "Selective assembly of Au-Fe_3O_4 nanoparticle heterodimers." *Microchemica Acta*, 182(13), 2293-2298.
- Dewi, M. R., **Laufersky, G.**, & Nann, T. (2014). "A highly efficient ligand exchange reaction on gold nanoparticles: preserving their size, shape and colloidal stability." *RSC Advances*, 4(64), 34217-34220.

Conference Presentations

- Feb. 2019 – 9th International Conference on Advanced Materials and Nanotechnology (AMN9) – *"Tuning Indium Phosphide Quantum Dots: From Theory to Practice"*
- Nov. 2017 – 26th Annual Massey-Victoria Symposium – Chemistry Postgraduate Student Seminar Day – *"Zinc Activation for Improved InP Quantum Dot Syntheses"*
- Nov. 2016 – MacDiarmid Institute Annual Symposium – *"Indium Phosphide Quantum Dots: Revising the Role of Zinc"*
- June 2016 – 9th Annual Dodd-Walls Centre Symposium – *"InP Synthesis: Striving for Full Spectrum Homogeneity in a III-V Nanoparticle System"*

Conference Posters

- July 2018 – Gordon Research Seminar & Conference – Colloidal Semiconductor Nanocrystals – *"Understanding Halide Dependence in Indium Phosphide Quantum Dot Syntheses"*
- July 2016 – Gordon Research Conference – Colloidal Semiconductor Nanocrystals – *"Indium Phosphide Synthesis: Striving for Full Spectrum Homogeneity in a III-V System"*
- Dec. 2015 – 7th International Chemical Congress of Pacific Basin Societies (Pacifichem) – *"Electrochemical Reduction of Carbon Dioxide Utilizing InP QDs and Au_{25} Clusters"*
- Nov. 2015, 2016, 2017, 2018 – MacDiarmid Institute Annual Symposia

  "Manipulating Halide Concentrations in Indium Phosphide QD Syntheses"

  "Zinc Activation for Improved InP Quantum Dot Syntheses"

  "Understanding Reduction Mechanisms in Indium Phosphide QD Syntheses"

  "Electrochemical Reduction of Carbon Dioxide Utilizing Small Metal Clusters"

Contents

List of Figures

List of Tables

List of Abbreviations

AO	atomic orbital
CB	conduction band
cps	counts per second
CTAB	cetyltrimethylammonium bromide
CTAC	cetyltrimethylammonium chloride
CTAX	cetyltrimethylammonium halide
DFT	density functional theory
ECP	effective core potential
E_F	Fermi energy level
eq.	equivalent(s)
Et	ethyl (-CH_2CH_3) group
FWHM	full-width at half-maximum
HF	Hartree-Fock
HOAc	acetic acid
HOMO	highest occupied molecular orbital
IEFPCM	integral equation formalism variant of the polarized continuum model
IR	infrared
IRC	intrinsic reaction coordinate
IRF	instrument response function
JCPDS	Joint Committee on Powder Diffraction Standards
KS	Kohn-Sham
LCAO	linear combination of atomic orbitals
LED	light emitting diode
L.H.S.	left hand side
MA	myristic acid
Me	methyl (-CH_3) group
MO	molecular orbital
NMR	nuclear magnetic resonance
OAm	oleylamine
OAmCl	oleylammonium chloride
OAmX	oleylammonium halide
OD	optical density
ODE	1-octadecene
OOCR	carboxylic acid-terminated hydrocarbon
PCM	polarized continuum model
P(DEA)$_3$	tris(diethylamino)phosphine
PLQY	photoluminescent quantum yield
QD	quantum dot
R.H.S.	right hand side
SCF	self-consistent field
SD	Slater determinant
STO	Slater-type orbital
TCSPC	time-correlated single-photon counting

TEM	transmission electron microscope
TMS	trimethylsilyl group
TOP	tri-*n*-octylphosphine
TOPO	tri-*n*-octylphosphine oxide
UV-Vis	ultraviolet to visible light
VB	valence band
XRD	X-ray diffraction
ZnP	zinc-activated aminophosphine

Chapter 1

Introduction

The advent of nanoscience significantly impacted materials science fields as the rush to improve particle syntheses led to more questions than answers. Nanosized particles have obvious surface area to volume improvements over their larger counterparts, which inherently allow for improved per-mass performance in most materials. However, the drive to synthesize smaller and smaller materials saw the rise of non-classical phenomena that could be manipulated by factors such as particle size, shape, and surface chemistry. The reduced number of atoms instigated the discretization of energy states while the size regime itself initiated quantum mechanical contributions to material behaviors. The onset of properties such as the localized surface plasmon resonance of metallic materials, the superparamagnetism of iron oxide, and the fluorescence of semiconductors at the nanoscale incited a wealth of research to explain and control such effects.

The field has greatly matured in recent decades, resulting in increasing use throughout diverse areas of research. Topics such as environmental remediation, energy harvesting and storage, catalysis, and medicine have all seen improvements based on the incorporation of nanomaterials. Industrial efforts have found use for nanoparticles in the development of technologies such as better batteries, higher resolution displays, and improved sensing platforms. Interest has even touched the public domain enough that basic principles of nanoscience are now being routinely taught in secondary education programs. While this acceleration of progress has resulted in a great degree of reproducibility, control, and utilization of nanoparticle syntheses, some particularly difficult branches of the field are far behind the more advanced front runners. Research into covalent materials – such as Group IV silicon and germanium or III-V gallium and indium pnictides – often struggles, as forming nanoscale crystalline particles of these compounds is synthetically challenging. Materials such as cadmium selenide may have pulled ahead in terms of total research mass, but their reliance on carcinogenic materials mean that they have limits on industrial upscaling and wide-spread implementation.

Indium pnictides (InE; E = N, P, As, Sb) show particular promise as the materials can potentially display luminescence over the UV, visible, near-infrared, and mid-infrared regions, respectively. However, they have fallen behind their more ionic II-VI counterparts due to the lack of easy-to-handle precursors and high oxygen- and moisture-sensitivity. The implementation of tris(dialyklamino)phosphines for the synthesis of InP quantum dots has revitalized interest in indium phosphide (as well as the other pnictides), as these precursors are significantly less hazardous than previous components. Due to the newness of the compounds to the field and the deviations from standard practices necessary to employ them, there is much to be discovered about how these aminophosphines form nanomaterials. It is hoped that determining a reaction mechanism will allow for the development of safer, improved syntheses that can be used by a wider range of chemists and produce industrially competitive materials.

The work presented herein outlines an effort to elucidate this aminophosphine mechanism of action and establish new synthetic routes for quality indium phosphide nanomaterials. The specific aims for this endeavor are as follows:

- Identify a reduction mechanism for the conversion of aminophosphines into indium phosphide.
- Examine the impact of different halides on this mechanism.
- Design new indium phosphide syntheses based on the mechanistic understanding developed.

Each of these targets is the focus of a Chapter in this thesis, which are accompanied by their own introductions and bibliographies. For the Chapters with heavy synthesis or instrumentation, there will also be a Section containing the relevant details explicitly. Before these however, Chapter 2 outlines the background necessary for the remainder of the work. A brief explanation of quantum dots and their general properties will be provided along with an examination of historical improvements of semiconductor nanoparticle syntheses. While these focus on II-VI materials, a comparison of these improvements to indium phosphide syntheses will be made alongside presentations of the current state of III-V semiconductor nanoparticle syntheses. This will be concluded with an overview of computational chemistry and its applicability to synthetic mechanisms. Chapter 3 will examine the mechanism of aminophosphine conversion to InP nanomaterials and the consequence of zinc chloride incorporation. Synthetic schemes manipulating this mechanism and spectroscopic data discussing the resulting particle quality will also be included. Using computational chemistry, Chapter 4 details the mechanistic effects of changing halides, focusing on understanding the impacts of different geometries on molecular energies and their potential impact on the reaction scheme. Chapter 5 then distills that theoretical work into a series of synthetic adaptations that aimed at manipulating the halide concentration with various additional compounds. Finally, the results are summarized in Chapter 6 along with a discussion and outline of further work that would benefit the field. Together, these should yield a more complete understanding of the synthesis of indium phosphide nanomaterials with aminophosphine precursors and facilitate their incorporation into non-specialist and industrial applications.

Chapter 2

Background

2.1 Quantum Dots

Materials can be roughly separated into metals, semiconductors, or insulators, depending on the nature of their electrical conductivity. This can be more accurately described utilizing Fermi levels (E_F) and band energies to determine a degree of conductivity, which can be demonstrated in Figure 2.1. In bulk materials, atomic or molecular orbitals blend into bands of bonding (valence) and anti-bonding (conduction) interactions, the energy difference between which is called a band gap. E_F is effectively a measure of the average energy level of electrons in a material and its placement in relation to the valence and conduction bands determines how easy it is to push an electron across the gap to conduct. In a metal, the Fermi level lies in one of the bands, indicating a thermodynamic ease of populating excited states. To contrast, insulators have E_F in the band gap, requiring a lot of energy to promote an electron to the conduction band. Semiconductors lie between these two states, with E_F being in the band gap but with the difference between bands being significantly smaller than in an insulator. Therefore, the energy to promote electrons is a manageable quantity usually on the ultraviolet to visible (UV-Vis) or infrared (IR) energy scales, allowing for controlled conductive processes and making them attractive for many electronics applications.

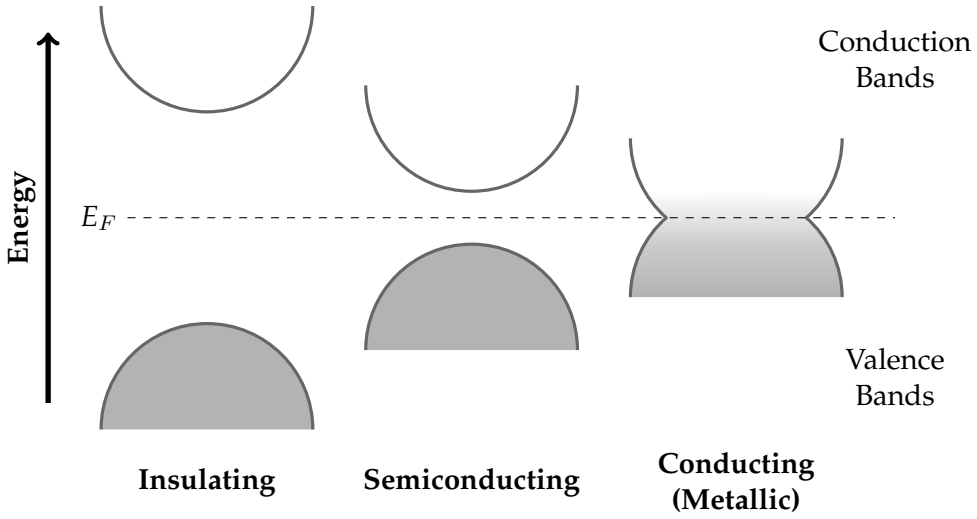

FIGURE 2.1: Generic energy diagram of valence and conduction bands for different types of materials with an example effective Fermi level, E_F.

When materials absorb energy, the electrons promoted to conduction band states leave behind charge voids in the valence band called holes, which are analogous to positively charged particles. As electrons and holes have opposite charges, they experience a number of attractive forces which result in the species generally existing in electron-hole pairs, referred to as excitons. The pair can be modeled similarly to a hydrogen atom and the typical interaction distance of the pair is called the exciton Bohr radius, r_{Bohr}. This material-specific quantity describes a probabilistic distance

the excited electron can travel from the hole and sets important size regimes. Equation 2.1 shows that it is dependent on the effective masses of the electron and hole as well as the dielectric constant of the crystal in question. When a crystalline structure has a radius much larger than its Bohr radius ($r \gg r_{Bohr}$) it is described as "bulk" material and electronically behaves the same regardless of size. Semiconductors in this regime have large band structures with broad absorption spectra initiating from the band gap energy and usually exhibit continuous absorption through higher (UV) energies. Electronic behavior can be tuned through processes such as carrier doping or the growth of particular facets, but these practices are typically limited in how far they can alter the crystal. Due to the large volume, excitons from absorption events generally have plenty of non-radiative decay pathways arising from high phonon density due to thermal population.

$$r_{Bohr} = \frac{\hbar^2 \varepsilon}{e^2} \left(\frac{1}{m_e} + \frac{1}{m_h} \right) \tag{2.1}$$

When $r \leq r_{Bohr}$, a semiconducting crystal becomes electronically confined as the exciton experiences repulsion from the physical boundary of the crystal's edge.[1–3] Because the size is below the Bohr radius, the electron and hole can also move independently throughout the particle. Although Coulombic forces ensure interaction between the species, the unpairing results in a number of phenomena such as increased exciton lifetime, decreased multiexciton generation, and even independent stabilities of the electron and hole for surface vs core localization. Due to this confinement, there are also increases in radiative electron-hole recombination pathways due to i) significantly fewer phonon states for de-excitations and ii) spatial separation from other excitons. This results in previously "dark" materials becoming emissive, sometimes with near unity photoluminescent quantum yields (PLQY).[4] However, the repulsion from the boundary edge of the crystal imposes an energetic barrier to the conduction of electrons and results in an effectively increased band gap. As exciton Bohr radii are usually on the nanoscale, this additional energy changes with size; as a particle shrinks, the boundary surface area to core volume ratio gets larger and so increases the change in energy.[5] Therefore, the band gap is dependent on size twofold: smaller particles have higher repulsive boundary energies as well as fewer unit cells to form electronic bands. Together, this can result in engineered products with narrow, discrete absorption and emission spectra, size-tunable to energies significantly greater than that of the bulk material band gap.

The theoretical nanoparticle above is usually described as a sphere due to the ease of depicting confinement by a single variable, r. The effect of confinement can then be modeled as a quantum mechanical particle-in-a-box and such particles are generally termed "quantum dots" due to their zero-dimensions of electronic propagation. While particle shape can change the degree of confinement (and therefore

energy of the band gap) by changing the size and shape of the particle-in-a-box problem, as long as the whole crystal falls into the $r \leq r_{Bohr}$ regime, it is still considered a quantum dot (QD). Structures with only 1- and 2-dimensional confinement exist and display different band behaviors,[6] which are illustrated in Figure 2.2. When only 2 dimensions are confined (i.e. r_x, $r_y \leq r_{Bohr}$; $r_z \gg r_{Bohr}$), the materials are referred to as quantum rods or wires. Their excitonic behaviors are similar to QDs, but display a higher energy tail to their absorption spectra due to the state blending in the z-direction. In 1-dimensionally confined quantum wells ($r_x \leq r_{Bohr}$; r_y, $r_z \gg r_{Bohr}$), the band discretization results in increasing blocks of energy. Both wires and wells hold a number of interesting applications due properties such as their polarizability, multiple exciton generation, and enhanced electron-hole separation. However, further explorations of these materials are beyond the scope of this work.

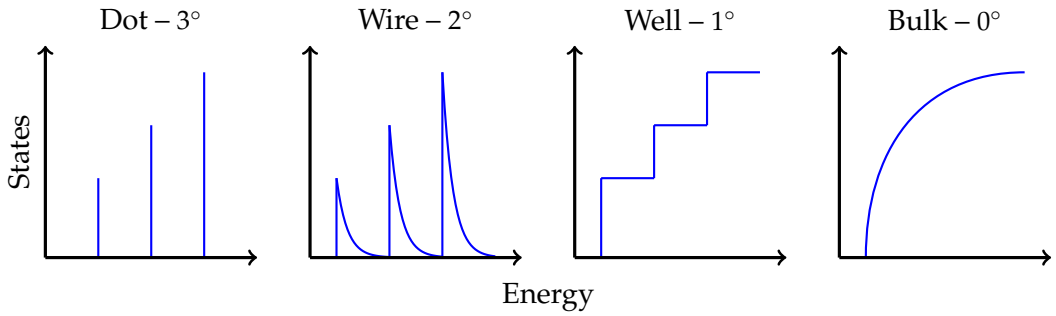

FIGURE 2.2: Representative density of states diagrams for different degrees of dimensional confinement, adapted with permissions from Gogna *et al.*[7] Copyright 2007 John Wiley and Sons.

Techniques to synthesize nanomaterials are as varied as the scientists who make them. Top-down methods, such as ultrasonic exfoliation, ball milling, and chemical etching, take a sample of bulk material and break or otherwise generate smaller particles from it. While these techniques can produce large quantities of evenly-composed material, they generally yield limited control over the final product and produce polydisperse sizes and shapes of nanomaterials. As most parameters of quantum-confined materials are size- and shape-dependent, this can result in confusing and irreproducible data. Ultra-high vacuum techniques can offer more control: disks of bulk materials are fragmented and the resulting particles fly through the vacuum chamber to land on a collection substrate or analytical device. These sputtered materials can be precisely isolated by electromagnetic selection techniques during their flight, so the resultant data can be analyzed for one size, mass, or charge distribution. While this results in excellent data, the amount of material produced is far less than necessary for practical applications.

Bottom-up methods, where crystals are grown from homogeneous solutions of molecular precursors, are often preferable as they offer a greater degree of control. Molecular beam epitaxy is the equivalent ultra-high vacuum technique to sputtered materials, and while it does yield atomically-precise nanoparticles, it still suffers from batch size restrictions. Taking advantage of the mature crystal growth field,

a number of colloidal synthetic routes have been developed and expanded to include nanoparticle materials. Among others, sol-gel, solvothermal, microemulsion, and hot-injection syntheses have afforded significant control over nanoparticle size, shape, and surface chemistry. As colloids, the resulting materials are generally stable in fluids which allow for easy solution processing and reduces the inhalation and contamination risks posed by nanoparticle powders. The next section will examine the theories of forming nanoparticles in solution, as the subsequent Chapters will rely on them heavily. Much of Section 2.2 will be adapted from a previous publication.[8]

2.2 How to Make a Nanoparticle

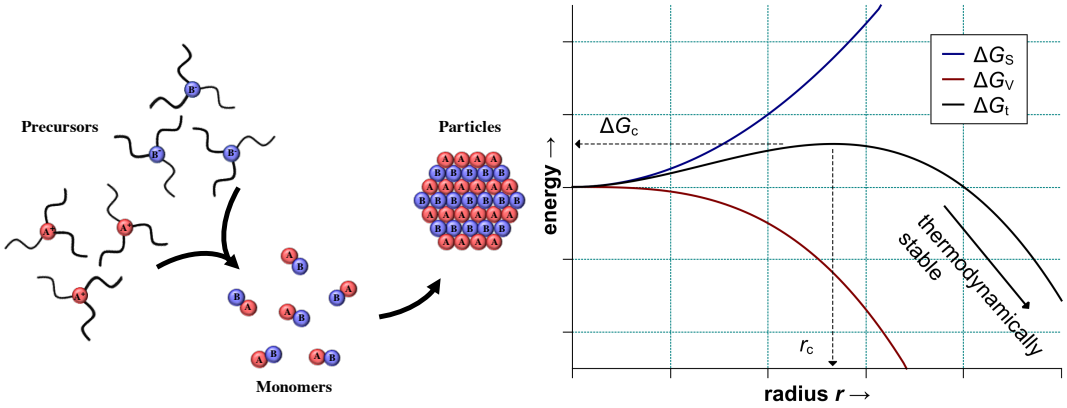

FIGURE 2.3: (Left) A simple diagram of the formation of monomers of a binary compound AB from precursor sources and their assembly into a particle. (Right) Free energies of formation of a surface, ΔG_S, a volume, ΔG_V, and a total spherical nanoparticle, $\mathbf{\Delta} G_\mathbf{t}$.

Particle formation is often thought of in terms of the generation and consumption of "monomers" of material. For the simple reaction outlined in left of Figure 2.3, the precursors A^+ and B^- undergo a redox reaction to form one AB unit, which is referred to as a monomer. While the reactants should be very soluble in the solvent, monomers generally are not, so they tend to aggregate together to minimize energy. This is called nucleation and forms a new phase that is a solid, and therefore heterogeneous to the reaction solution. The two media then have an energy difference that arises at the interface, which is often referred to as "surface energy" or "surface tension", γ. The creation of surfaces is then unfavorable, so small particles with high surface areas are unstable and likely to break down to monomers.

$$\Delta G_t = 2\pi r^2 \gamma + \frac{4}{3}\pi r^3 \Delta G_V^* \tag{2.2}$$

While making a surface is taxing, large volumes are stabilizing forces, and these two factors combine in Equation 2.2 to describe the total free energy of the particle

with regards to size[†]. The right side of Figure 2.3 illustrates these contributions, and it can be seen that there is some critical size, r_c, after which the addition of monomers makes nuclei more stable instead of less. Thus, particles can minimize the effect of their surface energy by growing to larger and larger sizes. While surface energy is clearly an important factor, several more variables influence the interplay of nucleation and growth, which will be discussed in more detail in the following sections.

2.2.1 Nucleation

When the concepts shown in the last section are scrutinized with any degree of detail, the ideas of insoluble monomers and unstable nuclei can seem to conflict. One way to reconcile this is to imagine the graph of Figure 2.3 as a step-wise function of discrete sizes instead. Then a chemical equation, such as $AB + (AB)_x \leftrightarrow (AB)_{x+1}$, can be drawn to relate two small clusters of monomers. A series of such equations can then be used to relate all clusters to one another and establishes an equilibrium. For small sizes, these additions are all unstable, so the equilibria favor the L.H.S., and there is a constant flux of growth and dissolution. However, once a cluster reaches the critical size, the energy to add a monomer is less than for a monomer to be removed. Then the equilibrium shifts and the stable particle grows as the unstable clusters lose monomers.

This large and complex barrier to nucleation means that it doesn't happen in typical solutions. Some imbalance is required to force a new phase to form, and manipulating concentration is the most common method to affect this. Supersaturation, s, is a useful term in the literature and depicts how much a solution is over-concentrated. There are different ways of calculating this, but the nanoparticle field tends to use $s = [M]/[M]_0$[††], which is on the scale of ∼1000-10000 in real solutions.

The factors that affect ΔG_c and r_c can be identified through a brief derivation of Equation 2.2. It can be seen through Equations 2.3 and 2.4 that increasing the supersaturation not only lowers the energy barrier of nucleation; it also shifts the critical size to smaller clusters. Together, these changes allow for more nuclei to be stabilized easier and sharply raise the rate of particle formation. Figure 2.4 (left) displays the dramatic influence that different concentrations and temperatures can have on the nucleation rate.

$$r_c = \frac{2\gamma V_m}{RT \ln s} \qquad (2.3) \qquad\qquad \Delta G_c = \frac{16\pi\gamma^3 V_m^2}{3(RT \ln s)^2} \qquad (2.4)$$

[†]Assumes a spherical particle of radius r and surface energy γ. A per-volume free energy ΔG_V^* is derived by the bulk material properties divided by the molar volume, V_m

[††]The concentration of monomers in the reaction solution, $[M]$, compared to the concentration of monomers in a solution in contact with an infinite plane of bulk material that would result in no net growth or dissolution of that plane, $[M]_0$. Yes, that confusing relationship *is* what they decided to go with.

Equations 2.3 and 2.4 also show the surface energy at the solid-liquid interface can impact both r_c and ΔG_c. If the two phases are very similar, then γ will be small and particles will not be difficult to stabilize. As with the discussion on s, this ease of formation results in faster nucleation rates, and Figure 2.4 (right) shows this effect for different surface energies. However, the interface between a solid and liquid will always be very high in energy due to their natural electronic differences. If stable nuclei do form, they will be very large and often beyond the nanoscale. When making nanoparticles, which are fundamentally high surface area materials, the interface must be altered to lower this strain. Typically this is done by introducing ligands, which are chemicals that help to make compounds more soluble. Generally, they have two "sides", one which has an affinity for the compound and the other that better matches the solution. When bound to particles, these can lower the surface energy and allow nanoscale nuclei to be stabilized.

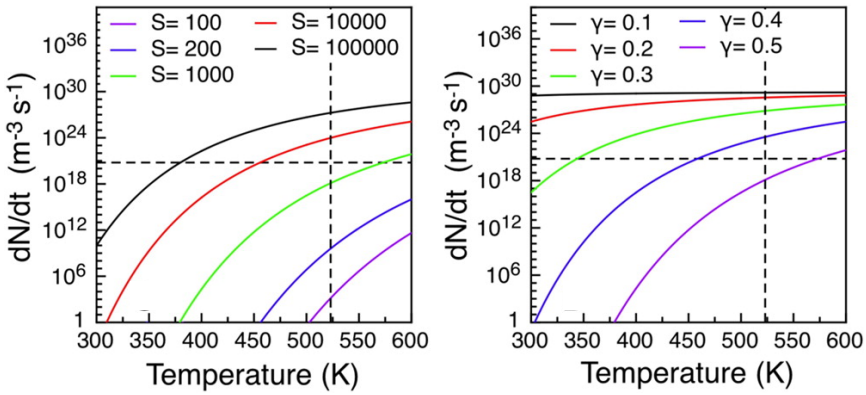

FIGURE 2.4: The effect of different supersaturations (left) and surface energies (right) on the nucleation rate. Reprinted with permission from van Embden *et al.*[9] Copyright 2015 American Chemical Society.

2.2.2 Growth

Once stable nuclei exist, the remaining monomers can easily attach to the surface and increase the size of the particle. This growth depletes the concentration of free monomers, which results in a reduction in s and a corresponding increase in r_c. Then, the particles that were previously stable begin to dissolve and results in a net transfer of mass from small particles to the larger ones still above r_c. This phenomenon is called Ostwald ripening and, as seen in Figure 2.5, can result in a broad distribution of sizes if it is allowed to proceed.

Regardless of size, no material is exempt from either growth or dissolution. Both behaviors occur for any given particle, albeit to different degrees depending on how much larger or smaller it is than the critical radius. These processes can be controlled either by the reaction rates of the growth and dissolution or by the diffusion of the monomers to the surface, whichever is slowest. If the addition (or removal) of a monomer has a high activation energy, it can be assumed to be slow and the rate of

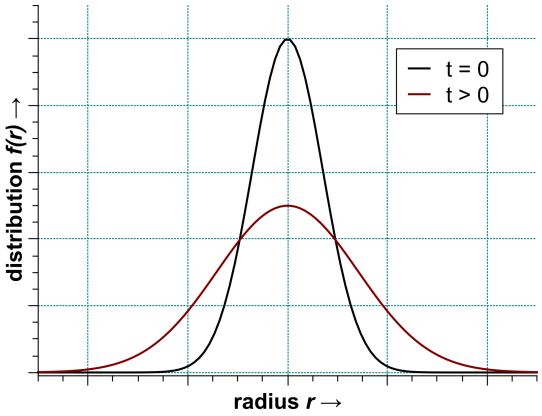

FIGURE 2.5: Evolution of a Gaussian distribution of nanoparticles with time following Ostwald ripening.

diffusion can be neglected. If the activation energy is low instead, then the change in size will be dependent on the rate of diffusion of monomers towards (and away) from the particle surface.

$$k_g(r) = k_g^0 \exp\left(-\alpha \frac{2\gamma V_m}{rRT}\right) \quad (2.5) \qquad k_d(r) = k_d^0 \exp\left((1-\alpha)\frac{2\gamma V_m}{rRT}\right) \quad (2.6)$$

The activated complex theory can be altered to model the kinetics of monomers interacting with a curved surface of a nanoparticle. Equations 2.5 and 2.6 then give the rates of growth and dissolution, respectively, where k_g^0 and k_d^0 are the corresponding rates for a plane of bulk material[†] and α is the transfer coefficient such that $0 \leq \alpha \leq 1$. These relationships are dependent on size, as a particle will appear more like a flat surface the larger it grows. The two rates and the solubility of the bulk material are then related as $K_{eq} = k_g^0/k_d^0 = c^*$.

Fick's first law can describe the diffusion of the monomers towards or away from the surface. Figure 2.6 illustrates the change in concentration with distance from a surface if the flux of materials is assumed to occur as a steady-state relationship. The concentration of monomers begins to vary from that of the bulk solution, c_b, once it reaches some threshold distance, δ, which is described as the diffusion layer. In this zone, monomers are continuously more scarce until c_i, the concentration of material at the interface of the surface. As the sizes of nanoparticles are generally smaller

[†]i.e. $k_g^0 = B_g \exp(-\Delta\mu_g^0/RT)$. Developed from the Arrhenius equation with B_g as the pre-exponential factor and $\Delta\mu_g^0$ as the activation energy for the addition of a monomer to an infinite plane. The corresponding relationships for the removal of a monomer are subscripted with d instead.

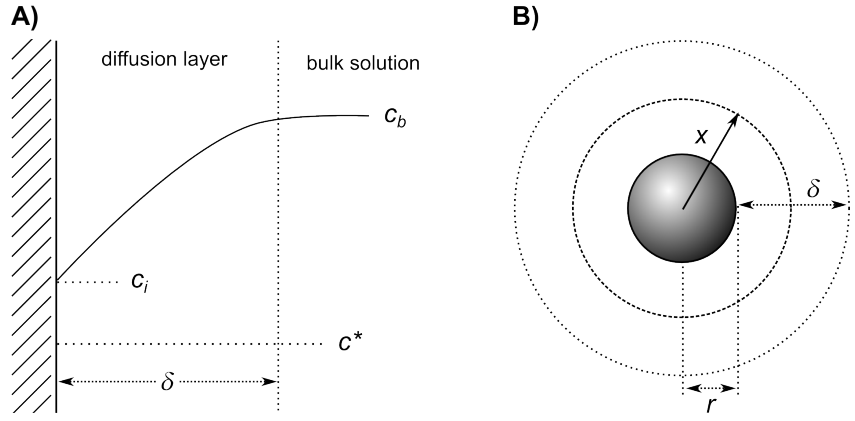

FIGURE 2.6: Diffusion of reagent to (A) a surface and (B) a spherical nanoparticle, with δ as diffusion layer thickness, c_b as bulk reagent concentration, c^* as solubility and c_i as reagent concentration at the particle surface. Adapted with permissions from Sugimoto.[10] Copyright 1987 Elsevier.

than δ, the description of the flux of monomers near them simplifies to Equation 2.7.

$$J = 4\pi x^2 D\frac{dc}{dx} \xrightarrow[\text{state}]{\text{steady}} 4\pi D\frac{r(r+\delta)}{\delta}(c_b - c_i) \xrightarrow{r \ll \delta} 4\pi Dr(c_b - c_i) \tag{2.7}$$

$$J = J_g - J_d \tag{2.8}$$

$$4\pi Dr(c_b - c_i) = 4\pi r^2 \left(k_g(r)c_i - k_d(r)\right) \Rightarrow \tag{2.9}$$

$$c_i(r) = \frac{rk_d(r) + Dc_b}{rk_g(r) + D} \tag{2.10}$$

The total change in the number of monomers that make up the particle must equal the net flux of materials to and from the surface. The per-area effects of these processes on the concentration can be described as the R.H.S. of Equation 2.9 if first-order growth and zeroth-order dissolution kinetics are assumed. When combined with Equation 2.7, this reveals that the amount of material at the interface changes with the size of the nanoparticle. The difference in amount of material can be directly related to the change in size, which can be determined through the combination of Equation 2.7 and 2.10, as seen below.

$$\frac{dr}{dt} = J\frac{V_m}{4\pi r^2} = V_m D\left(\frac{k_g(r)c_b - k_d(r)}{rk_g(r) + D}\right) \tag{2.11}$$

The growth rate dr/dt can be either positive (growth) or negative (dissolution). If this is set to zero to describe a critical radius of no net change, a lengthy derivation results in the same relationship as Equation 2.3. The magnitude of this rate increases the further a given particle is from r_c, which is illustrated nicely in Figure 2.7. This plot also shows that the rate of growth tends to become larger for smaller particles and higher supersaturations. Thus, in a distribution of growing particles, smaller particles grow faster than larger ones, which results in a narrowing of the overall size

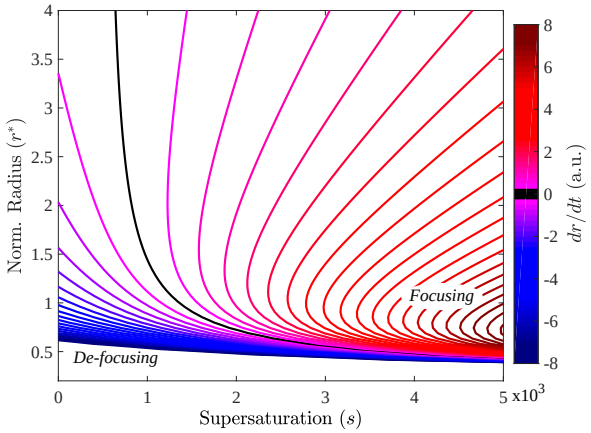

FIGURE 2.7: Contour plot of the size-dependent rates of nanoparticle growth, as determined by Equation 2.11. The contours have 0.4 a.u. spacing and the critical radius of $dr/dt = 0$ is presented in black.

distribution. This is sometimes called "focusing", and it is important to notice that it occurs only in reactions with large s. For low concentrations of monomers and/or very small particle sizes (bottom left of Figure 2.7), the growth rate is negative and the ensemble ripens like the one depicted in Figure 2.5.

2.2.3 Practical Considerations

While nucleation and growth have been presented here as sequential phenomena, in real solutions they often occur at the same time. In a normal synthesis, precursors A^+ and B^- are combined and heated to the reaction temperature together. This design produces a smooth rise in s over time, and the concentration eventually reaches some minimal level that prompts nucleation. While stable nuclei begin to grow in size, new particles are still forming because dr/dt is relatively small near r_c, which means it takes some time for s to drop below the nucleation threshold. Once that point is passed, the diverse range of nanoparticles then grow and shrink at different rates as r_c changes with decreasing monomer concentration. Because the amount of precursors limit the reaction, processes like these that compete for resources usually result in a broad array of final particle sizes. The best syntheses are therefore ones that separate the nucleation and growth phases as much as possible. If the solution can be allowed to undergo each process independently, then the final ensembles are often of higher quality and more size-pure.

Of the many techniques aimed at this isolation, the hot injection method is likely the most prolific and is adaptable for a wide range of materials. This scheme relies on at least one precursor being added to the reaction solution after it has reached the reaction temperature. When the withheld compound is injected into the main vessel, a two-fold effect is observed. First, the separation allows A^+ and B^- to be combined well above the T and s thresholds for nucleation. The inflation of these creates an artificial spike in the supersaturation and results in a massive rate of nucleation.

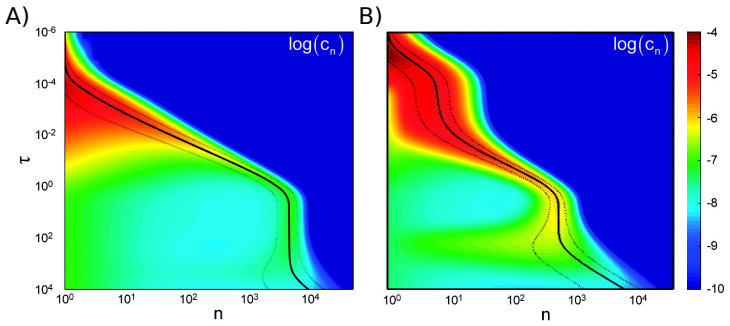

FIGURE 2.8: Concentration profiles as a function of cluster size, η, and scaled time, τ, of A) a synthesis with constant temperature ($T_\infty/T_0 = 1$) and B) a hot injection synthesis with high initial and reduced growth temperatures ($T_\infty/T_0 = 0.8$). Color scale corresponds to the log of the concentration. The solid and dashed black lines correspond to the mean of the size distribution and one standard deviation above and below the mean. Reprinted with permission from Rempel *et al.*[11] Copyright 2009 American Chemical Society.

Second, adding a "cold" precursor to a hot solution generates a net temperature drop in the system. The reduction inhibits new stable nuclei from forming and favors growth processes instead. These alterations then combine to create an intense burst of nucleation followed by a growth period with high s that instigates size focusing. Figure 2.8 compares Monte-Carlo simulations of each method and shows that using a hot-injection design inherently produces greater quantities of size-pure particles.

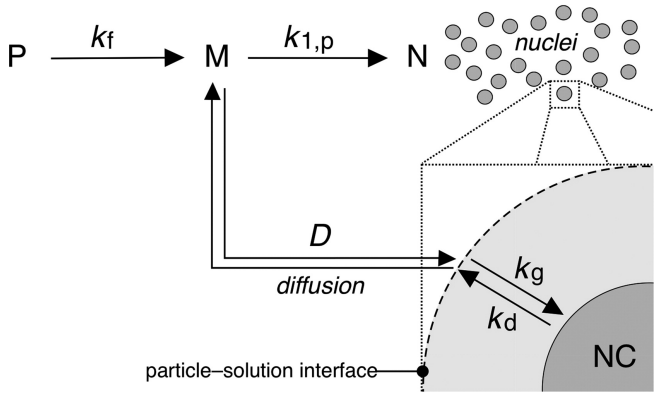

FIGURE 2.9: Total schematic of nanoparticle formation. Here, **P**recursors form **M**onomers with a rate of k_f which then precipitate into **N**uclei at a rate of $k_{1,p}$. More monomers then **D**iffuse towards (or away from) these nuclei to grow (or dissolve) nanocrystals, **NC**, at a rate of k_g (or k_d). Reprinted with permission from van Embden *et al.*[9] Copyright 2015 American Chemical Society.

Although the discussions here have focused on the consumption of monomers, the methods and rates of producing them are as equally important. Figure 2.9 outlines a more comprehensive view of the processes that form nanoparticles. Because the monomers are poorly soluble and the rates of their creation and use are quite high, the reactions here are said to be quasi-steady state. This conclusion means that the rates of precursor conversion, k_f, can directly impact the interplay between nucleation and growth.

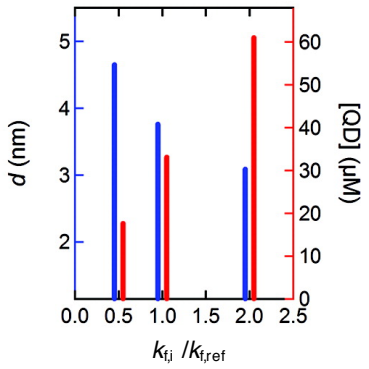

FIGURE 2.10: Resulting nanoparticle average diameters (blue) and concentrations (red) of simulated syntheses with altered precursor conversion rates, $k_{f,i}$. The horizontal axis is the rate relative to $k_{f,ref}$, such that $k_{f,ref}/k_{f,ref} \equiv 1$. Reprinted with permissions from Abe *et al.*[12] Copyright 2012 American Chemical Society.

Conceptually, a fast conversion rate should increase the saturation of the solution and result in more nucleation. How this affects the growth and dissolution of particles, however, is a bit more difficult to imagine. Monte-Carlo simulations can offer some insight into how the various other rates change with different k_f, as they can describe how a known array of particles changes over time for a set of predefined conditions.[12] Interestingly, the degrees of particle growth and decay in the systems were also found to scale with the rates of the precursors. This relationship created very similar time frames for the nucleation and ripening phases of the reactions, which meant that the initial nucleation events dictated the total number of particles in the final solutions. The particles then grew to their final sizes, which were simply a function of the remaining monomers divided among the total number of particles. The results of this effect are depicted in Figure 2.10 and imply that smaller nanoparticles may arise from faster precursor conversion rates if all other factors are equal.

In summary, the synthesis of nanoparticles from solutions can be broken up into three stages: precursor reaction, nucleation, and growth. The rates of reactions, surface energies, temperatures, and concentrations all have dramatic effects on each aspect of the particle formation. While this implies inherent degrees of overlap between these phases, the best reactions are those that can separate them as much as possible. Therefore, a large amount of research is focused on understanding precursor conversion and physically or temporally isolating the growth stages from each other.

2.3 Cadmium Chalcogenides

The vast majority of colloidal quantum dot literature is on cadmium chalcogenides as many of the initial breakthroughs began with cadmium sulfide (CdS). While these QDs are interesting, the material's large bulk band gap and small exciton Bohr radius

demonstrated limited utility. Table 2.1 shows cadmium selenide (CdSe) nanomaterials are potentially capable of tuning through the entire visible spectrum, which became a useful tool for exploring the quantum confinement regime. Although the telluride compounds could pose a more advantageous material due to the larger r_{Bohr}, their small band gap makes accessing the blue-green emission difficult as the degree of confinement must be much larger. As tellurium materials are also oxygen sensitive due to the preference for a 4+ oxidation state, CdSe materials have seen the largest focus of research. In turn, this has resulted in mature synthetic, surface modification, and device-incorporation procedures which allow CdSe QDs to continue to dominate the field.

	E_g (eV)	Dielectric constant (ε)	Electron effective mass (m_e)	Hole effective mass (m_h)	r_{Bohr} (nm)
CdS	2.42	5.7	0.165	0.8	2.36
CdSe	1.74	6.1	0.13	0.6	3.02
CdTe	1.44	7.2	0.14	0.35	3.81

TABLE 2.1: Bulk band gap and exciton Bohr radii of cadmium chalcogenides, as calculated from Equation 2.1.

2.3.1 History

Initial reports of cadmium-based quantum dots began appearing from widely varied crystallization disciplines. From arrested precipitation of salts in aqueous solutions,[13] to micelle-templated particle growth,[14] to decomposition of single-source molecular precursors in refluxing solvent,[15] investigations delved into as many techniques as were available to find the best parameters for narrow size distributions and absorption spectra. While useful, many syntheses were limited to a single size produced after ripening mechanics had stabilized particle distributions.[16] To isolate different sizes, usually large experimental changes such as concentration or micelle diameter were made, which can result in unpredictable shifts in particle distribution and quality. The syntheses were also complicated through the use of highly toxic or flammable chalcogen materials such as H_2S or bis(trimethylsilyl)selenide ($(TMS)_2Se$).

The landmark work of Murray *et al.* began to focus the field on organometallic precursors in organic solvents. As seen in the left of Figure 2.11, CdSe nanoparticles from ∼1.2-11.5 nm diameters were controllably synthesized by altering the reaction temperature.[17, 18] Centered on the reaction of dimethylcadmium in tri-*n*-octylphosphine oxide (TOPO), this work demonstrated the first example of hot-injection for nanoparticle syntheses. This is achieved experimentally by heating the solvent to the nucleation temperature (300 °C in this case) and rapidly injecting a room temperature solution of the reaction precursor(s). As discussed in Section 2.2,

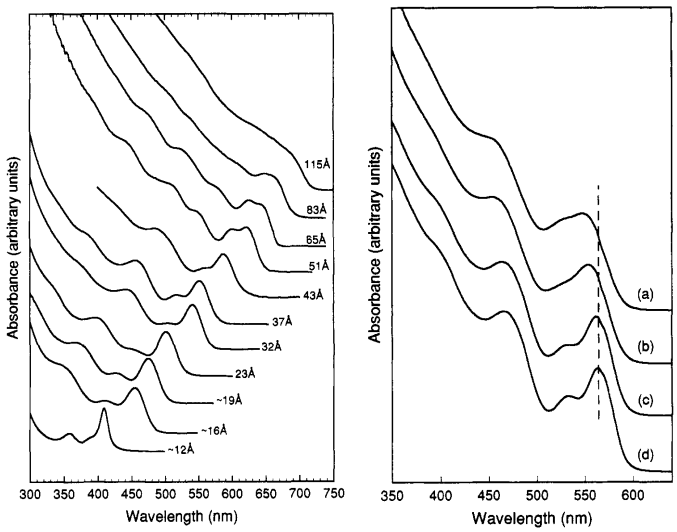

FIGURE 2.11: (Left) Absorption spectra of CdSe quantum dots synthesized with a hot-injection technique in tri-*n*-octylphosphine oxide at a range of temperatures. (Right) Effects of size-selective precipitation on a sample, with increasing precipitations (a) through (d). Reprinted with permission from Murray *et al.*[17] Copyright 1993 American Chemical Society.

the large supersaturation and temperature reduction from this produces homogeneous nanoparticle seeds which then use the remaining precursors in solution to evenly increase their diameters and result in monodisperse products.

In order to enhance sample purity, the authors also showed size selective precipitation to be a viable technique to isolate monodisperse samples. In this method, nanoparticle powders are suspended in a solvent compatible with the surface chemistry. Here, it is assumed that more polar phosphorus-oxygen moiety from TOPO is attached to the particle surface, which then means it has long hydrocarbon chains that are exposed to the reaction solution. These are generally compatible with nonpolar compounds, so solutions such as toluene, hexane, and chloroform are good sovlents to use . An antisolvent such as methanol or ethanol is then added drop-wise to this optically clear (not to be confused with colorless) solution until the mixture begins to flocculate. With stirring, the turbidity disappears, and more antisolvent is added drop-wise just until the stirring fails to redisperse the particles. Due to larger particles having the largest interparticle attraction, they are the first to precipitate when the solvent mixture polarity is perturbed by the antisolvent. These are then pelleted via centrifugation and the resulting precipitate and supernatant can be further purified through more rounds of selective precipitation, the effects of which can be seen on the right in Figure 2.11.[†] In this manner, a polydisperse synthetic route can still be accurately analyzed if enough care is taken during the precipitations.

[†]Due to the strong size correlation of quantum dots to UV-Vis light, peak characteristics in absorption spectra are often used as a measure of how mono- or polydisperse a given sample is. Typically, this is reported as the full-width at half-maximum (FWHM) of the lowest energy absorption feature, and smaller values should indicate more monodisperse size distributions. There are a number of factors that complicate this measure, and Appendix A highlights some key issues. In short however, it is fairly acceptable to use absorption FWHM to discuss InP sizes, less so for Cd-based materials.

This is especially useful for routes with long reaction times, those with close nucleation and growth temperatures, or those with low precursor activation energies.

The final contribution of this work was the evidence that the highly pyrophoric $(TMS)_2E$, which was the popular chalcogen source at the time, could be replaced with a milder phosphine-chalcogen complex with no loss in synthetic quality. Elemental sulfur, selenium, or tellurium could be easily combined with tri-*n*-octylphosphine (TOP) in a flask and heated/sonicated until the solution became homogeneous. This resulted in a TOP=E (E = S, Se, Te) precursor[19] that could be prepared in various concentrations, including 1:1 stoichiometries. While TOP does require the use of oxygen-free environments to avoid the formation of TOPO, simple Schlenk techniques and rubber septa are enough to keep this material for long-term use. As TOP-chalcogens are much easier to synthesize and handle than the trimethylsilyl-chalcogens, this represented a big step in the adaptation of these syntheses for non-specialist chemists.

2.3.2 Syntheses Today

In the following years, significant advances were made to make nanoparticle cadmium chalcogenide syntheses safer, faster, and with better yields. Adaptation of cadmium oxide (CdO) as the cadmium source instead of dimethylcadmium meant that the reaction was now completely with non-volatiles.[20] The addition of fatty amines like hexadecylamine focused nanoparticle sizes during syntheses, eliminating the need for the time consuming size-selective precipitation steps.[21] The use of fatty carboxylic or phosphonic acids to stabilize Cd^{2+} in solution allowed the substitution of the cheap non-coordinating 1-octadecene (ODE) for TOPO as solvent.[22] These improvements formed the basis of modern CdS, CdSe, and CdTe syntheses, with adjustments to exact formulations and concentrations driving optimizations.

With access to reliable and efficient synthetic routes, studies into mechanisms of nanoparticle formation began to take root. ^{1}H- and ^{31}P-NMR spectroscopy studies of the reaction solution over time showed the steady evolution of TOPO, even in air-free environments.[23] Further investigation suggested the TOP-Se precursor oxidized the acidic cadmium ligands during the formation of CdSe. Reactions done in excess chalcogen with strict control over cadmium showed formation of CdSe was proportionate with η_{Cd} x η_{Se}, suggesting the second order formation of the Cd-Se complex in Figure 2.12 is rate limiting. Insight from computational models of nucleation and growth processes led to the development of "post-focused" synthesis routes, with an emphasis of preserving chemical yields and size distributions for a range of nanoparticle sizes.[11, 24] Adaptations to robotic[25] and large scale reactions[26] demonstrated the utility of these investigations to generate simple and reliable processes.

With optimizations on cadmium core materials having reached its peak, considerable effort is now placed in identifying and tuning surface behaviors. Present

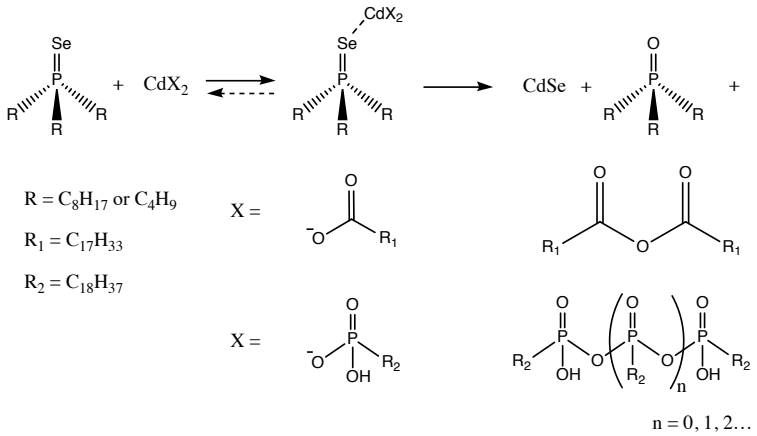

FIGURE 2.12: Mechanism of CdSe monomer formation from carboxylic and phosphonic acid precursors, adapted with permission from Liu *et al.*[23] Copyright 2007 American Chemical Society.

even in early reports,[27] the modification of quantum dot surfaces can impact solubility, stability, reactivity, and fluorescence. While core materials are usually highly crystalline, the high energy and strain of the nanoscale surfaces often result in dangling bonds and lattice defects.[28] These flaws can act as trap- or dark-states which can then result in reduced fluorescent yields or loss of emitted energy (broad, red shifted emission). In order to preserve color purity and improve quantum efficiencies, a number of strategies can be employed. The dangling bonds or traps can be directly removed via destructive techniques such as chemical etching[27] or high-intensity photobleaching[28] but the aggressive nature of these techniques can result in inhomogenous morphologies. The bonds can be passivated by electronically complimentary moieties in a ligand exchange process,[29] but these are usually inhibited by Langmuir isotherms and so require successive exchanges to reach completeness.[30]

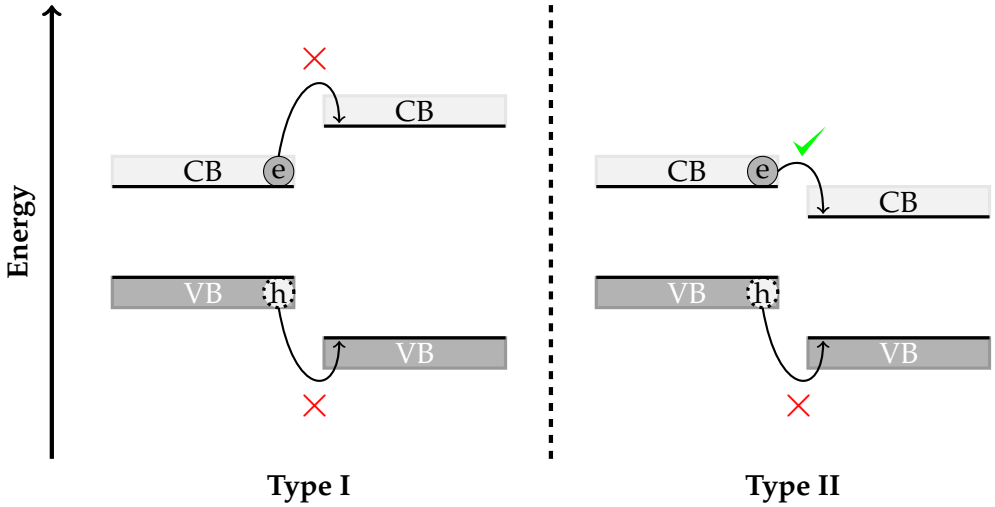

FIGURE 2.13: Example energy diagram of valence(VB) and conduction(CB) bands for different types of core/shell materials with excited electron (e) and hole (h) pairs. Arrows indicate the possibilities of transfer from the core to shell material.

The most widely used method of passivation is the controlled growth of a layer of another semiconductor on the surface of the initial material. These "core/shell" architectures can be designed in a number of ways depending on the application, but can be broadly classified as Type I and Type II by their band structures. As seen in Figure 2.13, Type I compounds utilize a shell material that has a wider band gap compared to the core; for CdSe, this is often zinc sulfide (ZnS) as their lattice parameters are similar enough to promote even shell growth. This can serve to electronically insulate the core and increase radiative electron-hole recombination as the nonradiative interactions with solvent or surface traps are reduced by the inability to transfer carriers out of the core.[21] Type II materials typically have one band of the shell placed such that one charge carrier can transfer to the shell but the other is trapped in the core. This physical separation extends the exciton lifetime and may assist in avenues such as multiple exciton generation or lasing. The slight loss of energy from band transfer also means that the emission can be red-shifted to reduce quenching by self-absorption. A cadmium sulfide or a blended CdSeS shell is often chosen for CdSe cores,[31] and advanced architectures such as dot-in-rods have been shown to further enhance the electron-hole separation.[32]

2.3.3 Applications

Due to their designable absorption and emission spectra, cadmium-based quantum dots have been utilized as fluorophores in a number of high-value technological applications. Inclusion into light-emitting diode (LED)[33–35] and lasing[36–39] technologies are obvious and popular choices, as electrical stimulation can yield specific-color emission while the small fluorophore diameter allows the reduction in device (or pixel) size without losing intensity. The broad absorption but single band gap emission also allows most QDs to be photoexcited by a single source. In downconversion LEDs[40] (absorption at high energy to yield emission at a lower energy), this allows easy color tunability for white light emitters, as ratios of red, green, and blue light can be easily adjusted by manipulating each QD concentration.

Their strong absorption features with effective electron-hole separations have also shown benefits for adapting these materials as solar harvesters. Dye sensitized solar cells have utilized them as dye replacements[41] as they are more stable for longer under harsher conditions, while also absorbing broad ranges of the visible spectrum. Due to many QDs having large Stokes shifts, they have also seen use as solar concentrators,[42–44] where the emitted light from solar absorption is trapped in the internal reflection planes of a glass and transmitted to solar collectors on the edges of the material. Further use as photochemical reactions centers are also possible,[45] as their tunable band gap placements make them attractive to generate specific products.

Because the majority of applications use protected core/shell materials, the solution interface of quantum dots can usually be modified to change particle solubility without significantly altering their emissive behavior. Surface exchanges can

swap the native fatty acids/amines for smaller pyridine,[30] bridging dithol,[46] or even water-soluble ligands such as mercaptoundecanoic acid or mercaptosuccinic acid.[47] This is a great advantage for biological applications, as their small size with bright fluorescence allows them to be used as non-bleaching fluorescent tags for biochemical studies[48] or even in rapid point-of-care detection devices.[49] Their high surface area also allow them to be conjugated with markers for specific cell types or disease states, to be decorated with molecules designed to initiate cellular uptake, or to be loaded with drugs to treat a condition. Utilizing combinations of these methods can even allow for a multi-platform diagnostic, therapeutic, and analytical tool.

While the applications discussed so far are intended as alternatives to current fluorophores, there are a number of new technologies being theorized and developed that stem from the unique properties of quantum dots. Utilization as a single-photon emitter has opened up a number of pathways in quantum computing and cryptology. The ability to stimulate and count individual photons emerging from single quantum dots is closer to becoming reality due to extensive photonics research. Highly engineered particles have begun to demonstrate simultaneous non-bleaching, anti-bunching, and non-blinking, all of which are necessary to ensure high stimulation-detection probabilities.[50–52]

Despite the relatively low amount of material utilized by nanotechnologies, cadmium-based products face numerous hurdles regarding health and safety and consumer regulations on local, national, and international levels. Matters become more complicated when designing materials for biological applications: strict size, passivation, and ligand requirements[53, 54] inhibit much of the utility for cadmium QDs as diagnostic, therapeutic, or research materials. As such, there is a practical limit of these materials for large scale manufacture and distribution.

2.4 Indium Pnictides

Indium pnictides are III-V materials utilizing In^{3+} and an element from the Group 15 nitrogen family (pnictogens, E^{-3}). Low-toxicity indium phosphide is the logical replacement for cadmium chalcogenides as its small direct band gap of 1.34 eV and large exciton Bohr radius suggest tuning emission from far-red through UV radiation should be possible. Table 2.2 shows the arsenic- and antimony-based nanomaterials, although toxic, also generate interest as specific near- and mid-IR absorptive materials respectively. Infrared emission is fascinating as a biological fluorescent label due to its visibility through tissues and bone, opening opportunities for these materials as real-time *in vivo* imaging dyes. The theoretical advantages presented by nanomaterials in narrow linewidths and high fluorescent yields also create opportunities for developing improved lasers, infrared cameras, and even room-temperature devices due to the electronically confined nature of the products.

	E_g (eV)	Dielectric constant (ε)	Electron effective mass (m_e)	Hole effective mass (m_h)	r_{Bohr} (nm)
InP	1.34	12.4	0.067	0.65	10.80
InAs	0.36	14.6	0.022	0.41	37.00
InSb	0.165	17.7	0.014	0.1	69.28

TABLE 2.2: Bulk band gap and exciton Bohr radii of indium pnictides, as calculated from Equation 2.1.

2.4.1 Indium Phosphide

Indium phosphide (InP) nanomaterials have been attractive alternatives to cadmium chalcogenides for decades due to their reduced toxicity[55–57] while potentially emitting over a large spectral range. However, a number of barriers presented challenges to produce quality materials; struggles to achieve crystallinity, monodispersity, and control over reaction rates caused InP popularity to fall behind that of the cadmium chalcogenides. Recently, a few breakthroughs have resulted in a bloom of papers furthering the quality, reproducibility, and accessibility of InP quantum dot syntheses. These new works combined with the push for non-toxic fluorophores for industrial applications have galvanized the field, however there is much to be understood about the formation of these materials.

As with the cadmium-based materials, initial reports of nanosized InP crystals sprouted from a variety of disciplines. However, it was quickly established that only highly reactive phosphorus sources could produce materials small enough to display confinement effects; phosphine gas (H_3P),[58] white and red elemental phosphorus (P_4), and tris(trimethylsilyl)phosphine ($(TMS)_3P$)[59] were investigated for suitability. Of these, $(TMS)_3P$ became the most widely used, as its popularity as a source in molecular beam epitaxial techniques[60] ensured commercial availability. The first colloidal suspensions of InP quantum dots were synthesized in TOPO, but under unusually intense conditions.[61] At temperatures ≤ 240 °C, the indium salt and $(TMS)_3P$ precursors formed amorphous particles, with no distinct absorption, emission, or crystallographic features. Above this temperature, it still required 3 days to reach chemical completeness, and although spectroscopic features were present, the peak widths of the band gap absorption were quite broad. In similar work, Guzelian *et al.* used size selective precipitation to isolate precise samples from a 6 day, 265 °C reaction[62] and showed the long elevated temperature plus a 3 day annealing sequence produced highly crystalline confined materials from ∼2-5 nm in diameter.

Problems with polydispersity, non-crystallinity, and high temperatures abound with III-V syntheses due to their covalent nature.[63] The separation of nucleation and growth phases necessary for monodisperse samples becomes difficult when precursor conversions require substantial energy to form InP monomer subunits. While more reactive precursors such as H_3P and P_4 can be used at lower temperatures, the

materials synthesized still require an annealing step at elevated temperatures to produce crystalline particles. This process often instigates Ostwald ripening mechanics and can lead to broadened size distributions.

While typical photoluminescent quantum yields of cadmium-based core materials reach ~30-40%, annealed and size-selected InP quantum dots rarely emit above 1%. This is due to a persistent thin amorphous or defect-heavy layer on the nanoparticle surface which promotes non-radiative decay. As with CdSe, chemical treatment with alcoholic solutions of hydrofluoric acid can be employed to remove this troublesome layer and increase PLQY to ~40%, but again this leads to broadening from inhomogeneous etching.[64, 65] The implementation of a zinc sulfide shell is often more reliable,[66] as the Type I junction can relieve surface strain and affect a more crystalline interface. Zinc selenide shells are also useful, as their lattice parameters match those of indium phosphide much better.[67] However, the nearness of the conduction bands means a reduced confinement of the exciton and red-shifted absorption and emission energies. Blended ZnSeS/ZnS layers have been shown to provide the best of both options, producing reduced lattice mismatch while still displaying a strong Type I confinement and minimal red-shift.[68, 69]

Like CdSe, implementing non-coordinating solvent systems like 1-octadecene also served to reduce the need for size-selective precipitations in InP nanomaterials. Interestingly, years passed between the initial report[70] (by the same authors of the Cd-ODE report) and a thorough investigation of time, temperature, and the alkyl chain length of the fatty acid ligand.[71] Due to the increased monodispersity, one-pot core/shell growth procedures proved to push PLQY upwards of ~70% and reduced emission FWHM to <60 nm by reducing the exposure of the core to oxygen.[72–74] This afforded greater stability of the materials to air, as well as allowed harsher procedures such as aqueous ligand exchanges to be used, and became the standard for InP syntheses.[75]

While $(TMS)_3P$ is easier to handle when compared to phosphine gas or elemental phosphorus, it is still highly pyrophoric, requiring the use of a glovebox to ensure oxygen- and moisture-free environments. The hazardous and sensitive nature of this phosphine presents challenges for the casual user, industrial upscaling, and even overseas distribution. Therefore, the field was energized when a new class of safer aminophosphines began to be utilized for InP syntheses.[76] Experimental optimizations have brought these new precursors near to par with $(TMS)_3P$,[67, 77] but there is much to be understood about their mechanism, which will be outlined in Chapter 3. The motivation of this work is to identify the conversion mechanism of this P(III) aminophosphine into the P(-III) of InP nanomaterials, which should indicate better ways to design the synthesis for improved nanoparticle quality. Examination of the aminophosphine mechanism will also lend insight to the the synthesis of other InE nanomaterials with aminopnictine corollaries and inspire novel ways of synthesizing those materials.

2.4.2 Indium Arsenide

With the bulk band gap energy corresponding to ~3.5 μm light, the quantum confinement of indium arsenide (InAs) materials suggests nanoparticles absorbing and emitting short wavelength infrared energy could be achieved. Although IR detectors and lasers are also desirable technologies, the penetration depth of infrared energy[78] for tissue and bone means these nanomaterials are highly sought after as fluorescent labels for less-invasive *in vivo* studies.[79, 80] Table 2.2 shows the small effective electron mass and high dielectric constant make InAs quantum dots also interesting materials to investigate for energy applications such as harvesters for solar cells.[81, 82] A confined heavy hole with extremely light electron mass allows multiple carrier generation with much more efficient onset and yields than those of the bulk or nanostructured II-VI materials.[83] Additionally, capping the QDs with small inorganic clusters has demonstrated high electron mobility and ambipolar photocurrents.[84, 85]

The synthesis of indium arsenide nanomaterials progressed along similar lines to that of their phosphide counterparts. Arsine gas was replaced with $(TMS)_3As$,[86] shelling improved photoluminescent quantum yields and linewidths,[87] and non-coordinating solvents reduced polydispersity.[70] However, problems still persist as the high precursor reactivity causes depletion of the InAs monomer concentration for the formation of ultra-small, stable clusters.[88] If uncontrolled, this results in broadened size distributions as Ostwald ripening dominates particle growth, especially for the formation of larger crystals. Reaction design can turn this high reactivity into advantages: temperature-dependent postfocusing[88] or continuous precursor injection[89] strategies can manage to synthesize a range of InAs particle sizes with PLQY ~50-90% while preserving narrow size distributions.

While the high reactivity of $(TMS)_3As$ can be compensated against, alternative precursor sources have been investigated for a more controlled monomer conversion. Single-source materials,[90] organoarsines,[91] and silylamides[92] have been used but pale in comparison to the quality of the trimethylsilyl-based syntheses. Initially, aminoarsines yielded poor results,[93] but have since been reexamined. Utilizing the understanding of the tris(dialyklamino)phosphine conversions, tris(dimethylamino)arsine was used to successfully produce a range of InAs nanomaterials with moderate (PLQY ~30%, FWHM ~100 nm) photoluminescent quality.[94] While these results were better than the previous reports, tris(diethylamino) phosphine had to be used as the reducing agent to facilitate the As(III) to As(-III) conversion. Similarly, another study found that diisobutylaluminum hydride had to be included to reduce the aminoarsine as well.[95] Study into the mechanism of these reductions should lead to better reaction designs for improved size distributions and chemical yields.

2.4.3 Indium Antimonide

Following the trend going down the group, indium antimonide (InSb) has the smallest bulk band gap of Table 2.2 and therefore should produce materials that can be

tuned through mid-IR energies. In addition to the shifted spectral range, InSb also has a number of properties making it a quite interesting material to study. Possessing the highest room-temperature electron mobility and smallest exciton binding energy of all known semiconductors means that bulk InSb is already useful for ultrafast electronic circuits. The largest known exciton Bohr radius of any material also implies that any quantum confinement should produce materials of significant interest to electronic and photovoltaic applications.[96]

Unfortunately, there are very few nanoscale indium antimonide syntheses reported. The first report of InSb quantum dots appeared in 2008 and utilized a "hot"-injection synthesis of $(TMS)_3Sb$ into In-ODE solutions to produce nanomaterials similarly to the arsenic and phosphorus analogues.[97] However, as the synthesis was performed at 100 °C and limited characterization was undertaken, the crystallinity and composition of the materials are suspect. The first full demonstration of colloidal InSb QD synthesis arrived years later, with the use of Sb-silylamide precursors.[98] The introduction of a strong reducing agent was necessary to form polydisperse, aggregated nanoparticles that had to be provided with ligands post-synthesis and size-selectively precipitated to perform further analyses. Another study used In-silylamide with aminostibine in a variety of concentration ratios, temperatures, and solvents and were able to controllably generate a variety of sizes and InSb crystal phases.[99] Outside of these two reports, one laser-ablation[100] and one microwave-assisted synthesis[101] have been reported to produce nanoscale InSb, but both methods yielded polydisperse, low-quality materials. Although the lack of concerted research in the field provides little guidance, it also presents opportunities to publish new avenues of study.

2.5 Computational Chemistry

While many aspects of quantum dot syntheses can be inferred by the rate of nanoparticle growth and the properties of the final products, oftentimes discussions of precursor interactions stem from assumptions on the mechanism of conversions. On one hand, these can sometimes be validated: in binary systems such as Cd-COOR/TOP-Se or In-COOR/$(TMS)_3P$, the rates of reactions with varying precursor concentrations can elucidate the difference between a first- and second-order formation of monomers. This implies the difference between Figure 2.12 being limited by the equation on the right or left respectively, and is generally accepted as adequate. On the other hand however, multi-step mechanisms are less intuitive and require more careful handling. As intermediates are often short-lived and not easily observable though standard techniques, computational chemistry can provide insight into the likelihood of structure formation and chart a map of reaction pathways.

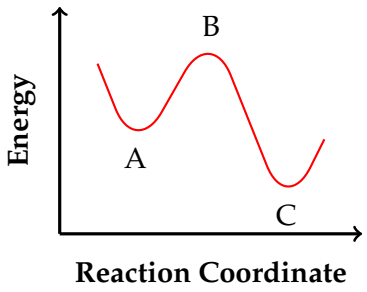

FIGURE 2.14: A simple potential energy surface of the reaction $A \rightarrow C$ through a transition state, B.

2.5.1 Potential Energy Surfaces

The central pillar of computational chemistry is the potential energy surface, which connects species by changes in some internal coordinate(s), $\boldsymbol{R}$, with the energy of the species, $E(\boldsymbol{R})$. Figure 2.14 outlines a typical energy dependence of a coordinate which changes state A to state C. Both states are energetic minima, with C being the "global minimum" as it is the lowest in energy. This two dimensional surface appears similar to a generic energy diagram of a chemical reaction: reactants transform to products after passing through some energetic barrier. In terms of free energy, if the products are lower in energy than the reactants, then the reaction is thermodynamically favorable. This is much the same for the potential energy surface: if a minimum is lower in energy than another (or the lowest of all, i.e. "global"), then it is more stable. While this comparison is easy to make, it is less easy to actually computationally find minima.

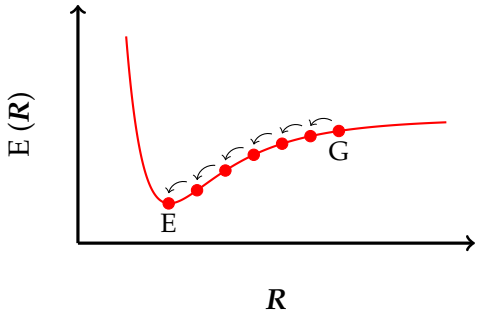

FIGURE 2.15: Lennard-Jones potential of a H–H bond distance. Minimization steps from a "guess", G, to the equilibrium minimum E.

Thinking of the potential energy of a molecule of H_2, as the distance between two H nuclei arbitrarily far apart come closer together, they experience attractive dispersion forces which lower the overall energy of the system. If they come too close together however, they experience steric repulsion which significantly increases the energy of the molecule. These two interactions form a Lennard-Jones potential, depicted in Figure 2.15, that has a minimum value E. This value is also called the equilibrium geometry as it is the most stable energy. If nothing was known about the scale or where this curve was placed in terms of total energy, a guess, G, at the

coordinate of interest could be made and the energy calculated. The energy of several guesses could be compared and this might yield a rough sketch of the potential energy surface, but finding the minimum this way would be time consuming and highly inaccurate. Assuming this surface is a continuous function, then for every point on the curve there is also a slope, defined by the first derivative of the energy with respect to the coordinate. Also known as the force of the coordinate, if the slope of the guess coordinate is zero, this indicates a stationary point. The second derivative at this point then indicates the difference between minima, maxima, and asymptotes, as seen in Equation 2.13. Thus, locating a minimum from a given guess coordinate can then be done as in Figure 2.15 by calculating the first derivative and taking small steps in the direction of "steepest descent" until the slope reaches a near-zero value. As these are numerical techniques, the calculations generally continue until an acceptably small cutoff parameter set by the user is reached.

$$\frac{dE}{dR} = 0 \text{ for stationary points} \tag{2.12}$$

$$\frac{d^2E}{dR^2} > 0 \text{ for minima} \qquad \frac{d^2E}{dR^2} = 0 \text{ for asymptotes} \qquad \frac{d^2E}{dR^2} < 0 \text{ for maxima} \tag{2.13}$$

While seemingly straightforward, the example depicted in Figure 2.15 is simplified to one variable. In real scenarios, the energy of the H_2 molecule actually depends on six variables: $E(x_1, y_1, z_1, x_2, y_2, z_2) = E(\mathbf{q})$, one for each Cartesian coordinate of each atom. This is where the term *surface* arises, as this simple two atom molecule now has six independent axes which map a multidimensional surface of potential energy. This then demands that locating stationary points requires:

$$\frac{\delta E}{\delta \mathbf{q}} = 0 \implies \frac{\delta E}{\delta x_1} = \frac{\delta E}{\delta y_1} = \cdots = \frac{\delta E}{\delta z_2} = 0 \tag{2.14}$$

Evaluating the second derivative of this surface $\delta(\delta E/\delta \mathbf{q})/\delta \mathbf{q}$ becomes complicated as several non-zero cross terms ($\delta^2 E/\delta q_i \delta q_j$ for $i \neq j$) exist at stationary points. The complete set of partial second derivatives is referred to as the Hessian, **H**, and this can be normalized in order to invoke the logic of Equation 2.13. Through common matrix diagonalization displayed in Equation 2.15, the Cartesian coordinates can be transformed into orthogonal normal coordinates, l_i. The set of normal coordinates, **L**, correspond to eigenvectors and the related eigenvalues, **f**, can be used to classify stationary points as minima, maxima, or asymptotes.

$$\mathbf{H} = \begin{pmatrix} \frac{\delta^2 E}{\delta x_1^2} & \frac{\delta^2 E}{\delta x_1 \delta y_1} & \cdots & \frac{\delta^2 E}{\delta x_1 \delta z_2} \\ \frac{\delta^2 E}{\delta y_1 \delta x_1} & \frac{\delta^2 E}{\delta y_1^2} & \cdots & \vdots \\ \vdots & \vdots & \ddots & \vdots \\ \frac{\delta^2 E}{\delta z_2 \delta x_1} & \cdots & \cdots & \frac{\delta^2 E}{\delta z_2^2} \end{pmatrix} \xrightarrow{\mathbf{f} = \mathbf{L}^t \mathbf{H} \mathbf{L}} \mathbf{f} = \begin{pmatrix} \frac{\delta^2 E}{\delta l_1^2} & 0 & \cdots & 0 \\ 0 & \frac{\delta^2 E}{\delta l_2^2} & \cdots & \vdots \\ \vdots & \vdots & \ddots & \vdots \\ 0 & \cdots & \cdots & \frac{\delta^2 E}{\delta l_6^2} \end{pmatrix} \tag{2.15}$$

In addition to identifying key points on the potential energy surface, the eigenvectors can unveil other important information about the molecule. As the normal coordinates are comprised of linear combinations of Cartesian vectors, each l_i yields trajectories that displace the atoms of the molecule. For coordinates with eigenvalues that equal zero, the vectors result in no net change in energy. These correspond directly to physical phenomena: for the linear H_2 molecule, this is observable as three translations along and two rotations about the Cartesian axes. The remaining coordinate, which has a non-zero eigenvalue, is related to a molecular vibration of the H–H bond stretch. Because the second derivative is positive, this identifies a minimum, as any change in the bond length represents climbing out of the potential well and increasing energy. The eigenvalue can even be directly related to the frequency of that vibration, v_i, by Equation 2.16, where $(\delta^2 E/\delta l_i^2) = k_i$ and μ is the reduced mass of the molecule. Therefore, a geometry optimization of N atoms will minimize the $3N$ forces of Equation 2.14 to find a stationary point. After which, the $3N \times 3N$ Hessian will be normalized to identify $3N$ eigenvectors and eigenvalues. These normal coordinates yield molecular transformations and calculations with $3N - 6$ (or $3N - 5$ for linear molecules) positive force constants identify minima. These correspond directly to the familiar degrees of vibrational freedom and are related to molecular bends and stretches.

$$v_i = \frac{1}{2\pi}\sqrt{\frac{k_i}{\mu}} \tag{2.16}$$

While the calculation of equilibrium geometries is extremely useful, the real power of computational chemistry arises with the identification of transition states on the potential energy surface. There exists a potential energy pathway connecting any two minima on the PES, and the lowest energy saddle point of this is referred to as the transition state, observable in Figure 2.14 as *B*. Much like minima, the transition state exhibits zero force and possess $3N - 6$ non-zero force constants. However, one of the molecular vibrations will have an negative eigenvalue (yielding in an imaginary vibrational frequency), which implies the vibration will cause a reduction in energy instead of a gain. Following the corresponding eigenvector will result in an intrinsic reaction coordinate (IRC) pathway that becomes either geometry *A* or *C* at the next minimum, depending on if the vector is followed forward or backward. This is therefore a first order saddle point and if more than one force constant is negative, this is said to be a second (or higher) order transition. Typically, a geometry like this is held to not be a true transition state, as it implies it is not the lowest energy pathway between the two states.

Although they are mathematically very similar to minima, there exist no general strategies, such as steepest descent, to find saddle points. This makes the identification of transition state structures very challenging and is often the most time-consuming aspect of computational chemistry. The calculations of these structures are well worth the effort though, as they directly relate to concepts such as activation energies and rates of reactions.

2.5.2 Quantum Mechanics

The geometry optimization strategies in the previous section require some expression of the molecular energy to implement. Methods utilizing classical physics, such as molecular mechanics, can assign forms of energy based on the potential and kinetic energy contributions of molecular stretches, bends, torsions, and electrostatic interactions as well as corrections for interrelated properties. These require parameterized constants to accurately match computed systems to known geometries and vibrational behaviors. As there are diverse bonding environments, so too are there diverse sets of constants, called force fields, which apply most accurately to the specific subsets of molecules they were optimized for. The energy terms in molecular mechanics calculations tend to be relatively simple to compute, resulting in heavy use with large systems composed of roughly similar bonding environments (e.g. polymers, biomolecules, solvent simulations, etc). Although force fields now exist for many kinds of interactions, the need for parameterization means that exploring new environments, or those with little known vibrational or crystallographic data, becomes difficult. Quantum mechanics however, can provide a useful strategy for studying these ill-defined molecular systems.

$$\lambda = \frac{h}{p} = \frac{h}{mv} \tag{2.17}$$

Investigations into the specific properties of electrons and nuclei led to the development of the wave-particle dichotomy. According to Equation 2.17, which is the de Broglie equation, all particles can also be described as waves, where p, v, and m are the momentum, speed, and mass of a particle respectively. However, Planck's constant h is quite small, so only particles with small mass (i.e. electrons) have appreciable wavelengths. There then exists some wave function, Ψ, that describes these systems. The hallmark of quantum mechanics is Equation 2.18, which states for a given wave function, operators ϑ exist which return e scalars as properties of that system.

$$\vartheta\Psi = e\Psi \tag{2.18}$$

The complex conjugate of Ψ, $|\Psi^*\Psi|$, gives the probability density of the wave function. As most chemical structures work in the real space and it is assumed they exist somewhere in the space examined, this yields $\int |\Psi^2| = 1$. These properties culminate in in Equation 2.19, which states that an operator, $\hat{H}$, exists that yields the energy, E, for a given wave function (i.e. atom/molecule).

$$\hat{H}\Psi = E\Psi \tag{2.19}$$

More colloquially known as the Schrödinger equation, this relationship is the basis for quantum mechanical calculations of energy. To explore Equation 2.19, examining the 1-dimensional kinetic energy of an electron moving in the x direction

proves useful. From classical mechanics, a wave can be described by Equation 2.20.

$$\frac{\delta^2}{\delta x^2}u(x,t) = \frac{1}{v^2}\frac{\delta^2}{\delta t^2}u(x,t) \tag{2.20}$$

Assuming functions exists such that $u(x,t)$ is separable (i.e. $u(x,t) = \Psi(x)f(t)$) allows:

$$f(t)\frac{\delta^2}{\delta x^2}\Psi(x) = \frac{1}{v^2}\Psi(x)\frac{\delta^2}{\delta t^2}f(t) \tag{2.21}$$

If the solution for the time-dependent function is taken as the typical $f(t) = Ae^{i\omega t} + C$, then this simplifies to the following Equation when normalized.

$$\frac{\delta^2}{\delta x^2}\Psi(x) = -\frac{\omega^2}{v^2}\Psi(x) = -\frac{4\pi^2}{\lambda^2}\Psi(x) = -\frac{4\pi^2 m^2 v^2}{h^2}\Psi(x) \tag{2.22}$$

Providing $E_{kin} = \frac{1}{2}mv^2$ and $\hbar = \frac{h}{2\pi}$ then allows:

$$\frac{\delta^2}{\delta x^2}\Psi(x) = -\frac{2m}{\hbar^2}E\Psi(x) \tag{2.23}$$

$$-\frac{\hbar^2}{2m}\frac{\delta^2}{\delta x^2}\Psi(x) = E\Psi(x) \quad \Rightarrow \tag{2.24}$$

$$\hat{H} = -\frac{\hbar^2}{2m}\frac{\delta^2}{\delta x^2} \tag{2.25}$$

Equation 2.25 is then the Hamiltonian operator which yields the 1-dimensional kinetic energy when applied to a wave expression. This also indicates that the corresponding wave function solution is one that is twice differentiable and yields the same function, perhaps with some coefficient. A function that meets those criteria is a sinusoidal curve, however it can be easily seen that the Schrödinger equation has many solutions.

$$\hat{H}\Psi_a(x) = E(a)\Psi_a(x) \tag{2.26}$$

$$\Psi_a(x) = \sin\left(\frac{2\pi}{\lambda}ax\right) \tag{2.27}$$

$$a = 1, 2, ... \tag{2.28}$$

The integer value a is referred to as a quantum number, and the lowest energy value ($a = 1$) is taken as the ground state energy. Although this can be expanded to more dimensions where $\hat{H} = -\hbar^2\nabla^2/2m$, only the kinetic energy of a single electron has been considered; the Hamiltonian for real molecules is significantly more complex. Equation 2.29 includes the kinetic energies of each electron (indexed with i, j) as well as the nuclei (indexed with k, l), alongside terms for the electron-nuclei attractions as well as interelectron and internuclear repulsions. Further terms can be added to account for external electric or magnetic fields, relativistic effects, or any

number of other significant contributions.

$$\hat{H} = -\sum_i \frac{\hbar^2}{2m_e}\nabla^2 - \sum_k \frac{\hbar^2}{2m_n}\nabla^2 - \sum_i \sum_k \frac{e^2 Z_k}{r_{ik}} + \sum_{i<j} \frac{e^2}{r_{ij}} + \sum_{k<l} \frac{e^2 Z_k Z_l}{r_{kl}} \tag{2.29}$$

The increased complexity has significant consequences on the Schrödinger equation. Primarily, solutions for wave functions of more than one particle do not exist. In order to utilize quantum mechanics, a number of approximations have to be made. Although they are not perhaps "true" solutions, these manipulations have proven mathematically rigorous and compare well with experimental evidence. First, the Born-Oppenheimer approximation states that nuclei will appear stationary to electrons due to the difference between their masses, so their wave functions will behave independently and can be solved separately.

$$\hat{H}_{el} = -\sum_i \frac{\hbar^2}{2m_e}\nabla^2 - \sum_i \sum_k \frac{e^2 Z_k}{r_{ik}} + \sum_{i<j} \frac{e^2}{r_{ij}} \tag{2.30}$$

$$\hat{H}_{nuc} = -\sum_k \frac{\hbar^2}{2m_n}\nabla^2 + \sum_{k<l} \frac{e^2 Z_k Z_l}{r_{kl}} = V_N \tag{2.31}$$

$$(\hat{H}_{el} + V_N)\Psi_{el} = E_{el}\Psi_{el}(q_i; q_k) \tag{2.32}$$

As the nuclei are treated as stationary, V_N is a constant and often left out of Equation 2.32 until the end of the calculation. While this has simplified many things, Equation 2.30 still includes multiple particles, the wave function for which has already been stated to not have a solution. Similarly to Equation 2.32, the orbital approximation allows a multielectron wave function Ψ to be estimated from a collection of 1-electron wave functions ψ_i (with corresponding operators, $\hat{h}_i$) for a fixed molecular geometry. This forms a molecular orbital (MO) which describe the energy and localization of an electron across the molecule. Thus the electronic Hamiltonian, hereafter referred to as just $\hat{H}$, can be written for N electrons across M nuclei as:

$$\hat{H} = \sum_{i=1}^{N} \hat{h}_i \tag{2.33}$$

$$\hat{h}_i = -\frac{\hbar^2}{2m_e}\nabla_i^2 - \sum_{k=1}^{M} \frac{e^2 Z_k}{r_{ik}} \tag{2.34}$$

Note that as only one electron is examined, electron-electron repulsions are left out of Equation 2.34. Therefore, a correction term $V_i\{j\}$ is included, which utilizes the probability density, ρ, of the other electrons, j where $j \neq i$, in reference to the one examined. The one-half term in the final sum accounts for the double counting of electrons that would occur (i.e. for $i = a, j = b$ and $i = b, j = a$) while allowing the relationship to be fully integrable over all space.[†]

[†]These equations are still not entirely correct, as they only examine Coulomb interactions. A more complete representation is expressed later in Equations 2.50 – 2.54.

$$\hat{h}_i = -\frac{\hbar^2}{2m_e}\nabla_i^2 - \sum_{k=1}^{M}\frac{e^2 Z_k}{r_{ik}} + V_i\{j\} \tag{2.35}$$

$$V_i\{j\} = \sum_{i\neq j}\int \frac{\rho_j}{r_{ij}} d\mathbf{r} = \frac{1}{2}\sum_{i\neq j}\iint \frac{|\psi_i|^2|\psi_j|^2}{r_{ij}} d\mathbf{r}_i d\mathbf{r}_j \tag{2.36}$$

This presents an interesting problem however, as this implies that in order to find wave functions, you must first know the wave functions. To handle this, the self-consistent field (SCF) method was developed. First, guess wave functions are provided to construct the first operators, $\hat{h}_i$. Solutions to $\hat{h}_i\psi_i = e_i\psi_i$ then yield new ψ_i, which then construct a new 1-electron Hamiltonians. This iterative process continues until there is negligible change between the new and old wave functions (i.e. convergence). The electronic energy is then

$$\hat{H}\Psi = \hat{H}\psi_1\psi_2...\psi_N \tag{2.37}$$

$$= \sum_{i}^{N}\hat{h}_i\psi_1\psi_2...\psi_N \tag{2.38}$$

$$= \sum_{i}^{N} e_i\psi_1\psi_2...\psi_N \tag{2.39}$$

$$= \left(\sum_{i}^{N} e_i\right)\Psi = E\Psi \tag{2.40}$$

The 1-electron Schrödinger equation for hydrogen has definite solutions of the form $\varphi = e^{-r}/\sqrt{\pi}$. Therefore, a linear combination of these atomic orbitals (LCAO), such as Equation 2.41, could be used to form a guess of the more complex molecular orbitals. A set of K functions of φ_i, referred to as the basis set, can be used with a set of weighting coefficients a_i to form the often unintuitive MO wave functions.

$$\psi = \sum_{i=1}^{K} a_i\varphi_i \tag{2.41}$$

These hydrogenic orbitals, or Slater-type orbitals (STO), become computationally cumbersome for double electron integrals such as $V_i\{j\}$ and Equation 2.36, which don't often have analytic solutions. However, Gaussian functions of these integrals do have analytic solutions and a sum of Gaussians like those in Equation 2.42 can approximate an STO. Increasing the number of primitive functions, X, can more accurately model the STO, but typically three functions is a modest approximation and are designated as an STO-3G basis set.

$$e^{-\alpha r} \approx \sum_{i}^{X} c_i e^{-\beta r^2} = \varphi \tag{2.42}$$

As they are getting expensive, these φ orbitals are generally calculated once (for each orbital of each atom type) before being applied throughout the computation. However, this can make it difficult for different bonding environments of the same atom within one molecule (i.e. the alkyl-, aromatic-, and carboxyl-carbons of phenylacetic acid), as they may have different electronic behavior. To accommodate this, oftentimes the valence and core electrons are treated differently.

$$\varphi_{1s} = \sum_{i}^{3} c_{i_{1s}} e^{-\beta r^2} \tag{2.43}$$

$$\varphi_{2s_A} = \sum_{i}^{2} c_{i_{2s_A}} e^{-\beta r^2} \tag{2.44}$$

$$\varphi_{2s_B} = e^{-\beta r^2} \tag{2.45}$$

Equations 2.43 - 2.45 are an example of a split-valence basis set, where the oxygen core $1s$ electrons can be described as before with one orbital comprised of three Gaussians. But the valence $2s$ orbital is modeled with two orbital functions, φ_{2s_A} and φ_{2s_B}, in which the allocated Gaussians are split into two and one contributions, respectively. Although there are the same number of Gaussian functions that would have normally been utilized, the coefficients of φ_{2s_A} and φ_{2s_B} present in Equation 2.41 are now variables to be optimized with each environment. Demonstrated on the left in Figure 2.16, this can allow for a range of $2s$ orbital sizes to occur, but makes this basis set (labeled 3-21G) computationally more expensive. Termed "double-ζ basis sets", these can be expanded with more primitives to provide more control. Adding more core functions, such as in 6-21G or 6-31G, can increase accuracy as more functions can better model the STO. Adding more split-valence contributions (e.g. the triple-ζ 6-311G basis) can increase flexibility as more variables exist for optimization. Naturally, these additional functions also significantly increase computation time.

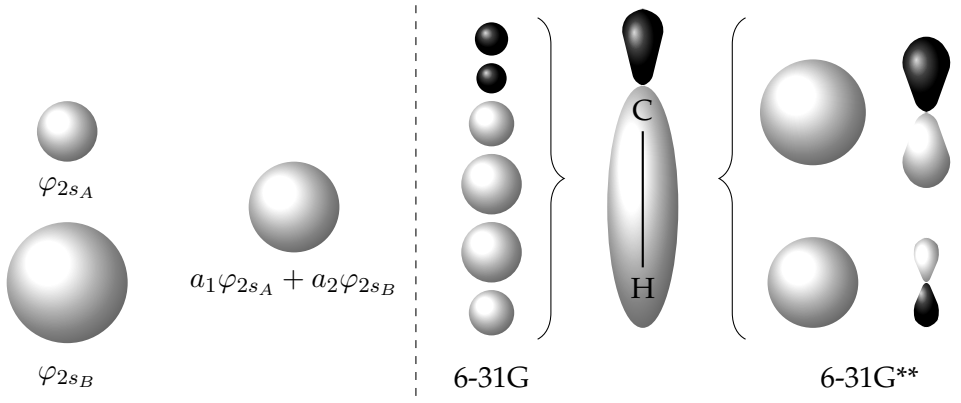

FIGURE 2.16: (Left) Example of a split-valence 3-21G basis set forming an orbital of intermediate size. (Right) Different basis set representations of a C–H σ bond using delocalized s functions (6-31G) or localized polarized p functions (6-31G**).

Although non-intuitive, Gaussian s-type orbitals are capable of modeling many chemical bonding environments if allowed to localize away from nuclei, such as in Figure 2.16. However, it can be necessary to include a large number of s orbitals to model difficult interactions, which can hamper computational efficiencies. The inclusion of p- and d-type functions can improve basis sets to better depict polarized and diffuse bonds, respectively. Chemically, this arises as orbital hybridization (sp, sp^2, sp^3, etc.) and basis sets such as 6-31G** in Figure 2.16 can better model asymmetric electron densities. As p- and d-type orbitals are much more expensive than s orbitals, they are often only included if the environment is complex or heavily asymmetric. Clearly, choosing an appropriate basis set is significant and impacts computational accuracy, costs, and trustworthiness.

Quantum numbers were briefly introduced with Equations 2.26 - 2.28 and are appropriately handled within the solutions to the Schrödinger equation using Hamiltonians that have been presented so far. The principle quantum number ($n = 1, 2, ..$) responsible for electron shell assignment, angular momentum ($l = 1, 2, ..., n - 1$) designating the shape of the electron orbital, and the magnetic quantum number ($m = -l, -l + 1, ..., 0, ..., l - 1, l$) accounting for the orientation of the orbital are all folded into the AO (and therefore MO) representations. However, it was determined that at least one more key quantum number existed and needed to be included. Termed "spin" with eigenvalues of $\pm\hbar/2$, this was found to explain why a beam of silver atoms splits into two beams after passing through a magnetic field.

As the Pauli exclusion principle states that no two electrons can have the same exact quantum numbers, new orthonormal spin eigenfunctions, α and β, had to be developed. This also proscribed that no more than two electrons can exist in a molecular orbital, giving rise to the spin-pairing of electrons as is generally understood today. Mathematically, the Pauli exclusion principle more accurately states that the electronic wave functions are antisymmetric and therefore must change sign if two electrons swap positions. Given P_{ij}, an operator that interchanges the coordinates of i and j, this appears in a simple example as Equation 2.46.

$$P_{12}\Psi(\mathbf{q}_1(1), \mathbf{q}_2(2)) = \Psi(\mathbf{q}_2(1), \mathbf{q}_1(2)) = -\Psi(\mathbf{q}_1(1), \mathbf{q}_2(2)) \tag{2.46}$$

Constructing a wave function to accommodate spin might look something like $\Psi = \psi_a(1)\alpha(1)\psi_b(2)\alpha(2)$, but by applying P_{ij}, it can be seen that the antisymmetry requirement is not fulfilled.

$$\begin{aligned} P_{12}[\psi_a(1)\alpha(1)\psi_b(2)\alpha(2)] &= \psi_b(1)\alpha(1)\psi_a(2)\alpha(2) \\ &\neq -\psi_a(1)\alpha(1)\psi_b(2)\alpha(2) \end{aligned} \tag{2.47}$$

By slightly altering the wave function to Equation 2.48, it is seen that interchanging the positions now produces the desired effect.

$$\Psi = \frac{1}{\sqrt{2}}[\psi_a(1)\alpha(1)\psi_b(2)\alpha(2) - \psi_a(1)\alpha(1)\psi_b(2)\alpha(2)] \tag{2.48}$$

This new wave function is actually the two-coordinate case for a matrix determinant, which can be expanded for N electrons where χ is a spin orbital, the product of ψ_i with a spin function. Called the Slater determinant (SD), the wave function of Equation 2.49 changes signs when any two rows or columns are interchanged, which accurately models the antisymmetry necessary to properly account for the Pauli exclusion principle.

$$\Psi_{SD} = \frac{1}{\sqrt{N!}} \begin{vmatrix} \chi_1(1) & \chi_2(1) & \cdots & \chi_N(1) \\ \chi_1(2) & \chi_2(2) & \cdots & \chi_N(2) \\ \vdots & \vdots & \ddots & \vdots \\ \chi_1(N) & \chi_2(N) & \cdots & \chi_N(N) \end{vmatrix} \tag{2.49}$$

Additionally, the Slater determinant serves to correctly include spin-repulsion effects for electrons of the same spin, which were unaccounted for in the non-interacting case of Equation 2.36. If two electrons ($i = 1, j = 2$) of the same spin (α) are examined, then their wavefunctions (ψ_a and ψ_b), could be evaluated by combining Equation 2.36 and Equation 2.49 as follows.

$$\int {}^3\Psi_{SD}\frac{1}{\mathbf{r}_{12}}{}^3\Psi_{SD}d\mathbf{r}_1 d\omega_1 d\mathbf{r}_2 d\omega_2 \tag{2.50}$$

$$\begin{aligned} &= \frac{1}{2}\left[\int |\psi_a(1)|^2|\alpha(1)|^2\frac{1}{\mathbf{r}_{12}}|\psi_b(2)|^2|\alpha(2)|^2\ d\mathbf{r}_1 d\omega_1 d\mathbf{r}_2 d\omega_2\right. \\ &\quad - 2\int \psi_a(1)\psi_b(1)|\alpha(1)|^2\frac{1}{\mathbf{r}_{12}}\psi_a(2)\psi_b(2)|\alpha(2)|^2 d\mathbf{r}_1 d\omega_1 d\mathbf{r}_2 d\omega_2 \\ &\quad \left. + \int |\psi_b(2)|^2|\alpha(2)|^2\frac{1}{\mathbf{r}_{12}}|\psi_a(1)|^2|\alpha(1)|^2 d\mathbf{r}_1 d\omega_1 d\mathbf{r}_2 d\omega_2\right] \end{aligned} \tag{2.51}$$

$$\begin{aligned} &= \frac{1}{2}\left[\int |\psi_a(1)|^2\frac{1}{\mathbf{r}_{12}}|\psi_b(2)|^2 d\mathbf{r}_1 d\mathbf{r}_2\right. \\ &\quad - 2\int \psi_a(1)\psi_b(1)\frac{1}{\mathbf{r}_{12}}\psi_a(2)\psi_b(2) d\mathbf{r}_1 d\mathbf{r}_2 \\ &\quad \left. + \int |\psi_b(2)|^2\frac{1}{\mathbf{r}_{12}}|\psi_a(1)|^2 d\mathbf{r}_1 d\mathbf{r}_2\right] \end{aligned} \tag{2.52}$$

$$\begin{aligned} &= \int |\psi_a(1)|^2\frac{1}{\mathbf{r}_{12}}|\psi_b(2)|^2 d\mathbf{r}_1 d\mathbf{r}_2 \\ &\quad - \int \psi_a(1)\psi_b(1)\frac{1}{\mathbf{r}_{12}}\psi_a(2)\psi_b(2) d\mathbf{r}_1 d\mathbf{r}_2 \end{aligned} \tag{2.53}$$

$$= J_{ab} - K_{ab} \tag{2.54}$$

These two electrons of the same spin are typically said to have triplet degeneracy

or be in a triplet state[†], denoted here by ${}^3\Psi_{SD}$. Comparisons with Equation 2.36 show that J_{ab} is just the Coulomb integral from before. However, this is affected by the new term, K_{ab}, which reduces the electron-electron repulsion we would expect to see in electrons. This energy is exactly the same if electrons change position ($i = 2, j = 1$) and is thus called the exchange integral.

However, this is only the case for two electrons of the same spin. Equation 2.50 can be reevaluated for two electrons of opposite spins, $\alpha(1), \beta(2)$, which are said to be in a singlet state represented by ${}^1\Psi_{SD}$. The largest consequence of this is the $|\alpha(1)|^2$ and $|\alpha(2)|^2$ of middle term of Equation 2.51 become $\alpha(1)\beta(1)$ and $\alpha(2)\beta(2)$, respectively. As α and β are orthogonal eigenfunctions, this term collapses to 0 and only the J_{ab} term remains at the end. Equation 2.35 can now be more accurately rewritten as the 1-electron Fock operator seen in Equation 2.55. The prefactor of 2 for the Coulomb integral arises from each electron experiencing repulsion from both singlet and triplet interactions, while exchange only occurs for the latter.

$$f_i = -\frac{\hbar^2}{2m_e}\nabla_i^2 - \sum_{k=1}^{M}\frac{e^2 Z_k}{r_{ik}} + 2J_i - K_i \tag{2.55}$$

Taken all together on a very basic level, this means that with a given Hamiltonian, basis set, and geometry, molecular spin-orbitals can be formed from a self-consistent field procedure, which can then be used to calculate the energy of the molecule. If an optimization process is utilized, a new geometry is chosen so $\delta E/\delta \mathbf{q} \rightarrow 0$ and the procedure is re-initiated from the SCF step until the minimization criteria are reached. While feasible for most calculations, this encompassing electron accounting becomes unwieldy for heavy atoms. Not only does the computational cost of correlating more electrons become taxing, so too does the Hamiltonian, as the high velocity of core electrons require relativistic terms to accurately model their energy. Methods involving effective core potentials (ECPs) can offer a reduction in calculation time as well as increased accuracy while eliminating the need for a more complicated operator. Primarily, the innermost core electrons are removed and treated separately with a variety of methods to generate a potential about the atomic nuclei. Then the remaining (valence) electrons are treated as above, with the core potentials incorporated into the nuclear Hamiltonian of Equation 2.32. ECPs are usually included into basis sets as core electron behaviors are largely unchanged from system to system, allowing dramatically faster computation times for electron-heavy systems.

[†]The interaction of two particles of $\pm 1/2$ spin result in a net angular momentum of 1 or 0. For the case of $s = 1$, the angular momentum has equivalent likelihood to be represented by any the three rotational axes of physical space. For $s = 0$ (spin-paired), the momentum collapses trivially and is described as a singlet state. This is better described quantum mechanically, but the reader is directed elsewhere[102] for a more rigorous explanation.

2.5.3 Density Functional Theory

The above methodology outlines the procedures of Hartree-Fock (HF) calculations, which draw heavily upon molecular orbital theory. As such, the 1-electron orbitals are chemically intuitive so using them to build the Slater determinant makes sense. However, once improvements such as interelectron correlation corrections are introduced, the form of the resulting wavefunction becomes messy and unintuitive. Because the Hamiltonian only requires the atomic numbers and positions of nuclei alongside the total number of electrons examined, an operator could be developed that relies upon one variable. Equations 2.56 and 2.57 show that electron density, ρ, could be used to construct the Hamiltonian.

$$N = \int \rho(\mathbf{r}) d\mathbf{r} \tag{2.56}$$

$$\left.\frac{\delta \bar{\rho}(r_A)}{\delta r_A}\right|_{r_A=0} = -2Z_A\bar{\rho}(0) \tag{2.57}$$

The form of the Hamiltonian, however, presents a small difficulty. As potential and kinetic energies are separable, the potential energy contributions of the electron density can be easily accounted for with classical mechanics. The attraction of the density towards k nuclei and repulsion of "electron" a with "electron" b, respectively, are as follows:

$$V_{ne}[\rho(\mathbf{r})] = \sum_{k}^{nuclei} \int \frac{Z_k}{|\mathbf{r} - \mathbf{r}_k|}\rho(\mathbf{r}) d\mathbf{r} \tag{2.58}$$

$$V_{ee}[\rho(\mathbf{r})] = \frac{1}{2}\iint \frac{\rho(\mathbf{r}_a)\rho(\mathbf{r}_b)}{|\mathbf{r}_a - \mathbf{r}_b|} d\mathbf{r}_a d\mathbf{r}_b \tag{2.59}$$

The kinetic energy of the density is a more nebulous concept. Equation 2.25 and the 3-dimensional corollaries are no longer applicable as the continuous charge distribution imposed by ρ involves no distinct particles. To address this issue, a system was envisioned in which an infinite volume held an infinite number of electrons. The space in which the electrons move has a uniform positive charge and the electrons have non-zero density. This system, termed "jellium" or a uniform electron gas, was found to possess a kinetic energy of the form

$$T_{ueg}[\rho(\mathbf{r})] = \frac{3}{10}(3\pi^2)^{2/3} \int \rho^{5/3}(\mathbf{r}) d\mathbf{r} \tag{2.60}$$

Equations 2.58 - 2.60 are all functions that depend on ρ, but the density itself is a function of position in space, $\mathbf{r}$. These functions of functions are termed "functionals" and the collection of V and T above outline the first attempts at defining a density functional theory (DFT).[103, 104] Unsurprisingly, this initial functional was largely inaccurate and a significant portion of the error stemmed from the assumptions of Equation 2.59. A number of methods were developed to include interelectron correlation and exchange contributions to this term,[105–107] but it wasn't until

the 1965 breakthrough of Kohn and Sham that DFT functionals saw significant improvement.[108] They observed that the largest source of complexity, computational costs, and errors were associated with the electron-electron interactions. If the system was instead taken to be one that was completely non-interacting, but with the same ground-state density of the fully interacting system, an energy minimization would result in geometries identical to those of the real system.

$$E[\rho(\mathbf{r})] = T_{ni}[\rho(\mathbf{r})] + V_{ne}[\rho(\mathbf{r})] + V_{ee}[\rho(\mathbf{r})] + \Delta T[\rho(\mathbf{r})] + \Delta V_{ee}[\rho(\mathbf{r})] \tag{2.61}$$

The energy functional of such a system can be separated into component parts, such as in Equation 2.61. The first three terms are classical expressions for the 1-electron kinetic energy, nuclear attraction, and electron-electron repulsion as defined previously. However, the final two terms are new and refer to the correction to the kinetic energy arising from electron-electron interaction and all non-classical corrections to the electron-electron repulsion energy, respectively. These two terms are often handled together as the "exchange-correlation energy", E_{xc}, and Equation 2.62 depicts such a functional of N electrons across M nuclei.

$$\begin{aligned} E[\rho(\mathbf{r})] = &\sum_{i}^{N} \left(-\frac{1}{2} \int \nabla_i^2 \rho(\mathbf{r}) d\mathbf{r} - \sum_{k}^{M} \int \frac{Z_k}{\mathbf{r}_i - \mathbf{r}_k} \rho(\mathbf{r}) d\mathbf{r} \right) \\ &+ \sum_{i}^{N} \frac{1}{2} \iint \frac{\rho(\mathbf{r}_i)\rho(\mathbf{r}')}{\mathbf{r}_i - \mathbf{r}'} d\mathbf{r}_i d\mathbf{r}' + E_{xc}[\rho(\mathbf{r})] \end{aligned} \tag{2.62}$$

As the terms of the Slater determinant in Equation 2.49 account for the spatial correlation of individual electrons, electron density can be represented with orbitals, given $\rho = \sum_{i=1}^{N} |\chi_i|^2$. For the usual orbital-optimization processes, this yields a 1-electron Kohn–Sham (KS) operator

$$\hat{h}_i^{KS} = -\frac{1}{2}\nabla_i^2 - \sum_{k}^{M} \frac{Z_k}{\mathbf{r}_i - \mathbf{r}_k} + \int \frac{\rho(\mathbf{r}')}{\mathbf{r}_i - \mathbf{r}'} d\mathbf{r}' + V_{xc} \tag{2.63}$$

where

$$V_{xc} = \frac{\delta E_{xc}}{\delta \rho} \tag{2.64}$$

and with pseudo-eigenvalues satisfying

$$\hat{h}_i^{KS} \chi_i = \varepsilon_i \chi_i \tag{2.65}$$

Once again, needing to use electron density to find electron density invokes a self-consistent field methodology whereby Equations 2.62 –2.65 are iteratively solved to minimize ε_i (and therefore E). Despite the implementation of orbital wavefunctions, presenting a 1-electron function such as $\rho(\mathbf{r})$ in terms of other 1-electron functions (i.e. χ_i) is not an approximation, provided the new functions are orthonormal.

Unfortunately, the form of E_{xc} (and therefore V_{xc}) is unknown and the efforts to approximate these energies are the key differences of the various DFT functionals. The exchange-correlation energies can be handled separately, such as $E_{xc} = E_x + E_c$, as different research arises about how to approximate each term best.

The form of Equation 2.65 and the use of spin orbitals strongly resembles HF methodologies, which has allowed programs to be easily re-tooled for either HF or DFT calculations. The main difference between the two fields is motivational: in Hartree-Fock theory, the Hamiltonian is formed from approximations chosen because of their exact solutions, whereas DFT has an exact Hamiltonian for which one portion is of unknown form and needs to be approximated. While seemingly pedantic, this difference has resulted in two very different flavors of quantum mechanical computational chemistry.

Although HF and DFT are different, a series of methodologies tie the two together in more than just shared programming. Adiabatic connection methods envision a smooth switching between fully non-interacting systems and the exact, real system.[109, 110] By construction, the Slater determinant of the KS orbitals have expectation values matching the exact exchange energy for a non-interacting system. Thus, HF calculations with KS orbitals will yield a significant portion of E_{xc}. The remaining portion is then some fraction, $0 \leq z \leq 1$, of the fully interacting system (approximated as E_{xc} calculated using a DFT functional) with the exact non-interacting energy removed.

$$E_{xc} = E_x^{HF} + z(E_{xc}^{DFT} - E_x^{HF}) \tag{2.66}$$

The degree of interaction can be chosen as the researcher deems appropriate, such as $z = 0.5$ in the "half and half" method,[111] but it is often empirically optimized to find the best fit to experimental data. While the introduction of this one parameter improved correlation to test data sets, the utilization of three such variables, as in the B3LYP functional,[111–114] has become very popular due to its significantly improved fit. While these functionals yield consistent results, the parametrization renders the functional unintuitive. To address this, a collection of "zero" parameter adiabatic connection methods were developed whereby z was chosen *a priori*. Of these, PBE0 has gained popularity due to its grounding in perturbation theory[115] as well as versatility over a wider array of binding environments, making it applicable for more exotic calculations. The functional is attractive to quantum mechanical purists as well, as both the main PBE functional[116] and adiabatic E_{xc} calculation contain no empirically parameterized variables.

These improved functionals alongside tools such as ECP basis sets have resulted in larger and more complex calculations being able to be performed and trusted. Unfortunately, due to the number of atoms and electrons involved with semiconductor nanoparticles, quantum dots with sizes $r \geq 1.5$ nm are still too large to be easily handled with atomistic density functional computations.[117–119] While new methods of handling large systems are demonstrating promise,[120] DFT is most often used by the quantum dot community to model small clusters as a starting point to

extrapolate data about larger systems. Plane-wave calculations, which use DFT on repeating unit cells to acquire state information of large (infinite) surfaces, are also used to probe phenomena such as ligand compatibility,[121–123] redox activity,[124] and the effect of defects.[125]

Historically, synthetic chemists prefer to rely upon more tangible experimental techniques such as NMR or mass spectroscopy for confirmations of plausible mechanisms. However, with the increasing accessibility of supercomputing and applicability of DFT to diverse binding environments, the field has begun delving into computational chemistry for more detailed explanations of complicated precursor to monomer conversions. Time-dependent *ab initio* calculations have suggested InP precursors undergo indium-rich intermediates, such as In_4P clusters, and complex inter-molecule reductions with $(TMS)_3P$-based syntheses.[126] The same group also showed the preference of small In_xP_y (where $x, y \leq 22$) to form amorphous particles with high coordination numbers over typical crystalline lattices,[127] a fact well-known in the literature but with few concrete explanations. Due to the newness of InP synthesis routes with aminophosphines as precursors, only one study has invoked computational chemistry to explain portions of that mechanism.[77] This preliminary effort highlighted the need for more extensive analysis, and describes the motivation of the work presented hereafter. The identification a more detailed mechanism will create opportunities for purposeful experimental design and shed light on adapting aminoarsines and aminostibines for InAs and InSb materials, respectively.

Bibliography

[1] R. Rossetti, J. L. Ellison, J. M. Gibson, and L. E. Brus, "Size effects in the excited electronic states of small colloidal CdS crystallites," *The Journal of Chemical Physics*, vol. 80, no. 9, pp. 4464–4469, 1984.

[2] S. V. Nair, S. Sinha, and K. C. Rustagi, "Quantum size effects in spherical semiconductor microcrystals," *Physical Review B*, vol. 35, no. 8, pp. 4098–4101, 1987.

[3] L. Brus, "Electronic wave functions in semiconductor clusters: experiment and theory," *The Journal of Physical Chemistry*, vol. 90, no. 12, pp. 2555–2560, 1986.

[4] S. Abe, J. J. Joos, L. I. D. J. Martin, Z. Hens, and P. F. Smet, "Hybrid remote quantum dot/powder phosphor designs for display backlights," *Light Sci Appl.*, vol. 6, p. e16271, 2017.

[5] S. Baskoutas and A. F. Terzis, "Size-dependent band gap of colloidal quantum dots," *Journal of Applied Physics*, vol. 99, no. 1, p. 013708, 2006.

[6] L. Brus, "Quantum crystallites and nonlinear optics," *Applied Physics A*, vol. 53, no. 6, pp. 465–474, 1991.

[7] M. S. Dresselhaus, G. Chen, M. Y. Tang, R. G. Yang, H. Lee, D. Z. Wang, Z. F. Ren, J. P. Fleurial, and P. Gogna, "New Directions for Low-Dimensional Thermoelectric Materials," *Advanced Materials*, vol. 19, no. 8, pp. 1043–1053, 2007.

[8] G. Laufersky and T. Nann, "1.01 - Physical Chemistry of Nanoparticle Syntheses," *Comprehensive Nanoscience and Nanotechnology (Second Edition)*, pp. 1–16, 2019.

[9] J. van Embden, A. S. R. Chesman, and J. J. Jasieniak, "The Heat-Up Synthesis of Colloidal Nanocrystals," *Chemistry of Materials*, vol. 27, no. 7, pp. 2246–2285, 2015.

[10] T. Sugimoto, "Preparation of monodispersed colloidal particles," *Advances in Colloid and Interface Science*, vol. 28, pp. 65–108, 1987.

[11] J. Y. Rempel, M. G. Bawendi, and K. F. Jensen, "Insights into the Kinetics of Semiconductor Nanocrystal Nucleation and Growth," *Journal of the American Chemical Society*, vol. 131, no. 12, pp. 4479–4489, 2009.

[12] S. Abe, R. K. Čapek, B. De Geyter, and Z. Hens, "Tuning the Postfocused Size of Colloidal Nanocrystals by the Reaction Rate: From Theory to Application," *ACS Nano*, vol. 6, no. 1, pp. 42–53, 2012.

[13] J. J. Ramsden, S. E. Webber, and M. Graetzel, "Luminescence of colloidal cadmium sulfide particles in acetonitrile and acetonitrile/water mixtures," *The Journal of Physical Chemistry*, vol. 89, no. 13, pp. 2740–2743, 1985.

[14] M. L. Steigerwald, A. P. Alivisatos, J. M. Gibson, T. D. Harris, R. Kortan, A. J. Muller, A. M. Thayer, T. M. Duncan, D. C. Douglass, and L. E. Brus, "Surface derivatization and isolation of semiconductor cluster molecules," *Journal of the American Chemical Society*, vol. 110, no. 10, pp. 3046–3050, 1988.

[15] J. G. Brennan, T. Siegrist, P. J. Carroll, S. M. Stuczynski, L. E. Brus, and M. L. Steigerwald, "The preparation of large semiconductor clusters via the pyrolysis of a molecular precursor," *Journal of the American Chemical Society*, vol. 111, no. 11, pp. 4141–4143, 1989.

[16] P. W. Voorhees, "The theory of Ostwald ripening," *Journal of Statistical Physics*, vol. 38, no. 1, pp. 231–252, 1985.

[17] C. Murray, D. J. Norris, and M. G. Bawendi, "Synthesis and characterization of nearly monodisperse CdE (E= sulfur, selenium, tellurium) semiconductor nanocrystallites," *Journal of the American Chemical Society*, vol. 115, no. 19, pp. 8706–8715, 1993.

[18] C. B. Murray, M. Nirmal, D. J. Norris, and M. G. Bawendi, "Synthesis and structural characterization of II-VI semiconductor nanocrystallites (quantum dots)," *Zeitschrift für Physik D Atoms, Molecules and Clusters*, vol. 26, no. 1, pp. 231–233, 1993.

[19] R. A. Zingaro, B. H. Steeves, and K. Irgolic, "Phosphine tellurides," *Journal of Organometallic Chemistry*, vol. 4, no. 4, pp. 320–323, 1965.

[20] Z. A. Peng and X. Peng, "Formation of High-Quality CdTe, CdSe, and CdS Nanocrystals Using CdO as Precursor," *Journal of the American Chemical Society*, vol. 123, no. 1, pp. 183–184, 2001.

[21] D. V. Talapin, A. L. Rogach, A. Kornowski, M. Haase, and H. Weller, "Highly Luminescent Monodisperse CdSe and CdSe/ZnS Nanocrystals Synthesized in a Hexadecylamine-Trioctylphosphine Oxide-Trioctylphospine Mixture," *Nano Letters*, vol. 1, no. 4, pp. 207–211, 2001.

[22] W. W. Yu and X. Peng, "Formation of High-Quality CdS and Other II-VI Semiconductor Nanocrystals in Noncoordinating Solvents: Tunable Reactivity of Monomers," *Angewandte Chemie International Edition*, vol. 41, no. 13, pp. 2368–2371, 2002.

[23] H. Liu, J. S. Owen, and A. P. Alivisatos, "Mechanistic Study of Precursor Evolution in Colloidal Group II-VI Semiconductor Nanocrystal Synthesis," *Journal of the American Chemical Society*, vol. 129, no. 2, pp. 305–312, 2007.

[24] Z. Hens and R. K. Čapek, "Size tuning at full yield in the synthesis of colloidal semiconductor nanocrystals, reaction simulations and experimental verification," *Coordination Chemistry Reviews*, vol. 263, pp. 217–228, 2014.

[25] E. M. Chan, C. Xu, A. W. Mao, G. Han, J. S. Owen, B. E. Cohen, and D. J. Milliron, "Reproducible, High-Throughput Synthesis of Colloidal Nanocrystals for Optimization in Multidimensional Parameter Space," *Nano Letters*, vol. 10, no. 5, pp. 1874–1885, 2010.

[26] M. Protière, N. Nerambourg, O. Renard, and P. Reiss, "Rational design of the gram-scale synthesis of nearly monodisperse semiconductor nanocrystals," *Nanoscale Research Letters*, vol. 6, no. 1, p. 472, 2011.

[27] L. Spanhel, M. Haase, H. Weller, and A. Henglein, "Photochemistry of colloidal semiconductors. 20. Surface modification and stability of strong luminescing CdS particles," *Journal of the American Chemical Society*, vol. 109, no. 19, pp. 5649–5655, 1987.

[28] X. Wang, L. Qu, J. Zhang, X. Peng, and M. Xiao, "Surface-Related Emission in Highly Luminescent CdSe Quantum Dots," *Nano Letters*, vol. 3, no. 8, pp. 1103–1106, 2003.

[29] G. Kalyuzhny and R. W. Murray, "Ligand Effects on Optical Properties of CdSe Nanocrystals," *The Journal of Physical Chemistry B*, vol. 109, no. 15, pp. 7012–7021, 2005.

[30] I. Lokteva, N. Radychev, F. Witt, H. Borchert, J. Parisi, and J. Kolny-Olesiak, "Surface Treatment of CdSe Nanoparticles for Application in Hybrid Solar Cells: The Effect of Multiple Ligand Exchange with Pyridine," *The Journal of Physical Chemistry C*, vol. 114, no. 29, pp. 12784–12791, 2010.

[31] W. K. Bae, L. A. Padilha, Y.-S. Park, H. McDaniel, I. Robel, J. M. Pietryga, and V. I. Klimov, "Controlled Alloying of the Core–Shell Interface in CdSe/CdS Quantum Dots for Suppression of Auger Recombination," *ACS Nano*, vol. 7, no. 4, pp. 3411–3419, 2013.

[32] L. Carbone, C. Nobile, M. De Giorgi, F. D. Sala, G. Morello, P. Pompa, M. Hytch, E. Snoeck, A. Fiore, I. R. Franchini, M. Nadasan, A. F. Silvestre, L. Chiodo, S. Kudera, R. Cingolani, R. Krahne, and L. Manna, "Synthesis and Micrometer-Scale Assembly of Colloidal CdSe/CdS Nanorods Prepared by a Seeded Growth Approach," *Nano Letters*, vol. 7, no. 10, pp. 2942–2950, 2007.

[33] J. Kwak, W. K. Bae, D. Lee, I. Park, J. Lim, M. Park, H. Cho, H. Woo, D. Y. Yoon, K. Char, S. Lee, and C. Lee, "Bright and Efficient Full-Color Colloidal Quantum Dot Light-Emitting Diodes Using an Inverted Device Structure," *Nano Letters*, vol. 12, no. 5, pp. 2362–2366, 2012.

[34] V. L. Colvin, M. C. Schlamp, and A. P. Alivisatos, "Light-emitting diodes made from cadmium selenide nanocrystals and a semiconducting polymer," *Nature*, vol. 370, no. 6488, pp. 354–357, 1994.

[35] M. Achermann, M. A. Petruska, D. D. Koleske, M. H. Crawford, and V. I. Klimov, "Nanocrystal-Based Light-Emitting Diodes Utilizing High-Efficiency Nonradiative Energy Transfer for Color Conversion," *Nano Letters*, vol. 6, no. 7, pp. 1396–1400, 2006.

[36] J. Xu and M. Xiao, "Lasing action in colloidal CdS/CdSe/CdS quantum wells," *Applied Physics Letters*, vol. 87, no. 17, p. 173117, 2005.

[37] I. Moreels, G. Rainò, R. Gomes, Z. Hens, T. Stöferle, and R. F. Mahrt, "Nearly Temperature-Independent Threshold for Amplified Spontaneous Emission in Colloidal CdSe/CdS Quantum Dot-in-Rods," *Advanced Materials*, vol. 24, no. 35, pp. OP231–OP235, 2012.

[38] C. Dang, J. Lee, C. Breen, J. S. Steckel, S. Coe-Sullivan, and A. Nurmikko, "Red, green and blue lasing enabled by single-exciton gain in colloidal quantum dot films," *Nat Nano*, vol. 7, no. 5, pp. 335–339, 2012.

[39] B. Guzelturk, Y. Kelestemur, M. Olutas, S. Delikanli, and H. V. Demir, "Amplified Spontaneous Emission and Lasing in Colloidal Nanoplatelets," *ACS Nano*, vol. 8, no. 7, pp. 6599–6605, 2014.

[40] Y. Yuan and M. Krüger, "Polymer-Nanocrystal Hybrid Materials for Light Conversion Applications," *Polymers*, vol. 4, no. 1, p. 1, 2011.

[41] P. V. Kamat, "Boosting the Efficiency of Quantum Dot Sensitized Solar Cells through Modulation of Interfacial Charge Transfer," *Accounts of Chemical Research*, vol. 45, no. 11, pp. 1906–1915, 2012.

[42] A. F. A. M. L. N. J. H. H. D. v. S. W. G. J. H. M. Bomm, J.; Büchtemann, "Fabrication and spectroscopic studies on highly luminescent CdSe/CdS nanorod polymer composites," *Beilstein Journal of Nanotechnolology*, vol. 1, pp. 94–100, 2010.

[43] F. Purcell-Milton and Y. K. Gun'ko, "Quantum dots for Luminescent Solar Concentrators," *Journal of Materials Chemistry*, vol. 22, no. 33, pp. 16687–16697, 2012.

[44] F. Meinardi, A. Colombo, K. A. Velizhanin, R. Simonutti, M. Lorenzon, L. Beverina, R. Viswanatha, V. I. Klimov, and S. Brovelli, "Large-area luminescent solar concentrators based on 'Stokes-shift-engineered' nanocrystals in a mass-polymerized PMMA matrix," *Nat Photon*, vol. 8, no. 5, pp. 392–399, 2014.

[45] P. Kalisman, Y. Nakibli, and L. Amirav, "Perfect Photon-to-Hydrogen Conversion Efficiency," *Nano Letters*, vol. 16, no. 3, pp. 1776–1781, 2016.

[46] E. Zillner, S. Fengler, P. Niyamakom, F. Rauscher, K. Köhler, and T. Dittrich, "Role of Ligand Exchange at CdSe Quantum Dot Layers for Charge Separation," *The Journal of Physical Chemistry C*, vol. 116, no. 31, pp. 16747–16754, 2012.

[47] W. R. Algar and U. J. Krull, "Luminescence and Stability of Aqueous Thioalkyl Acid Capped CdSe/ZnS Quantum Dots Correlated to Ligand Ionization," *ChemPhysChem*, vol. 8, no. 4, pp. 561–568, 2007.

[48] U. Resch-Genger, M. Grabolle, S. Cavaliere-Jaricot, R. Nitschke, and T. Nann, "Quantum dots versus organic dyes as fluorescent labels," *Nat Meth*, vol. 5, no. 9, pp. 763–775, 2008.

[49] J. Kim, M. J. Biondi, J. J. Feld, and W. C. W. Chan, "Clinical Validation of Quantum Dot Barcode Diagnostic Technology," *ACS Nano*, vol. 10, no. 4, pp. 4742–4753, 2016.

[50] B. Ji, E. Giovanelli, B. Habert, P. Spinicelli, M. Nasilowski, X. Xu, N. Lequeux, J.-P. Hugonin, F. Marquier, J.-J. Greffet, and B. Dubertret, "Non-blinking quantum dot with a plasmonic nanoshell resonator," *Nat Nano*, vol. 10, no. 2, pp. 170–175, 2015.

[51] G.-C. Shan, Z.-Q. Yin, C. H. Shek, and W. Huang, "Single photon sources with single semiconductor quantum dots," *Frontiers of Physics*, vol. 9, no. 2, pp. 170–193, 2014.

[52] X. Brokmann, E. Giacobino, M. Dahan, and J. P. Hermier, "Highly efficient triggered emission of single photons by colloidal CdSe/ZnS nanocrystals," *Applied Physics Letters*, vol. 85, no. 5, pp. 712–714, 2004.

[53] W. Liu, H. S. Choi, J. P. Zimmer, E. Tanaka, J. V. Frangioni, and M. Bawendi, "Compact Cysteine-Coated CdSe(ZnCdS) Quantum Dots for in Vivo Applications," *Journal of the American Chemical Society*, vol. 129, no. 47, pp. 14530–14531, 2007.

[54] E. Oh, R. Liu, A. Nel, K. B. Gemill, M. Bilal, Y. Cohen, and I. L. Medintz, "Meta-analysis of cellular toxicity for cadmium-containing quantum dots," *Nat Nano*, vol. 11, no. 5, pp. 479–486, 2016.

[55] V. Brunetti, H. Chibli, R. Fiammengo, A. Galeone, M. A. Malvindi, G. Vecchio, R. Cingolani, J. L. Nadeau, and P. P. Pompa, "InP/ZnS as a safer alternative to CdSe/ZnS core/shell quantum dots: in vitro and in vivo toxicity assessment," *Nanoscale*, vol. 5, no. 1, pp. 307–317, 2013.

[56] G. Lin, Q. Ouyang, R. Hu, Z. Ding, J. Tian, F. Yin, G. Xu, Q. Chen, X. Wang, and K.-T. Yong, "In vivo toxicity assessment of non-cadmium quantum dots in BALB/c mice," *Nanomedicine: Nanotechnology, Biology and Medicine*, vol. 11, no. 2, pp. 341–350, 2015.

[57] H. Chibli, L. Carlini, S. Park, N. M. Dimitrijevic, and J. L. Nadeau, "Cytotoxicity of InP/ZnS quantum dots related to reactive oxygen species generation," *Nanoscale*, vol. 3, no. 6, pp. 2552–2559, 2011.

[58] H. Uchida, T. Ogata, and H. Yoneyama, "Preparation of size-quantized indium phosphide in zeolite cages," *Chemical Physics Letters*, vol. 173, no. 1, pp. 103–106, 1990.

[59] T. Douglas and K. H. Theopold, "Molecular precursors for indium phosphide and synthesis of small III-V semiconductor clusters in solution," *Inorganic Chemistry*, vol. 30, no. 4, pp. 594–596, 1991.

[60] M. D. Healy, P. E. Laibinis, P. D. Stupik, and A. R. Barron, "The reaction of indium(III) chloride with tris(trimethylsilyl)phosphine: a novel route to indium phosphide," *Journal of the Chemical Society, Chemical Communications*, no. 6, pp. 359–360, 1989.

[61] O. I. Micic, C. J. Curtis, K. M. Jones, J. R. Sprague, and A. J. Nozik, "Synthesis and Characterization of InP Quantum Dots," *The Journal of Physical Chemistry*, vol. 98, no. 19, pp. 4966–4969, 1994.

[62] A. A. Guzelian, J. E. B. Katari, A. V. Kadavanich, U. Banin, K. Hamad, E. Juban, A. P. Alivisatos, R. H. Wolters, C. C. Arnold, and J. R. Heath, "Synthesis of Size-Selected, Surface-Passivated InP Nanocrystals," *The Journal of Physical Chemistry*, vol. 100, no. 17, pp. 7212–7219, 1996.

[63] J. R. Heath, "Covalency in semiconductor quantum dots," *Chemical Society Reviews*, vol. 27, no. 1, pp. 65–71, 1998.

[64] O. I. Mićić, J. Sprague, Z. Lu, and A. J. Nozik, "Highly efficient band-edge emission from InP quantum dots," *Applied Physics Letters*, vol. 68, no. 22, pp. 3150–3152, 1996.

[65] O. I. Mićić, K. M. Jones, A. Cahill, and A. J. Nozik, "Optical, Electronic, and Structural Properties of Uncoupled and Close-Packed Arrays of InP Quantum Dots," *The Journal of Physical Chemistry B*, vol. 102, no. 49, pp. 9791–9796, 1998.

[66] S. Haubold, M. Haase, A. Kornowski, and H. Weller, "Strongly Luminescent InP/ZnS Core–Shell Nanoparticles," *ChemPhysChem*, vol. 2, no. 5, pp. 331–334, 2001.

[67] M. D. Tessier, D. Dupont, K. De Nolf, J. De Roo, and Z. Hens, "Economic and Size-Tunable Synthesis of InP/ZnE (E = S, Se) Colloidal Quantum Dots," *Chemistry of Materials*, vol. 27, no. 13, pp. 4893–4898, 2015.

[68] J. Lim, W. K. Bae, D. Lee, M. K. Nam, J. Jung, C. Lee, K. Char, and S. Lee, "InP@ZnSeS, Core@Composition Gradient Shell Quantum Dots with Enhanced Stability," *Chemistry of Materials*, vol. 23, no. 20, pp. 4459–4463, 2011.

[69] J. Lim, M. Park, W. K. Bae, D. Lee, S. Lee, C. Lee, and K. Char, "Highly Efficient Cadmium-Free Quantum Dot Light-Emitting Diodes Enabled by the Direct Formation of Excitons within InP@ZnSeS Quantum Dots," *ACS Nano*, vol. 7, no. 10, pp. 9019–9026, 2013.

[70] D. Battaglia and X. Peng, "Formation of High Quality InP and InAs Nanocrystals in a Noncoordinating Solvent," *Nano Letters*, vol. 2, no. 9, pp. 1027–1030, 2002.

[71] D. W. Lucey, D. J. MacRae, M. Furis, Y. Sahoo, A. N. Cartwright, and P. N. Prasad, "Monodispersed InP Quantum Dots Prepared by Colloidal Chemistry in a Noncoordinating Solvent," *Chemistry of Materials*, vol. 17, no. 14, pp. 3754–3762, 2005.

[72] S. Xu, S. Kumar, and T. Nann, "Rapid Synthesis of High-Quality InP Nanocrystals," *Journal of the American Chemical Society*, vol. 128, no. 4, pp. 1054–1055, 2006.

[73] L. Li and P. Reiss, "One-pot Synthesis of Highly Luminescent InP/ZnS Nanocrystals without Precursor Injection," *Journal of the American Chemical Society*, vol. 130, no. 35, pp. 11588–11589, 2008.

[74] S. B. Brichkin, "Synthesis and properties of colloidal indium phosphide quantum dots," *Colloid Journal*, vol. 77, no. 4, pp. 393–403, 2015.

[75] R. Xie, D. Battaglia, and X. Peng, "Colloidal InP Nanocrystals as Efficient Emitters Covering Blue to Near-Infrared," *Journal of the American Chemical Society*, vol. 129, no. 50, pp. 15432–15433, 2007.

[76] W.-S. Song, H.-S. Lee, J. Lee, D. Jang, Y. Choi, M. Choi, and H. Yang, "Amine-derived synthetic approach to color-tunable InP/ZnS quantum dots with high fluorescent qualities," *Journal of Nanoparticle Research*, vol. 15, no. 6, pp. 1–10, 2013.

[77] A. Buffard, S. Dreyfuss, B. Nadal, H. Heuclin, X. Xu, G. Patriarche, N. Mézailles, and B. Dubertret, "Mechanistic Insight and Optimization of InP Nanocrystals Synthesized with Aminophosphines," *Chemistry of Materials*, vol. 28, no. 16, pp. 5925–5934, 2016.

[78] X. Michalet, F. F. Pinaud, L. A. Bentolila, J. M. Tsay, S. Doose, J. J. Li, G. Sundaresan, A. M. Wu, S. S. Gambhir, and S. Weiss, "Quantum Dots for Live Cells, in Vivo Imaging, and Diagnostics," *Science*, vol. 307, no. 5709, pp. 538–544, 2005.

[79] R. Xie, K. Chen, X. Chen, and X. Peng, "InAs/InP/ZnSe core/shell/shell quantum dots as near-infrared emitters: Bright, narrow-band, non-cadmium containing, and biocompatible," *Nano Research*, vol. 1, no. 6, pp. 457–464, 2008.

[80] P. M. Allen, W. Liu, V. P. Chauhan, J. Lee, A. Y. Ting, D. Fukumura, R. K. Jain, and M. G. Bawendi, "InAs(ZnCdS) Quantum Dots Optimized for Biological Imaging in the Near-Infrared," *Journal of the American Chemical Society*, vol. 132, no. 2, pp. 470–471, 2010.

[81] S. H. Lee, C. Jung, Y. Jun, and S. W. Kim, "Synthesis of colloidal InAs/ZnSe quantum dots and their quantum dot sensitized solar cell (QDSSC) application," *Optical Materials*, vol. 49.

[82] Y. Takeda and T. Motohiro, "Requisites to realize high conversion efficiency of solar cells utilizing carrier multiplication," *Solar Energy Materials and Solar Cells*, vol. 94, no. 8, pp. 1399–1405, 2010.

[83] R. D. Schaller, J. M. Pietryga, and V. I. Klimov, "Carrier Multiplication in InAs Nanocrystal Quantum Dots with an Onset Defined by the Energy Conservation Limit," *Nano Letters*, vol. 7, no. 11, pp. 3469–3476, 2007.

[84] W. Liu, J.-S. Lee, and D. V. Talapin, "III–V Nanocrystals Capped with Molecular Metal Chalcogenide Ligands: High Electron Mobility and Ambipolar Photoresponse," *Journal of the American Chemical Society*, vol. 135, no. 4, pp. 1349–1357, 2013.

[85] J. Jang, W. Liu, J. S. Son, and D. V. Talapin, "Temperature-Dependent Hall and Field-Effect Mobility in Strongly Coupled All-Inorganic Nanocrystal Arrays," *Nano Letters*, vol. 14, no. 2, pp. 653–662, 2014.

[86] R. L. Wells, C. G. Pitt, A. T. McPhail, A. P. Purdy, S. Shafieezad, and R. B. Hallock, "The use of tris(trimethylsilyl)arsine to prepare gallium arsenide and indium arsenide," *Chemistry of Materials*, vol. 1, no. 1, pp. 4–6, 1989.

[87] Y.-W. Cao and U. Banin, "Synthesis and Characterization of InAs/InP and InAs/CdSe Core/Shell Nanocrystals," *Angewandte Chemie International Edition*, vol. 38, no. 24, pp. 3692–3694, 1999.

[88] R. Xie and X. Peng, "Synthetic Scheme for High-Quality InAs Nanocrystals Based on Self-Focusing and One-Pot Synthesis of InAs-Based Core–Shell Nanocrystals," *Angewandte Chemie International Edition*, vol. 47, no. 40, pp. 7677–7680, 2008.

[89] D. Franke, D. K. Harris, O. Chen, O. T. Bruns, J. A. Carr, M. W. B. Wilson, and M. G. Bawendi, "Continuous injection synthesis of indium arsenide quantum dots emissive in the short-wavelength infrared," vol. 7, p. 12749, 2016.

[90] M. A. Malik, P. O'Brien, and M. Helliwell, "A new synthesis of InAs quantum dots from [*t*-$Bu_2AsInEt_2]_2$," *Journal of Materials Chemistry*, vol. 15, no. 14, pp. 1463–1467, 2005.

[91] H. Uesugi, M. Kita, and T. Omata, "Synthesis of size-controlled colloidal InAs quantum dots using triphenylarsine as a stable arsenic source," *Journal of Crystal Growth*, vol. 416, no. Supplement C, pp. 134–141, 2015.

[92] A. Das, A. Shamirian, and P. T. Snee, "Arsenic Silylamide: An Effective Precursor for Arsenide Semiconductor Nanocrystal Synthesis," *Chemistry of Materials*, vol. 28, no. 11, pp. 4058–4064, 2016.

[93] M. Green, S. Norager, P. Moriarty, M. Motevalli, and P. O'Brien, "On the synthesis and manipulation of InAs quantum dots," *Journal of Materials Chemistry*, vol. 10, no. 8, pp. 1939–1943, 2000.

[94] V. Grigel, D. Dupont, K. De Nolf, Z. Hens, and M. D. Tessier, "InAs Colloidal Quantum Dots Synthesis via Aminopnictogen Precursor Chemistry," *Journal of the American Chemical Society*, vol. 138, no. 41, pp. 13485–13488, 2016.

[95] V. Srivastava, E. M. Janke, B. T. Diroll, R. D. Schaller, and D. V. Talapin, "Facile, Economic and Size-Tunable Synthesis of Metal Arsenide Nanocrystals," *Chemistry of Materials*, vol. 28, no. 18, pp. 6797–6802, 2016.

[96] "Group IV Elements, IV-IV and III-V Compounds. Part b - Electronic, Transport, Optical and Other Properties," *Group III Condensed Matter*.

[97] C. M. Evans, S. L. Castro, J. J. Worman, and R. P. Raffaelle, "Synthesis and Use of Tris(trimethylsilyl)antimony for the Preparation of InSb Quantum Dots," *Chemistry of Materials*, vol. 20, no. 18, pp. 5727–5730, 2008.

[98] W. Liu, A. Y. Chang, R. D. Schaller, and D. V. Talapin, "Colloidal InSb Nanocrystals," *Journal of the American Chemical Society*, vol. 134, no. 50, pp. 20258–20261, 2012.

[99] M. Yarema and M. V. Kovalenko, "Colloidal Synthesis of InSb Nanocrystals with Controlled Polymorphism Using Indium and Antimony Amides," *Chemistry of Materials*, vol. 25, no. 9, pp. 1788–1792, 2013.

[100] N. G. Semaltianos, E. Hendry, H. Chang, M. L. Wears, G. Monteil, M. Assoul, V. Malkhasyan, V. Blondeau-Patissier, B. Gauthier-Manuel, and V. Moutarlier, "ns or fs pulsed laser ablation of a bulk InSb target in liquids for nanoparticles synthesis," *Journal of Colloid and Interface Science*, vol. 469, no. Supplement C, pp. 57–62, 2016.

[101] K. Yaemsunthorn, T. Thongtem, S. Thongtem, and C. Randorn, "Synthesis of InSb nanocrystals in an air atmosphere and their photocatalytic activity from near-infrared to ultra-violet," *Materials Science in Semiconductor Processing*, vol. 68, no. Supplement C, pp. 53–57, 2017.

[102] C. J. Cramer, *Essentials of Computational Chemistry: Theories and Models*. West Sussex, England: Wiley, 2nd ed., 2004.

[103] L. H. Thomas, "The calculation of atomic fields," *Mathematical Proceedings of the Cambridge Philosophical Society*, vol. 23, no. 5, pp. 542–548, 2008.

[104] E. Fermi, *Collected papers (Note e memorie)*. Chicago: Chicago University of Chicago Press, 1962.

[105] F. Bloch, "Über die Quantenmechanik der Elektronen in Kristallgittern," *Zeitschrift für Physik*, vol. 52, no. 7, pp. 555–600, 1929.

[106] P. A. M. Dirac, "Note on Exchange Phenomena in the Thomas Atom," *Mathematical Proceedings of the Cambridge Philosophical Society*, vol. 26, no. 3, pp. 376–385, 2008.

[107] J. C. Slater, "A Simplification of the Hartree-Fock Method," *Physical Review*, vol. 81, no. 3, pp. 385–390, 1951.

[108] W. Kohn and L. J. Sham, "Self-Consistent Equations Including Exchange and Correlation Effects," *Physical Review*, vol. 140, no. 4A, pp. A1133–A1138, 1965.

[109] H. Hellmann, "Zur Rolle der kinetischen Elektronenenergie für die zwischenatomaren Kräfte," *Zeitschrift für Physik*, vol. 85, no. 3, pp. 180–190, 1933.

[110] R. P. Feynman, "Forces in Molecules," *Physical Review*, vol. 56, no. 4, pp. 340–343, 1939.

[111] A. D. Becke, "A new mixing of Hartree–Fock and local density-functional theories," *The Journal of Chemical Physics*, vol. 98, no. 2, pp. 1372–1377, 1993.

[112] C. Lee, W. Yang, and R. G. Parr, "Development of the Colle-Salvetti correlation-energy formula into a functional of the electron density," *Physical Review B*, vol. 37, no. 2, pp. 785–789, 1988.

[113] S. H. Vosko, L. Wilk, and M. Nusair, "Accurate spin-dependent electron liquid correlation energies for local spin density calculations: a critical analysis," *Canadian Journal of Physics*, vol. 58, no. 8, pp. 1200–1211, 1980.

[114] P. J. Stephens, F. J. Devlin, C. F. Chabalowski, and M. J. Frisch, "Ab Initio Calculation of Vibrational Absorption and Circular Dichroism Spectra Using Density Functional Force Fields," *The Journal of Physical Chemistry*, vol. 98, no. 45, pp. 11623–11627, 1994.

[115] J. P. Perdew, M. Ernzerhof, and K. Burke, "Rationale for mixing exact exchange with density functional approximations," *The Journal of Chemical Physics*, vol. 105, no. 22, pp. 9982–9985, 1996.

[116] J. P. Perdew, K. Burke, and M. Ernzerhof, "Generalized Gradient Approximation Made Simple," *Physical Review Letters*, vol. 77, no. 18, pp. 3865–3868, 1996.

[117] A. Fernando, K. L. D. M. Weerawardene, N. V. Karimova, and C. M. Aikens, "Quantum Mechanical Studies of Large Metal, Metal Oxide, and Metal Chalcogenide Nanoparticles and Clusters," *Chemical Reviews*, vol. 115, no. 12, pp. 6112–6216, 2015.

[118] J. Yin, M. Kumar, Q. Lei, L. Ma, S. S. K. Raavi, G. G. Gurzadyan, and C. Soci, "Small-Size Effects on Electron Transfer in P3HT/InP Quantum Dots," *The Journal of Physical Chemistry C*, vol. 119, no. 47, pp. 26783–26792, 2015.

[119] M. Del Ben, R. W. A. Havenith, R. Broer, and M. Stener, "Density Functional Study on the Morphology and Photoabsorption of CdSe Nanoclusters," *The Journal of Physical Chemistry C*, vol. 115, no. 34, pp. 16782–16796, 2011.

[120] N. Weeks and K. Tvrdy, "Atomistic Modeling of Quantum Dots at Experimentally Relevant Scales Using Charge Equilibration," *The Journal of Physical Chemistry A*, vol. 121, no. 48, pp. 9346–9357, 2017.

[121] J. T. Margraf, A. Ruland, V. Sgobba, D. M. Guldi, and T. Clark, "Theoretical and Experimental Insights into the Surface Chemistry of Semiconductor Quantum Dots," *Langmuir*, vol. 29, no. 49, pp. 15450–15456, 2013.

[122] K. Kim, D. Yoo, H. Choi, S. Tamang, J.-H. Ko, S. Kim, Y.-H. Kim, and S. Jeong, "Halide–Amine Co-Passivated Indium Phosphide Colloidal Quantum Dots in Tetrahedral Shape," *Angewandte Chemie*, vol. 128, no. 11, pp. 3778–3782, 2016.

[123] C. E. Rowland, W. Liu, D. C. Hannah, M. K. Y. Chan, D. V. Talapin, and R. D. Schaller, "Thermal Stability of Colloidal InP Nanocrystals: Small Inorganic Ligands Boost High-Temperature Photoluminescence," *ACS Nano*, vol. 8, no. 1, pp. 977–985, 2014.

[124] Z. Ren, Z. Wang, R. Wang, Z. Pan, X. Gong, and X. Zhong, "Effects of Metal Oxyhydroxide Coatings on Photoanode in Quantum Dot Sensitized Solar Cells," *Chemistry of Materials*, vol. 28, no. 7, pp. 2323–2330, 2016.

[125] N. P. Brawand, M. B. Goldey, M. Vörös, and G. Galli, "Defect States and Charge Transport in Quantum Dot Solids," *Chemistry of Materials*, vol. 29, no. 3, pp. 1255–1262, 2017.

[126] L. Xie, Q. Zhao, K. F. Jensen, and H. J. Kulik, "Direct Observation of Early-Stage Quantum Dot Growth Mechanisms with High-Temperature Ab Initio Molecular Dynamics," *The Journal of Physical Chemistry C*, vol. 120, no. 4, pp. 2472–2483, 2016.

[127] Q. Zhao, L. Xie, and H. J. Kulik, "Discovering Amorphous Indium Phosphide Nanostructures with High-Temperature ab Initio Molecular Dynamics," *The Journal of Physical Chemistry C*, vol. 119, no. 40, pp. 23238–23249, 2015.

Chapter 3

Aminophosphine Mechanism

Quantum dots have emerged as materials for a wide variety of high-value products due to their tailorable band gap energies. While particles made from heavy metals usually make the best materials and have the easiest syntheses, public health concerns limit the scale of their use. As mentioned in Section 2.4.1, indium phosphide (InP) quantum dots are much more biocompatible than the more popular cadmium chalcogenides. However, the standard syntheses are difficult at best and dangerous at worst, which inhibits their more widespread use. For indium-based materials to rise to the forefront, new methods need to be developed that are safer, reliable, and tunable to a wide range of sizes.

This chapter discusses new methods for creating InP quantum dots in a safer, less technical manner. Herein, particular focus is spent on using aminophosphine precursors and how they behave very differently from more familiar sources of phosphorus. A brief description of the known aspects of their mechanisms is followed by our studies using density functional theory. Understanding the unique impact of zinc salts in this synthesis then allows for the design of better reaction schemes. A comparison with literature methods shows the new processes can produce brighter and more efficient quantum dots. Much of the work presented here has now been published,[1] but this chapter gives an intimate view of our motivations and results[†].

3.1 Literature Mechanism Overview

Tris(dialkylamino) phosphines, $P(NR_2)_3$, are much needed and welcome precursors for InP syntheses.[2] As other phosphorus sources are often highly flammable and explosive, these new alternatives herald a new era of easy-to-make, biologically friendly quantum dot syntheses. However, many parts of these new reactions make it difficult to apply standard methods to improve the materials. One significant aspect is the need to use primary amine solvents to see any particle growth.

Class	Example	Result
Primary Amines	Butylamine Octylamine Dodecylamine Oleylamine	QDs
Secondary Amines	Dioctylamine	–
Tertiary Amines	Trioctylamine	–
Other	Trioctylphosphine	–

TABLE 3.1: Solvents compatible with aminophosphine precursors. Adapted with permissions from Tessier *et al.*[3] Copyright 2016 American Chemical Society.

Results such as those in Table 3.1 led initial researchers to believe that the protic NH_2R solvents were creating PH_3 *in situ*.[2] However, ^{1}H-NMR and ^{31}P-NMR

[†]Sections of the published paper say some of the methods make spherical particles. Shape is difficult to confirm with such small nanoparticles, but more recent, careful examination by others in our group have seen more tetrahedral character using the same synthetic approach. Thus, this thesis treats all InP cores made with aminophosphines as tetrahedral, which agrees with literature.

spectroscopy showed the solvent instead transaminated the aminophosphine in a reaction such as Equation 3.1.[3,4] This observations also accounted for conclusions that there were few differences between using $P(NMe_2)_3$ and $P(NEt_2)_3$ and allowed the phosphorus to then interact with soluble In^{3+}.

$$P(NMe_2)_3 + 3\ NH_2R \longrightarrow P(NHR)_3 + 3\ HNMe_2 \tag{3.1}$$

Standard literature often prescribes a 2 In : 1 P molar ratio, but the chemical yields of syntheses using aminophosphines in those concentrations are quite poor. Interestingly, optimization found that a 1 In : 3.6 P ratio achieved chemical completeness,[5] which reversed the trend of previous research. This nearly four-fold saturation of phosphorus was later attributed to the self-reduction of the aminophosphine to generate a P(-III) product (such as in InP). When nanoparticles formed, NMR and mass spectroscopy found a presence of $P(NHR)_4^+$ in concentrations roughly three times that of InP product isolated.[3,4] Those works then proposed Equation 3.2 as the redox reaction responsible for QD formation.

$$InCl_3 + P(NHR)_3 + 3\ P(NHR)_3 \longrightarrow InP + 3\ P(NHR)_4Cl \tag{3.2}$$

While the above equation rationalized the precursor behaviors, it failed to explain how such a multistep reduction would occur. Buffard *et al.* proposed an iterative 2-step reaction in which an $InCl_3{\cdot}P(NHR)_3$ coordination complex underwent an acid/base deprotonation to form an In–P species. This compound then interacted with a second $P(NHR)_3$ to perform the disproportionation[4] and the cycle repeated twice to yield InP products.

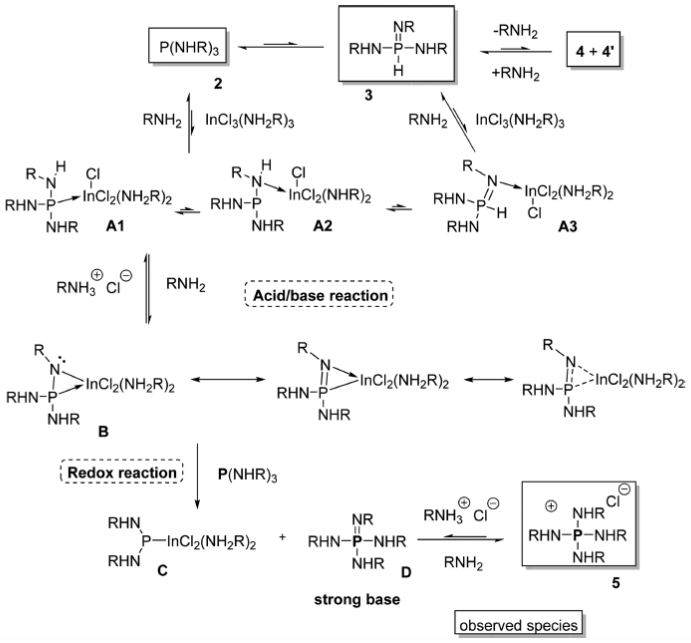

FIGURE 3.1: Mechanism of the 1-electron disproportionation of $P(NHR)_3$ to form an In–P complex, adapted with permissions from Buffard *et al.*[4] Copyright 2016 American Chemical Society.

Although this is a more comprehensive description than Equation 3.2, minimal evidence of this reaction pathway was present in the publication. Compounds **2**, **3**, **4**/**4'**, and **5** were all confirmed by NMR or MS techniques and only structures **A1**, **A2**, and **A3** were examined with DFT. While **A1** was found to be the most stable conformer, there were no computational or experimental confirmations of the structures of **B**, **C**, or **D**. As these are the crux of the proposed reaction, we began our investigations by assessing the likelihood of these geometries in this system.

Density functional theory calculations were performed with the PBE0 hybrid functional,[6] the def2-SVP (Ahlrichs) basis-set[7] of double-ζ quality, and Grimme's empirical D3 dispersion-correction[8] was applied. In order to model the effect of the solvent, the Polarizable Continuum Model (PCM) using the integral equation formalism variant (IEFPCM)[9–27] was used with oleylamine (OAm) as the solvent in all cases.[28] This level of theory is referred to as PBE0-D3/def2-SVP/PCM_{OAm}.

All structures were optimized to tight geometry convergence criteria[29] and frequency calculations at the same level of theory were carried out at 453.15 K (180 °C) in order to ensure that the obtained structures correspond to minima (or first-order transition structures) on the potential energy surface[30] at the required synthesis temperature. When modeling the primary amines used in the QD synthesis, ethylamine (NH_2Et) was used to more appropriately represent the steric component in addition to the electronic profile of a long chain fatty amine. All quantum chemical calculations were carried out with the *Gaussian 09* suite of programs (Revision D.01)[31] and molecular graphics were rendered with WebMO.[32]

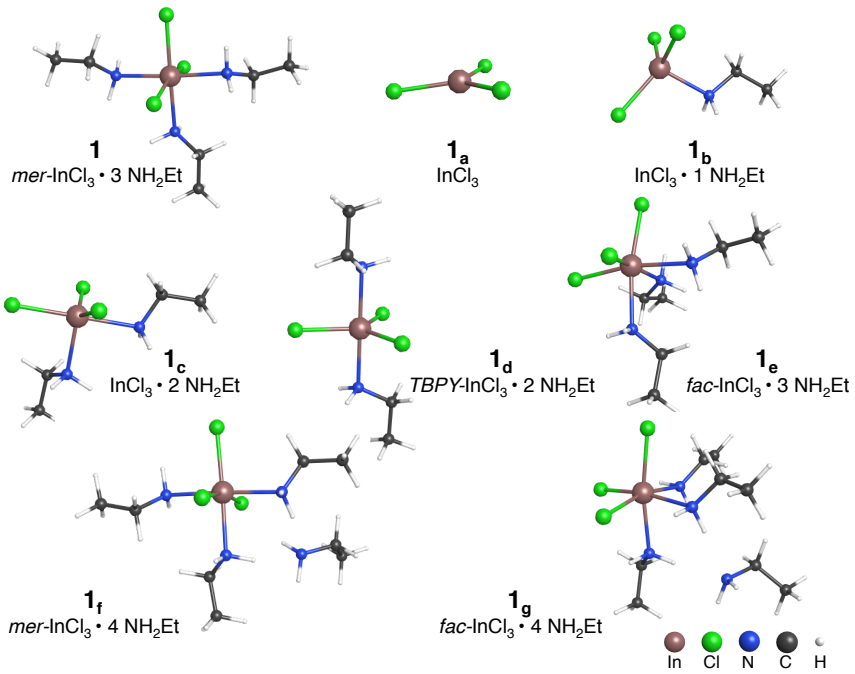

FIGURE 3.2: Geometries of $InCl_3$ solvation complexes at the PBE0-D3/def2-SVP/PCM_{OAm} level of theory.

	ΔE	ΔU	ΔH	ΔG
1	0.00	0.00	0.00	0.00
$\mathbf{1_a}$	83.93	79.75	82.45	31.33
$\mathbf{1_b}$	43.96	41.23	43.03	7.15
$\mathbf{1_c}$	27.00	25.68	26.58	7.98
$\mathbf{1_d}$	16.83	15.63	16.53	-3.21
$\mathbf{1_e}$	3.76	2.96	2.96	5.82
$\mathbf{1_f}$	-15.59	-14.08	-14.98	1.61
$\mathbf{1_g}$	13.11	14.62	13.72	31.19

TABLE 3.2: Difference in energies as compared to **1**, calculated as the sum of $InCl_3 \cdot N$ NH_2Et and $4 - N$ free NH_2Et as determined at the PBE0-D3/def2-SVP/PCM_{OAm} level of theory.

Ethylamine molecules were added to an $InCl_3$ salt structure until the first solvation sphere was filled to simulate the dissolution of the salt in synthesis experiments. As seen in Figure 3.2, three of these ligands were sufficient to passivate the indium center. Further additions (as seen with $\mathbf{1_f}$ and $\mathbf{1_g}$) localized in the second solvation shell, so these geometries were rejected despite improvements in energies. Geometry $\mathbf{1_d}$ was also rejected despite a more favorable free energy because the electronic, internal, and enthalpic energies were significantly less stable. Although Buffard *et al.* reported facial $InCl_3 \cdot 3$ NH_2Et to be the lowest energy structure,[4] the meridional conformer **1** proved to be more stable at this level of theory. As such, it was used in further calculations to model the In$\cdots$P interaction.

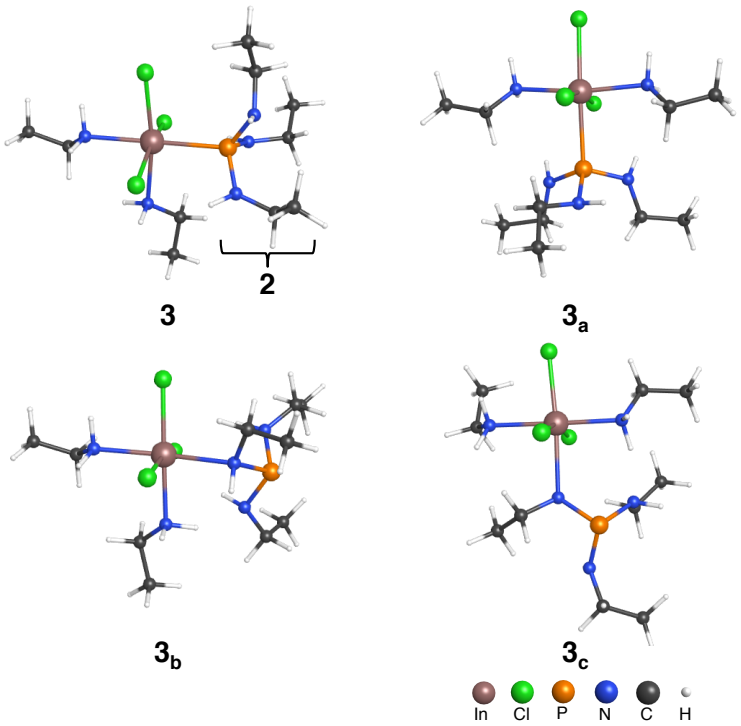

FIGURE 3.3: Geometries of $InCl_3 \cdot P(NHEt)_3$ conformers at the PBE0-D3/def2-SVP/PCM_{OAm} level of theory.

The phosphorus precursor was modeled with $P(NHEt)_3$ due to the immediate transamination of tris(dialkylamino)phosphines in primary amine solvents (depicted in Figure 3.3 as **2**). Similarly to the literature cadmium selenide mechanism in

Figure 2.12, the indium complex and aminophosphine must first datively bind before forming a full In–P bond. To achieve this, **2** must displace one of the ethylamine ligands surrounding the indium center. The lowest energy conformers of several In$\cdots$P and In$\cdots$N binding environments are shown in Figure 3.3. Complex **3** best matches the lowest energy structure of Buffard *et al.*, despite their modeling of a *fac*-conformer. Geometries $\mathbf{3_a}$ and $\mathbf{3_b}$ are also similarly stable and so require further study.

The acid-base reaction was checked by comparing energies of separate reactants to those of the products. For the chemical equation $A+B \rightarrow C+D$, the energy difference can be calculated as $\Delta E = (E_C + E_D) - (E_A + E_B)$. The various changes in energy are then used to identify possible reaction paths. If the difference between products and reactions is negative or slightly positive, this indicates a likely reaction. In this way, the conformers of Figure 3.3 were combined with N NH_2Et molecules and systemically examined for deprotonated products.

	ΔE	ΔU	ΔH	ΔG
3	0.00	0.00	0.00	0.00
$\mathbf{3_a}$	-0.16	-0.32	-0.32	0.21
$\mathbf{3_b}$	-0.47	-1.06	-1.06	-0.06
$\mathbf{3_c}$	5.66	4.79	4.79	8.55

TABLE 3.3: Difference in electronic, internal, enthalpic, and free energies (in kcal/mol) of In·**2** conformers as compared to **3** at the PBE0-D3/def2-SVP/PCM_{OAm} level of theory.

	A	B^α	C^β	D^γ	ΔE	ΔU	ΔH	ΔG
1	**3**	1	A^+	*c*-[N=P*$InCl_3(NH_2Et)_2$]$^-$	65.21	63.95	63.95	68.21
2	**3**	1	ACl	*c*-N=P*$InCl_2(NH_2Et)_2$	48.94	48.40	48.40	46.34
3	**3**	2	ACl	*c*-N=P*$InCl_2(NH_2Et)_3$	22.53	23.15	22.25	39.13
4	$\mathbf{3_a}$	1	A^+	*t*-[N=P*$InCl_3(NH_2Et)_2$]$^-$	56.83	55.78	55.78	58.07
5	$\mathbf{3_a}$	1	ACl	*c*-N=P*$InCl_2(NH_2Et)_2$	34.67	34.23	34.23	31.08
6	$\mathbf{3_a}$	2	ACl	*c*-N=P*$InCl_2(NH_2Et)_3$	17.54	18.41	17.51	33.20
7	$\mathbf{3_a}$	2	ACl	*t*-N=P*$InCl_2(NH_2Et)_3$	15.07	15.98	15.08	30.33
8	$\mathbf{3_b}$	1	A^+	*c*-[P=N*$InCl_3(NH_2Et)_2$]$^-$	50.41	47.84	47.84	56.95
9	$\mathbf{3_b}$	1	ACl	*t*-P=N*$InCl_2(NH_2Et)_2$	26.24	25.99	25.99	24.01
10	$\mathbf{3_b}$	1	ACl	*c*-P=N*$InCl_2(NH_2Et)_2$	32.75	32.35	32.35	31.15
11	$\mathbf{3_b}$	2	ACl	*t*-P=N*$InCl_2(NH_2Et)_3$	8.35	9.05	8.15	27.53
12	$\mathbf{3_c}$	1	A^+	*t*-[P=N*$InCl_3(NH_2Et)_2$]$^-$	47.06	46.01	46.01	49.83
13	$\mathbf{3_c}$	1	ACl	*c*-P=N*$InCl_2(NH_2Et)_2$	26.05	26.11	26.11	21.95
14	$\mathbf{3_c}$	2	ACl	*c*-P=N*$InCl_2(NH_2Et)_3$	16.99	18.21	17.30	32.90

$^\alpha$ N NH_2Et $^\beta$ A^+: $[NH_3Et]^+$, ACl: $[NH_3Et]Cl$ $^\gamma$ *c*: *cis*, *t*: *trans*

TABLE 3.4: Difference in electronic, internal, enthalpic, and free energies (in kcal/mol) of a series of test acid-base reactions, $A + B \rightarrow C + D$, using $\Delta X = (X_C + X_D) - (X_A + X_B)$ at the PBE0-D3/def2-SVP/PCM_{OAm} level of theory.

Despite the widely varied set of test reactions examined in Table 3.4, none of the deprotonation schemes were found to be feasible. Reaction 11 had the lowest energy, as the inclusion of an additional ethylamine on the indium center lowered the electronic energy. However, this increased the order of the products which resulted in a significant rise in free energy. While requirements for "acceptable" ΔG values can be flexible, the reduction in ΔE was not enough to justify pursuing Reaction 11 as a mechanism.

While none of the products of Table 3.4 were found to be likely, other avenues

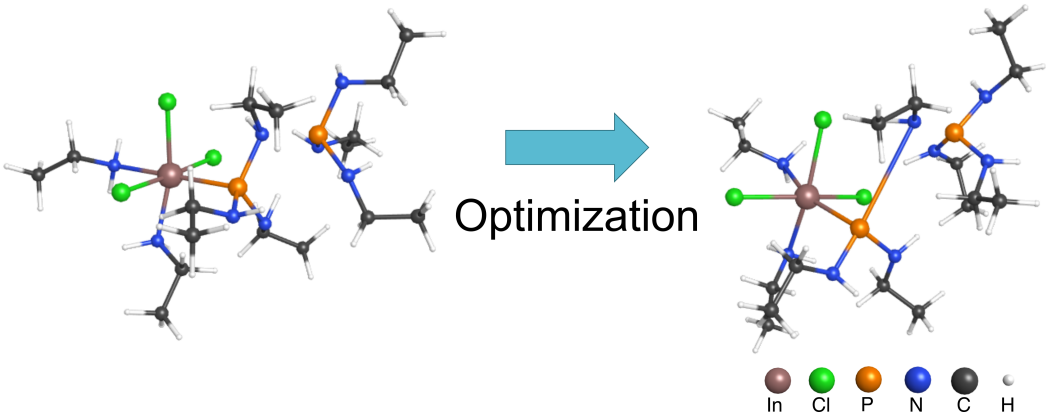

FIGURE 3.4: Initial (left) and final (right) structures of a geometry optimization where a second aminophosphine begins close to the first. Identified at the PBE0-D3/def2-SVP/PCM$_{\mathrm{OAm}}$ level of theory.

inspired potential mechanisms. Calculations that were intended as control studies found that the P(NHR)$_4^+$ product stabilized when a second aminophosphine started close to the one passivating the indium, such as on the left of Figure 3.4. This result suggested that the aminophosphine redox could occur without having to access a deprotonated intermediate. As such, the formation of the complexes in Figure 3.3 and their reactions with a second aminophosphine were examined in more detail.

3.2 Ligand Exchange and Disproportionation

Although a double-ζ basis set proved useful to screen reactions, moving to a larger triple-ζ basis set was deemed necessary. The increased computational costs were justified when minima shifted with the improved MO qualities. The calculations presented in the following sections used the def2-TZVP (Ahlrichs) basis-set[7] of triple-ζ quality, referred to as PBE0-D3/def2-TZVP/PCM$_{\mathrm{OAm}}$. As seen in Table 3.5, the use of a more sophisticated basis set refined the calculated geometries and eliminated the bridged In–N–P conformers of $\mathbf{3_b}$ and $\mathbf{3_c}$ as probable products.

	ΔE	ΔU	ΔH	ΔG
3	0.00	0.00	0.00	0.00
$\mathbf{3_a}$	0.42	0.28	0.28	0.71
$\mathbf{3_b}$	4.10	3.49	3.49	5.40
$\mathbf{3_c}$	7.63	7.03	7.04	9.06

TABLE 3.5: Difference in electronic, internal, enthalpic, and free energies (in kcal/mol) of In·**2** conformers as compared to **3** at the PBE0-D3/def2-TZVP/PCM$_{\mathrm{OAm}}$ level of theory.

While the comparisons of $A+B \rightarrow C+D$ are useful for screening potential candidates, they fail to describe the actual chemistry that is occurring. In order to properly model their interaction, the components A and B should be combined in a single calculation and probed to determine a mechanism of action. As with the previous calculations, several orientations of A–B should be examined to determine the lowest energy starting minimum. Then the two components can be pushed together to affect some reaction. Ideally, this would result in geometries similar to $C + D$, but computational

experiments like this frequently yield surprising new pathways. From a barrage of these calculations on the same system, the most stable starting, transition, and final geometries can be obtained. Comparisons of these energies then give a logical reaction pathway and can yield information about reaction rates as well as populations of reactants and products at equilibrium.

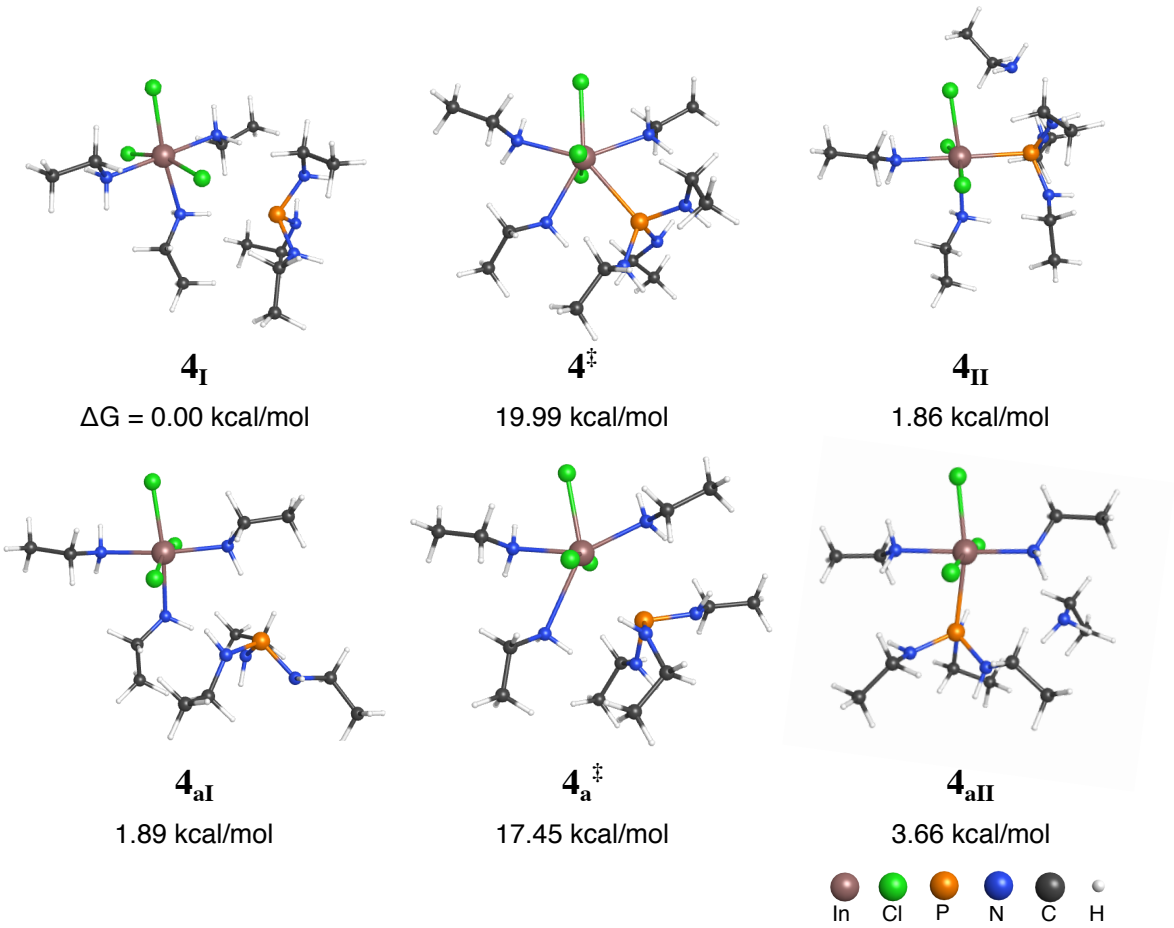

FIGURE 3.5: Geometries of In·P ligand exchanges at the PBE0-D3/def2-TZVP/PCM_{OAm} level of theory with the deviations in free energy from geometry $\mathbf{4_I}$ included. Portions of foreground ligands faded for clarity.

Because of the energetic similarity of **3** and $\mathbf{3_a}$, Figure 3.5 combines **1** and **2** in different ways to model the ligand exchange that would result in either product. The initial $\mathbf{4_I}/\mathbf{4_{aI}}$ geometries are passivated by hydrogen bonding, which allow the reactants to stabilize close to each other before the exchange. As the In$\cdots$P distance shrinks, the compounds pass through a transition state, $\mathbf{4}^{\ddagger}/\mathbf{4}_{\mathbf{a}}^{\ddagger}$, for which the ΔG can be interpreted as the activation energy. After the transition state, the complexes relax to the terminal geometries $\mathbf{4_{II}}/\mathbf{4_{aII}}$, where an NH_2Et molecule has been shifted to the second solvation sphere in favor of a P→In dative bonding environment. The ΔG of these final geometries can then be used to determine equilibria among the structures[†].

[†]The concentration a species B, p_B, can be related to species A by $p_B/p_A = 10^{-(G_B - G_A)/RT}$

The activation energy for the formation of $\mathbf{3_a}$ is much lower than that of **3**. This difference implies a reaction rate two orders of magnitude faster for the $\mathbf{4_a}$ pathway[†], which might make it more preferable. However, given the 453.15 K reaction temperature and the ΔG of the four minima, only $\sim$1% of molecules will exist as $\mathbf{4_{aII}}$ at equilibrium compared to the $\sim$10% as $\mathbf{4_{II}}$. Therefore, despite the conformers **3** and $\mathbf{3_a}$ being similar in energy, the geometries of Figure 3.5 support the preferential formation of **3**. The removal of the now extraneous ethylamine in $\mathbf{4_{II}}$ to form **3** can be considered trivial due to the reaction proceeding in excess solvent.

Following the ligand exchange, **3** interacts with an additional aminophosphine molecule, **2**, in a complex reaction illustrated in Figure 3.6. Initially, the $N_{(1)}\cdots H_{(4)}$ and $N_{(5)}\cdots H_{(1)}$ hydrogen bonds stabilize the two compounds to form $\mathbf{5_I}$. These serve to passivate a portion of the steric repulsion that would be introduced from the approach of the $P_{(2)}$ lone pair. When $P_{(2)}$ is close enough to $N_{(1)}$ in geometry $\mathbf{5}^{\ddagger}$, the MOs of the lone pairs of both moieties blend with the $P_{(1)}$–$N_{(1)}$ bond. This interaction facilitates a one electron transfer from $P_{(2)}$ to $P_{(1)}$ resulting in the formation of a $N_{(1)}$–$P_{(2)}$ bond. The now reduced $P_{(1)}$ in $\mathbf{5_{II}}$ displays a stronger In–P bond as well as a new lone pair. Supported by the shape of the HOMOs of these structures, presented later in Figure 3.15, this transition provides a logical interaction for the dual redox role of the aminophosphine in this synthesis.

Although ΔG from $\mathbf{5_I}$ to $\mathbf{5_{II}}$ is an unfavorable 3.60 kcal/mol, this could be mitigated with a modest increase in temperature above the 180 °C of our calculations. Specific syntheses have shown better products at temperatures as high as 300 °C,[33] so this requirement is not unusual. Table 3.9 shows $\mathbf{5_{II}}$ is electronically similar to its starting minimum, however, the entropic loss of 9.29 cal/mol-K accounts for only 1.79% of molecules as products at equilibrium. This low yield can create difficulties for utilizing this precursor for nanoparticle syntheses.

[†] As derived from the Eyring Equation, k = $k_b T/h * exp(-\Delta G^{\ddagger}/RT)$

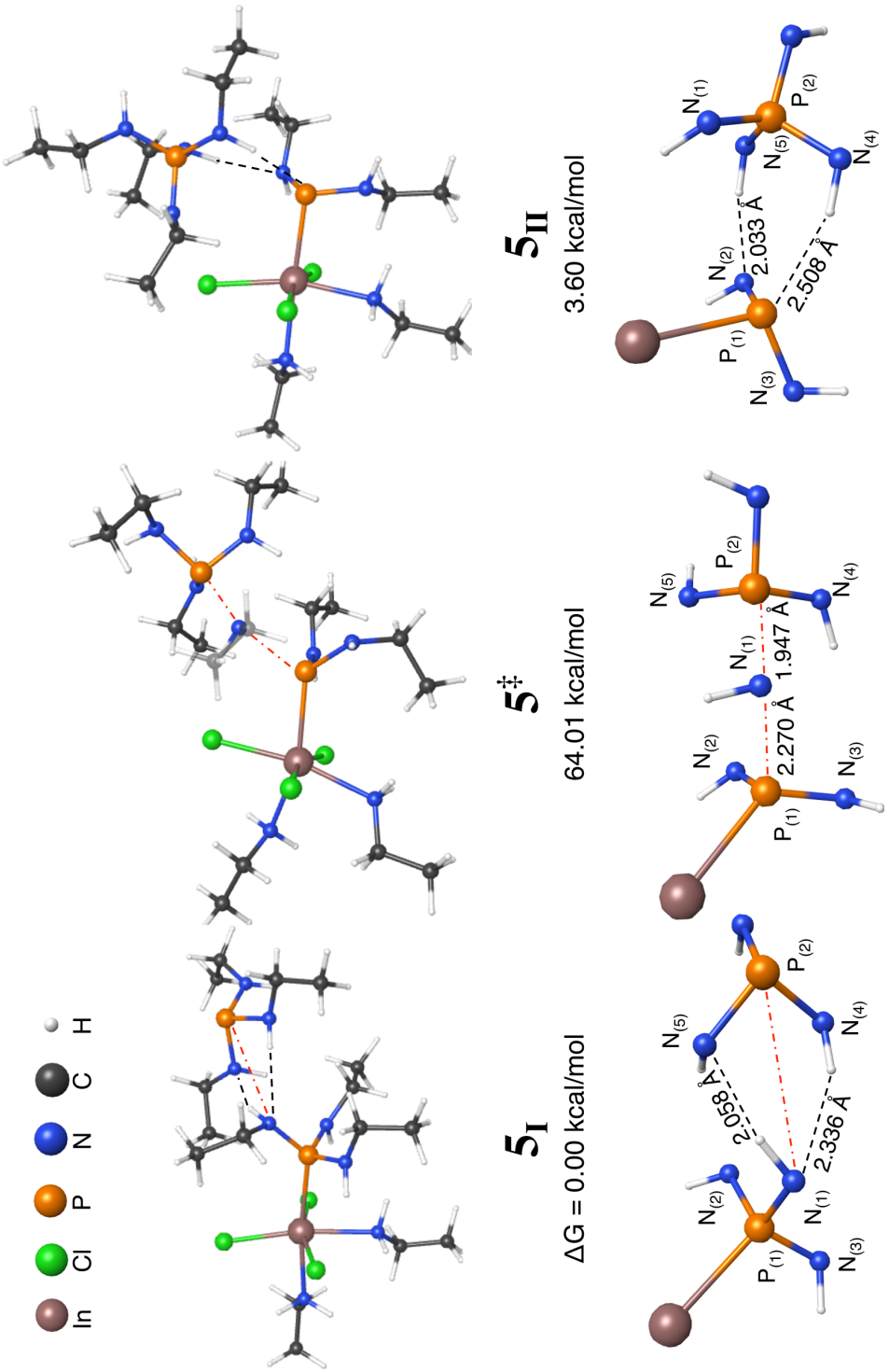

FIGURE 3.6: Geometries of the starting, transition, and terminal structures of the disproportionation reaction with changes in free energy (top) and a close-up view of their hydrogen binding environment (bottom). References to particular hydrogen atoms, $H_{(x)}$, follow the labeling of the nitrogen, $N_{(x)}$, to which they are bound.

3.3 Zinc-Activated Mechanism

While these reactions appear sluggish and unstable, the literature shows these precursors can rapidly produce nanoparticles.[3–5] One anomaly that could impact this is the high concentration of zinc salts prescribed in these syntheses. Up to 1 In : 5 Zn ratios were found to result in a decrease in the full width at half maximum of the lowest energy absorption peak of the InP QD samples,[5] implying increased homogeneity. These high concentrations of zinc suggest it may play a fundamental role in the reduction mechanism of aminophosphine precursors.

Regardless of the phosphorus source, zinc salts are present in a large number of high-quality InP QD syntheses. Despite this, studies tend to focus on indium-phosphorus interactions[34] and any work on the role of zinc compounds often treat them as surface passivants in one form or another.[35–38] This is generally due to the observations that these reactions can be done without zinc at about the same rates, albeit with poorer quality. Therefore, many traditional $(TMS)_3P$ InP syntheses include a 1 In : 1 Zn ratio and assume minimal interaction. However, while the new aminophosphine reaction can be done without the presence of ZnX_2,[33] the striking increase in zinc salt content for narrow distributions[5] in this synthesis suggests zinc affects more than just surface passivation. Recently, Koh *et al.* proved with DFT that the inclusion of zinc salts into $(TMS)_3P$ syntheses serves to stabilize the phosphine. This dramatically improves size distributions by ensuring the formation InP monomers instead of oligomer clusters.[39] Similarly, we show the use of zinc halides with aminophosphines can lower the reaction energies and improve the favorability of products.

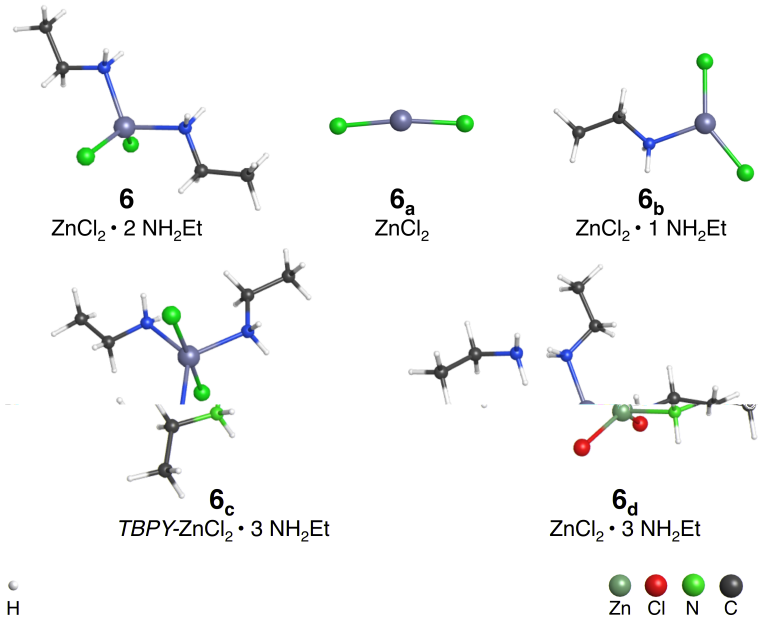

FIGURE 3.7: Geometries of $ZnCl_2$ solvation complexes at the PBE0-D3/def2-TZVP/PCM_{OAm} level of theory.

As with the indium salt, NH_2Et were added to $ZnCl_2$ until the first solvation sphere was filled, as in Figure 3.7. Examining Table 3.6 shows tetrahedral $ZnCl_2{\cdot}2\ NH_2Et$, **6** to be the most stable structure. Although $\mathbf{6_c}$ and $\mathbf{6_d}$ have lowered electronic energy due to the increased passivation from an additional nitrogen lone pair, the entropic contributions deem them less favorable. Despite being rejected, $\mathbf{6_c}$ will prove to be an interesting template for intermediary reactions due to its electronic stability.

	ΔE	ΔU	ΔH	ΔG
6	0.00	0.00	0.00	0.00
$\mathbf{6_a}$	42.92	39.90	41.70	14.25
$\mathbf{6_b}$	20.54	18.98	19.88	5.27
$\mathbf{6_c}$	-10.53	-9.00	-9.90	6.71
$\mathbf{6_d}$	-9.49	-8.00	-8.90	7.73

TABLE 3.6: Difference in electronic, internal, enthalpic, and free energies (in kcal/mol) as compared to **6**. Energies calculated as the sum of $ZnCl_2 \cdot N\ NH_2Et$ and $3 - N$ free NH_2Et as determined at the PBE0-D3/def2-TZVP/PCM_{OAm} level of theory.

Several kinds of zinc–phosphorus–indium interactions were trailed as potential energy-lowering mechanisms. Of these, displacing an ethylamine of **6** with the aminophosphine was found to be best. The aminophosphine was found to bind through one of its nitrogen lone pairs, instead of through the phosphorus like one might expect. Unlike the ligand exchanges of the In·P reaction, this was seen to occur as a multi-step process involving several changes in the coordination number of zinc. As with the optimized geometry in **6**, the initial complex is tetrahedral about the metal center in $\mathbf{7_a}$ and can be seen in Figure 3.9. This simple geometry is perturbed as the N$\cdots$Zn distance shrinks and the structure then proceeds through interesting 5-coordinate ($\mathbf{7_e}$ and $\mathbf{7_g}$), intermediates. This process then reverses as an ethylamine is removed in favor of the nitrogen lone pair on the aminophosphine.

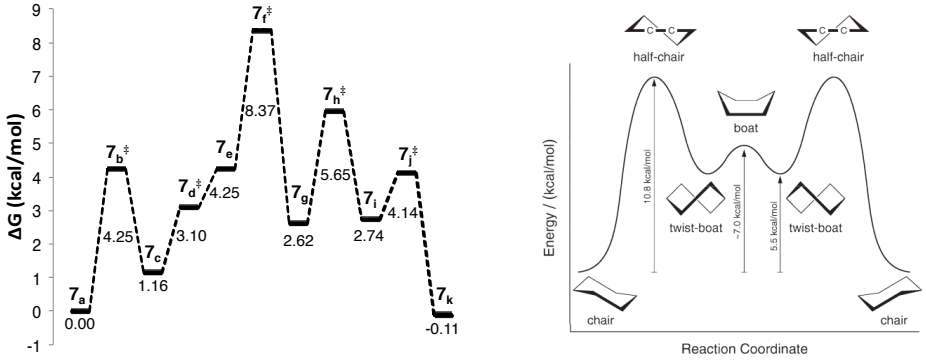

FIGURE 3.8: (Left) Diagram of the change in free energy of the zinc-aminophosphine interaction of Figure 3.9 with a cyclohexane inversion (right), as adapted with permission from Nelson *et al.*[40] Copyright 2011 American Chemical Society.

The free energy diagram of the various steps is depicted in the left of Figure 3.8, which shows this interaction to be a low-energy activation with nearly equal start and end products. As such, ∼56% of molecules exist as $\mathbf{7_k}$ at equilibrium, which can likely be tailored to higher yields with reaction design. The first geometry has a high degree of hydrogen bonding between **6** and **2** that results in a large initial energy barrier presented by $\mathbf{7_b^{\ddagger}}$. The series of reactions from $\mathbf{7_c}$–$\mathbf{7_g}$ constitute the next

significant activation energy as the Cl–Zn–Cl bond angle increases from 132.37° to 189.57°. Although unconventional, geometry $\mathbf{7_g}$ benefits from the electronic stability similar to that of $\mathbf{6_c}$, which allows it to be a relatively low energy intermediate. This also creates resistance to perturbing the structure, as evidenced by the height of $\mathbf{7_h^{\ddagger}}$. Once it is disrupted, the chlorines relax to the typical tetrahedral binding environment, $\mathbf{7_k}$, and kick off an ethylamine. The energy profile of this activation by zinc can be easily compared to that of a cyclohexane inversion,[40] as seen in the right of Figure 3.8. Because the half-chair transition states have similar barriers to our process, $\mathbf{7_k}$ should form just as frequently.

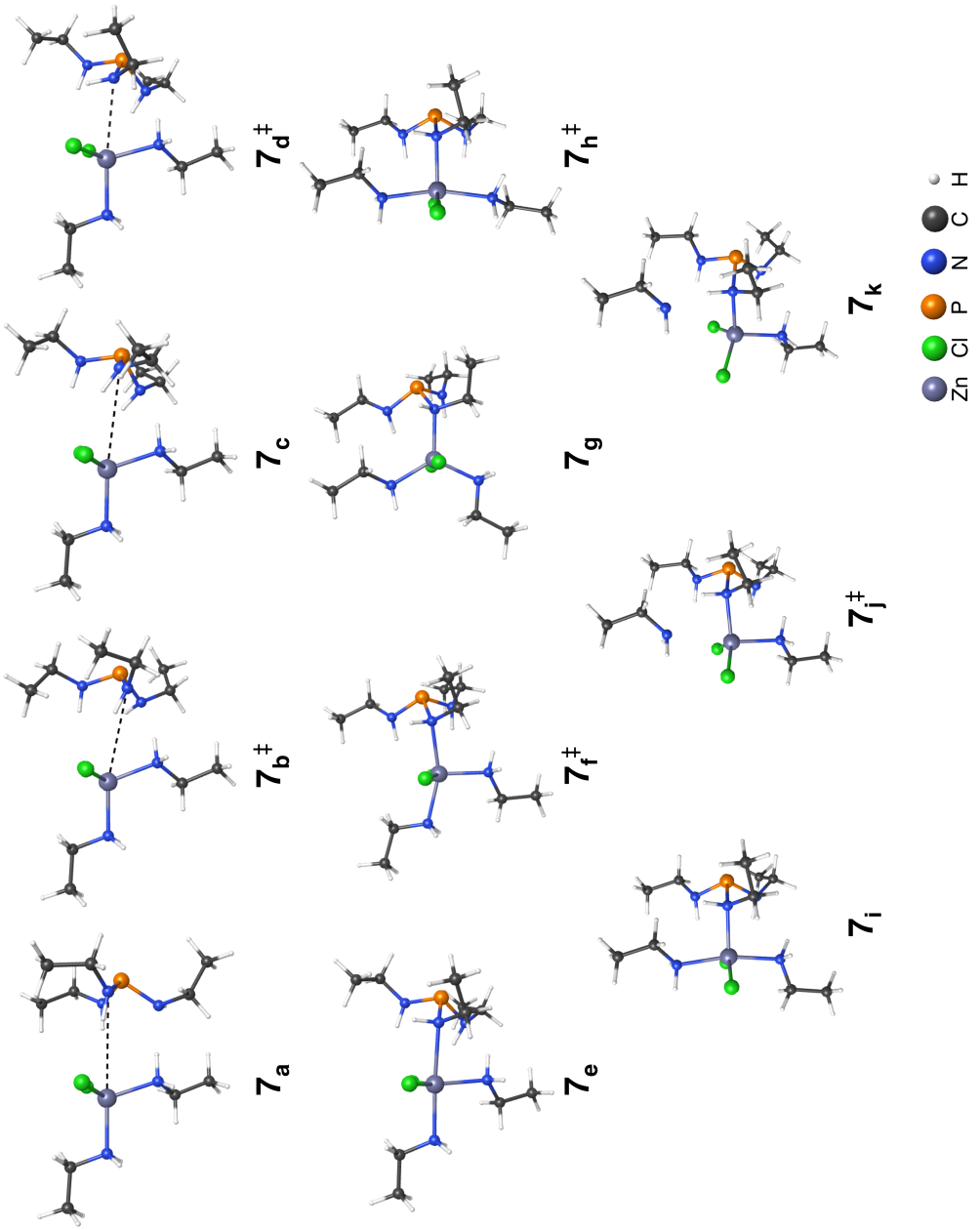

FIGURE 3.9: Geometries of zinc–aminophosphine interaction at the PBE0-D3/def2-TZVP/PCM_{OAm} level of theory.

Ligand Exchange

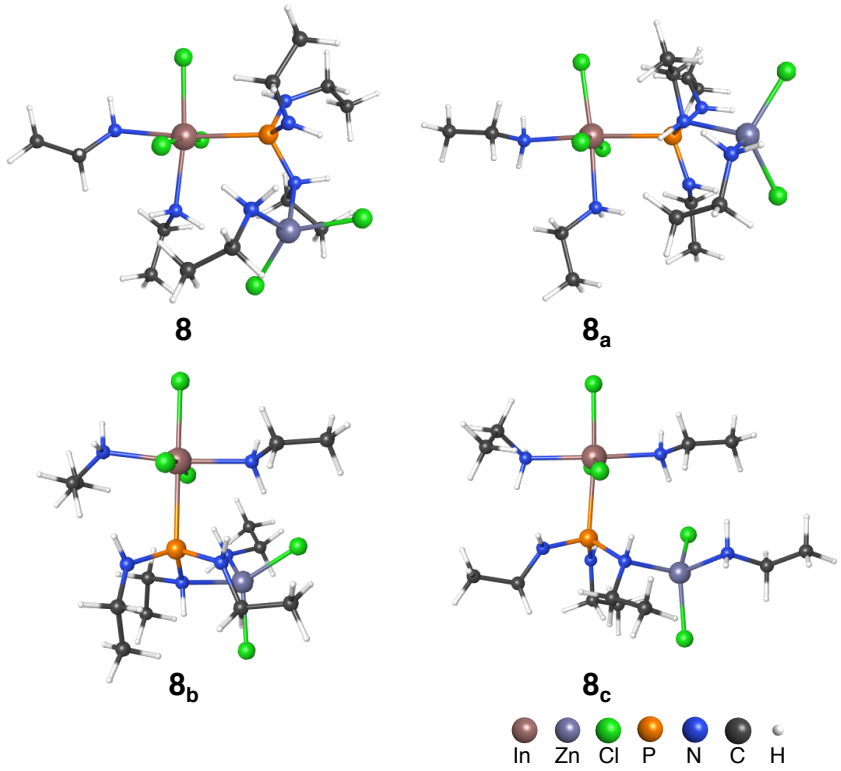

FIGURE 3.10: Various In·**ZnP** conformers at the PBE0-D3/def2-TZVP/PCM_{OAm} level of theory.

Due to the abundance of a bridged Zn–N–P product (**ZnP**), ligand exchanges of the indium center were examined with this activated phosphine. As with **3**, a number of orientations were considered to identify likely products and the lowest energy conformers are compared in Figure 3.10. While each displays a P→In environment, geometries **8** and $\mathbf{8_a}$ replace an outer ethylamine, while $\mathbf{8_b}$ and $\mathbf{8_c}$ replace the middle ligand. Of these best structures, **8** is clearly the most stable according to Table 3.7 and was explored to determine a ligand exchange process.

	ΔE	ΔU	ΔH	ΔG
8	0.00	0.00	0.00	0.00
$\mathbf{8_a}$	3.64	3.54	3.54	2.56
$\mathbf{8_b}$	6.87	6.72	6.72	7.30
$\mathbf{8_c}$	6.57	6.24	6.24	7.53

TABLE 3.7: Difference in electronic, internal, enthalpic, and free energies (in kcal/mol) of the structures of Figure 3.10 as compared to **8**.

As with the zinc-free ligand exchange, the process described in Figure 3.11 begins with the two components hydrogen-bound to each other. They then proceed through a 7-coordinate transition state and the process ends with **8** and a free ethylamine. Unlike the structures examined in Section 3.2, the significantly negative ΔG means the majority of conformers are as the terminal $\mathbf{9_{II}}$ at equilibrium. The reduced activation energy also results in a rate constant 55x that of $\mathbf{4}^{\ddagger}$. When taken together, these improvements imply that a mixed solution of indium, zinc, and aminophosphine will have a majority of precursors as **8** both initially and at equilibrium. This

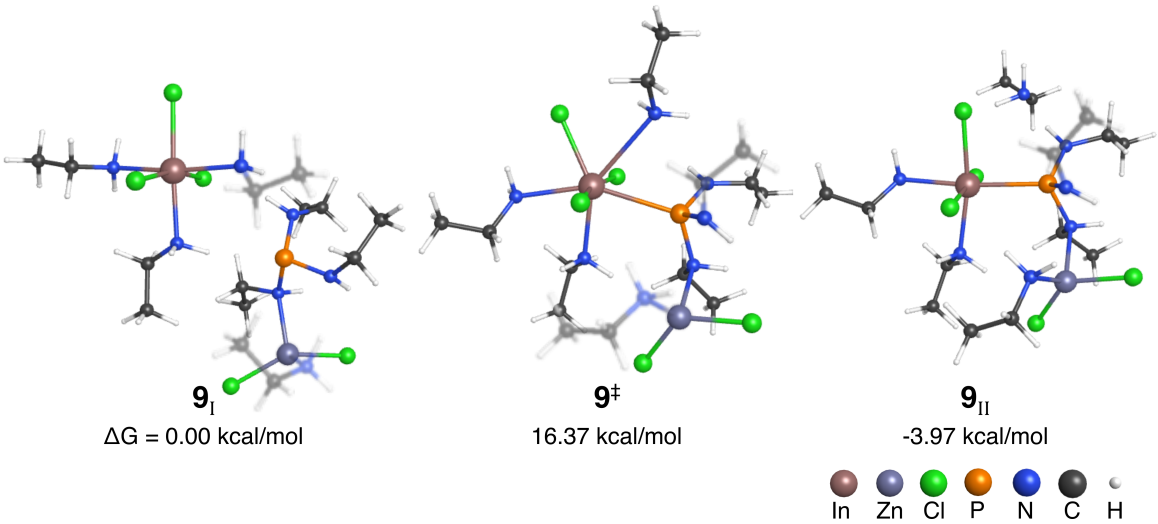

FIGURE 3.11: Ligand exchange of the activated aminophosphine for the formation of **8** at the PBE0-D3/def2-TZVP/PCM_{OAm} level of theory. Corresponding free energy values displayed as the difference from the initial minimum.

degree of homogeneity is likely responsible for the improved FWHM in the synthesis with 1 In : 3.6 P : 5 Zn ratios by Tessier *et al.*[5]

Although these calculations show the presence of zinc produces stable materials, they do not provide clarity as to why these improvements occur. The typical candidates for the source of these changes would be differences in properties such as In$\cdots$P distances, bond angles, or changes in the molecular orbitals between the two schemes. However, the two sets of geometries appeared similar along most of these critical parameters. The only explanation was found when comparing the partial charges of the species. Figure 3.12 shows the molecular dipoles, which are calculated as the sum of partial charges across the calculation. The net horizontal moment can be attributed to the P$\cdots$In interaction, while the vertical moment corresponds to the In–Cl electron-withdrawing environments. The dipole of $\mathbf{4_{II}}$ suggests an In$\rightarrow$P instead of P$\rightarrow$In dative environment, which would reduce the ability of the aminophosphine to bind to the indium center.

In contrast, the zinc activated series appears to have the In–Cl and Zn–Cl moments effectively canceling each other. A strong P$\rightarrow$In bond develops as the reaction proceeds, which increases the effective passivation. This change likely occurs from the acidity of the zinc center and seems to be responsible for lowering ΔE. These differences show the benefits of an activated pathway and similar effects are seen in the disproportionation reaction of the next section.

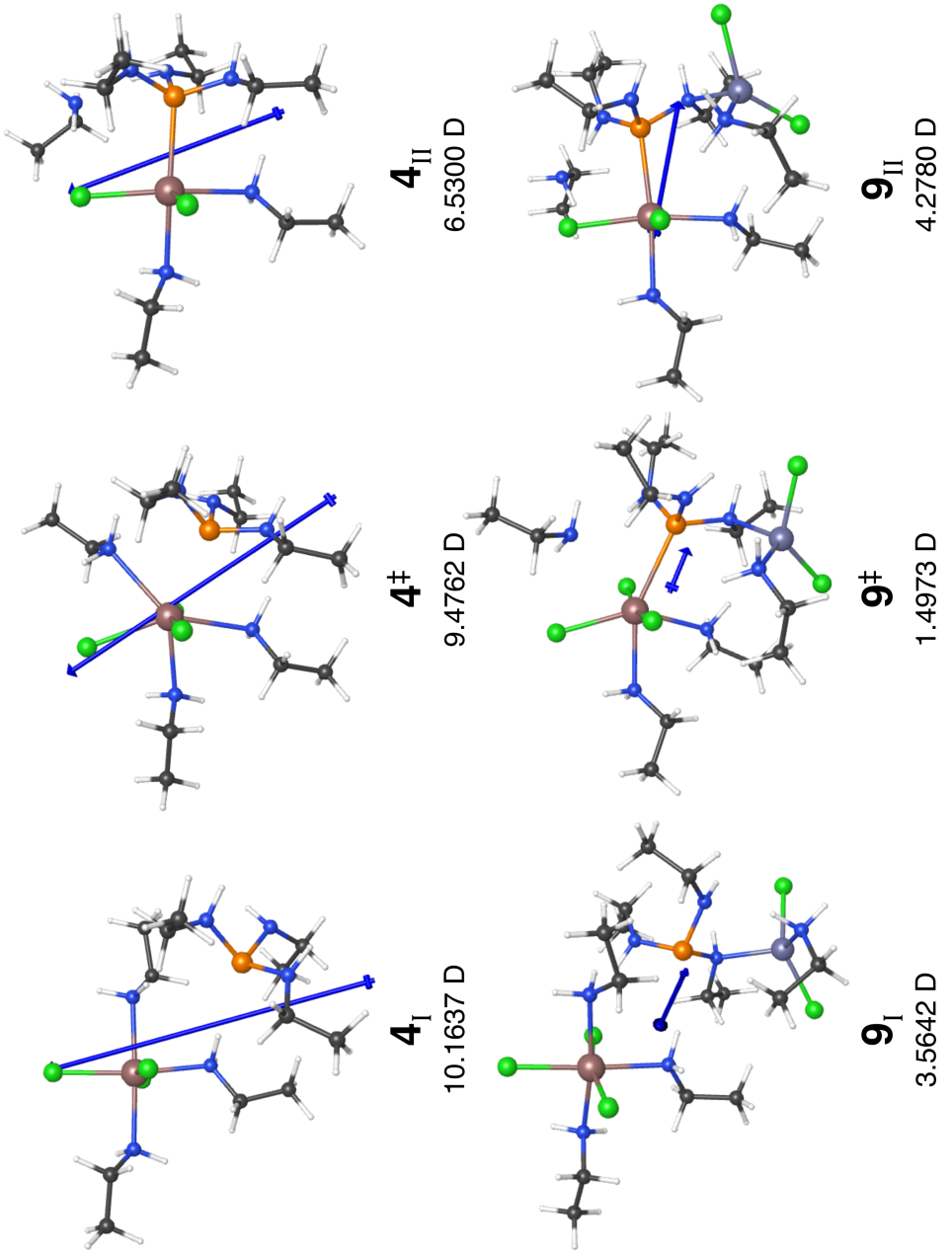

FIGURE 3.12: Dipole moments in Debye (D) about the zinc-free (top) and zinc-activated (bottom) ligand exchanges.

Disproportionation

Following the ligand exchange, the In·**ZnP** complex is exposed to a second aminophosphine as before, with the hydrogen bonds arranging a markedly similar binding environment to $\mathbf{5_I}$. Figure 3.14 shows a similar triangle, which again opens the $N_{(1)}$ to MO mixing as $P_{(2)}$ closes and transfers an electron, forming the $N_{(1)}$–$P_{(2)}$ bond (geometries $\mathbf{10_I}$, $\mathbf{10}^{\ddagger}$, and $\mathbf{10_{II}}$, respectively).

The highest occupied molecular orbitals of these structures are displayed in figure 3.15. As these are the most reactive orbitals, they can reveal information about how the electron transfer occurs. Surprisingly, it appears the mechanism is nearly identical among the structures of the two schemes. However, the zinc-activated reaction is much preferred, which can be seen by the improved stability of its geometries. The reduced activation energy yields a rate constant four orders of magnitude faster than $\mathbf{5}^{\ddagger}$ and 99.996% of molecules are converted at equilibrium.

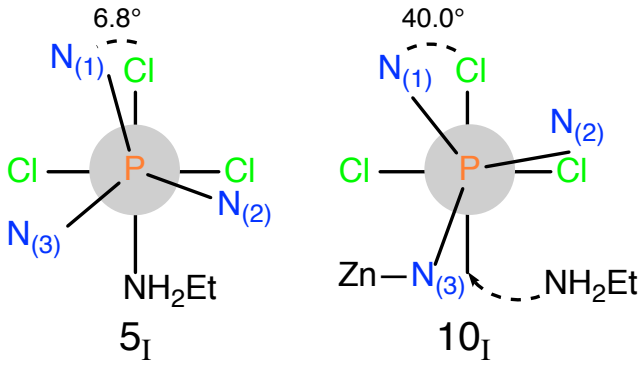

FIGURE 3.13: Newman projections of geometries from the disproportionation reactions.

The largest structural difference between the initial conformers seems to be the dihedral about the In·P bond in Figure 3.13. With the presence of zinc, this expands from 6.8° to 40.0° due to increased hydrogen bonding from the Zn–Cl bonds. Interestingly, removing the zinc from $\mathbf{10_I}$ and optimizing the structure results in $\mathbf{5_I}$, confirming that this conformational change is a direct result of the activation.

According to Table 3.8, the presence of the acidic zinc center shrinks the initial $N_{(1)} \cdots P_{(2)}$ distance by 7.19%. As the second **2** has less distance to cross, this results in the lowered activation barrier to $\mathbf{10}^{\ddagger}$. However, the differences in the binding environments of the post-reaction minima, $\mathbf{5_{II}}$ and $\mathbf{10_{II}}$, are more significant. Due to the reduction of $P_{(1)}$ and the formation of a second lone pair, the electronegative amines have longer phosphorus-amine and shorter phosphorus-indium distances than the pre-reaction minima. This indicates a stronger In–P bond while the lengthened bonds of the remaining amines may ease their removal in subsequent reductions. A 15% decrease in $Zn \cdots N_{(2)}$ distance with the disproportionation suggests the zinc further serves to passivate the remaining amine lone pairs, which reduces molecular strain and strengthens the In-P bond. This is evidenced in Table 3.9 by

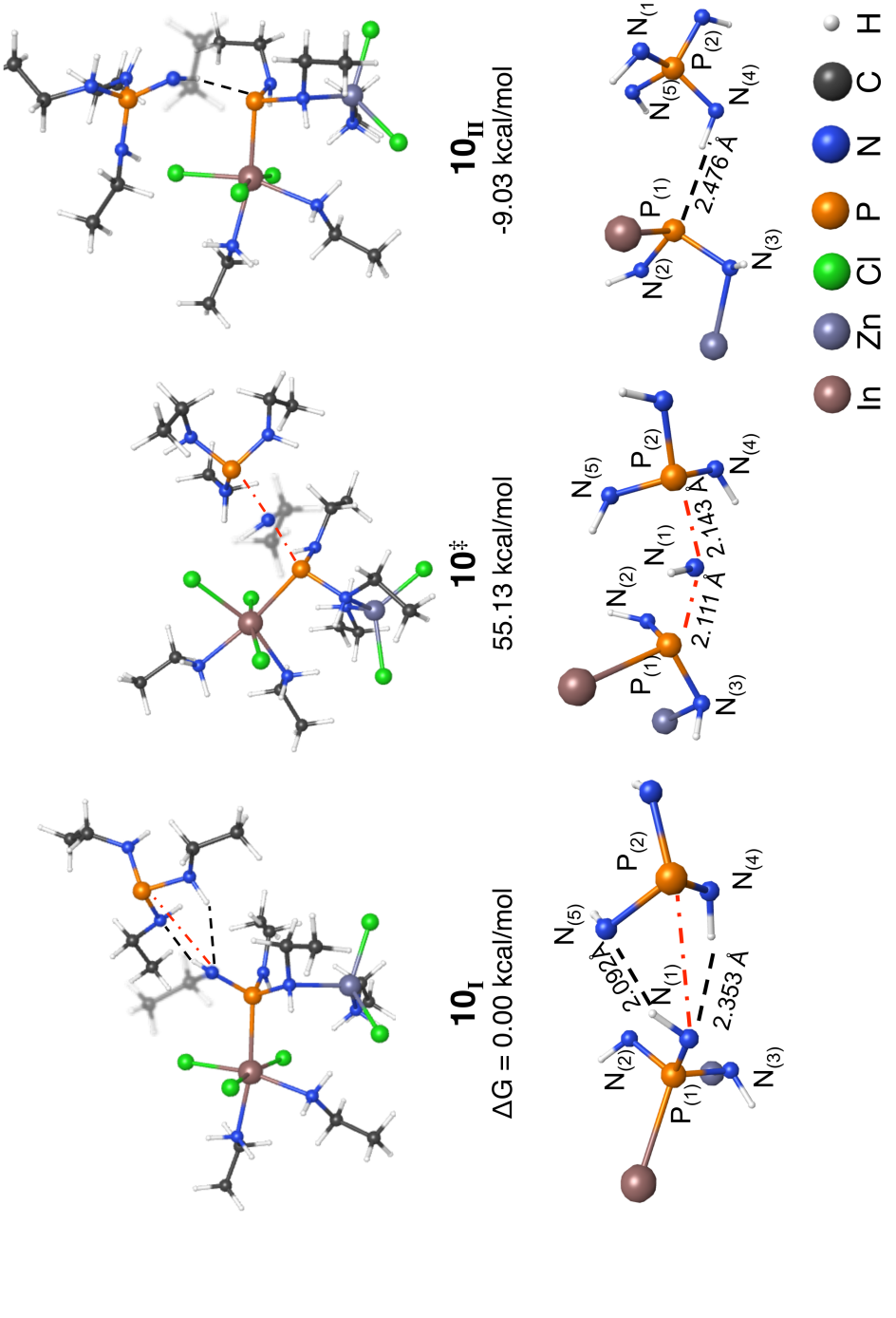

FIGURE 3.14: Geometries and energies of the zinc-activated disproportionation reaction (top) with reoriented and close-up views of the reaction area (bottom). Portions of the foreground ligands faded throughout for clarity

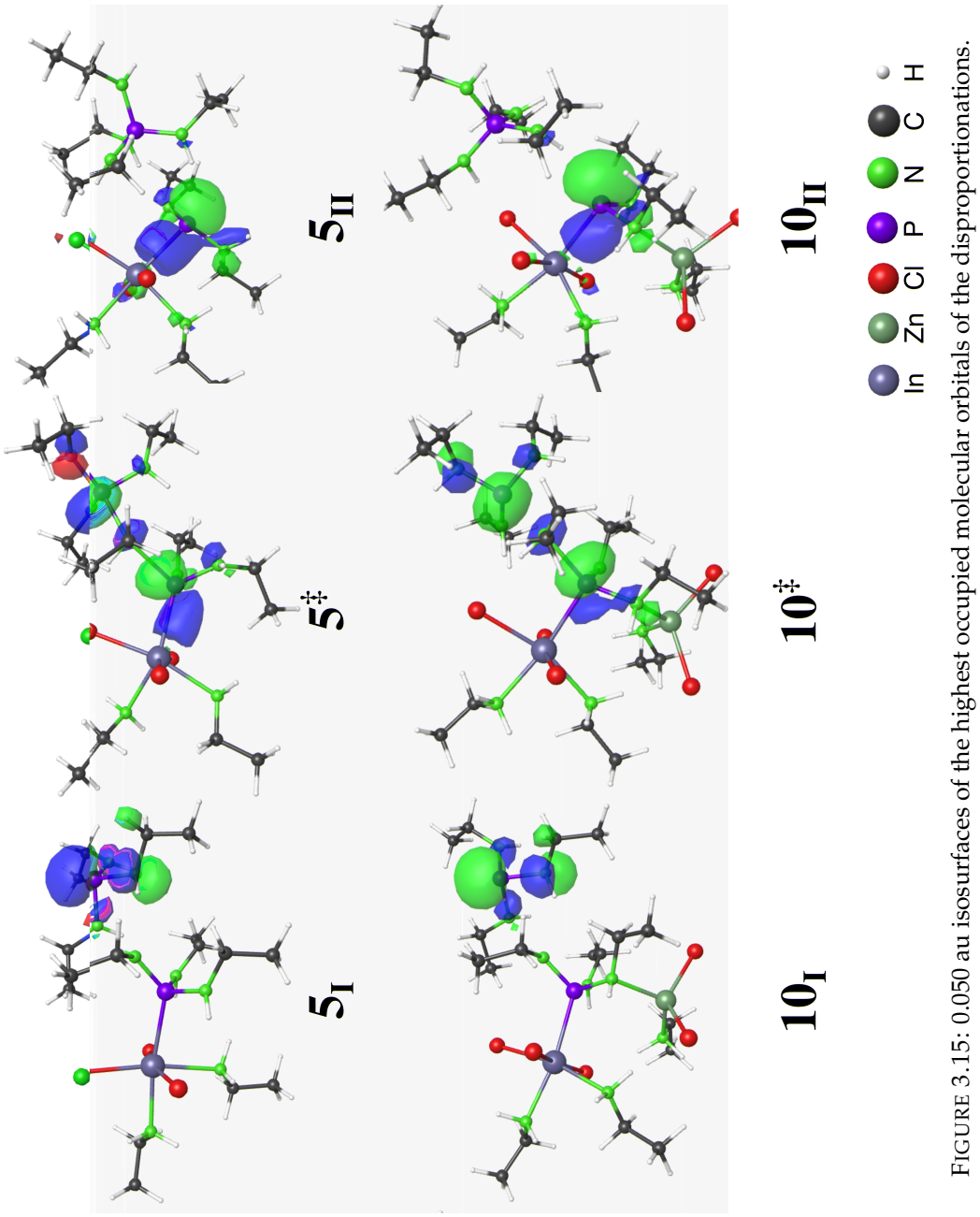

FIGURE 3.15: 0.050 au isosurfaces of the highest occupied molecular orbitals of the disproportionations.

the reduction in both ΔE and total MO band placement presented by the salt inclusion, which are major contributions for the favorability of this path over the zinc-free reaction.

	$\mathbf{5_I}$	$\mathbf{5^‡}$	$\mathbf{5_{II}}$	$\mathbf{10_I}$	$\mathbf{10^‡}$	$\mathbf{10_{II}}$
$P_{(1)}$–$N_{(2)}$	1.656	1.661	**1.732**	1.635	1.681	**1.697**
$P_{(1)}$–$N_{(3)}$	1.658	1.698	**1.725**	1.746	**1.790**	**1.799**
Zn–$N_{(2)}$	–	–	–	3.416	**2.994**	**2.917**
Zn–$N_{(3)}$	–	–	–	2.196	2.126	**2.107**
In–$P_{(1)}$	2.623	2.594	2.568	2.655	2.604	**2.560**

TABLE 3.8: Selected bond distances in Å throughout the disproportionation steps of both reactions. Values corresponding to more than ± 3% deviation from starting minima ($\mathbf{5_I}$ or $\mathbf{10_I}$) are indicated with positive shifts in **red** and negative in **blue**.

	ΔE [a]	ΔU [a]	ΔH [a]	ΔG [a]	C_v [b]	S [b]	HOMO[c]
$\mathbf{5_I}$*	0.00	0.00	0.00	0.00	220.88	373.04	-5.96
$\mathbf{5^‡}$	61.50	61.21	61.21	64.01	220.50	366.87	-4.14
$\mathbf{5_{II}}$	0.01	-0.61	-0.61	3.60	220.39	363.75	-5.36
$\mathbf{10_I}$*	0.00	0.00	0.00	0.00	263.06	434.72	-6.10
$\mathbf{10^‡}$	52.56	51.95	51.96	55.13	261.90	427.71	-4.90
$\mathbf{10_{II}}$	-8.43	-8.47	-8.47	-9.03	262.74	435.97	-5.90

[a]kcal/mol [b]cal/mol-K [c]eV

TABLE 3.9: Thermodynamic calculations for the zinc-free (top) and zinc-bound (bottom) disproportionation reactions including the highest occupied molecular orbital energies. Electronic, internal, enthalpic, and free energies presented as deviation from each minima (*).

This work presents a probable scheme for the reaction of indium and aminophosphine precursors. The binding of zinc to the aminophosphine has been shown to be rapid with at least half of the phosphorus molecules activated when the system reaches equilibrium. The presence of a zinc halide has been shown to reduce the number of possible binding modes, increase the stability of end products, and improve the rates of both the ligand exchange and disproportionation reactions. The increase in P–N bond length of the reduced species suggests that further reductions by other aminophosphines may be more reactive. However, modeling these interactions such as this will be complicated by the likelihood of small cluster formation during the early stages of growth.[41, 42] Although including $ZnCl_2$ lowered the activation energy, 55.13 kcal/mol is still unrealistic given how easily quantum dots form in these systems. Alternative reaction schemes, such as those involving a proton-shuttle, may need to be examined.

3.4 Synthetic Adaptations

Using the knowledge gained in the last section, we designed syntheses to isolate the activation processes from the In-P formation. Swapping the zinc salt to less acidic complexes, such as zinc bromide and zinc iodide, was envisioned as a way to tune reaction rates and control particle growth. While selecting larger halides has already been used to shift InP quantum dot sizes, the reactions that changed the zinc salts produced poorer-quality materials than those that altered the indium compounds.[5] The band gap absorptions of the nanoparticles made with zinc bromide and zinc iodide were significantly broad, with the calculated full width half maxima (FWHM) reaching values >80 nm. Because the size of the particles determines the energy of the exciton feature, the magnitude of this suggests the produced materials are very polydisperse. These broad size distributions can be a sign of competing reactions, such as a zinc-free pathway interfering with an activated one.

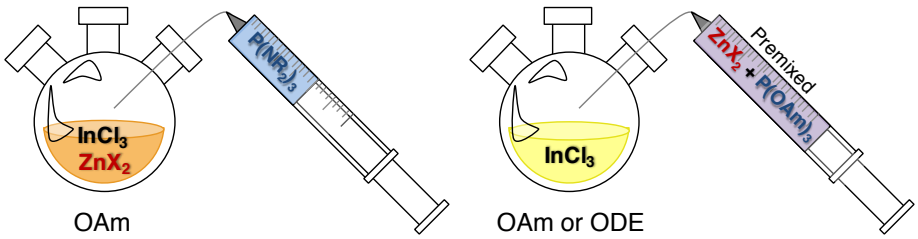

FIGURE 3.16: Diagram of a 1-pot reaction (left) in which $P(NEt_2)_3$ (blue) is injected into a hot solution of indium (yellow) and zinc salts (red) versus a 2-pot reaction (right) in which the aminophosphine is premixed with oleylamine (OAm) and zinc salts before injection into a hot solution of indium salts in oleylamine or 1-octadecene (ODE).

In this section, these literature 1-pot reactions were compared to several 2-pot schemes which were intended to isolate the zinc and phosphorus precursors to allow the activation to occur before particles began to grow. Full details are available in Section 3.5, but as depicted in Figure 3.16, zinc halides and the tris(diethylamino)phosphine ($P(DEA)_3$) were first combined in oleylamine and allowed to react. High zinc and phosphorus along with low amine concentrations were chosen to increase $\mathbf{7_k}$ as a product. This solution was then injected into a second reaction containing the indium precursors to generate the nanoparticles.

Initially, the studies with a 2-pot synthesis in oleylamine produced odd results. As the reaction progressed, samples of the solution were removed and quenched in toluene before being examined with UV-Vis absorption spectroscopy. The time it takes to develop spectral features can then yield information about the rate of reaction as well as particle sizes throughout the experiment. When comparing to the results from the literature process (Figure 3.17A), the 2-pot reaction seems to struggle to begin, as evidenced by the lack of features in the visible region until ~5 min of reaction in Figure 3.17B. This lag in reactivity was initially thought to be from the difference in injection volume between the two syntheses (0.45 mL vs. 4 mL), but

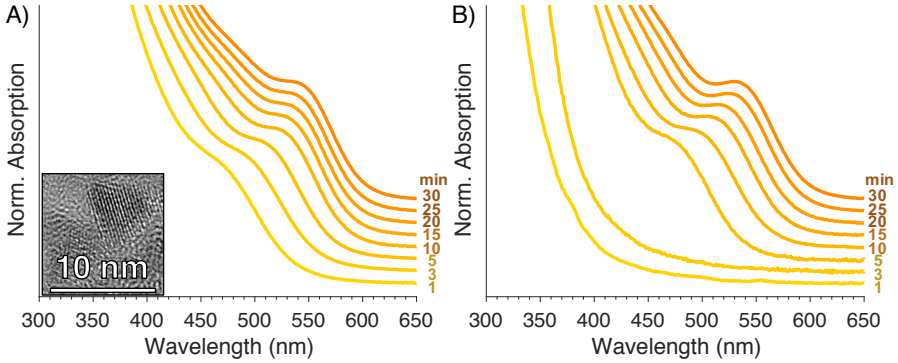

FIGURE 3.17: Absorption spectra of aliquots dispersed in toluene taken during core growth of A) 1-pot oleylamine and B) 2-pot oleylamine syntheses using $ZnCl_2$; inset is a representative TEM of the 1-pot sample.

preheating the syringe and injected solution to minimize the thermal shock did little to change this phenomenon. Despite this, the similarity in the position of the peak maximum means materials reached a similar average size by the end of the reaction at $t = 30$ min.

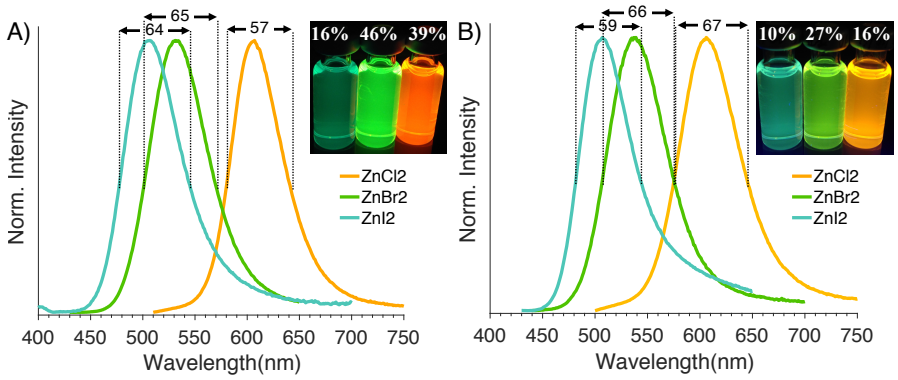

FIGURE 3.18: Emission spectra of cleaned A) 1-pot OAm and B) 2-pot OAm InP/ZnS materials synthesized with varying zinc halides, annotated with FWHM values in nm. Insets are photographs of the particles dispersed in toluene and labeled with the percent PLQY of each sample: ZnI_2 (left), $ZnBr_2$ (center), and $ZnCl_2$ (right).

As discussed in Section 2.4.1, materials based on InP are rarely emissive without changing their surfaces in some way.[43–45] A conventional technique to handle this is the growth of a shell of another semiconductor material on the surface of the particles. This shell then protects the core material and allows for further treatments that could otherwise jeopardize the quality of the particles. Common shells include zinc sulfide (ZnS) and zinc selenide (ZnSe), as their lattices are similar to InP, their band gaps should not interfere with the properties of the core, and they are biocompatible. The core/shell particles presented here are produced by the slow introduction of ZnS precursors to the core reactions after a reaction time of ~20 minutes followed by a temperature ramp. More specific experimental details can be found in Section 3.5.

	1-pot OA			2-pot OA		
	$ZnCl_2$	$ZnBr_2$	ZnI_2	$ZnCl_2$	$ZnBr_2$	ZnI_2
Abs (nm)	570	473	423	568	478	428
Ems (nm)	607	531	507	606	538	502
$FWHM_{Abs}$ (nm)	40	58	53	52	59	52
$FWHM_{Ems}$ (nm)	58	65	64	67	66	64
$PLQY^{True}$ (%)	39.45	46.30	16.12	16.29	27.34	10.15
τ_μ [a] (ns)	69.97	70.74	65.92	95.67	75.14	76.22
spread[b]	0.97	0.56	0.71	1.07	0.73	0.90
dark photons[c] (%)	3.83	1.23	1.92	5.94	2.94	4.18

[a] Mean lifetime from a lognormal distribution of lifetimes fit to TCSPC data
[b] σ/μ of the lognormal distribution
[c] Percentage of TCSPC data attributed to tail baseline counts

TABLE 3.10: Spectroscopic data for InP/ZnS samples synthesized with various zinc halides in oleylamine. Data from the 2-pot samples have been colored to indicate if the values are better or worse than those made with the literature 1-pot method.

Because the time studies appeared promising, the two reactions were repeated with the growth of a ZnS shell. Additional syntheses with different zinc salts were also examined to observe the effects of the larger halides on particle quality. Figure 3.18 shows the emission spectra of the various InP/ZnS materials are very similar between the two methods. However, it is immediately apparent that those made in a 2-pot synthesis are less bright overall, as confirmed by their photoluminescent quantum yields (PLQYs). A closer look at some of the other spectroscopic qualities, such as those in Table 3.10, produces some troubling conclusions. The absorption and emission maxima of corresponding syntheses are nearly identical, so the average particle sizes can be assumed to be the same between the two methods. However, the increased absorption and emission FWHM shows the distribution of these sizes are worse in the 2-pot method. The photoluminescent lifetime data also shows these QDs take longer to emit and the energy gets stuck in nonemissive trap states nearly twice as often.

$$ZnX_2 \cdot 2\,NH_2R + P(NHR)_3 \rightarrow ZnX_2 \cdot NH_2R \cdot P(NHR)_3 + NH_2R \tag{3.3}$$

The source of the drop in quality could be from an abrupt change to the precursor equilibrium during the reaction. Because the activation reaction is governed by Equation 3.3, it is sensitive to the concentration of the primary amine. Taking the activated materials from one pot and injecting them into a solution of excess oleylamine would then drive them to separate back into the reactants on the L.H.S. of Equation 3.3. The delayed onset of band gap absorption features in the early times of Figure 3.17B supports this conclusion. The lack of reaction indicates that this phenomenon affects precursor conversion, which then results in a wide range of sizes and defect-rich particles.

In order to avoid back-conversion, the solvent of the indium solution in the second pot was changed to 1-octadecene (ODE) instead of oleylamine. Because InX_3 salts are not soluble in this new reaction, three equivalents of myristic acid were also

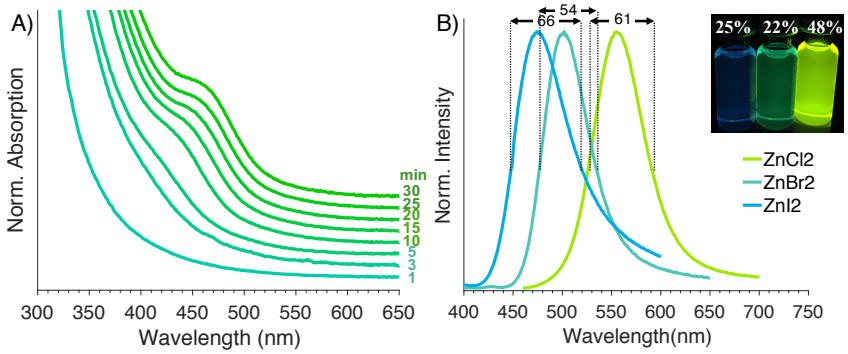

FIGURE 3.19: A) Absorption spectra of aliquots dispersed in toluene taken during core growth of an ODE-3MA synthesis with $ZnCl_2$. Emission spectra of cleaned B) InP/ZnS materials synthesized with varying zinc halides, annotated with FWHM values in nm. Insets are photographs of the particles dispersed in toluene and labeled with the percent PLQY of each sample: ZnI_2 (left), $ZnBr_2$ (center), and $ZnCl_2$ (right).

included as ligands to bind to the In^{3+}, so this design is referred to as ODE-3MA. When the aminophosphine complex was introduced to this new solution, distinct color changes were seen only after ~10 minutes of reaction. As seen in Figure 3.19A, the synthesis also produced materials that were smaller and with worse size distributions than those created with oleylamine. The slow reactivity and highly polydisperse products hint that the myristic acid may be interfering with the In–P bond formation. This conclusion is not unusual, as many literature sources show that fatty acids bind strongly to indium.[46] These ligands may obstruct the aminophosphine ligand exchange, which would slow the nanoparticle growth.

Despite this disadvantage, the smaller sizes posed an interesting avenue to explore, so a layer of ZnS was grown on these ODE-3MA cores to observe the behavior of their emission. Interestingly, these core/shell particles showed a few improvements from the oleylamine reactions, which can be seen in Figure 3.19B. The quantum dots made with $ZnCl_2$ and ZnI_2 displayed higher PLQY, which suggests fewer trap states, and the $ZnBr_2$ synthesis also had a reduced emission FWHM, which indicates narrower size distributions.

While the ODE-3MA method is a new use for the aminophosphine precursors, the particles were not exceptionally bright. However, the ability to work in a new solvent inspired the adaptation of a $(TMS)_3P$-based synthesis by Nann and coworkers.[47] The ligand system for the indium solution was replaced with a 1 indium : 1 fatty acid : 2 fatty amine ratio, which matched that of the previous publication. This method is referred to as ODE-1MA, and the reduction in the amount of fatty acid resulted in much brighter and more efficient particles.

As seen in Figure 3.20B and Table 3.11, the particles made with the new $ZnCl_2$ and $ZnBr_2$ syntheses showed reduced emission FWHM and faster photoluminescent lifetimes compared to ODE-3MA, with quantum yields that surpassed those of the 1-pot oleylamine reactions. Additionally, these quantum dots displayed reduced dark currents and narrowed lifetime distributions. When these properties are taken

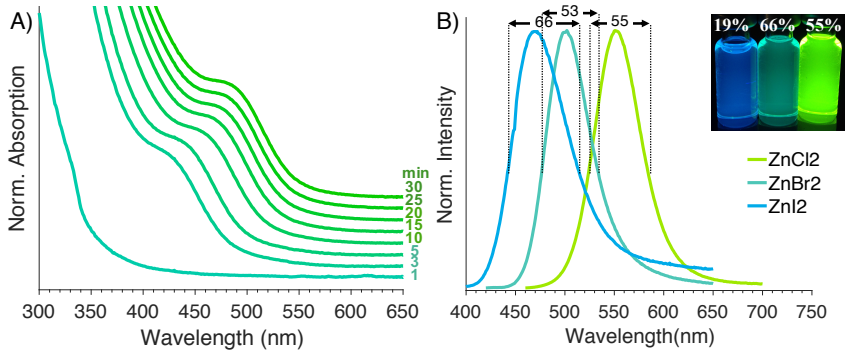

FIGURE 3.20: A) Absorption spectra of aliquots dispersed in toluene taken during core growth of an ODE-1MA synthesis. B) Emission spectra of cleaned InP/ZnS materials synthesized with varying zinc halides, annotated with FWHM values in nm. Insets are photographs of the particles dispersed in toluene and labeled with the percent PLQY of each sample: ZnI_2 (left), $ZnBr_2$ (center), and $ZnCl_2$ (right).

all together, they suggest materials with a smaller range of sizes, fewer dark/trap states, and more streamlined emissive pathways. The $ZnCl_2$ synthesis is of particular interest as the τ_μ of 48.15 ns and only 0.31% dark current suggest it to be the most efficient material examined here.

Interestingly, all of the samples made in ODE have spectral blue shifts when compared to their oleylamine-based analogs. This change indicates increased quantum confinement, which then suggests the ODE syntheses create particles that are of much smaller volumes. Such a shift could be attributed to the tight binding of fatty acid functional groups, which would also explain the initially sluggish growth kinetics. In-carboxylate bonds have been shown to be difficult to displace, and DFT studies often force $In(OOCR)_3$ complexes to be under-coordinated in order for the phosphorus compounds to react with them.[46] However, the full effects of ODE on this synthesis are discussed at length in Section 5.3.

Kim *et al.* discussed the halide passivation of the indium-rich (111) surfaces typical of these syntheses and found that while chlorine bound quite strongly due to its negative charge, the slabs had to be co-passivated by a dative lone pair in a 3 Cl^- : 1 NH_2Me concentration.[33] A carboxylic acid group may then be able to serve in both roles and drive out the other ligands, which is likely given the low solubility of halides in a non-coordinating solvent like ODE. Regardless of the source, the combination of reduced amine content and the introduction of fatty acid ligands appears to shift the particles to much smaller sizes.

Frustratingly, every use of ZnI_2 seems to produce poor quantum dots. Although they have comparable or better absorption FWHM, these samples have lower PLQYs despite being made with the same processes that generated quality materials with the use of chlorides or bromides. The notable red defect tail emission in Figures 3.18, 3.19, and 3.20 alongside the very long lifetimes and large dark currents seen in Table 3.11 point to the iodide reactions creating nanoparticles with high degrees of trap states. The sterics of the large halide may be contributing to this problem, as it could

	1-pot OA			2-pot OA		
	$ZnCl_2$	$ZnBr_2$	ZnI_2	$ZnCl_2$	$ZnBr_2$	ZnI_2
Abs (nm)	570	473	423	568	478	428
Ems (nm)	607	531	507	606	538	502
$FWHM_{Abs}$ (nm)	40	58	53	52	59	52
$FWHM_{Ems}$ (nm)	58	65	64	67	66	64
$PLQY^{True}$ (%)	39.45	46.30	16.12	16.29	27.34	10.15
$\tau_\mu{}^a$ (ns)	69.97	70.74	65.92	95.67	75.14	76.22
spread^b	0.97	0.56	0.71	1.07	0.73	0.90
dark photons^c (%)	3.83	1.23	1.92	5.94	2.94	4.18

	ODE-3MA			ODE-1MA		
	$ZnCl_2$	$ZnBr_2$	ZnI_2	$ZnCl_2$	$ZnBr_2$	ZnI_2
Abs (nm)	508	448	416	515	439	405
Ems (nm)	555	501	475	551	502	470
$FWHM_{Abs}$ (nm)	57	51	45	54	55	59
$FWHM_{Ems}$ (nm)	61	54	67	56	53	67
$PLQY^{True}$ (%)	48.19	22.19	24.90	54.83	66.50	19.47
$\tau_\mu{}^a$ (ns)	58.37	71.57	135.8	48.15	69.87	104.0
spread^b	0.71	0.61	1.41	0.62	0.65	1.26
dark photons^c (%)	2.11	2.17	6.00	0.31	1.64	2.51

[a] Mean lifetime from a lognormal distribution of lifetimes fit to TCSPC data
[b] σ/μ of the lognormal distribution
[c] Percentage of TCSPC data attributed to tail baseline counts

TABLE 3.11: Spectroscopic data for samples synthesized with various zinc halides. Data from the 2-pot samples have been colored to indicate if the values are better or worse than those made with the literature 1-pot method.

limit the availability of more reactants to reach the surface and allow for more defects to form during InP core growth. The case of 1-pot oleylamine is intriguing, however, as most spectroscopic properties are on par with or better than the other halides, yet ZnI_2 still only exhibits a 16.12% PLQY. The bulkier halide may also interfere with ZnS shell growth or reduce crystallinity, both of which would result in a poorly-confined core and lower fluorescent yield. However, a more detailed study on ZnI_2 interactions would be necessary to understand the cause more fully.

As a direct result of our studies with DFT, these new, safer precursors can now be used in systems based on 1-octadecene and fatty acids. The resulting particles are of similar quality to those in the literature,[3,5] but because the method does not use a glovebox, its ease will allow a broader swath of research and industry to create these quantum dots. While this chapter establishes a larger understanding of the precursor mechanisms, more work needs to be done to understand and reliably tune the reaction fully. Investigating the exact role of the halide in these systems may guide changes so the reactions that use iodides can produce quality materials. If this synthesis could be adapted to be halide-free, the method may become even simpler as less hygroscopic materials are easier to handle and store at length.

3.5 Experimental Details

List of Chemicals Indium chloride (Sigma-Aldrich, anhydrous 99.999%), zinc chloride (Sigma-Aldrich, anhydrous 97%), zinc bromide (Sigma-Aldrich, anhydrous 98%), and zinc iodide (Sigma-Aldrich, 98%) were stored in a common air-desiccator. Tris-(diethylamino) phosphine (Sigma-Aldrich, 97%) and trioctylphosphine (Sigma-Aldrich, 97%) were stored under nitrogen with septa and accessed with Schlenk techniques. Oleylamine (Sigma-Aldrich, 70%), 1-octadecene (Sigma-Aldrich, 90%), myristic acid (Merck, 98%), zinc undecylenate (Merck), sulfur (BDA, sublimed), toluene (ROMIL, 99.9%), and ethanol (Fisher, 99.99%) were used as received and stored under ambient conditions.

1-pot synthesis of InP cores Nanoparticles were synthesized using a modification of literature methods.[5] Typically, 100 mg (0.45 mmol) $InCl_3$, 2.2 mmol of zinc halide (300 mg $ZnCl_2$, 495 mg $ZnBr_2$, or 702 mg ZnI_2), and 5.0 mL (15 mmol) of oleylamine were degassed at 120 °C under vacuum for 1 hour before flushed with nitrogen atmosphere and heated to 180 °C. 0.45 mL (1.6 mmol) tris(diethylamino)phosphine was injected and allowed to stir for 30 minutes before rapidly cooling to 70 °C. The reaction solution was diluted with toluene and centrifuged (5 min, 10,000 rpm) to separate any solid precipitate. The supernatant was cleaned twice with toluene/ethanol precipitation and centrifugation (10 min, 10,000 rpm). The resulting nanoparticle precipitate was dispersed in toluene for further analysis.

2-pot synthesis of InP cores 100 mg (0.45 mmol) $InCl_3$ and 10.0 mL (30 mmol) of oleylamine were degassed at 120 °C under vacuum for 1 hour before being put under nitrogen atmosphere and raised to 180 °C. Separately, 2.2 mmol of zinc halide (300 mg $ZnCl_2$, 495 mg $ZnBr_2$, or 702 mg ZnI_2) and 3.0 mL (9.1 mmol) oleylamine were degassed at 120 °C under vacuum for 30 minutes. The zinc solution was put under nitrogen atmosphere and 0.45 mL (1.6 mmol) tris(diethylamino)phosphine was injected and the solution stirred for 30 minutes. The temperature was then increased to 150 °C and 1.0 mL (3.0 mmol) of additional oleylamine was introduced and briefly allowed to mix before loading the zinc-phosphorus solution into a syringe and quickly injecting into the hot indium-oleylamine solution. The reaction was allowed to react for 30 minutes before rapidly cooling to 70 °C. The solution was cleaned and prepared as above.

Non-coordinating synthesis of InP cores (ODE-3MA) 100 mg (0.45 mmol) $InCl_3$, 338 mg (1.35 mmol) myristic acid (MA), and 10.0 mL (31 mmol) of 1-octadecene (ODE) were degassed at 120 °C under vacuum for 1 hour before being put under nitrogen atmosphere and raised to 180 °C. Separately, 2.2 mmol of zinc halide (300 mg $ZnCl_2$, 495 mg $ZnBr_2$, or 702 mg ZnI_2) and 3.0 mL (9.0 mmol) oleylamine were degassed at 120 °C under vacuum for 30 minutes. The zinc solution was put under nitrogen atmosphere and the temperature increased to 150 °C. 0.45 mL (1.6 mmol) tris(diethylamino)phosphine was injected and the solution stirred for 30 minutes.

1.0 mL (3.1 mmol) of additional ODE was introduced and briefly allowed to mix before loading the zinc-phosphorus solution into a syringe and quickly injecting into the hot In-ODE solution. The reaction was allowed to react for 30 minutes before rapidly cooling to 70 °C. The solution was cleaned and prepared as above.

Adapted synthesis of InP cores (ODE-1MA) 100 mg (0.45 mmol) $InCl_3$, 113 mg (0.45 mmol) myristic acid, 0.3 mL (0.9 mmol) oleylamine, and 10.0 mL (31 mmol) of 1-octadecene (ODE) were degassed at 120 °C under vacuum for 1 hour before being put under nitrogen atmosphere and raised to 180 °C. Separately, 2.2 mmol of zinc halide (300 mg $ZnCl_2$, 495 mg $ZnBr_2$, or 702 mg ZnI_2) and 3.0 mL (9.0 mmol) oleylamine were degassed at 120 °C under vacuum for 30 minutes. The zinc solution was put under nitrogen atmosphere and the temperature increased to 150 °C. 0.45 mL (1.6 mmol) tris(diethylamino)phosphine was injected and the solution was stirred for 30 minutes. 1.0 mL (3.1 mmol) of additional ODE was introduced and briefly allowed to mix before loading the zinc-phosphorus solution into a syringe and quickly injecting into the hot In-ODE solution. The reaction was allowed to react for 30 minutes before rapidly cooling to 70 °C. The solution was cleaned and prepared as above.

Synthesis of InP/ZnS core/shell materials A literature method was used to grow a shell of zinc sulfide in situ.[5] The core syntheses were carried out as above, however after 20 minutes of core growth, 1 mL saturated TOP-S (2.2 M) was slowly injected into the reaction solution. At 60 minutes, the temperature was increased to 200 °C. At 120 minutes, 0.7 g of zinc $(undecylenate)_2$ in 1.0 mL TOP and 3.0 mL ODE was slowly injected while the temperature was increased to 220 °C. At 150 minutes, 0.7 mL saturate TOP-S was slowly injected while the temperature was increased to 240 °C. At 180 minutes, 0.35 g $Zn(undecylenate)_2$ in 0.5 mL TOP and 1.5 mL ODE was slowly injected while the temperature was increased to 260 °C. At 210 minutes, the reaction was rapidly cooled to 70 °C and the solution was cleaned and prepared as above.

TEM Transmission electron microscope images were obtained using a JEOL 2100F FEG TEM operated at 200 kV. InP QD samples were initially purified using either centrifuge separation followed by two washing steps with toluene/ethanol as solvent /anti-solvent or via size-exclusion column with BioRad S-X1 beads and toluene as eluent. A drop of purified QD solution was allowed to dry on a holey carbon TEM substrate (ProSciTech, 200 mesh Cu grid) which was then left in a desiccator overnight to dry completely before any imaging.

Absorption UV-Vis absorption spectra were obtained with the use of a quartz cuvette loaded in a Cary® Bio-50 spectrometer equipped with a Xenon flash lamp. Samples were scanned from 300-800 nm with a 0.1 s dwell time and background-subtracted with a toluene blank. Absorption FWHM were determined from examining the min and max values of 1^{st} derivative of each sample's exciton absorption

peak according to a literature method.[5]

$$FWHM = \sqrt{2\,ln(2)}\,(\lambda_{max} - \lambda_{min}) \tag{3.4}$$

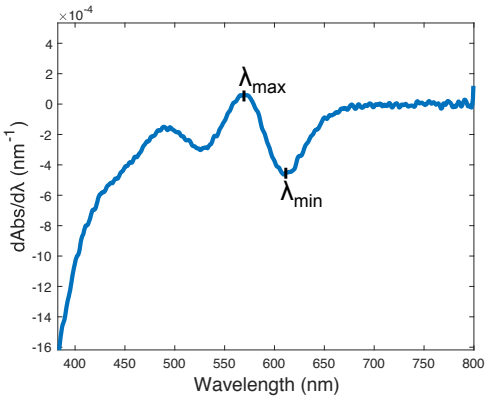

FIGURE 3.21: Example first derivative absorption used to determine FWHM.

Emission Photoluminescence data were obtained with the use of a quartz cuvette loaded in an Edinburgh Instruments FLS980 spectrophotometer equipped with a continuous Xenon lamp, single-grating excitation and emission monochrometers, and a Hamamatsu R928P thermoelectrically-cooled photomultiplier tube detector. Typical emission spectra resulted from 5 scans of 0.2 s dwell time each, utilizing moderate excitation ($\Delta\lambda$ = 1-4 nm) and fine emission ($\Delta\lambda$ <0.5 nm) bandwidths, optimizing peak signal to ~300,00 counts per second (cps) with sample optical density (OD) <0.1 au at excitation wavelength. Integrating sphere measurements were performed with a direct excitation geometry and 5 scans of 0.2 s dwell time each, utilizing broad excitation ($\Delta\lambda$ = 10-12 nm) and fine emission ($\Delta\lambda$ <0.5 nm) bandwidths, optimizing detected excitation peak signal to ~750,000 cps with sample optical density <0.1 au at excitation wavelength. Care was taken to preserve bandwidths and emission intensity between sample and blank measurements for accurate quantum yield calculations.

Quantum Yields (PLQY^{True}) were calculated using an integrating sphere and correcting the observed QY for self-absorption effects with a standard 90°, 1 cm path length, <0.1 au OD emission scan (PL$_{90°}$) according to a literature method. The fraction, *a*, of self-absorbed light due to the increased path length of an integrating sphere was determined by tail-matching a background-subtracted integrating sphere emission scan to that of PL$_{90°}$, as outlined in Figure 3.23 and Equation 3.6 below.

$$PLQY^{Obs} = \frac{\int_c^d (PL_{sphere} - blank_{sphere})}{\int_a^b (blank_{sphere} - PL_{sphere})} * 100\% \tag{3.5}$$

$$a = \frac{\int_c^d PL_{90°} - (PL_{sphere} - blank_{sphere})}{\int_c^d PL_{90°}} \tag{3.6}$$

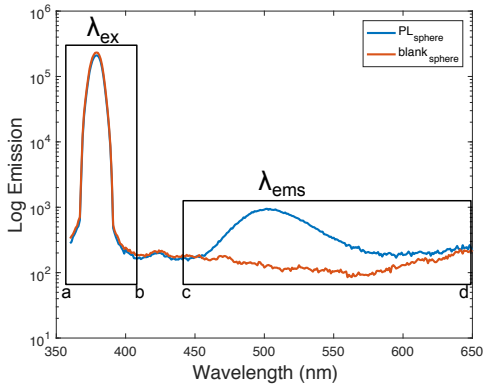

FIGURE 3.22: Scattering and emission peaks with a toluene blank and InP/ZnS sample with λ_{ex} = 380nm, $\Delta\lambda_{ex}$= 12 nm.

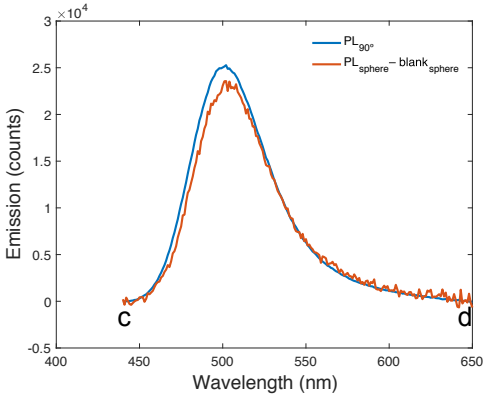

FIGURE 3.23: Blank-subtracted integrating sphere emission scaled to tail-match a standard PL_{90° spectrum.

$$PLQY^{True} = \frac{PLQY^{Obs}}{(1 - a + a * \frac{QY^{Obs}}{100})} \tag{3.7}$$

Photoluminescent lifetimes were determined through time correlated single photon counting (TCSPC) for each sample using a 380 nm picosecond pulsed laser and an Edinburgh Instruments FLS980 spectrophotometer. Samples were excited and emission monochrometers were set to peak maxima from PL_{90° spectra with $\Delta\lambda$=20 nm, ensuring laser intensity resulted in emission <1% of laser pulse cps. Signals were collected from 1 or 2 μs pulse rates divided across 8192 time bins until one bin registered 10,000 counts. Instrument response functions (IRF) were recorded for each sample using a scattering solution at the same pulse rates with λ_{Ems}=380 nm, $\Delta\lambda$=20 nm, 10,000 max counts, and ~1,000 cps laser intensity. The IRF was subtracted from each sample and the tail was fit to a number of decay functions (Equations 3.8 – 3.13) using randomly selected initial parameters which were analytically minimized to optimize probabilistic likelihood. These random fits were performed 10 times each, with the best of each of the 5 models kept to compare across all of the

samples. Random fitting also included a horizontal baseline fit corresponding to signal detected outside the general characteristic decay. As excitons stuck in trap states can spontaneously emit through phenomena such as phonon coupling, the fraction of this baseline that accounts for total decay signal is presented as "dark counts" and can correspond to trap or dark exciton states. Although the triexponential was frequently found to fit the data the best, the model can generate equivalently good fits for drastically different parameters so was rejected. The log-normal distribution was the next best fit, and so was chosen for sample comparisons as is an apt model due to the heterogeneity inherent in nanoparticle syntheses.

$$\text{Monoexponential :} \quad f(t;\tau) = \mathrm{e}^{-t/\tau} \tag{3.8}$$

$$\text{Biexponential :} \quad f(t;\theta_i,\tau_i) = \theta_1\mathrm{e}^{-t/\tau_1} + \theta_2\mathrm{e}^{-t/\tau_2} \tag{3.9}$$

$$\text{Triexponential :} \quad f(t;\theta_i,\tau_i) = \theta_1\mathrm{e}^{-t/\tau_1} + \theta_2\mathrm{e}^{-t/\tau_2} + \theta_3\mathrm{e}^{-t/\tau_3} \tag{3.10}$$

$$\text{Stretched :} \quad f(t;\tau,\beta) = \mathrm{e}^{(-t/\tau)^\beta} \tag{3.11}$$

$$\text{Lognormal :} \quad g(\tau;\mu,\sigma) = \frac{1}{\tau\sigma\sqrt{2\pi}}\exp\left(-\frac{(log\tau-\mu)^2}{2\sigma^2}\right) \tag{3.12}$$

$$f(t;\mu,\sigma) = \int_0^\infty g(\tau;\mu,\sigma)\frac{1}{\tau}\mathrm{e}^{(-t/\tau)}d\tau \tag{3.13}$$

ZnCl2 1-pot

	Mono	Bi		Tri			Stretch	Lognormal
R2	0.9619	0.9966			0.9994		0.9721	0.9987
loglikelihood	-10315924	-10260841.9636			-10257653.4824		-10277069.7193	-10259465.3729
dark photons	0.080285	0.0410			0.0311		0.0575	0.0383
Tau	52.3611	32.51597	147.9778	20.46535	58.97293	253.5658	52.8882	69.9674
theta		0.69767	0.30233	0.31805	0.53912	0.14282		0.9721
beta							0.8128	
mu								3.9154
sigma								0.8157

FIGURE 3.24: Example of the parameters of one sample fit with each decay function. Dark photons presented as the fraction of total counts existing as the baseline. Theta for the lognormal distribution is the spread (standard deviation divided by the mean) of the distribution.

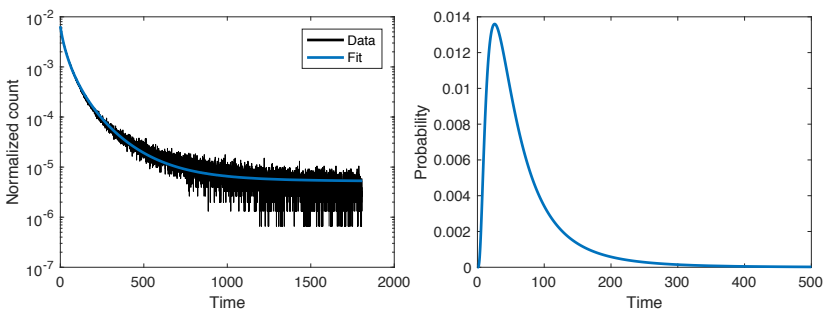

FIGURE 3.25: Example of a fit (left) using a lognormal distribution of lifetimes (right).

Bibliography

[1] G. Laufersky, S. Bradley, E. Frécaut, M. Lein, and T. Nann, "Unraveling aminophosphine redox mechanisms for glovebox-free InP quantum dot syntheses," *Nanoscale*, vol. 10, no. 18, pp. 8752–8762, 2018.

[2] W.-S. Song, H.-S. Lee, J. Lee, D. Jang, Y. Choi, M. Choi, and H. Yang, "Amine-derived synthetic approach to color-tunable InP/ZnS quantum dots with high fluorescent qualities," *Journal of Nanoparticle Research*, vol. 15, no. 6, pp. 1–10, 2013.

[3] M. D. Tessier, K. De Nolf, D. Dupont, D. Sinnaeve, J. De Roo, and Z. Hens, "Aminophosphines: A Double Role in the Synthesis of Colloidal Indium Phosphide Quantum Dots," *Journal of the American Chemical Society*, vol. 138, no. 18, pp. 5923–5929, 2016.

[4] A. Buffard, S. Dreyfuss, B. Nadal, H. Heuclin, X. Xu, G. Patriarche, N. Mézailles, and B. Dubertret, "Mechanistic Insight and Optimization of InP Nanocrystals Synthesized with Aminophosphines," *Chemistry of Materials*, vol. 28, no. 16, pp. 5925–5934, 2016.

[5] M. D. Tessier, D. Dupont, K. De Nolf, J. De Roo, and Z. Hens, "Economic and Size-Tunable Synthesis of InP/ZnE (E = S, Se) Colloidal Quantum Dots," *Chemistry of Materials*, vol. 27, no. 13, pp. 4893–4898, 2015.

[6] C. Adamo and V. Barone, "Toward reliable density functional methods without adjustable parameters: The PBE0 model," *J. Chem. Phys.*, vol. 110, pp. 6158–6169, 1999.

[7] F. Weigend and R. Ahlrichs, "Balanced basis sets of split valence, triple zeta valence and quadruple zeta valence," *Phys. Chem. Chem. Phys.*, vol. 7, p. 3297, 2005.

[8] S. Grimme, J. Antony, S. Ehrlich, and H. Krieg, "A consistent and accurate ab initio parameterization of density functional dispersion correction (DFT-D) for the 94 elements H-Pu," *J. Chem. Phys.*, vol. 132, p. 154104, 2010.

[9] S. Miertuš, E. Scrocco, and J. Tomasi, "Electrostatic Interaction of a Solute with a Continuum. A Direct Utilization of ab initio Molecular Potentials for the Prevision of Solvent Effects," *Chem. Phys.*, vol. 55, pp. 117–129, 1981.

[10] S. Miertuš and J. Tomasi, "Approximate Evaluations of the Electrostatic Free Energy and Internal Energy Changes in Solution Processes," *Chem. Phys.*, vol. 65, pp. 239–245, 1982.

[11] J. L. Pascual-Ahuir, E. Silla, and I. Tuñón, "GEPOL: An improved description of molecular-surfaces. 3. A new algorithm for the computation of a solvent-excluding surface," *J. Comp. Chem.*, vol. 15, pp. 1127–1138, 1994.

[12] M. Cossi, V. Barone, R. Cammi, and J. Tomasi, "Ab initio study of solvated molecules: A new implementation of the polarizable continuum model," *Chem. Phys. Lett.*, vol. 255, pp. 327–335, 1996.

[13] V. Barone, M. Cossi, and J. Tomasi, "A new definition of cavities for the computation of solvation free energies by the polarizable continuum model," *J. Chem. Phys.*, vol. 107, pp. 3210–3221, 1997.

[14] B. Mennucci and J. Tomasi, "Continuum solvation models: A new approach to the problem of solute's charge distribution and cavity boundaries," *J. Chem. Phys.*, vol. 106, pp. 5151–5158, 1997.

[15] B. Mennucci, E. Cancès, and J. Tomasi, "Evaluation of Solvent Effects in Isotropic and Anisotropic Dielectrics and in Ionic Solutions with a Unified Integral Equation Method: Theoretical Bases, Computational Implementation and Numerical Applications," *J. Phys. Chem. B*, vol. 101, pp. 10506–10517, 1997.

[16] V. Barone and M. Cossi, "Quantum calculation of molecular energies and energy gradients in solution by a conductor solvent model," *J. Phys. Chem. A*, vol. 102, pp. 1995–2001, 1998.

[17] M. Cossi, V. Barone, B. Mennucci, and J. Tomasi, "Ab initio study of ionic solutions by a polarizable continuum dielectric model," *Chem. Phys. Lett.*, vol. 286, pp. 253–260, 1998.

[18] V. Barone, M. Cossi, and J. Tomasi, "Geometry optimization of molecular structures in solution by the polarizable continuum model," *J. Comp. Chem.*, vol. 19, pp. 404–417, 1998.

[19] R. Cammi, B. Mennucci, and J. Tomasi, "Second-order Møller-Plesset analytical derivatives for the polarizable continuum model using the relaxed density approach," *J. Phys. Chem. A*, vol. 103, pp. 9100–9108, 1999.

[20] M. Cossi, V. Barone, and M. A. Robb, "A direct procedure for the evaluation of solvent effects in MC-SCF calculations," *J. Chem. Phys.*, vol. 111, pp. 5295–5302, 1999.

[21] J. Tomasi, B. Mennucci, and E. Cancès, "The IEF version of the PCM solvation method: An overview of a new method addressed to study molecular solutes at the QM ab initio level," *J. Mol. Struct. (Theochem)*, vol. 464, pp. 211–226, 1999.

[22] R. Cammi, B. Mennucci, and J. Tomasi, "Fast evaluation of geometries and properties of excited molecules in solution: A Tamm-Dancoff model with application to 4-dimethylaminobenzonitrile," *J. Phys. Chem. A*, vol. 104, pp. 5631–5637, 2000.

[23] M. Cossi and V. Barone, "Solvent effect on vertical electronic transitions by the polarizable continuum model," *J. Chem. Phys.*, vol. 112, pp. 2427–2435, 2000.

[24] M. Cossi and V. Barone, "Time-dependent density functional theory for molecules in liquid solutions," *J. Chem. Phys.*, vol. 115, pp. 4708–4717, 2001.

[25] M. Cossi, N. Rega, G. Scalmani, and V. Barone, "Polarizable dielectric model of solvation with inclusion of charge penetration effects," *J. Chem. Phys.*, vol. 114, pp. 5691–5701, 2001.

[26] M. Cossi, N. Rega, G. Scalmani, and V. Barone, "Energies, structures and electronic properties of molecules in solution with the C-PCM solvation model," *J. Comp. Chem.*, vol. 24, no. 669-681, 2003.

[27] J. Tomasi, B. Mennucci, and R. Cammi, "Quantum mechanical continuum solvation models," *Chem. Rev.*, vol. 105, pp. 2999–3093, 2005.

[28] Eps=3.10, EpsInf=2.1304, RSolv=4.088 as determined from Horikoshi *et al.*,[48] the square of the refractive index, and Stearn-Eyring equation respectively.

[29] maximum gradient: 1.5×10^{-5}, RMS gradient: 1.0×10^{-5}, maximum displacement 6.0×10^{-5}, RMS displacement 4.0×10^{-5}.

[30] In order to confirm the exact structure of reagents and products that correspond to each elementary step in the reaction mechanism, intrinsic reaction coordinate (IRC) calculations[49–51] were carried out for every transition structure presented that unambiguously confirm the reaction sequence.

[31] M. J. Frisch, G. W. Trucks, H. B. Schlegel, G. E. Scuseria, M. A. Robb, J. R. Cheeseman, G. Scalmani, V. Barone, B. Mennucci, G. A. Petersson, H. Nakatsuji, M. Caricato, X. Li, H. P. Hratchian, A. F. Izmaylov, J. Bloino, G. Zheng, J. L. Sonnenberg, M. Hada, M. Ehara, K. Toyota, R. Fukuda, J. Hasegawa, M. Ishida, T. Nakajima, Y. Honda, O. Kitao, H. Nakai, T. Vreven, J. A. Montgomery, Jr., J. E. Peralta, F. Ogliaro, M. Bearpark, J. J. Heyd, E. Brothers, K. N. Kudin, V. N. Staroverov, R. Kobayashi, J. Normand, K. Raghavachari, A. Rendell, J. C. Burant, S. S. Iyengar, J. Tomasi, M. Cossi, N. Rega, J. M. Millam, M. Klene, J. E. Knox, J. B. Cross, V. Bakken, C. Adamo, J. Jaramillo, R. Gomperts, R. E. Stratmann, O. Yazyev, A. J. Austin, R. Cammi, C. Pomelli, J. W. Ochterski, R. L. Martin, K. Morokuma, V. G. Zakrzewski, G. A. Voth, P. Salvador, J. J. Dannenberg, S. Dapprich, A. D. Daniels, Ö. Farkas, J. B. Foresman, J. V. Ortiz, J. Cioslowski, and D. J. Fox, "Gaussian 09 Revision D.01." Gaussian Inc. Wallingford CT, 2009.

[32] J. Schmidt and W. Polik, "WebMO Enterprise, version 17.0.012e." `http://www.webmo.net/`, November 2017.

[33] K. Kim, D. Yoo, H. Choi, S. Tamang, J.-H. Ko, S. Kim, Y.-H. Kim, and S. Jeong, "Halide–Amine Co-Passivated Indium Phosphide Colloidal Quantum Dots in Tetrahedral Shape," *Angewandte Chemie*, vol. 128, no. 11, pp. 3778–3782, 2016.

[34] P. Allen, B. Walker, and M. Bawendi, "Mechanistic Insights into the Formation of InP Quantum Dots," *Angewandte Chemie*, vol. 122, no. 4, pp. 772–774, 2010.

[35] S. Xu, J. Ziegler, and T. Nann, "Rapid synthesis of highly luminescent InP and InP/ZnS nanocrystals," *Journal of Materials Chemistry*, vol. 18, no. 23, pp. 2653–2656, 2008.

[36] F. Pietra, L. De Trizio, A. W. Hoekstra, N. Renaud, M. Prato, F. C. Grozema, P. J. Baesjou, R. Koole, L. Manna, and A. J. Houtepen, "Tuning the Lattice Parameter of In_xZn_yP for Highly Luminescent Lattice-Matched Core/Shell Quantum Dots," *ACS Nano*, vol. 10, no. 4, pp. 4754–4762, 2016.

[37] K. Huang, R. Demadrille, M. G. Silly, F. Sirotti, P. Reiss, and O. Renault, "Internal Structure of InP/ZnS Nanocrystals Unraveled by High-Resolution Soft X-ray Photoelectron Spectroscopy," *ACS Nano*, vol. 4, no. 8, pp. 4799–4805, 2010.

[38] U. T. D. Thuy, P. Reiss, and N. Q. Liem, "Luminescence properties of In(Zn)P alloy core/ZnS shell quantum dots," *Applied Physics Letters*, vol. 97, no. 19, p. 193104, 2010.

[39] S. Koh, T. Eom, W. D. Kim, K. Lee, D. Lee, Y. K. Lee, H. Kim, W. K. Bae, and D. C. Lee, "Zinc–Phosphorus Complex Working as an Atomic Valve for Colloidal Growth of Monodisperse Indium Phosphide Quantum Dots," *Chemistry of Materials*, vol. 29, no. 15, pp. 6346–6355, 2017.

[40] D. J. Nelson and C. N. Brammer, "Toward Consistent Terminology for Cyclohexane Conformers in Introductory Organic Chemistry," *Journal of Chemical Education*, vol. 88, no. 3, pp. 292–294, 2011.

[41] L. Xie, Q. Zhao, K. F. Jensen, and H. J. Kulik, "Direct Observation of Early-Stage Quantum Dot Growth Mechanisms with High-Temperature Ab Initio Molecular Dynamics," *The Journal of Physical Chemistry C*, vol. 120, no. 4, pp. 2472–2483, 2016.

[42] D. C. Gary, M. W. Terban, S. J. L. Billinge, and B. M. Cossairt, "Two-Step Nucleation and Growth of InP Quantum Dots via Magic-Sized Cluster Intermediates," *Chemistry of Materials*, vol. 27, no. 4, pp. 1432–1441, 2015.

[43] O. I. Mićić, J. Sprague, Z. Lu, and A. J. Nozik, "Highly efficient band-edge emission from InP quantum dots," *Applied Physics Letters*, vol. 68, no. 22, pp. 3150–3152, 1996.

[44] O. I. Mićić, K. M. Jones, A. Cahill, and A. J. Nozik, "Optical, Electronic, and Structural Properties of Uncoupled and Close-Packed Arrays of InP Quantum Dots," *The Journal of Physical Chemistry B*, vol. 102, no. 49, pp. 9791–9796, 1998.

[45] S. Haubold, M. Haase, A. Kornowski, and H. Weller, "Strongly Luminescent InP/ZnS Core–Shell Nanoparticles," *ChemPhysChem*, vol. 2, no. 5, pp. 331–334, 2001.

[46] J. Y. Kim, A. H. Steeves, and H. J. Kulik, "Harnessing Organic Ligand Libraries for First-Principles Inorganic Discovery: Indium Phosphide Quantum Dot Precursor Design Strategies," *Chemistry of Materials*, vol. 29, no. 8, pp. 3632–3643, 2017.

[47] S. Xu, S. Kumar, and T. Nann, "Rapid Synthesis of High-Quality InP Nanocrystals," *Journal of the American Chemical Society*, vol. 128, no. 4, pp. 1054–1055, 2006.

[48] S. Horikoshi, H. Abe, T. Sumi, K. Torigoe, H. Sakai, N. Serpone, and M. Abe, "Microwave frequency effect in the formation of Au nanocolloids in polar and non-polar solvents," *Nanoscale*, vol. 3, no. 4, pp. 1697–1702, 2011.

[49] K. Fukui, "The path of chemical-reactions - The IRC approach," *Acc. Chem. Res.*, vol. 14, pp. 363–368, 1981.

[50] H. P. Hratchian and H. B. Schlegel, "Accurate reaction paths using a Hessian based predictor-corrector integrator," *J. Chem. Phys.*, vol. 120, pp. 9918–9924, 2004.

[51] H. P. Hratchian and H. B. Schlegel, "Using Hessian updating to increase the efficiency of a Hessian based predictor-corrector reaction path following method," *J. Chem. Theory Comput.*, vol. 1, pp. 61–69, 2005.

Chapter 4

Mechanistic Halide Dependence

The synthesis of InP materials with aminophosphines has a remarkable dependence on the choice in indium and zinc precursors. The source of the large changes in spectral behaviors by the selection of different halide salts is one of the last remaining puzzles of this system. Currently, our understanding only allows us to create materials with a few discrete absorption and emission profiles. While nine combinations of precursors are available, the methods using indium and zinc iodides are expensive and make poor quantum dots. With the iodides removed, the number of reactions reduces to four materials, which is not a large degree of tunability (although, this number can be doubled by changing the reaction solvent). Therefore, understanding the nature of this shift in spectral behaviors with changing halide content is necessary to expand the range of attainable quantum dots.

As outlined in Section 2.2, the critical processes of nanoparticle formation can be summarized simply as precursor conversion, nucleation, and growth, and altering a halide can impact each of these in different ways. Using DFT, this Chapter first examines how the conversion mechanism could be affected by various salts. Many parameters such as bond angles, dipoles, and molecular orbitals are analyzed to give reason to the differences in structures and energies for different combinations of precursors.

4.1 Computational Comparisons

The most obvious effect that the different salts could have on the synthesis is by altering one or more parts of the reaction mechanism. Larger anions may present some steric bulk that interferes with a transition state and slows its conversion. However, they may also create more stable products as they tend to be good leaving groups. As with Chapter 3, the changes in the mechanism will be examined with DFT, and different InX_3 and ZnX_2 will be probed independently.

The geometries of Chapter 3 were used as a scaffold for the calculations presented here. Before beginning the various halide series, the chloride structures were optimized with the "oleylamine" solvent removed. As this was a custom solvent model, its use complicates the computation and produces structures that are difficult to compare to those found in the literature. This change also has the added benefit of being more comparable to the 2-pot syntheses with ODE, as the low dielectric of 1-octadecene is generally assumed to be close to what is used for the standard gas phase calculations[†].

The most significant difference between the two sets of structures is that the complicated zinc activation of Figure 3.9 simplifies in the gas phase. Figure 4.1 shows this mechanism reduces down to only having one intermediate minimum, with a clear

[†]i.e. none

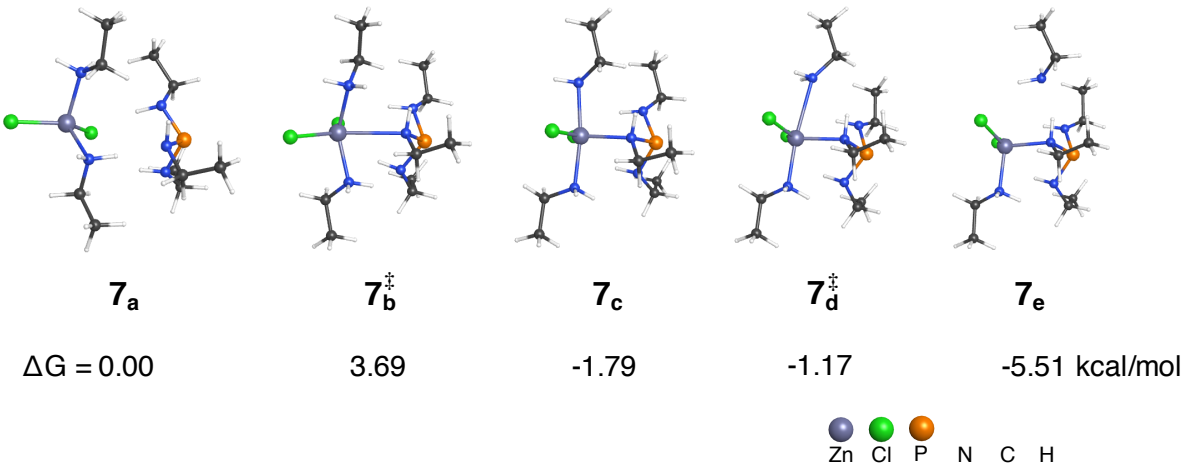

FIGURE 4.1: New geometries of the zinc activation process at the PBE0-D3/def2-TZVP level of theory. Clearly there are fewer geometries and all energies are significantly less than those presented in Figure 3.9.

path for how the zinc adds to the aminophosphine. Outside of these new geometries, the remaining structures were practically identical[†], and all the conclusions of the previous chapter remain intact. In Appendix B, Tables B.1 and B.2 directly compare the energetics of the two methods and show that the gas phase calculations are globally lower in energy than those done with the solvent model.

As with the previous chapter, the DFT calculations were performed with the PBE0 hybrid functional,[1] the def2-TZVP (Ahlrichs) basis-set[2] of triple-ζ quality, and Grimme's empirical D3 dispersion-correction[3] was applied. This level of theory is referred to as PBE0-D3/def2-TZVP. The same convergence criteria[4] and levels of rigor[5] of the previous chapter were applied to the structures presented herein. All quantum chemical calculations were carried out with the *Gaussian 09* suite of programs (Revision D.01)[6] and molecular graphics were rendered with WebMO.[7] Complete energetic comparisons of the final structures are presented in Appendix B.

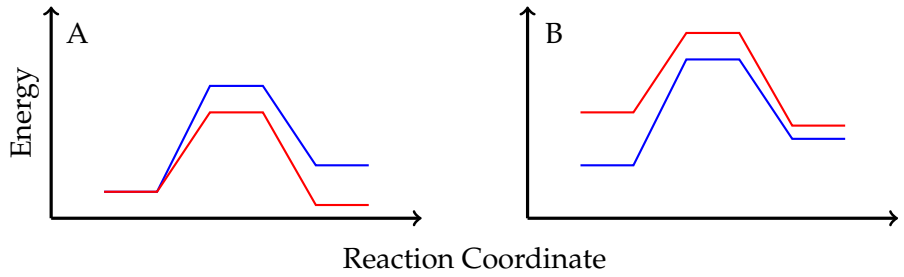

FIGURE 4.2: A) Diagram of two reaction pathways where the initial geometry is set to $\Delta G = 0$. B) The same pathways but with comparison to some common energy point instead. Although the red path is energetically favorable from start to finish, it is not globally favorable.

[†]The zinc-free ligand exchange structures of $\mathbf{4_a}$ also gained an intermediate and the energies of that pathway were lowered. However, $\mathbf{4_{II}}$ and $\mathbf{9_{II}}$ were still significantly more stable so it is ignored.

Although energies like those in Figure 4.1 are useful, they are difficult to compare across schemes with substantial differences[†]. These ΔG are problematic because each reaction sets the starting geometry to $\Delta G = 0$, but gives no information about how one path relates to another. Figure 4.2 shows how a reaction that seems favorable may, in fact, be higher energy when the two paths are compared to some common point. Thus, a more rigorous method of comparing pathways is needed to examine the very diverse chemical environments shown in the rest of this chapter.

$$\begin{aligned} G_g(\mathbf{R}) = G(\mathrm{InCl_3}) + G(\mathrm{InBr_3}) + G(\mathrm{InI_3}) + G(\mathrm{ZnCl_2}) \\ + G(\mathrm{ZnBr_2}) + G(\mathrm{ZnI_2}) + 2\,G(\mathrm{P(NHEt)_3}) \end{aligned} \tag{4.1}$$

$$\begin{aligned} G_g(\mathbf{7_a}) = G(\mathbf{7_a}) + G(\mathrm{InCl_3}) + G(\mathrm{InBr_3}) + G(\mathrm{InI_3}) \\ + G(\mathrm{ZnBr_2}) + G(\mathrm{ZnI_2}) + G(\mathrm{P(NHEt)_3}) \end{aligned} \tag{4.2}$$

$$G_g(\mathbf{7_a}) - G_g(\mathbf{R}) = \Delta G_g(\mathbf{7_a}) \tag{4.3}$$

A "global" reference can be devised which would allow all of the various environments to be compared to each other. Equation 4.1 shows one such formulation, where the sum of the separate energies of all the isolated initial components defines the totally unreacted start point. Then, the energies of the reaction structures are adjusted by adding those of the "unused" compounds, as in Equation 4.2. The difference between these two quantities is now a measure of how the total system changes in response to the reactions. Because $G_g(\mathbf{R})$ is composed of all the InX_3 and ZnX_2, the ΔG_g of reactions with various combinations of halides are directly comparable to each other. This method also has the added benefit of showing the relationship between the ligand exchange and disproportionation processes for a given set of halides. In this way, conclusions can be made about the total processes and how changing halides affects the mechanism of this reaction.[††]

4.2 Inhibiting Indium

With an understanding of ΔG and ΔG_g in hand, the effects of different halides on the indium center are examined to determine if larger anions accelerate or impede the reactions. It's important to outline these results because even in a synthesis that, for example, uses $InCl_3$ and $ZnBr_2$, the large amount of Br^- from the zinc center create an opportunity to exchange *in situ* with those on the indium and result in significant amounts of $InBr_3$. The zinc-free pathways (greyscale in the following Figures) are also investigated because they should have the same trends if the In–X bonds are the most significant contributors to the differences in mechanism. The following bar graphs of Figures 4.3 - 4.15 depict the differences in free energies calculated with

[†]i.e., even the simple switch from $ZnCl_2$ to $ZnBr_2$ in $\mathbf{7_a}$–$\mathbf{7_e}$ is significant because it adds $\sim 15\%$ more orbitals to the calculations.

[††]It is useful to note that ΔG values can be calculated from ΔG_g: $\Delta G_g(\mathbf{7_b^{\ddagger}}) - \Delta G_g(\mathbf{7_a}) = 3.69$ kcal/mol $= \Delta G(\mathbf{7_b^{\ddagger}})$.

both ΔG (full colors) and ΔG_g (lighter colors) for each step of the reaction. They are overlaid so the variable with the lowest magnitude is in front, even if it appears negligible.

4.2.1 Ligand Exchange

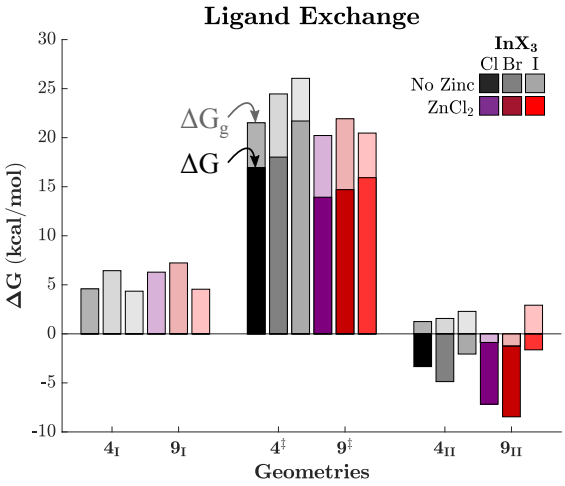

FIGURE 4.3: Free energies of the ligand exchange process for various indium halides at the PBE0-D3/def2-TZVP level of theory. The data in full color (ΔG) are differences from their respective starting geometries, $\mathbf{4_I}/\mathbf{9_I}$, while those in the lighter shade (ΔG_g) use the global reference method of Equation 4.3.

It is immediately evident that the two methods of analyzing free energy can produce very different accounts of the same structures. Although Figure 4.3 shows ΔG delivers nice trends between the zinc-free and $ZnCl_2$-activated ligand exchanges, many of them do not hold when examined with ΔG_g. The energies of the transition states appear to increase with larger halides when calculated with ΔG, but ΔG_g shows only that the zinc-activated reactions are faster than their zinc-free counterparts. Also, while all the products appeared very favorable with ΔG, using ΔG_g shows that most have little stability in the global scheme, with the "best" reaction ($InBr_3-ZnCl_2$) only achieving yields of ~80% at equilibrium.[†]

Exploring the electronic and entropic energies of these structures can resolve some of the discrepancies that appear between these two methods. As seen in Table 4.1, the entropy of the calculations, S, rises with halide size, which should result in a lowering of free energy. However, this is paired with an increase in electronic energy that limits the benefits of the larger disorder. This combination is heightened in the iodine reactions, where the small increase in disorder combined with a large increase in ΔE_g results in <8% of the compounds as the products at equilibrium. This observation is also supported by the longer In–P distances throughout the InI_3-based transitions, as found in Table C.5 and Table C.6. While this effect can be seen

[†]Using ΔG_g with $p_B/p_A = 10^{-(G_B-G_A)/RT}$ does not imply a 80:20 ratio of $\mathbf{9_{II}}$ to $\mathbf{9_I}$, but rather that ~20% of compounds are as $\mathbf{R}$, the set of fully dissociated starting materials. By the same metric, 0.03% of molecules exist as $\mathbf{9_I}$ at equilibrium due to its large positive ΔG_g.

in the bromine-based products, the small difference in electronic energy of $\mathbf{9_{II}}$ combined with its large S accounts for the $InBr_3{-}ZnCl_2$ synthesis being the most stable reaction examined here.

Interestingly, the $InI_3{-}ZnCl_2$ transition state (Figure 4.4) has an unusually high degree of disorder, which is perhaps why it doesn't trend with the set of ΔG values or the ΔG_g of its zinc-free analog. Both the aminophosphine and displaced ethylamine in $\mathbf{9}^{\ddagger}$ have much larger distances to the indium center in this reaction, which may be the source of this disorder and result in the more favorable reaction rate. The fact that this lengthening does not appear in the zinc-free analogs suggests that the acidity of $ZnCl_2$ may be allowing this to occur. The unusually large dipole in this geometry implies a strong positive charge on the indium center and a corresponding negative charge on the phosphorus. This indicates a strong P→In dative bond and the cancellation of the In–X moments by the $ZnCl_2$, as there appears to be no net charge imbalance outside of the In$\cdots$P interaction. The combination of the molecular dipole and long bond lengths is likely why the $InI_3{-}ZnCl_2$ reaction has a calculated reaction rate on par with $InCl_3{-}ZnCl_2$.

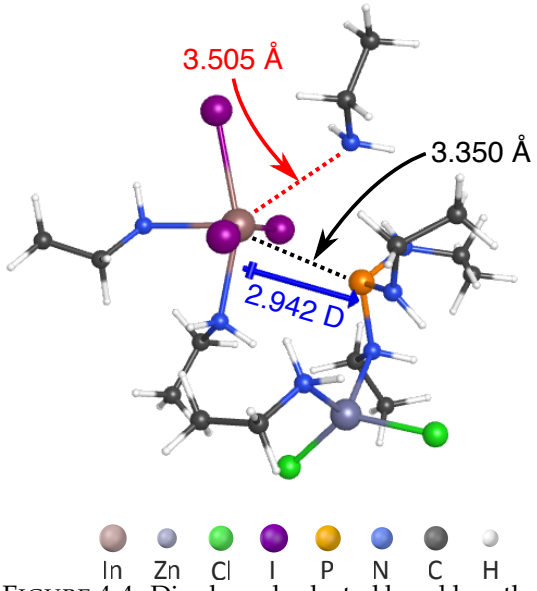

FIGURE 4.4: Dipole and selected bond lengths of the $InI_3{-}ZnCl_2$ transition state.

			ΔE_g	ΔU_g	ΔH_g	ΔG_g	S
Start	$\mathbf{4_I}$	$InCl_3$	-16.88	-15.51	-16.41	4.59	306.30
		$InBr_3$	-16.56	-15.35	-16.25	6.44	309.67
		InI_3	-17.11	-15.73	-16.63	4.35	318.66
	$\mathbf{9_I}$	$InCl_3$	-24.00	-23.31	-24.21	6.29	366.76
		$InBr_3$	-23.31	-22.51	-23.41	7.23	373.58
		InI_3	-23.91	-22.78	-23.68	4.55	384.09
TS	$\mathbf{4}^{\ddagger}$	$InCl_3$	-4.50	-4.06	-4.96	21.52	294.22
		$InBr_3$	-3.26	-2.93	-3.83	24.46	297.31
		InI_3	-2.00	-1.68	-2.58	26.05	301.76
	$\mathbf{9}^{\ddagger}$	$InCl_3$	-13.04	-12.77	-13.67	20.22	359.29
		$InBr_3$	-11.26	-10.93	-11.83	21.93	366.71
		InI_3	-10.43	-9.69	-10.59	20.47	377.84
End	$\mathbf{4_{II}}$	$InCl_3$	-20.35	-18.85	-19.75	1.25	306.30
		$InBr_3$	-19.95	-18.39	-19.29	1.57	313.72
		InI_3	-18.89	-17.29	-18.19	2.29	319.74
	$\mathbf{9_{II}}$	$InCl_3$	-31.75	-30.89	-31.79	-0.88	365.87
		$InBr_3$	-30.78	-29.55	-30.45	-1.24	376.74
		InI_3	-28.39	-27.40	-28.30	2.92	377.50

TABLE 4.1: Comparisons of the electronic, internal, enthalpic, and free energy differences (in kcal/mol) of the ligand exchange structures with different halides calculated using Equation 4.3 along side their entropic terms (S, cal/mol-K).

4.2.2 Disproportionation

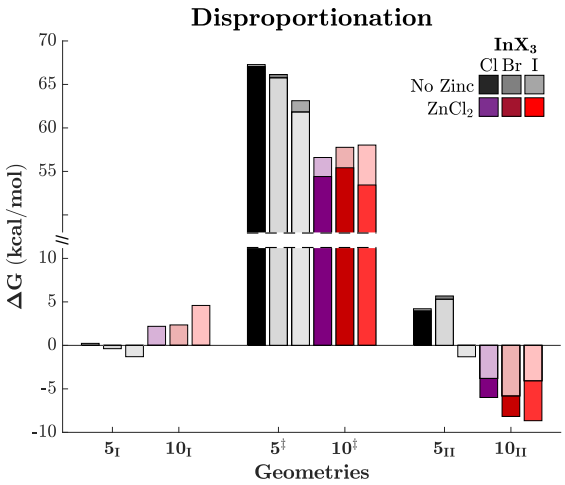

FIGURE 4.5: Free energies of the disproportionation process for various indium halides at the PBE0-D3/def2-TZVP level of theory. The data in full color (ΔG) are differences from their respective starting geometries, $\mathbf{5_I}/\mathbf{10_I}$, while those in the lighter shade (ΔG_g) use the global reference method of Equation 4.3.

While this analysis of the ligand exchange is vital, Chapter 3 showed the disproportionation phase is more likely to be the rate-limiting step. Comparing the pathways of the $InCl_3$ and $InCl_3-ZnCl_2$ calculations in Figure 4.5 shows that although the magnitudes of their ΔG are different from those in the previous Chapter, they draw the same conclusions. Interestingly, there are few differences between ΔG and ΔG_g in the zinc-free geometries due to the relatively small free energies of the starting structures. These $\mathbf{5_I}$ then suggest that even though the various $\mathbf{4_{II}}$ from Figure 4.3 are unfavorable, adding a second $P(NHEt)_3$ stabilizes the structures through the strong hydrogen bonding triangle, as seen before in Figure 3.6. When compared to the global reference $\mathbf{R}$, this passivation results in ~44%, 60%, and 81% of the $InCl_3$, $InBr_3$, and InI_3 precursors as $\mathbf{5_I}$, as compared to the ~20%, 15%, and 7% of their respective $\mathbf{4_{II}}$ structures.

Curiously, this relationship is reversed for the zinc-activated geometries of $\mathbf{10_I}$, all of which have equilibrium probabilities <10% when compared to the isolated starting structures of $\mathbf{R}$. The electronic energies of these structures (Table 4.2) appear to be responsible for this change in behavior, which goes against the logic of the last section. However, a closer look at the hydrogen bonds in these initial minima (Figure 4.6) shows the bulk of the differences arise from one dipole on the second aminophosphine. If this N–H bond (**green arrow**) is pointed towards the far N on the first aminophosphine, the electronic energy will be lowered, and the ΔG_g will be favorable. The presence of zinc, unfortunately, draws the lone pair of that far N towards itself, which means this key N–H dipole is unpassivated and $\mathbf{10_I}$ structures have positive ΔG_g.

This loss of electronic stability is heightened by the altered hydrogen bonds of the indium halides as well. Figure 4.6 shows the N–H$\cdots$X environments (A

		ΔE_g	ΔG_g	S	A	B	γ
$\mathbf{5_I}$	$InCl_3$	-24.92	0.23	375.01	2.413	2.439	112.03
	$InBr_3$	-26.40	-0.38	379.84	2.587	2.527	111.66
	InI_3	-27.00	-1.30	385.91	2.720	2.682	111.13
$\mathbf{10_I}$	$InCl_3$	-32.07	2.19	435.52	2.547	3.100	109.02
	$InBr_3$	-31.66	2.35	443.44	2.627	3.093	108.97
	InI_3	-30.37	4.59	446.39	2.766	3.194	108.81

TABLE 4.2: Comparisons of the global electronic and free energy differences (in kcal/mol) along side the entropic terms (S, cal/mol-K) and selected bond distances (Å) and angles (°) of the initial disproportionation structures from Figure 4.6 with different halides.

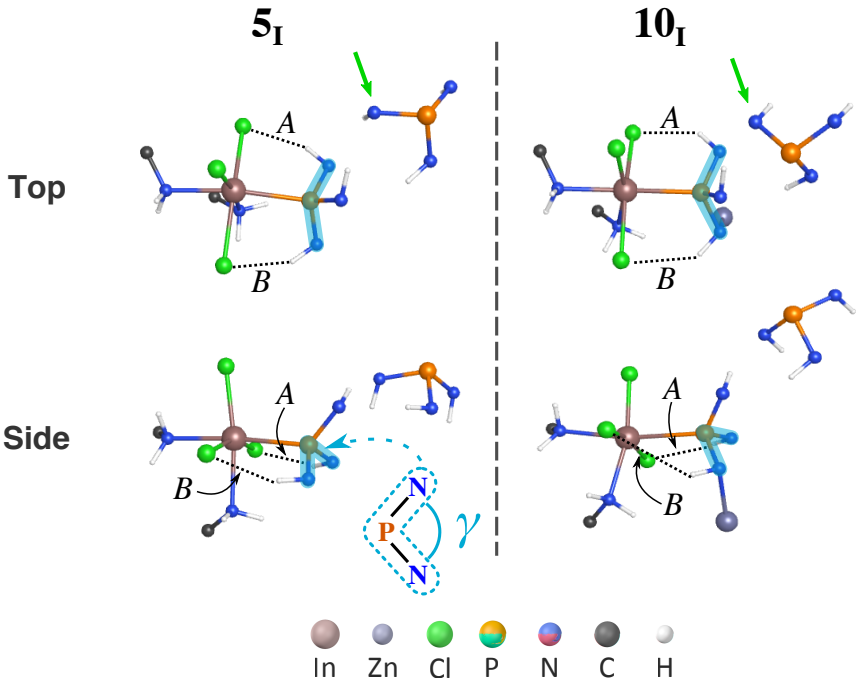

FIGURE 4.6: A closer examination of the initial disproportionation structures with most of the hydrocarbon chains omitted. Key hydrogen bonds (**black**, A and B) and bond angles (**cyan**, γ) are labelled. The direction of the indicated (**green arrow**) N–H on the second aminophosphine appears to be responsible for these structures being favorable or unfavorable.

and B) of the two schemes, and it can be seen that they are drastically different in the zinc-activated reaction. Where Table 4.2 shows the geometries of $\mathbf{5_I}$ have typical and practically symmetric amine-halide bond distances, those of $\mathbf{10_I}$ are much longer and thus more poorly passivating. Coupled with the narrowing N–P–N angle (**cyan**, γ) of the first aminophosphine, this results in more strain and accounts for the increasing instabilities of the geometries with $ZnCl_2$.

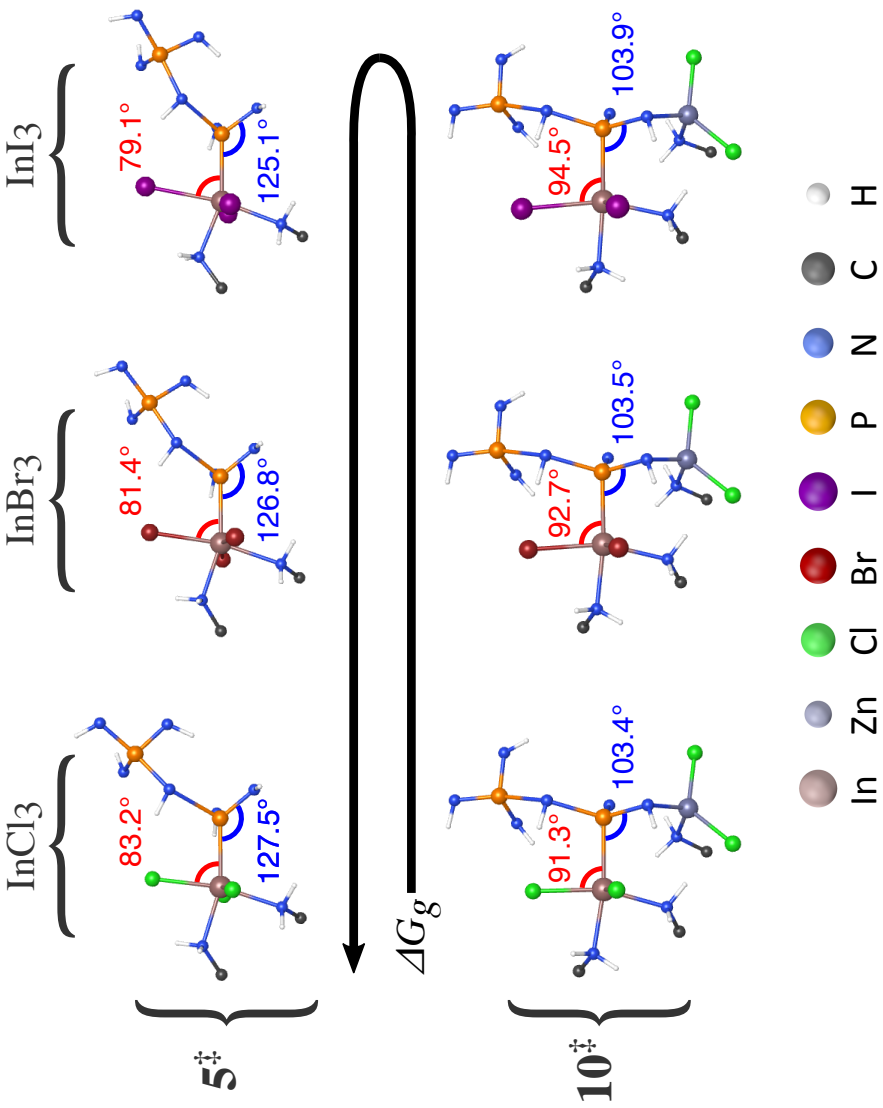

FIGURE 4.7: An examination of the disproportionation transition structures with most of the hydrocarbon chains omitted. Key bond angles (α and β) are labelled and the trend of their differences in global free energy (ΔG_g) are represented by the black arrow.

This reversed trend between the two regimes also carries over to the transition state calculations. The bar graph of Figure 4.5 indicates that increasing halide sizes on the indium center lower the ΔG_g for the zinc-free reactions but raise them for the zinc-activated pathways. Unlike the other structures discussed in this section, there are numerous fluctuations among these six geometries, and few appear to correlate to the differences in their free energies. Interestingly, the X–In–P and N–P–In angles of these structures appeared to trend in the same fashion as the ΔG_g. Both of these angles are depicted in Figure 4.7 and correlate in the same direction: the geometries with the most narrow angles are those with the lowest free energies. While the halide-metal-phosphorus angle (red, α) changes more drastically, it is not a "universal" parameter due to the angle from $\mathbf{10^{\ddagger}}$–$\mathbf{InCl_3}$ being wider than $\mathbf{5^{\ddagger}}$–$\mathbf{InI_3}$, but the former is still lower in energy. In this sense, the amine-phosphorus-metal angle (blue, β) is a better factor, as the energy-angle relationship is continuous. However, it still suffers regarding magnitude, i.e. the difference in angle from $\mathbf{10^{\ddagger}}$–$\mathbf{InCl_3}$ and $\mathbf{10^{\ddagger}}$–$\mathbf{InBr_3}$ is small, but the difference in energy is large.

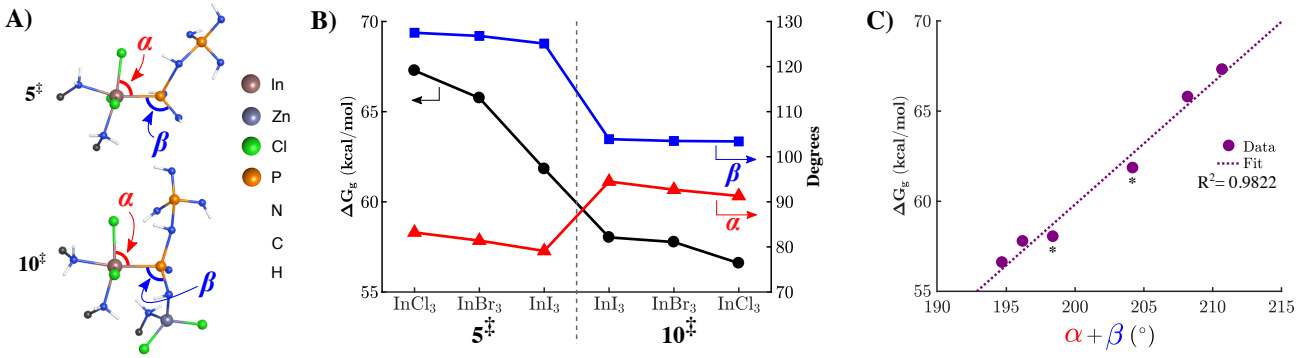

FIGURE 4.8: A) Representative geometries of the zinc-free ($\mathbf{5^{\ddagger}}$) and activated ($\mathbf{10^{\ddagger}}$) transition state geometries with key bond angles (α and β) labelled. B) The magnitudes of these are plotted along side their ΔG_g values. C) The correlation of the difference in global free energy to the sum α and β in these calculations. Data points indicated with (*) are from iodide-based geometries.

While these relationships are intriguing, the search for one parameter as the root of the differences in the energies of these structures is perhaps foolhardy. Given the complex nature of this reaction, it is unlikely that a single coordinate is responsible for the changes in the energies of these compounds. However, while alpha and beta are only middling predictors of ΔG_g on their own, they strongly correlate when taken together. Figure 4.8C shows that the sum of these two angles has a highly linear relationship with the changes in free energy of these structures, which is peculiar. Furthermore, if the "bad" calculations involving iodine are left out, the R^2 value increases to 0.9997. However, this is unusual because the ΔG_g of a calculation is several functionals removed from its molecular geometry[†], and it is curious that the sum of two physical parameters across six environments would correlate

[†]Free energy derived from a set of complicated partition functions, Q, which are functionals of electronic energy, which is a functional of electron density, which is a function of geometry: $G(Q(E(\rho(\mathbf{r}))))$

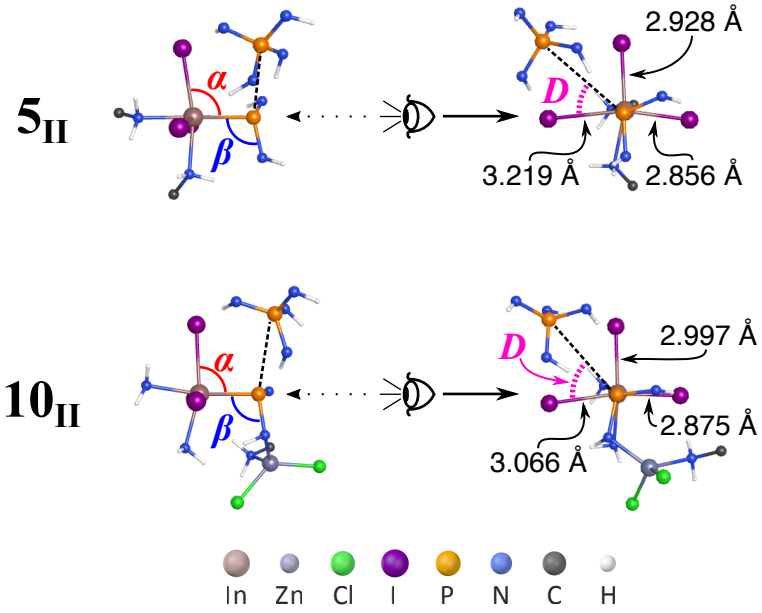

FIGURE 4.9: Two views of the simplified structures of the In_3-based zinc-free ($\mathbf{5_{II}}$) and activated ($\mathbf{10_{II}}$) disproportionation products. In–X bond lengths, key bond angles (α and β) a dihedral angle (D), are labelled.

as well as it does here. This sum doesn't make much physical sense, however, so interpreting its correlation to the free energy should be taken with a grain of salt.

In order to wrap up this analysis of different InX_3 on the mechanism, the free energies of the post-transition geometries can be compared to determine how stable the products are. Interestingly, the bar graph of Figure 4.5 shows the differences between the ΔG and ΔG_g of the $\mathbf{5_{II}}/\mathbf{10_{II}}$ structures are small, so the observations in this section will be the same regardless of the method used. As in Chapter 3, the zinc-free reactions are much less favorable than those of the activated pathway. The InI_3 reaction was the only $\mathbf{5_{II}}$ geometry that had a negative change in free energy, which can be primarily attributed to I^- being an excellent leaving group.

While all of these final structures had one In–X bond that was longer than the others from a drift towards $P(NHR)_4^+$ for charge passivation, most were on average <3% different than the remaining indium halide bonds. However, $\mathbf{5_{II}}$–$\mathbf{InI_3}$ boasted a 13.8% increase while $\mathbf{10_{II}}$–$\mathbf{InI_3}$ had more modest 4.4% lengthening. Figure 4.9 shows this dramatic change in the chemical environment and Table 4.3 outlines how it is propagated throughout the rest of the structure. Examining this data shows that the physical and electronic properties of $\mathbf{5_{II}}$–$\mathbf{InI_3}$ match much more closely to those of the $\mathbf{10_{II}}$ series than to the other zinc-free structures. Taken together, these relatively large shifts in the bonds around the indium center support iodine as an active leaving group, which affords more stability to $\mathbf{5_{II}}$–$\mathbf{InI_3}$.

Although these descriptions are enough to show why $\mathbf{5_{II}}$–$\mathbf{InI_3}$ deviates from the other indium halide calculations, none of the parameters in Table 4.3 are monotonic with ΔG_g. Though many of the relationships have a fair correlation with the changes in free energy, none are strong enough to be deemed most responsible for

		ΔG_g [a]	In–P (Å)	α (°)	β (°)	$\alpha + \beta$ (°)	D (°)	HOMO (eV)
$\mathbf{5_{II}}$	$InCl_3$	4.21	2.577	103.1	102.9	206.1	73.4	−5.14
	$InBr_3$	5.30	2.576	103.2	103.2	206.4	70.5	−5.19
	InI_3	−1.31	2.554	98.9	102.2	201.1	55.7	−5.34
$\mathbf{10_{II}}$	$InCl_3$	−3.80	2.559	93.5	100.9	194.5	52.8	−5.84
	$InBr_3$	−5.81	2.560	94.1	99.7	193.8	54.6	−5.92
	InI_3	−4.07	2.560	92.7	99.6	192.2	56.1	−5.94
[a] kcal/mol		R^2	0.4336	0.8543	0.9161	0.9162	0.8807	0.8619

TABLE 4.3: Various bond lengths, angles, and electronic properties of the terminal disproportionation geometries presented with their degree of correlation (R^2) to their respective global free energy differences. The dihedral bond, D, refers to the X–In–P–P dihedral angle for the foreground halide, as represented in Figure 4.9.

the molecular stability. As such, there does not yet appear to be one answer as to which property makes the disproportionation products favorable or not. While this ambiguity is frustrating, it is very typical of complex computational studies such as this one; the more concrete conclusions of the last sections were more serendipitous instead of 'par for the course.'

4.2.3 Indium Halide Summary

With all of the individual reactions outlined, the total In–P reduction pathways can be examined in full. Once again, ΔG_g becomes a very useful tool, as globally referring to the same energy point means that the free energies of every minimum can be directly compared. Equation 4.4 is just the familiar proportional relationship of p_B/p_A but has been expanded to relate all of the conformer stabilities to each other. Table 4.4 applies this to each set of InX_3 geometries; i.e., the row of $\mathbf{4/5}$–$InCl_3$ shows the relative percentages of each minimum in the zinc free synthesis with $InCl_3$. The initial reference point, $\mathbf{R}$, is included as well and implies that half of the precursors would remain completely unreacted at $t = \infty$. Statistically, it also appears that none of the materials in that reaction would stabilize as the redox product, making it the worst synthesis under these conditions.

$$p_A = \frac{10^{-\Delta G_g(A)/RT}}{\sum_{X}^{Conf.} 10^{-\Delta G_g(X)/RT}} * 100\% \tag{4.4}$$

Moving down Table 4.4 shows a gradual shift in the equilibrium of the minima towards the right. In the $InBr_3-ZnCl_2$ pathway, this results in a near total conversion of the precursors into the disproportionation products, starkly contrasting those of the zinc-free reactions. The $\mathbf{10_{II}}$–$\mathbf{InBr_3}$ geometry is so stable that if X in Equation 4.4 includes all the conformers of all the pathways, it still boasts a presence of 77% (Table C.7). While this is a fairly farfetched comparison[†], it provides a scope for how

[†]This scenario is one in which one equivalent of each salt ($InCl_3$, $InBr_3$...ZnI_2) and 2 equivalents of the aminophosphine were combined in solution, allowed to reach equilibrium, and no complex is allowed to progress beyond $\mathbf{5_{II}}/\mathbf{10_{II}}$.

much more stable the geometry is in comparison to the others.

		R	7_e	L		D		
				Start	End	Start	End	
4/5	$InCl_3$	49%	–	0%	12%	38%	0%	= 100%
	$InBr_3$	37%	–	0%	6%	56%	0%	= 100%
	InI_3	10%	–	0%	1%	44%	45%	= 100%
9/10	$InCl_3$	1%	6%	0%	3%	0%	89%	= 100%
	$InBr_3$	0%	1%	0%	1%	0%	98%	= 100%
	InI_3	1%	5%	0%	0%	0%	94%	= 100%

TABLE 4.4: Proportions of the conformers that exist as the ligand exchange (L) and disproportionation (D) minima of each reaction path at equilibrium, as calculated by Equation 4.4 for all X geometries in the pathway.

While ΔG_g comparisons are excellent indicators of stable products, they are only irrefutable on long time scales ($t = \infty^{\dagger}$). Given that much of the initial particle growth phase should be finished (and $\mathbf{5_{II}/10_{II}}$ should be consumed) by then, the stability of an intermediate product may not matter as much. Instead, the reaction rates may dictate the quantity and likelihood of product formation. If zeroth-order kinetics are assumed, the reaction rates can be determined from the $\Delta G_g^{\ddagger}$ of the various transition states. These calculated values are collected in Table 4.5 and show most of the $k^{\ddagger}(\mathrm{L})$ are on the same order of magnitude as the observed ligand exchange rates for CdSe quantum dot syntheses. The similarity in the initial mechanism and rates suggests a degree of analogy as well as confidence in these calculations.

		$k^{\ddagger}(\mathrm{L})$ s^{-1}	$k^{\ddagger}(\mathrm{D})$ s^{-1}	$\log(\mathrm{L}^*)$ dec	$\log(\mathrm{D}^*)$ dec
4/5	$InCl_3$	$4.0 * 10^{2}$	$3.4 * 10^{-20}$	−0.63	−5.15
	$InBr_3$	$1.5 * 10^{1}$	$1.8 * 10^{-19}$	−2.05	−4.43
	InI_3	$2.6 * 10^{0}$	$1.4 * 10^{-17}$	−2.82	−2.54
9/10	$InCl_3$	$1.7 * 10^{3}$	$4.8 * 10^{-15}$	0.00*	0.00*
	$InBr_3$	$2.5 * 10^{2}$	$1.3 * 10^{-15}$	−0.83	−0.57
	InI_3	$1.3 * 10^{3}$	$9.8 * 10^{-16}$	−0.12	−0.69

$\mathrm{L}^* = k^{\ddagger}(\mathrm{L})/k^{\ddagger *}(\mathrm{L})$ $\mathrm{D}^* = k^{\ddagger}(\mathrm{D})/k^{\ddagger *}(\mathrm{D})$

TABLE 4.5: Rates of the ligand exchange, $k^{\ddagger}(\mathrm{L})$, and disproportionation, $k^{\ddagger}(\mathrm{D})$, transitions with different indium halides calculated using the Eyring equation, $k^{\ddagger} = k_b T/h * \exp(-\Delta G_g^{\ddagger}/RT)$. The order of magnitude of reaction rates, $\log(k/k^*)$, relative to one geometry, (*), are also presented.

However, while this step was determined to be rate-limiting for CdSe,[8] it is not likely the case for these InP reactions. The total times and absorption profiles of the aminophosphine reactions suggest very different limiting schemes from typical CdSe or InP syntheses. In general, these "traditional" methods are stopped before $t = 5$ min because the particles enter ripening regimes which broaden their sizes.[9] This behavior is often a result of depleted precursor concentrations, which forces some particles to dissolve to allow others to grow. Contrary to this, Figures 3.17

[†]Experimentally, $t > 20$ min $\approx \infty$

and 3.19 show the aminophosphine syntheses appear to grow much more slowly and seem to stabilize particle sizes after $t = 25$ min. Because of the relationships in Figure 2.9, the sluggish growth rate implies that the precursor conversion rates should be much slower than those of CdSe, so the ligand exchange is not likely to be the limiting processes.

While the disproportionation step is more likely to be rate-limiting, the extremely large $\Delta G_g^\ddagger$ are still unrealistic. Without a better model to work with, it is hoped that the structures presented here will have the same trends as the "true" model. So a discussion of the relative rates of the reactions is more fruitful than examining the monumental timescales that would be necessary for the $\Delta G_g^\ddagger$ to be true.[†] The relative rates between two transition states are separated by about an order of magnitude for every ~2 kcal/mol of their differences in free energy differences, $\Delta(\Delta G_g^\ddagger)$, regardless of the actual $\Delta G_g^\ddagger$ values.[††] Thus, if the overall placements of $\Delta G_g^\ddagger$ are wrong but the $\Delta(\Delta G_g^\ddagger)$ are correct, then the reaction rates relative to one another will remain the same.

The activated $InCl_3-ZnCl_2$ reaction was taken to be the standard of comparison, and the logarithm of the relative rates are presented on the right of Table 4.5. This relation yields a negative order of magnitude for every other reaction, which confirms that both of the conversion processes are fastest with the $InCl_3-ZnCl_2$ system. Once again, the zinc-free disproportionations prove to be far more sluggish than all of the activated ones, with two orders of magnitude between the rates of the slowest **10** and the fastest **5** reactions. Unfortunately, the zinc-activated reactions seem to trend in the wrong way for them to be responsible for the shift in particle sizes. The calculated rates of the various $\mathbf{10}^\ddagger$ transitions slow with the larger indium anions, which should result in bigger particles if the In–X relationship controls the final quantum dot sizes[10] (Figure 2.10). While the trend is "correct" for the $\mathbf{5}^\ddagger$ transitions, their differences in magnitudes are dramatic, which should result in similarly dramatic consequences such as no reaction or particles that grow to bulk sizes. As neither relationship is able to explain the shifts in particle sizes with different halides, another aspect of the mechanism may be more impactful.

4.3 Softening Zinc

The second method where different halides could affect the reaction mechanism is through the zinc center. As the acidity and dipole of $ZnCl_2$ were found to change the In–P interactions, the reduced electronegativities of Br^- and I^- may be able to alter the rates of reaction as well. This softening of zinc may allow for more flexibility in the reaction space, which could ease the formation of critical structures. In this

[†] The time it takes for half of the $\mathbf{10_{II}}$–$\mathbf{InCl_3}$ to undergo disproportionation with $\Delta G_g^\ddagger$ is $t_{1/2} = \ln(2)/k^\ddagger = 4.56 * 10^6$ years. The number of reactions performed in the preparation of this thesis would have required being alive for ~51% of the age of the planet.

[††]This relationship is derived in Appendix A with Equations A.14–A.22 and illustrated in Figure A.8.

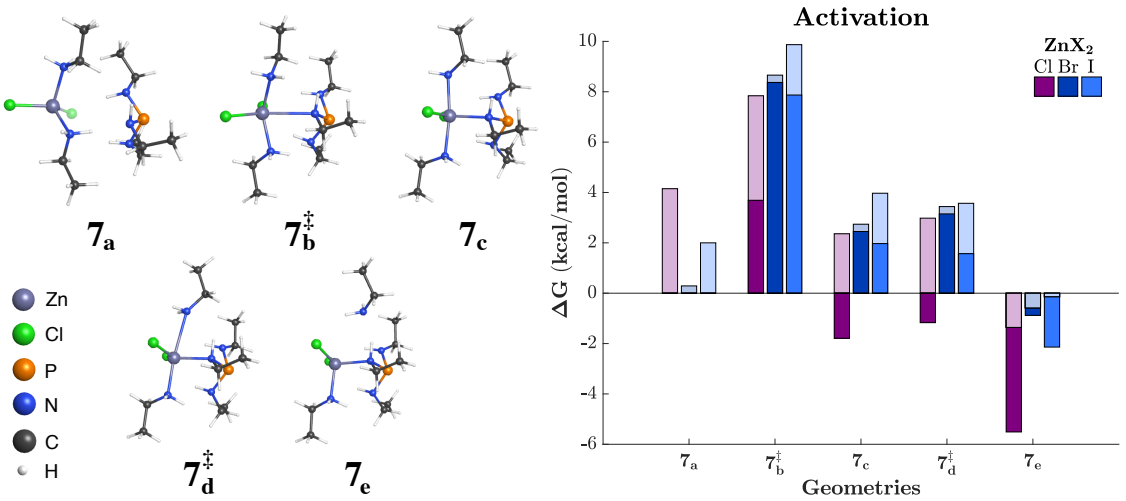

FIGURE 4.10: (Left) Reprinted geometries of the new activation pathway with $ZnCl_2$, as seen in Figure 4.1. (Right) Free energies of the activation process for various zinc halides at the PBE0-D3/def2-TZVP level of theory. The data in full color (ΔG) are differences from their respective starting geometries, $\mathbf{7_a}$, while those in the lighter shade (ΔG_g) use the global reference method of Equation 4.3.

section, the geometries involving $InCl_3-ZnX_2$ reactions are explored alongside the results of the InX_3-ZnCl_2 systems of the last section. This comparison should give scope as to which relationship is more meaningful in these interactions.

4.3.1 Activation

As with the last section, changing the halides on ZnX_2 did not result in any dramatic, paradigm-shifting differences for any of the processes examined here. Thus, the general mechanism remains the same, but the rates of each process and their proportions of stable products alters with the larger anions. Unlike the previous discussion, the observations here begin with the changes in the activation of the aminophosphine by ZnX_2. The left of Figure 4.10 (reprinted from Figure 4.1) shows the five geometries that are responsible for the passivation of the $-$NHR bonds by the zinc center and depicts a logical, two-step exchange. From $\mathbf{7_a}$–$\mathbf{7_c}$, the aminophosphine attaches to the ZnX_2 and forms a 5-coordinate intermediate. An ethylamine is then kicked off of the metal center in the much less taxing process of geometries $\mathbf{7_c}$–$\mathbf{7_e}$. The total energies of each structure with different halides are presented in the graph on the right of Figure 4.10 and show each process should be rapid and decently stable according to the <10 kcal/mol of their transitions and <0 kcal/mol of their $\mathbf{7_e}$ by ΔG_g.

It can be seen that there are significant differences in the energies of the initial geometries, $\mathbf{7_a}$. As these are used to set the baseline for ΔG, this results in major discrepancies between ΔG and ΔG_g. Comparing the various energetic contributions to the free energy (Tables C.1 and C.4) shows the variations in these structures have a large electronic component. Figure 4.11 shows a simplified examination of each starting conformer and indicates that $\mathbf{7_a}$–$\mathbf{ZnCl_2}$ is clearly an outlier. The indicated

hydrogen bonds show that the top phosphorus-amine is unpassivated in this structure, which is not the case for the bromide and iodide conformers. The angle $\mathbf{A_1}$ can quantify the closeness of the top zinc-ethylamine to the top phosphorus-amine, and shows they are clearly separated in $\mathbf{7_a}$–$\mathbf{ZnCl_2}$.

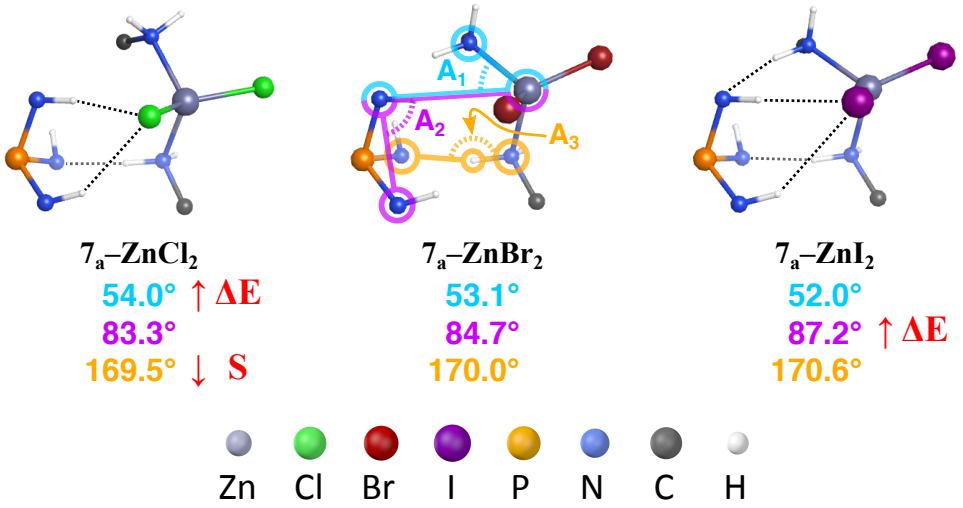

FIGURE 4.11: Starting geometries of the zinc activation process with various zinc halides. Key angles are indicated in cyan, $\mathbf{A_1}$, purple, $\mathbf{A_2}$, and yellow, $\mathbf{A_3}$. Impacts on their various energetic parameters as compared to $\mathbf{7_a}$–$\mathbf{ZnBr_2}$ are shown in red.

While these unpaired dipoles explain the large ΔE_g, there is also a noticeable decrease in entropy in this calculation. The linearity of angle $\mathbf{A_3}$ is a sign of the increased order of the system, which combines with the more positive ΔE_g to give a large free energy difference for this structure. The bromide and iodide geometries are much more favorable than the chloride due to the increased passivation. While they have very similar geometries, the $\mathbf{7_a}$–$\mathbf{ZnI_2}$ aminophosphine is slightly twisted away from the salt (angle $\mathbf{A_2}$). This shift is likely due to the steric bulk of the iodine and accounts for the increase in electronic energy seen in Figure 4.10.

The other $\mathbf{7_b}$–$\mathbf{7_e}$ geometries have small differences that can be considered together as "steric effects." Changes such as the slight lengthening of the Zn–amine bonds and the narrowing of the NH_2Et–Zn–NH_2Et angles are primarily caused by the increased electron density around the larger anions. These adjustments result in minor increases in electronic energies of the conformers, which yield ΔG_g values that have a modest spread of ~2 kcal/mol for every remaining stage of the activation. Unfortunately, this then means that the final geometries are increasingly less stable, with $\mathbf{7_e}$–$\mathbf{ZnI_2}$ only having a ΔG_g = -0.14 kcal/mol. While this means that only ~51% of conformers of the iodide reaction are as the final geometry, the sizeable initial ΔG_g means that

	R	7_a	7_c	7_e	
$ZnCl_2$	18%	0%	1%	81%	= 100%
$ZnBr_2$	27%	20%	1%	52%	= 100%
ZnI_2	44%	5%	0%	51%	= 100%

TABLE 4.6: Proportions of the activation minima of each ZnX_2 path at equilibrium, as calculated by Equation 4.4.

there are far fewer molecules as $\mathbf{7_a}$–$\mathbf{ZnI_2}$. Table 4.6 outlines the various percentages of the minima for a given reaction and shows that the majority end as $\mathbf{7_e}$ for all of the zinc halides.

4.3.2 Ligand Exchange

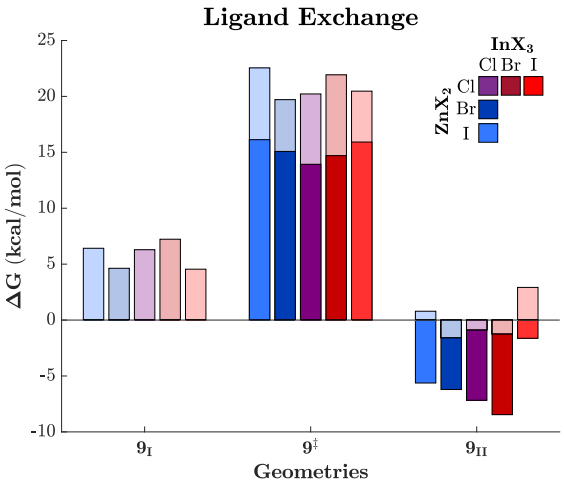

FIGURE 4.12: Free energies of the ligand exchange process for various halides at the PBE0-D3/def2-TZVP level of theory. The data in full color (ΔG) are differences from their respective starting geometries, $\mathbf{9_I}$, while those in the lighter shade (ΔG_g) use the global reference method of Equation 4.3.

Looking at the energies of the ligand exchange process in Figure 4.12 shows once again that bromine-containing reactions do not trend well with the other halides. In the case of these $\mathbf{9}$–$\mathbf{ZnBr_2}$ geometries, however, they appear to be uniformly more stable than their counterparts. This is opposed to the $\mathbf{9_I}/\mathbf{9^‡}$–$\mathbf{InBr_3}$ structures (dark red bars), which were less stable than the $InCl_3$–$ZnCl_2$ reaction. The origin of this strangeness is hard to pinpoint but may be due to a better balance between acidity and ligand flexibility. This middle ground could increase the disorder that comes from having a larger anion without taking away too much of the electronic stability gained from the zinc center.

	ΔG_g (kcal/mol)	In–P Å	D (°)
$ZnCl_2$	6.42	4.678	25.842
$ZnBr_2$	4.63	4.667	26.261
ZnI_2	6.29	4.688	24.618

TABLE 4.7: Select parameters of the $\mathbf{9_I}$–$\mathbf{ZnX_2}$ geometries.

The initial $\mathbf{9_I}$–$\mathbf{ZnX_2}$ geometries have the familiar small differences in bond lengths and angles from steric effects, but two parameters corresponded well to their changes in free energy. Figure 4.13 and Table 4.7 show that both the distance from the indium to the phosphorus and the degree of twisting (dihedral angle, D) between the

two components have consequences on the electronic energies of these compounds. While the In–P interaction seems natural to interpret, the dihedral angle is more confusing. Here, D can be understood in the typical fashion where the more eclipsed the two halves of the structure are, the worse the energy. Thus, the wider angle has less overlap and stress on the structure, resulting in lower ΔE_g.

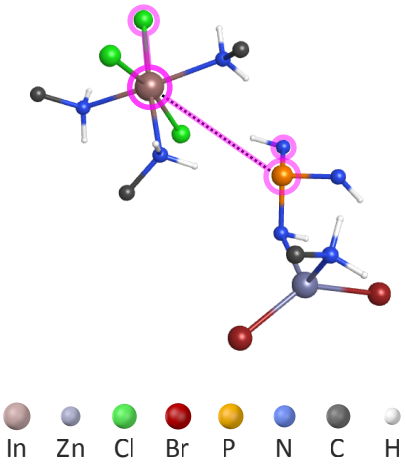

FIGURE 4.13: Simplified $\mathbf{9_I}$–$\mathbf{ZnBr_2}$ geometry showing the dihedral bond (magenta, D).

The zinc bromide-activated transition is the fastest ligand exchange seen in this work. Examining the structure in Figure 4.14 and Table 4.8 show there is an interesting correlation between bond lengths and energy. The longer the In–P distance (A) and the closer the leaving ethylamine (B) is to the indium, the lower the energy. This relationship suggests that the more similar to the $\mathbf{9_I}$ structures the transition is, the less energy is required to form the products. The widened angles, C and D, also suggest that all of the components about the indium center are more flexible in this system. Interestingly, none of these parameters are reflected in the $\mathbf{9^{\ddagger}}$–$\mathbf{InX_3}$ calculations, so these differences appear to be predominantly an effect of the zinc halide.

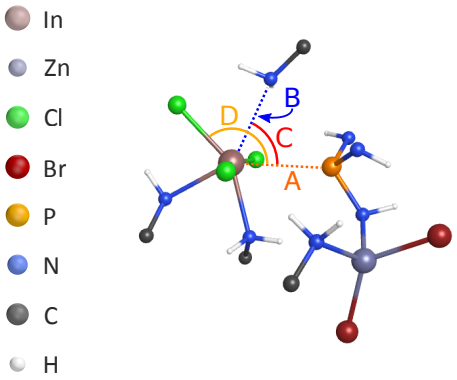

FIGURE 4.14: Simplified $\mathbf{9^{\ddagger}}$–$\mathbf{ZnBr_2}$ geometry showing key bonds and angles.

The trends in ΔG_g of the zinc-activated terminal geometries follow those of the $\mathbf{9_{II}}$–$\mathbf{InX_3}$, which is surprising given the different effects observed so far between

	ΔG_g (kcal/mol)	A Å	B Å	C (°)	D (°)
$ZnCl_2$	20.22	2.869	3.062	66.2	131.3
$ZnBr_2$	19.71	3.165	2.912	67.4	135.2
ZnI_2	22.55	2.902	3.095	65.2	130.4

TABLE 4.8: Select parameters of the $\mathbf{9^{\ddagger}}$–$\mathbf{ZnX_2}$ geometries.

indium and zinc halides. As the stability of $\mathbf{9_{II}}$–$\mathbf{InBr_3}$ had been attributed to a better balance between electronic energy and entropy, this was examined with the zinc halide structures as well. Table 4.9 shows the comparison of ΔE_g, ΔG_g, and S for each structure in Figure 4.12. If the $InCl_3$−$ZnCl_2$ energies are taken as a reference, the relative differences in these components can be compared. The $\Delta S/\Delta(\Delta E_g)$ relationship shows that introducing bromine on either indium or zinc results in a small increase in electronic energy but a substantial increase in disorder. The closeness in the ratio between $\mathbf{9_{II}}$–$\mathbf{ZnBr_2}$ and $\mathbf{9_{II}}$–$\mathbf{InBr_3}$ suggests that these effects scale on a per-bromine basis, which is potentially exploitable. While increasing [Br] above 3 for every indium would probably result in less stable structures from more electronic energy, a 1:1 ratio might be an interesting avenue to pursue[†].

	ΔE_g $^{\alpha}$	ΔG_g $^{\alpha}$	S $^{\beta}$	$\Delta(\Delta E_g)$ $^{\alpha}$	ΔS $^{\beta}$	Ratio$^{\gamma}$
ZnI_2	−29.54	0.79	375.56	2.21	9.69	2.0
$ZnBr_2$	−31.06	−1.58	373.99	0.69	8.12	5.3
$ZnCl_2/InCl_3$	−31.75	−0.88	365.87	0.00*	0.00*	–
$InBr_3$	−30.78	−1.24	376.74	0.97	10.87	5.1
InI_3	−28.39	2.92	377.50	3.36	11.63	1.6

$^{\alpha}$ kcal/mol $^{\beta}$ cal/mol-K $^{\gamma}$ $T\Delta S/\Delta(\Delta E_g)$, adjusted to be unitless

TABLE 4.9: Global electronic and free energy comparisons of the $\mathbf{9_{II}}$ structures with their entropy terms. Deviations from a reference geometry (*) in electronic energy, $\Delta(\Delta E_g)$, entropy, ΔS, and their ratio are also presented.

For the overall process of the activated ligand exchange, most of the structures and mechanisms are similar across all of the geometries. In terms of kinetics, ZnI_2 appears to offer the worst pathway with $InBr_3$ not far behind. As seen in the last section, InI_3 is problematic for thermodynamic reasons but has a strangely fast rate of reaction. While the all-chloride set of data displays average rates and conversion ratios, $InBr_3$ is a little slow but produces more stable products. Finally, an optimum amount of acidity and disorder appears in the $ZnBr_2$ structures and proves them to be the fastest and most favorable materials that undergo the ligand exchange.

[†] $\Delta(\Delta E_g)/Br \approx 0.33$ kcal/mol. Scale by 5.2 for ΔS, if E^0 are similar, $\Delta G_g \approx$ -1.66 kcal/mol. However, computationally the DFT calculations would take ∼300 jobs to figure out and how to achieve this in synthesis is a bit of a mystery.

4.3.3 Disproportionation

The redox behaviors of the ZnX_2-based reactions are the final piece of this mechanistic puzzle. Interestingly, Figure 4.15 shows their trends in ΔG_g seem to be similarly-behaved if slightly worse than the counterparts with InX_3, as the activation energies and final free energies of the $ZnBr_2$ and ZnI_2 geometries are on average ~1.5 kcal/mol higher than the $InBr_3$ and InI_3 calculations. While this does create slower and less favorable reactions, they are still all faster and more stable than the zinc-free **5–InX$_3$** geometries.

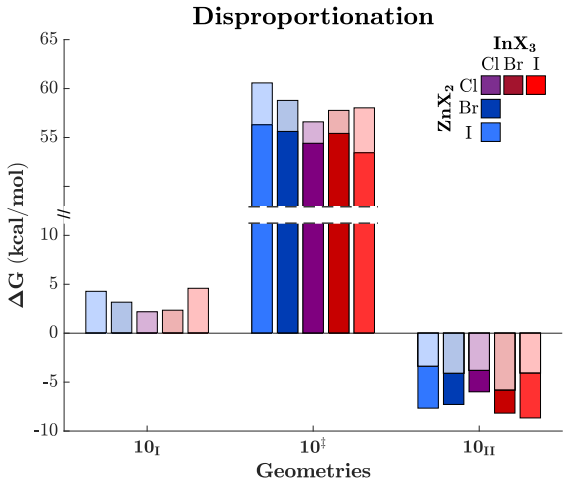

FIGURE 4.15: Free energies of the disproportionation process for various halides at the PBE0-D3/def2-TZVP level of theory. The data in full color (ΔG) are differences from their respective starting geometries, **10$_\mathbf{I}$**, while those in the lighter shade (ΔG_g) use the global reference method of Equation 4.3.

The initial **10$_\mathbf{I}$** structures can be examined in the same way as Figure 4.6 in Section 4.2.2. Looking at the differences in energies in Table 4.10 shows the largest contributions of changing halides is again due to electronic energies. The larger halides appear to reduce the passivation on the indium, regardless of the metal center in which they are present. While the various InX_3 cause steric inhibitions, the ZnX_2 appear to reduce the passivating ability of the zinc center, both of which cause a weaker In–P bond. This lengthened distance appears to be the most responsible for the increase in the ΔE_g of **10$_\mathbf{I}$–InX$_3$** geometries, but the **10$_\mathbf{I}$–ZnX$_2$** structures also show a much larger twisting of the aminophosphine away from the indium center. This disruption is shown by a simultaneous decrease in the lengths of bond A with an increase in bond B, the magnitude of which contribute to less stable ΔE_g, and therefore ΔG_g, of these geometries.

While the ZnX_2 disproportionation transitions can also be examined like in the previous Figure 4.8, the angles α and β appear less useful in these new geometries. Their sum correlates moderately well with the change in free energies (Figure 4.16B), but only if the zinc-free **5‡–InX$_3$** geometries are included. If these points (triangles) are removed, the correlation is immediately destroyed, and the R^2 value falls to 0.0087. One reason for this poor linearity is unusually large disorder found in

	ΔE_g [a]	ΔG_g [a]	S [b]	In–P (Å)	A (Å)	B (Å)	γ (°)
$InCl_3/ZnI_2$	-29.18	4.28	445.72	2.655	2.536	3.249	108.84
$InCl_3/ZnBr_2$	-30.93	3.17	440.61	2.648	2.534	3.164	108.97
$ZnCl_2/InCl_3$	-32.07	2.19	435.52	2.643	2.547	3.100	109.02
$InBr_3/ZnCl_2$	-31.66	2.35	443.44	2.649	2.627	3.093	108.97
$InI_3/ZnCl_2$	-30.37	4.59	446.39	2.673	2.766	3.194	108.81

[a] kcal/mol [b] cal/mol-K

TABLE 4.10: Global electronic and free energy comparisons of the $\mathbf{10_I}$ structures with their entropy terms. Select bond lengths and angles, determined in the same way as Figure 4.6 are also presented.

$\mathbf{10^{‡}–InI_3}$, which significantly lowers its ΔG_g beyond what has been seen in the other geometries. If this value is removed from consideration, Table C.8 shows the R^2 values improve for the relationships of α and β, but they still fail to achieve anything more than casual significance.

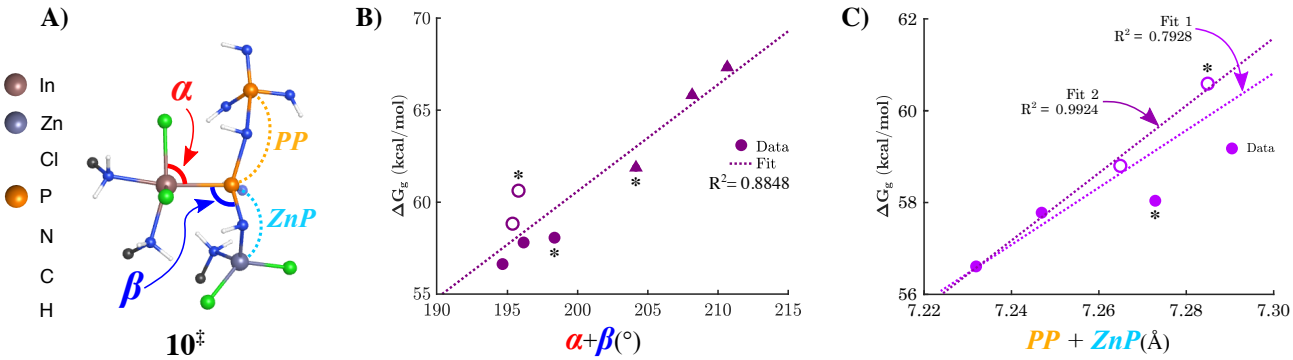

FIGURE 4.16: A) Simplified diagram of the $InCl_3-ZnCl_2$ disproportionation transition states with key bond angles and lengths labelled. B) The correlation of free energy to the sum of the α and β angles. C) The correlation of free energy to the sum of the PP and ZnP bond lengths. Zinc-free geometries are marked with triangles, those varying the zinc halide are presented as empty circles, ○, and calculations including iodine are noted with (*).

Instead of examining angles, intramolecular distances were found to trend better with the free energies of these disproportionations. The space between the metal center and activated phosphorus (ZnP) has a reasonably strong correlation on its own ($R^2 = 0.9123$ from Table C.8). However, this improves when the contribution from the phosphorus-phosphorus (PP) distance is included. Figure 4.16C shows that the sum of these two relationships is highly linear if the odd $\mathbf{10^{‡}–InI_3}$ data is removed (Fit 2).

The difference between using α+β or ZnP+PP falls to where in the molecular space the geometries are changing. For comparing $\mathbf{5^{‡}–InX_3}$ and $\mathbf{10^{‡}–InX_3}$, most of the differences are around the indium-phosphorus bond, which is why α+β is so powerful in Figure 4.8. However, when the ZnX_2 component is manipulated, there are fewer changes in that space, so the altered angles fail to describe the trend with free energy. The ZnP distance is fundamentally affected by the different ZnX_2

halides, so the changes are significant with free energy. Because the $\mathbf{5}^{\ddagger}$–$\mathbf{InX_3}$ geometries do not have a zinc center, they cannot be included in this consideration, so there is not one parameter "responsible" for all the ΔG_g of the $\mathbf{5}^{\ddagger}/\mathbf{10}^{\ddagger}$ geometries in this chapter.

	ΔE_g [a]	ΔG_g [a]	S [b]
$InCl_3/ZnI_2$	-38.01	-3.38	443.19
$InCl_3/ZnBr_2$	-39.15	-4.10	438.21
$InCl_3/ZnCl_2$	-39.86	-3.80	431.28
$InBr_3/ZnCl_2$	-40.17	-5.81	442.67
$InI_3/ZnCl_2$	-39.68	-4.07	445.00

[a] kcal/mol [b] cal/mol-K

TABLE 4.11: Global electronic and free energies of the $\mathbf{10_{II}}$ structures with their entropy terms.

Finally, the terminal $\mathbf{10_{II}}$–$\mathbf{ZnX_2}$ geometries are also very stable with regards to free energy. All of the $\mathbf{10_{II}}$ geometries have $\Delta G_g < -3.30$ kcal/mol, with $\mathbf{10_{II}}$–$\mathbf{InBr_3}$ being the most stable again. As with the discussion at the end of Section 4.2.2, the minor differences between the other pathways are hard to pin down to any one reason. However, the stability of $\mathbf{10_{II}}$–$\mathbf{InBr_3}$ is both from electronic and entropic contributions, as seen in Table 4.11. A slightly lower ΔE_g than $InCl_3$ and a relatively large increase in S yields the lowest free energy difference in this synthesis. The main determination from these calculations is that all of the final $\mathbf{10_{II}}$ geometries are probable products and a more holistic analysis is necessary to make any grand conclusions.

4.3.4 Zinc Halide Summary

By using Equation 4.4 with each full reaction pathway, it can be seen in Table 4.12 that the $\mathbf{10_{II}}$ geometries are the major products in all cases that have employed zinc activation. Interestingly, all other products occur in slightly larger portions than the $InCl_3-ZnCl_2$ reaction, even the $\mathbf{10_{II}}$–$\mathbf{ZnI_2}$ geometry. Despite many geometries with ZnI_2 having less favorable ΔG_g, the disproportionation product is much more stable than all the other conformers in its row. Therefore, a more significant fraction is allowed to exist as $\mathbf{10_{II}}$–$\mathbf{ZnI_2}$ at equilibrium.

	$\mathbf{R}$	$\mathbf{7_e}$	L		D		
			Start	End	Start	End	
$InCl_3/ZnI_2$	2%	3%	0%	1%	0%	94%	=100%
$InCl_3/ZnBr_2$	1%	2%	0%	6%	0%	91%	=100%
$InCl_3/ZnCl_2$	1%	6%	0%	4%	0%	89%	=100%
$InBr_3/ZnCl_2$	0%	1%	0%	0%	0%	99%	=100%
$InI_3/ZnCl_2$	1%	5%	0%	0%	0%	94%	=100%

TABLE 4.12: Proportions of the conformers that exist as the ligand exchange (L) and disproportionation (D) minima of each reaction path at equilibrium, as calculated by Equation 4.4 for all X geometries in the pathway.

Naturally, the very negative ΔG_g of the indium bromide calculation results in nearly all of its molecules reacting as $t \rightarrow \infty$. When all of the geometries of all of the pathways are compared to each other (Table C.9), 66% of the precursors are as $\mathbf{10_{II}}$–$\mathbf{InBr_3}$. Unsurprisingly, the remaining percentages are roughly scattered among the other $\mathbf{10_{II}}$ conformers in ratios reflecting their ΔG_g from Figure 4.15. This very stable geometry suggests that $InBr_3$ may dictate the thermodynamics of a mixed halide reaction.

	$k^{\ddagger}(\mathrm{L})$ s^{-1}	$k^{\ddagger}(\mathrm{D})$ s^{-1}	$\log(\mathrm{L}^*)$ dec	$\log(\mathrm{D}^*)$ dec
$InCl_3/ZnI_2$	$1.26 * 10^2$	$5.73 * 10^{-17}$	-1.12	-1.92
$InCl_3/ZnBr_2$	$2.95 * 10^3$	$4.18 * 10^{-16}$	0.25	-1.06
$InCl_3/ZnCl_2$	$1.67 * 10^3$	$4.76 * 10^{-15}$	0.00*	0.00*
$InBr_3/ZnCl_2$	$2.52 * 10^2$	$1.29 * 10^{-15}$	-0.82	-0.57
$InI_3/ZnCl_2$	$1.27 * 10^3$	$9.73 * 10^{-16}$	-0.12	-0.69

$\mathrm{L}^* = k^{\ddagger}(\mathrm{L})/k^{\ddagger *}(\mathrm{L})$ $\mathrm{D}^* = k^{\ddagger}(\mathrm{D})/k^{\ddagger *}(\mathrm{D})$

TABLE 4.13: Rates of the ligand exchange, $k^{\ddagger}(\mathrm{L})$, and disproportionation, $k^{\ddagger}(\mathrm{D})$, transitions with different indium halides calculated using the Eyring equation, $k^{\ddagger} = k_b T/h * \exp(-\Delta G_g^{\ddagger}/RT)$. The order of magnitude of reaction rates, $\log(k/k^*)$, relative to one geometry, (*), are also presented.

Kinetically, the aminophosphine conversion appears dominated by the ZnX_2 reactions. While the reaction rates in Table 4.13 have mixed trends from the ligand exchange process, they have a mean value of $\sim$1300 $\pm$ 1000 s^{-1}, which is moderately fast. In contrast, the ZnX_2 disproportionations slow by an order of magnitude with each step down the periodic table. Although this trend can also be seen in the activated InX_3 geometries, the effect is smaller despite the presence of an additional halide. The more significant effect of ZnX_2 over InX_3 confirms that the degree of zinc acidity has a direct impact on the aminophosphine conversion process.

4.4 Conclusions

This chapter developed a system to compare the energies of entire reaction pathways directly. The global reference method (Equation 4.1) was useful for relationships that are challenging to examine due to a varying number of electrons among the calculations. This tactic was also valuable for describing the energies of the starting structures, which was not possible with standard ΔG calculations. The ability to relate individual reaction processes (i.e., ligand exchange vs. disproportionation) to a common energy point also provided a measure of total product stability, as found in Tables 4.4 and 4.12. Altogether, the global reference was able to provide much more information than the standard comparison methods and was a valuable addition to this work.

Varying indium halides in this reaction had effects on the structures and energies of the aminophosphine conversion mechanism that were examined in detail. Shockingly, the sum of two internal angles, α and β, was found to be highly linear

with the change in free energy of the disproportionation structures. Because these angles focus on the space around the In–P bond, it is less surprising that different InX_3 affect this space so strongly. Outside of this correlation, however, the zinc-free reactions displayed few behaviors that trended well with the InX_3-ZnCl_2 geometries, which complicated the conclusions made about the effect of indium halides on this reaction. As the zinc-activated geometries are held to be more likely overall than their **4/5** counterparts, the conclusions from the InX_3-ZnCl_2 geometries are taken to be correct. These reactions are also more easily compared to the conformers with varying zinc halides, which helps produce a more complete picture of the halide interactions.

All of the activated calculations with bromine or iodine were lower in free energy than the $InCl_3-ZnCl_2$ pathway. The $InBr_3-ZnCl_2$ system was particularly stable, as its $\mathbf{10_{II}}$ geometry is 1.71 kcal/mol lower in energy than the next most stable conformers. Table 4.13 shows the disproportionation rates were found to be highly dependent on the size of the halides involved and those on the zinc center had a greater influence than those around the indium. Despite having one less iodine, the $InCl_3-ZnI_2$ system was far slower than the InI_3-ZnCl_2 system, which may help explain why the syntheses with iodides are much worse than the others. Interestingly, the ZnP and PP distances were found to have a significant impact on the free energies of the $\mathbf{10}^{\ddagger}$ geometries, which could possibly be manipulated to provide a tool to tune the reaction rates.

For structures that were outliers, the interplay between ΔE_g and S frequently determined why the conformer was stable or not. In the cases of the iodides, this usually meant that the compounds were much less passivated, and resulted in poor ΔG_g despite the increase in entropy that the larger halides presented. On the other hand, the bromides possessed the best of both worlds whereby they had only slightly worsened ΔE_g but much larger S, making them much more stable than their counterparts. From a synthetic perspective, this suggests that the InI_3 and ZnI_2 syntheses should be avoided while $InBr_3$ should probably be used as the indium source to make the best particles. Unfortunately, these conclusions do not provide a way to tune these reactions beyond the discrete sizes already developed in Chapter 3. Instead, new ways of incorporating halides must be developed to manipulate the concentration of various anions in the reaction solutions.

Bibliography

[1] C. Adamo and V. Barone, "Toward reliable density functional methods without adjustable parameters: The PBE0 model," *J. Chem. Phys.*, vol. 110, pp. 6158–6169, 1999.

[2] F. Weigend and R. Ahlrichs, "Balanced basis sets of split valence, triple zeta valence and quadruple zeta valence," *Phys. Chem. Chem. Phys.*, vol. 7, p. 3297, 2005.

[3] S. Grimme, J. Antony, S. Ehrlich, and H. Krieg, "A consistent and accurate ab initio parameterization of density functional dispersion correction (DFT-D) for the 94 elements H-Pu," *J. Chem. Phys.*, vol. 132, p. 154104, 2010.

[4] maximum gradient: 1.5×10^{-5}, RMS gradient: 1.0×10^{-5}, maximum displacement 6.0×10^{-5}, RMS displacement 4.0×10^{-5}.

[5] Many conformers were examined at lower levels of theory before deciding on the ones presented here, which agree with those in Chapter 3. After geometry optimization with PBE0-D3/def2-TZVP, frequency calculations at the same level of theory were carried out at 453.15 K (180 °C) in order to ensure that the obtained structures correspond to minima (or first-order transition structures) on the potential energy surface at the required synthesis temperature. In order to confirm the exact structure of reagents and products that correspond to each elementary step in the reaction mechanism, intrinsic reaction coordinate (IRC) calculations[11–13] were carried out for every transition structure presented herein that unambiguously confirm the reaction sequence. When modeling the primary amines used in the QD synthesis, ethylamine (NH_2Et) was used to more appropriately represent the steric component in addition to the electronic profile of a long chain fatty amine.

[6] M. J. Frisch, G. W. Trucks, H. B. Schlegel, G. E. Scuseria, M. A. Robb, J. R. Cheeseman, G. Scalmani, V. Barone, B. Mennucci, G. A. Petersson, H. Nakatsuji, M. Caricato, X. Li, H. P. Hratchian, A. F. Izmaylov, J. Bloino, G. Zheng, J. L. Sonnenberg, M. Hada, M. Ehara, K. Toyota, R. Fukuda, J. Hasegawa, M. Ishida, T. Nakajima, Y. Honda, O. Kitao, H. Nakai, T. Vreven, J. A. Montgomery, Jr., J. E. Peralta, F. Ogliaro, M. Bearpark, J. J. Heyd, E. Brothers, K. N. Kudin, V. N. Staroverov, R. Kobayashi, J. Normand, K. Raghavachari, A. Rendell, J. C. Burant, S. S. Iyengar, J. Tomasi, M. Cossi, N. Rega, J. M. Millam, M. Klene, J. E. Knox, J. B. Cross, V. Bakken, C. Adamo, J. Jaramillo, R. Gomperts, R. E. Stratmann, O. Yazyev, A. J. Austin, R. Cammi, C. Pomelli, J. W. Ochterski, R. L. Martin, K. Morokuma, V. G. Zakrzewski, G. A. Voth, P. Salvador, J. J. Dannenberg, S. Dapprich, A. D. Daniels, Ö. Farkas, J. B. Foresman, J. V. Ortiz, J. Cioslowski, and D. J. Fox, "Gaussian 09 Revision D.01." Gaussian Inc. Wallingford CT, 2009.

[7] J. Schmidt and W. Polik, "WebMO Enterprise, version 17.0.012e." http://www.webmo.net/, November 2017.

[8] J. S. Owen, E. M. Chan, H. Liu, and A. P. Alivisatos, "Precursor Conversion Kinetics and the Nucleation of Cadmium Selenide Nanocrystals," *Journal of the American Chemical Society*, vol. 132, no. 51, pp. 18206–18213, 2010.

[9] C. R. Bullen and P. Mulvaney, "Nucleation and Growth Kinetics of CdSe Nanocrystals in Octadecene," *Nano Letters*, vol. 4, no. 12, pp. 2303–2307, 2004.

[10] S. Abe, R. K. Čapek, B. De Geyter, and Z. Hens, "Tuning the Postfocused Size of Colloidal Nanocrystals by the Reaction Rate: From Theory to Application," *ACS Nano*, vol. 6, no. 1, pp. 42–53, 2012.

[11] K. Fukui, "The path of chemical-reactions - The IRC approach," *Acc. Chem. Res.*, vol. 14, pp. 363–368, 1981.

[12] H. P. Hratchian and H. B. Schlegel, "Accurate reaction paths using a Hessian based predictor-corrector integrator," *J. Chem. Phys.*, vol. 120, pp. 9918–9924, 2004.

[13] H. P. Hratchian and H. B. Schlegel, "Using Hessian updating to increase the efficiency of a Hessian based predictor-corrector reaction path following method," *J. Chem. Theory Comput.*, vol. 1, pp. 61–69, 2005.

Chapter 5

Synthetic Manipulations

Although the last chapter highlights the effect of halide content on the strength of zinc activation and the indium sterics, the ability to tune these behaviors is still very limited in these syntheses. The only available tool to adjust these effects continues to be swapping the indium or zinc precursors to different halide salts. While this can be effective to isolate a handful of sizes of nanoparticles, there is not a great deal of tunability outside of these specific profiles. The ability to freely probe the halide content in these reactions is necessary not only to produce new sizes of InP cores, but also to complete the picture of the mechanism that has been drawn thus far.

Unfortunately, there are few ways to include highly charged anions like Cl^-, Br^-, and I^- into these syntheses. The most significant hurdle occurs because of the long hydrocarbon chains that are necessary for a high boiling point solvent. These compounds are generally hydrophobic, which makes it challenging to introduce the highly polar compounds that are typical sources of halides. While coordinating solvents such as oleylamine can solubilize some salts like InX_3 or ZnX_2, they are still unable to incorporate the more ionic sodium or potassium salts, which are typical sources of anions. Even if these compounds could be used in this synthesis, free Na^+ or K^+ species may pose significant mechanistic complications if allowed to interfere with core growth. Therefore, a family of compounds is needed which is compatible with long chain hydrocarbons, can contain a range of halides, and will not pose a threat to the mechanistic integrity of the reaction.

5.1 Oleylammonium Halides

Looking towards the field of perovskites inspired the use of alkylammonium halides to satisfy these goals. Specifically, oleylammonium halides are of interest as they should be directly comparable with the solvent and ligand systems used so far in this work. As the preparation of these compounds are already reported[1,2] and are allegedly simple, it was envisioned that this would be an excellent way to probe the halide concentration in these reactions.

5.1.1 *Ex situ* Production

$$RNH_2 + HCl \longrightarrow RNH_3Cl \tag{5.1}$$

$$3\ RNH_3Cl + In(OAc)_3 \longrightarrow 3\ RNH_2 + InCl_3 + 3\ HOAc \tag{5.2}$$

In order to make the precursor, Equation 5.1 shows that equimolar amounts of oleylamine and the hydrohalic acid of choice are stirred together in excess ethanol to form RNH_3X, where R=$(CH_2)_8CH{=}CH(CH_2)_7CH_3$ and X=Cl,Br,or I. This solution is then cooled to 0 °C and left overnight under flowing inert atmosphere to evaporate some of the solvent. The solid is then to be collected by filtration, washed with diethyl ether to remove leftover reactants, and dried in a vacuum oven overnight. This process is particularly useful for oleylamine, as its melting point of 21 °C means

that it should wash away during the room temperature filtration and the acid adduct should stay as a solid. While other alkylamines could also be used, most are solids at room temperature, which would make isolating the products from the reactants difficult.

If the alkylammonium halide is to be a source of X^-, then combining it with a salt like indium acetate should result in the formation of indium halide in the solution. This reaction scheme is demonstrated in Equation 5.2 for X = Cl and shows that acetic acid (HOAc) would form in this situation, which should remove itself from the reaction solution during the degassing stage. Interestingly, the only other product is the primary amine, which creates an advantage if it matches the solvent of the reaction. Fewer byproducts mean an InP reaction implementing the chemistry of Equation 5.2 should match that of a reaction that uses indium halide salts from the start. This formulation is potentially a handy way of creating the more expensive and hygroscopic iodides in solution instead of having to purchase them.

In order to test this logic, solutions of InP core materials were grown comparing a standard $InCl_3$-based reaction to one using the precursor combination of Equation 5.2. Full synthetic details are available in Section 5.5, but in general 0.45 mmol (1 eq.) of indium precursors were dispersed in excess oleylamine (∼33 eq.). For the indium acetate solutions, oleylammonium chloride (OAmCl) was also included, with the amount varying for the molar equivalent desired. All solutions were then put under vacuum for 2 hours at 120 °C to remove any dissolved gasses, solvated water, and volatile byproducts like HOAc. The solutions were then put under nitrogen atmosphere and raised to 180 °C before the injection of 1.6 mmol (3.6 eq.) $P(DEA)_3$ was used to instigate nanoparticle growth.

Aliquots of the reactions were taken at various times and quenched in toluene. These samples were then centrifuged to remove any solid material and the supernatant was analyzed with UV-Vis absorption spectroscopy. After 30 minutes of reaction, the solutions remaining in the flasks were cooled and cleaned once with a toluene and ethanol precipitation. This precipitate was redispersed in toluene, centrifuged again to remove any solid materials, and then also examined with UV-Vis absorption. These spectra are then normalized by the height of their lowest energy absorption feature and colored according to its wavelength[†]. The baselines of these traces are then vertically shifted for clarity within a given graph while the standardized colors promote understanding across different Figures.

Manipulating the halide concentration with OAmCl paints an interesting picture when compared to the standard reactions presented thus far. It can be seen that nanoparticles made with the scheme of Equation 5.2 (Figure 5.1B) are smaller and blue-shifted from those in the $InCl_3$ reaction (Figure 5.1A). However, the first absorption peak is also much sharper throughout the synthesis, which indicates a smaller distribution of particle sizes. Additionally, if $In(OAc)_3$ is used without any

[†]hue (°) $= (650\text{ nm} - \lambda_{abs}) * 280°/(650\text{ nm} - 400\text{ nm}) - 50°$, which was arbitrarily chosen but consistently applied. This works best between $400 - 650$ nm, so graphs with $\lambda_{abs} \ll 400$ are often shown in greyscale instead.

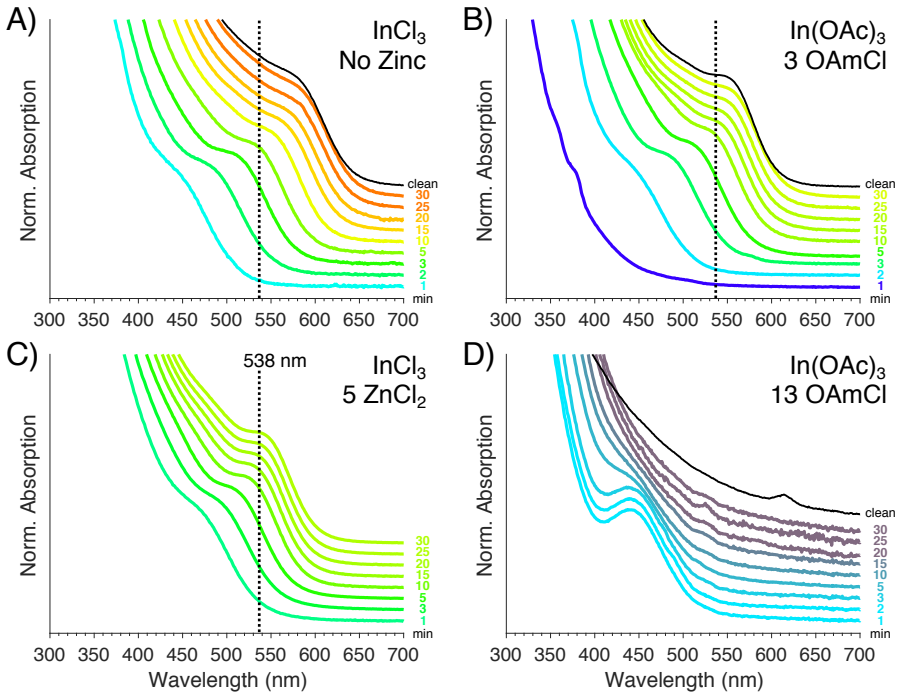

FIGURE 5.1: UV-Vis spectra of InP core materials dispersed in toluene taken over time with the indicated starting precursors. All are 1-pot reactions with oleylamine as solvent and the traces have been normalized and colored based on their lowest energy absorption feature. Black traces labelled as "clean" are samples that were precipitated once with ethanol and redispersed in toluene.

OAmCl, no particles can be grown at all, so using Equation 5.2 opens up a previously blocked avenue of research.

While Figure 5.1C is the same graph as seen in Figure 3.17A, the comparison of the same solution without zinc (Figure 5.1A) shows that the presence of $ZnCl_2$ forces an equilibrium size to occur. Both Figure 5.1A and B show that their peak positions red-shift and their widths broaden continuously over time. On the other hand, Figure 5.1C displays a constant peak position and shape after $t \approx 20$ min. This result could suggest that the increased [Cl^-] in Figure 5.1C is responsible for the stabilization, as having an excess of strong ligands may limit the ripening processes seen in the other two scenarios.

In order to check this excess ligand theory, the amount of OAmCl in the $In(OAc)_3$ synthesis was increased to 13 eq. to match the amount of [Cl^-] that would be available in the solution of 1 $InCl_3$: 5 $ZnCl_2$. Unfortunately, the spectra of Figure 5.1D show a drastically altered behavior from any of the syntheses examined in this thesis. An initial intense burst of nucleation appears to form a large number of small nuclei with $\lambda_{Abs} = 440$ nm. These particles seem to only be stable for ~3 min before broadening in size from ripening effects. This degradation in absorption features is also accompanied by an increasing amount of dark, solid precipitate over time. Together, these phenomena point to most of the precursors being consumed during the first burst of nucleation and then uncontrolled aggregation to bulk InP materials.

One explanation for this deviation from typical behavior is that the excess OAmCl

could be allowing for the production of highly reactive $H_xP(NHR)_{3-x}$ species. In Figure 5.1B, the acidic RNH_4^+ matches the [$^-$OAc], so should be consumed to produce acetic acid which is removed during the degassing phase. For the synthesis in Figure 5.1D however, the anions are unbalanced, so 10 eq of OAmCl remain in solution during the aminophosphine injection. Equations 5.3 and 5.4 depict how this residual acid could react to form variously reduced phosphines, all of which would be far more reactive than the standard $P(NHR)_3$. The near-instant formation of tiny, unstable particles seen in this synthesis strongly suggests a reaction much more on par with $(TMS)_3P$ than typical aminophosphine literature. Because H_3P and $(TMS)_3P$ are frequently held to be electronically equal,[3] this is not too wild of a comparison, as strong fatty acid ligands are typically employed to slow nucleation and growth to manageable rates in syntheses with P(-III) species.

$$13\ RNH_3Cl + In(OAc)_3 \longrightarrow 3\ RNH_2 + InCl_3 + 3\ HOAc + 10\ RNH_3Cl \tag{5.3}$$

$$10\ RNH_3Cl + P(NEt_2)_3 \longrightarrow \begin{matrix} HP(NEt_2)_2 \\ H_2P(NEt_2) \\ H_3P \end{matrix} + HNEt_2 + \cdots \tag{5.4}$$

Despite the utility seen in Figure 5.1 for OAmCl to produce interesting and quality InP materials, this manner of work was not pursued. This change in course was strictly due to the significant hurdles posed by the production and isolation of the oleylammonium halides. While literature reports suggest the synthesis to be straightforward, in practice, it is a messy, three-day endeavor with <10% yields[†]. Additionally, if the material produced was not kept rigerously moisture-free, it reverted to a liquid mix of oleylamine and hydrohalic acid. As such, further efforts to repeat, expand, or determine the mechanisms of these reactions were put on hold.

5.1.2 Generating OAmCl *in situ*

Attempts at forming oleylammonium halides *in situ* proceeded instead. Using their *ex situ* preparation as a guide, the desired reaction equivalents concentrated hydrohalic acid were diluted in minimal ethanol (1-2 mL). This mixture was then added to 5 mL of oleylamine and allowed to stir for 1 hour. 1 eq. $In(OAc)_3$ was then added and the solution was carefully placed under vacuum and heated to 70 °C for 30 min. The vessel was then subjected to the standard degassing, inert atmosphere, heating, and aminophosphine injection. Full details of these syntheses are presented in Section 5.5.

Comparing Figures 5.2A and 5.2B demonstrate that this is a viable method of reproducing the results from the *ex situ* preparation of OAmCl. While the *in situ* method shows a slight blue-shift and broadening, the peak maxima and general evolution over time are very similar between the two routes. This data is slightly

[†]This was for OAmCl. The bromides were so much worse that no publishable results could be obtained.

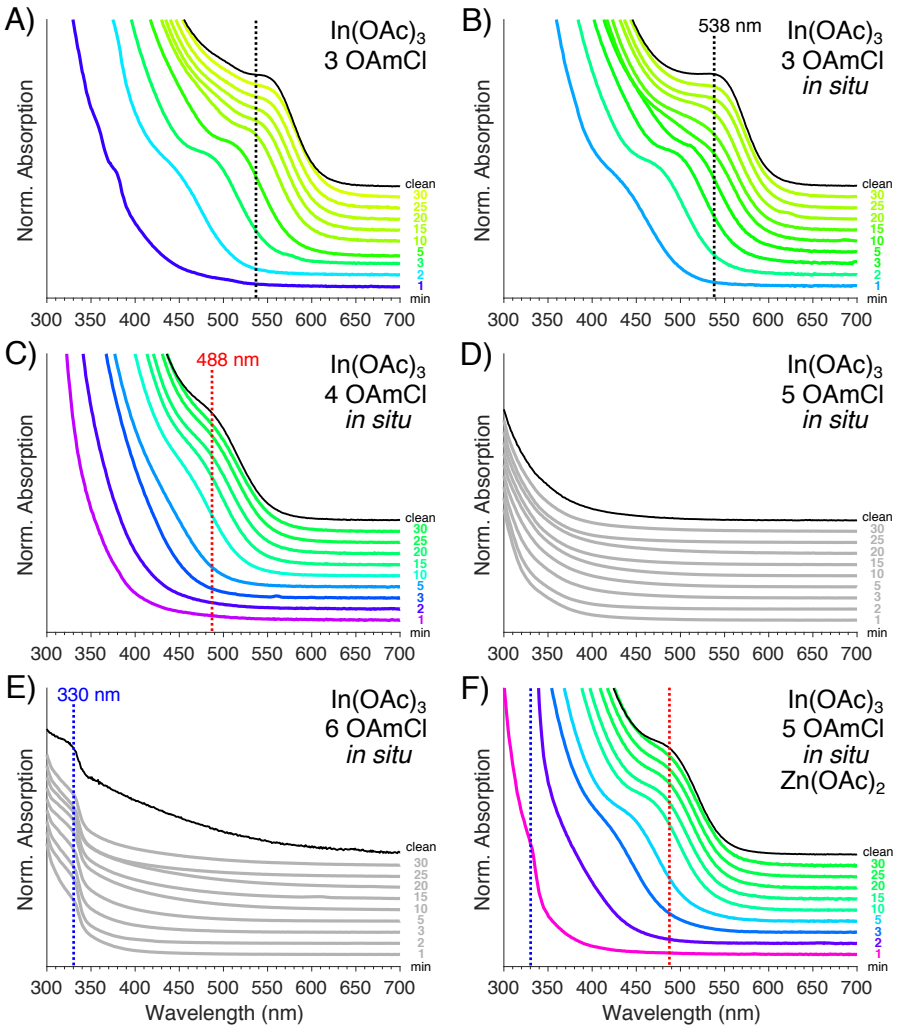

FIGURE 5.2: A UV-Vis absorption comparison of 1-pot InP core syntheses using A) isolated 3 OAmCl or B)–E) varying amounts of OAmCl produced *in situ* over time. F) A similar investigation of a synthesis with 5 OAmCl prepared *in situ* with the presence of 1 eq. of zinc acetate.

surprising given the deliberate inclusion of both water and ethanol into the reaction, but it appears that the degassing steps were able to remove most of these components. The slight worsening of particle quality seen from the broadened first absorption peak in Figure 5.2B compared to 5.2A, as well as a lack of second absorption feature at ~500 nm is a likely indication of trace amounts of these contaminants still in solution. However, the degree of similarity between the two time series outweigh the minor differences, so this implementation was continued.

Increasing the concentration of OAmCl to 4 eq. resulted in much smaller nanoparticles, which can be seen by the significant blue-shift in the lowest energy absorption features in Figure 5.2C. While the improved access to Cl^- may have resulted in better, faster capping of the InP cores, this synthesis was much broader in size distributions than its 3 eq. counterparts. The lack of distinct absorption features until after the final products were cleaned is evidence for a wide array of sizes. Although the spectra may be able to be improved with size-selective precipitation, the ratio of

time input to improvement was not worth the effort. Additionally, these InP core materials have been frequently found to aggregate with excessive washing, as the weak oleylamine ligands are gradually removed until particles become unstable.

Unfortunately, adding more OAmCl to these reactions did not further blue-shift the produced cores. Instead, 5 eq. of OAmCl did not instigate any particle growth, as can be seen by the featureless traces in Figure 5.2D. Oddly, the use of 6 eq. OAmCl shows a distinct peak at ~330 nm that is consistent throughout the traces of Figure 5.2E. While it is tempting to assign to this to a small $In_xP_yCl_z$ cluster, control experiments have found various indium and zinc salts to have small absorption features around this region as well. However, the persistence of the species throughout the growth and its ability to be precipitated is atypical of those controls and warrants further investigation.

Although using 5 eq. of OAmCl did not produce any particles, when 1 eq. of zinc acetate was included with the indium salts, the nanoparticle formation recovered. Curiously, Figure 5.2F show the wavelengths of the first absorption events over time are nearly identical in this synthesis to those from Figure 5.2C. Again, the presence of a zinc salt proves to sharpen the absorption features throughout the reaction, though the quality is still subpar when compared to Figure 5.2A or B. Additional $Zn(OAc)_2$ may further improve these size distributions, but that would require more OAmCl, which complicates the matter.

While the ratios of [Cl^-] and [$^-$OAc] are different in Figures 5.2C and F, the similarity of their spectra may hint at the equilibrium size being affected in a binary manner instead of as a continuous variable. If a given component reaches some threshold, one specific size of nanoparticle seems to stabilize. Here, the switching behavior may come from the presence of $^-$OAc, given it is the only component seen in both Figures 5.2D and F that increased concentration from one to the next. Still, the effect may be coming from RNH_4^+, as it is difficult to attribute the behavior to specific components from absorption experiments.

Now that it has been identified, this on/off effect can be seen throughout the work presented in this thesis. In Chapter 3, this binary logic explains the lack of differences between Figures 3.19 and 3.20 despite significant changes in [MA], which are typically found to have large impacts on nanoparticle sizes. It also supports why the positions of spectral features are insensitive to slight changes in precursor amounts[†] and why mixed precursor solutions (e.g. 1 $InCl_3$: 1 $InBr_3$) produce broadly absorbing, polydisperse materials. While this behavior is annoying from a view on tunability, it does impart robustness onto these syntheses that make them easier for a non-specialist researcher to reproduce.

[†]While it is important to always be consistent with the molar ratios of precursors, the hygroscopic nature of halides meant that working in open environments prioritized the speed of weighing more than accuracy. Regardless, syntheses with ±10% differences in mass were usually found to produce nearly identical absorption and emission behaviors.

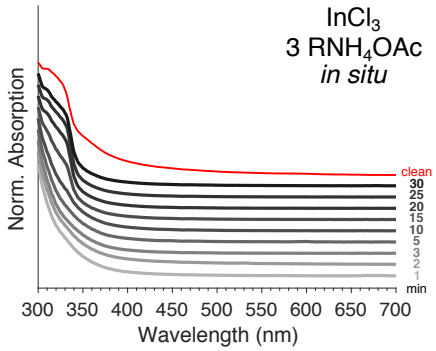

FIGURE 5.3: Evolution of UV-Vis absorption features of a solution containing $InCl_3$ and 3 eq. HOAc when introduced to $P(DEA)_3$.

Although making OAmCl *in situ* has been useful for unearthing interesting aspects of these precursors, the number of added components significantly complicates synthetic understanding. As seen in Figure 5.3, a control experiment revealed that acetic acid can also form an adduct with oleylamine. When HOAc was used instead of HCl and $InCl_3$ was used instead of $In(OAc)_3$, a strong peak evolved at ~330nm, which is consistent with the indium precursor or small In_xP_y cluster seen in Figure 5.2E. In addition to this feature, there a new absorption peak ~360nm was found in the cleaned precipitate, suggesting at least some growth or nucleation events occurred.

While this result opposes the previous assertion that all HOAc evaporates off under vacuum, it does support the scheme that most of the oleylamine·acid compounds replace the indium anions. Similarly, ethanol and water could also form adducts with oleylamine, which is present in excess as the solvent. Either a new method of implementing the *in situ* OAmCl needs to be developed to eliminate these possibilities, or a tremendous amount of controls need to be performed to isolate the effects of each component on the QD formation. Given the time investment and resources necessary for either of these options, this method was shelved until due diligence could be devoted to these efforts.

5.2 Cetyltrimethylammonium Halides

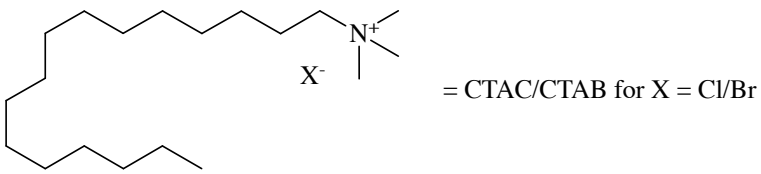

FIGURE 5.4: Generic chemical structure of the cetyltrimethylammonium halides.

As the presence of an acidic proton frequently complicated the last section, organic ammonium halides were examined as alternate anion sources. Seen in Figure 5.4, cetyltrimethylammonium halides[†] are common surfactant molecules that are used in a wide variety of fields including the formation of nanoparticles,[4] microemulsions,[5] and mesoporous materials.[6] While the bromide (referred to as CTAB) is far cheaper than the chloride (CTAC), both are available commercially and can be found in most chemical laboratories. Their polar R-$[NMe_3]^+$ head groups make them useful capping ligands while their long chain R=$(CH_2)_{15}CH_3$ make them compatible with low polarity solvents, both of which make them well-suited for these InP syntheses.

5.2.1 Investigating Core Growth

Similarly to the last section, the ammonium halide species were combined with indium acetate to replace the native $^-$OAc ligands with their halide anion. In a typical synthesis, 1.35 mmol (3 eq.) of CTAC or CTAB were stirred together with 0.45 mmol (1 eq.) of $In(OAc)_3$ and 5 mL ($\sim$ 33 eq.) of oleylamine. This solution was carefully degassed, put under an inert atmosphere, heated to 180 °C, and injected with 1.6 mmol of aminophosphine. Again, full synthetic details are available in Section 5.5.

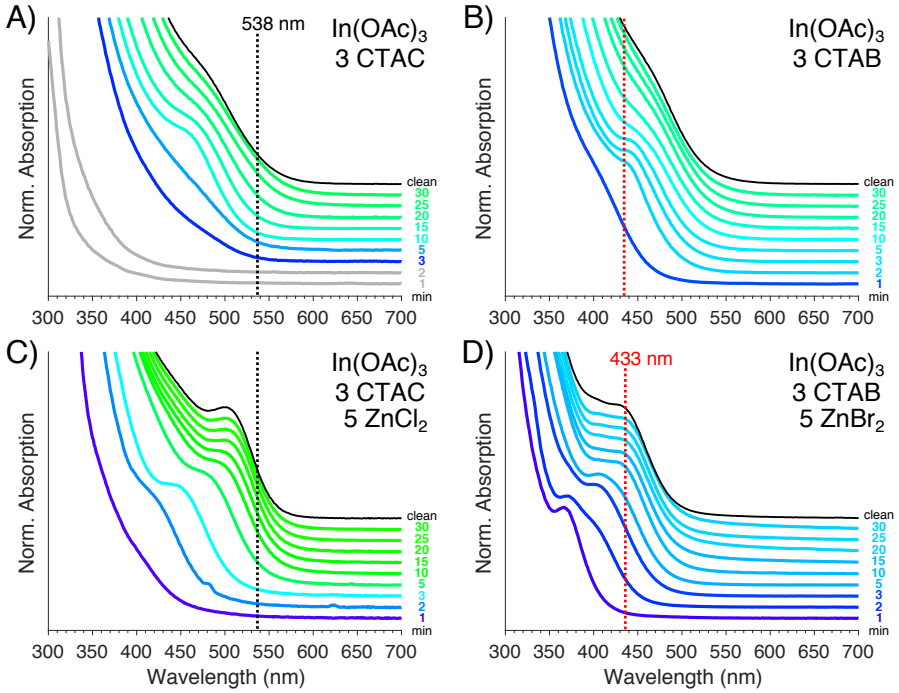

FIGURE 5.5: A UV-Vis absorption comparison of 1-pot InP core syntheses using A) CTAC and no zinc, B) CTAB and no zinc, C) CTAC with 5 $ZnCl_2$, or D) CTAB with 5 $ZnBr_2$.

It is immediately evident from Figure 5.5A that the use of cetyltrimethylammonium compounds results in much smaller particles than usual as the final peaks are

[†]Or hexadecyltrimethylammonium halides

significantly blue-shifted from the common λ_{Abs} = 538 nm of the previous section. If the relationship between particle sizes and surface energy (γ) is recalled from Sections 2.2.1 and 2.2.2, these small sizes are unsurprising as the polar $RNMe_3^+$ head group is generally held to be a strong ligand, which significantly lowers the surface energy of the particles.

Interestingly, the spectra of Figures 5.5A and B appear to follow growth and ripening processes more akin to "conventional" nanoparticle syntheses. After an early size-focusing period, there are distinct defocusing behaviors for $t > 5$ min in both syntheses. This broadening accompanied by a steady red-shift suggest the distribution of particles is becoming very polydisperse. These sort of phenomena are common in syntheses that rapidly deplete the precursor materials (as in typical hot injection syntheses) or otherwise disrupt ligand or particle equilibria mid-reaction.

While this new broadening may also be a factor of introducing strong ligands, Figures 5.5C and D show that stable equilibrium sizes can be recovered if matching ZnX_2 salts are included. The comparison of the spectra with CTAB are particularly interesting, as the mean size of the "good" distribution at $t = 3$ min in Figure 5.5B is preserved as $t \to \infty$ in Figure 5.5D with the inclusion of $ZnBr_2$. Although it is tempting to draw causational relationships between these two data sets, the early spectra of both syntheses are quite different, so the consistent "good" size is likely spurious. Regardless of the nature of their relationship, these syntheses produce incredibly small nanoparticles that are interesting in any case.

Although the syntheses with CTAC also show an improvement in peak characteristics with the addition of $ZnCl_2$, the peak maxima of Figures 5.5A and C do not align as well as those with CTAB. One factor of their ill-matching is the $t < 5$ min spectra of Figure 5.5, which are distinctly lacking in any absorption features. These empty traces can be attributed to the reduced solubility of CTAC and CTAB in these solutions, which was not recognized until several syntheses had been trialed. For this reaction, there is a slight turbidity that clears once the solution is held at 180 °C for ~5 minutes. Figures 5.5B–D are syntheses that had introduced this waiting time before aminophosphine injection, which is why there is distinct nanoparticle growth throughout the synthesis. Figure 5.5A should be repeated with this improvement, but the high cost and low availability of CTAC[†] meant that other syntheses were prioritized over this reaction.

While the double absorption peak of the core synthesis with 3 CTAB and 5 $ZnBr_2$ is a curious feature, it was not found to be very reproducible. The graphs in Figure 5.6 shows that although several syntheses display absorption events near 405 and 438 nm, the relative intensities of the two peaks changed with various degassing protocols. Of these schemes, only that of Figure 5.6B was able to be repeated with any degree of consistency. Although there appears to be a double feature in the early time frames, it seems to disappear for $t > 5$ min. This difference could either

[†] ~15 NZD per reaction with CTAC vs. 0.32 NZD per reaction for CTAB. The ~45x price difference means few people keep it in stock.

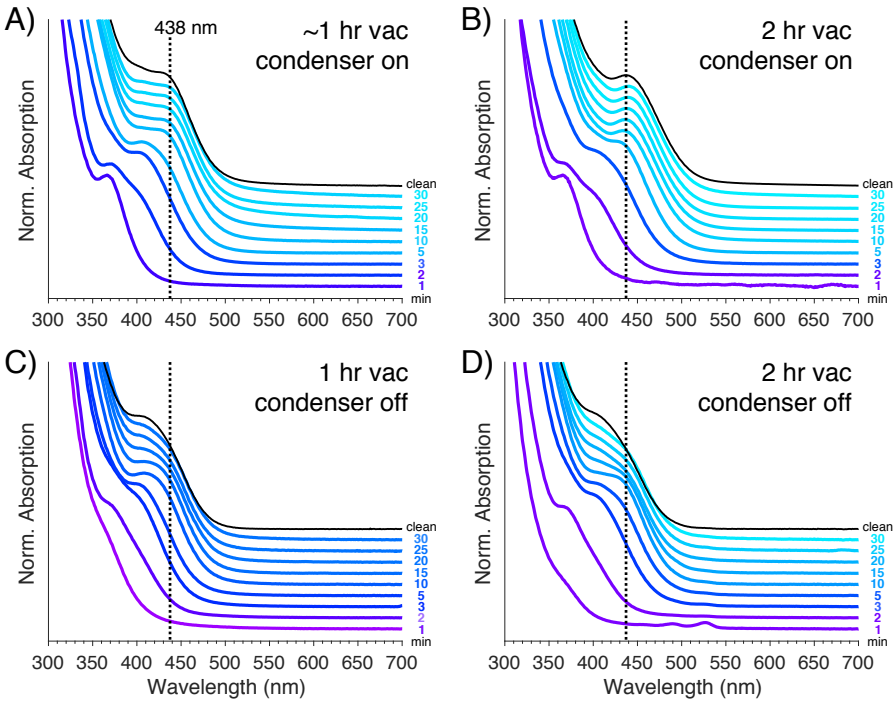

FIGURE 5.6: UV-Vis absorption traces over time of several batches of InP cores made with 3 CTAB and 5 $ZnBr_2$ using different degassing times and condensers filled with either air (condenser off) or flowing water (condenser on).

be due to the disappearance of the species that generated the 405 nm feature or to an increase in concentration or oscillator strength of the species that produced the 438 nm feature. In either case, the degassing protocol of Figure 5.6B was made the standard for aminophosphine QD reactions to avoid reproducibility issues in the future.

5.2.2 Tuning with Temperature

As with OAmCl, it was envisioned that using cetyltrimethylammonium halides would allow for a degree of tunability by manipulating the ratio of indium and halide precursors. However, it was found that any reaction that was not 1 $In(OAc)_3$ to 3 CTAB or CTAC was a failure. For syntheses with less halide, a black precipitate rapidly formed, which implied the nanoparticles immediately aggregated to bulk particles from too few ligands. For those with more, no stable nuclei were produced as the surface energy term was significantly reduced by the excess surfactant (see Figure 2.4B). Thus, manipulating the ratio of halides was found to be a dead end for these syntheses.

As changing the halide concentration could not be used, the effect of temperature on these core growths was investigated as a potential handle for size tunability. Figure 5.7 depicts several core growths held at elevated temperatures for the course of their reactions. Initially, the increase in temperature can be seen to red shift the $t = 1$ min trace, which is typical for an elevated reaction temperature. Interestingly,

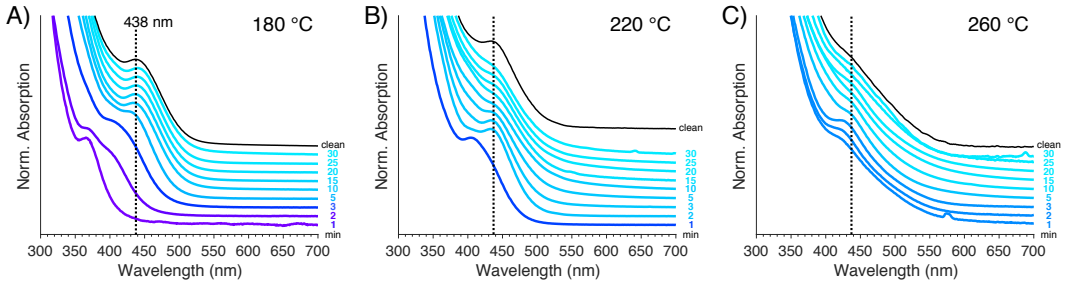

FIGURE 5.7: UV-Vis absorption traces over time of several batches of InP cores made with 3 CTAB and 5 $ZnBr_2$ with various injection temperatures.

at some point in the $t < 5$ min time points, each synthesis possesses a peak at ~440 nm of at least moderate quality. Additionally, while the peaks broaden over time for the cores grown at 220 °C and 260 °C, their peak maxima at the end of the reaction do not shift from this value. These phenomena could potentially indicate the buildup of a broadly absorbing byproduct in this reaction, especially given the good peak shape recovers after cleaning in the 220 °C synthesis.

The high quality of the cleaned products in Figure 5.7A and 5.7B made examining their core-shell architectures an exciting prospect. Similarly to the syntheses in Chapter 3, a ZnS shell was grown on the surface by the gradual introduction of zinc (undecylenate)$_2$ and TOP-S precursors. After 20 min of core growth, 1 mL of 2.2 M TOP-S was added to the reaction at a rate of 0.1 mL/min. For cores grown at higher temperatures, the solution was cooled to below 200 °C before the injection of TOP-S. The reaction was then stirred at 180 °C for 1 h before the careful introduction of 4 g zinc (undecylenate)$_2$ in 6 mL of an ODE/TOP solution. The reaction was set to 260 °C and an additional 1 mL TOP-S was slowly introduced as the temperature increased. The high temperature was maintained until the total reaction time reached 4 h and was then quickly cooled to room temperature. The core/shell nanoparticles were cleaned with toluene/ethanol precipitation and redispersed in toluene for analysis.

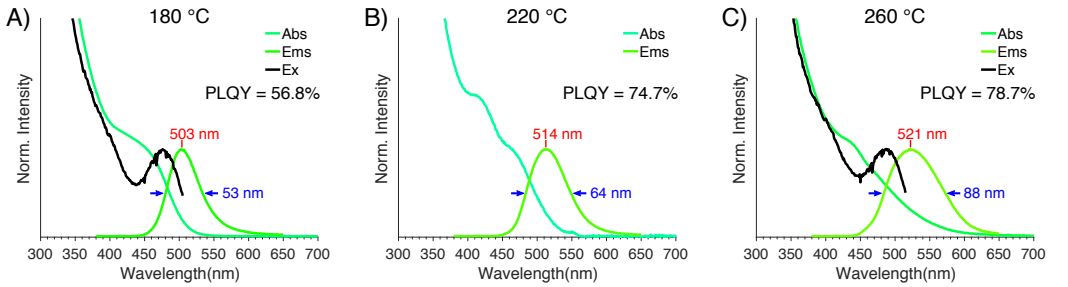

FIGURE 5.8: Absorption, emission, and excitation spectra several batches of cleaned InP/ZnS materials made with 3 CTAB and 5 $ZnBr_2$ at various core growth temperatures. Emission maxima (red text) and FHWM (blue text) are indicated along with the PLQY of each material.

The spectroscopic data made available in Figure 5.8 shows the interesting double peaks of the core materials carry through to the shelled nanoparticles. While

this results in broadening of the absorption features, the excitation spectra show that of the two features, the one highest in energy is not correlated with the sample emission. Instead, the lowest energy features of each excitation spectrum are much more well-defined than their absorption peaks. The positions of these peaks are typically associated with different exciton binding energies, which are dependent on the nanocrystal size. The narrow features of these excitation spectra then strongly suggest tight distributions of sizes in these materials, which would not be assumed from their broad absorption spectra.

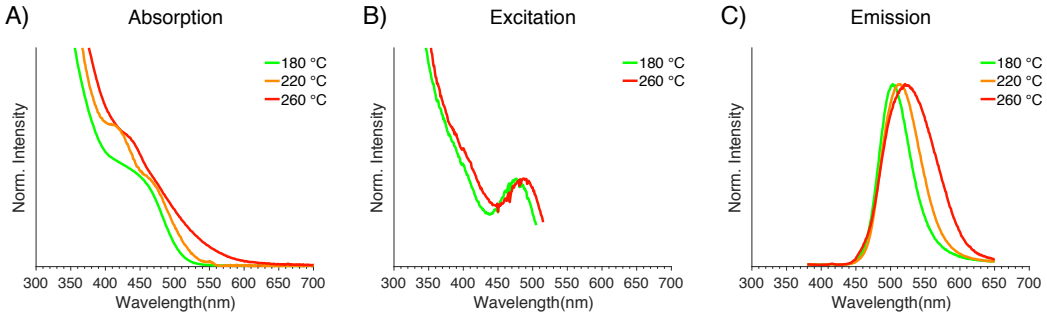

FIGURE 5.9: Normalized A) Absorption, B) Excitation, and C) Emission spectra of cleaned InP/ZnS materials made with 3 CTAB and 5 $ZnBr_2$ at various core growth temperatures. Spectra are identical to those from Figure 5.8 but recolored for clarity.

Despite the large increase in reaction temperature, the mean sizes of the nanoparticles did not appear to shift much between the reactions. When the spectra are overlaid as in Figure 5.9, it is much more obvious that the excitation and emission peak maxima did not increase significantly between 180 °C and 260 °C. Instead, the majority of the differences between the samples are related to an increase in the low energy emission as the growth temperature increased. An ideal emission spectrum would be perfectly symmetrical and Gaussian. Typically, however, additional contributions such as crystal defects, imperfect ligand passivation, and competitive exciton pathways result in energy losses that broaden the red side of the emission profile.

The small shift in excitation maxima then suggests that changes in particle sizes are not responsible for the differences in emission profiles. Instead, an increase in the number of crystal defects or the addition of another radiative pathway are options that are more likely to be tied to the increase in low energy emission seen in Figure 5.9C. While defects are more common to nanoparticles, defect-rich particles tend to have emission profiles with long low energy tails[†]. Because the spectra quickly return to their baselines in Figure 5.9C, another mechanism is likely responsible for this spectral broadening, but precisely identifying it is outside the bounds of this work.

Although larger emission FWHM and broad UV-Vis absorption spectra are not desirable, the increase in core growth temperature did raise the PLQY of the core/shell

[†]Typical examples of defect emission can be seen in the ZnI_2 traces of Figures 3.19 and 3.20

particles. Both the 220 °C and 260 °C syntheses showed that >70% of photons absorbed by the system were reemitted as visible light. This level of efficiency may be beneficial for research that prefers broad absorption or emission profiles such as the fields of photovoltaics or solar concentrators. As the 260 °C synthesis may be too broad, the 220 °C synthesis offers a good compromise between PLQY and spectral purity.

5.3 Using 1-Octadecene

Implementing 1-octadecene has led to consistent improvements in size distributions, emission profiles, and PLQY in these aminophosphine syntheses. While some reasoning for this has already been offered in the published work of Chapter 3, the use of zinc halides and myristic acid obscured the effect of ODE. Although these components were necessary to produce quality materials, a more systemic study is presented here to understand some of the many factors of these reactions. The following is a brief synthesis for the spectra in Figure 5.10A–F)

For oleylamine-based reactions, the 1-pot method was used with 5 mL of oleylamine and A) 0.45 mmol $InCl_3$ or D) 0.45 mmol $InCl_3$ and 2.25 mmol $ZnCl_2$. Each solution was then subjected to a 1 h degas, transition to inert atmosphere, and increase to 180 °C. The injection of 1.6 mmol $P(DEA)_3$ then instigated nanoparticle growth. For the octadecene-based reactions, a 2-pot method was used were the indium and phosphorus solutions were prepared separately. In B) and E), the indium solutions were prepared by combining 0.45 mmol $InCl_3$ and 1.35 mmol oleylamine in 10 mL ODE. In C) and F), the indium solutions were prepared by combining 0.45 mmol $InCl_3$, 0.45 mmol myristic acid (MA), and 0.90 mmol oleylamine in 10 mL ODE. These solutions were degassed for 1 h, transitioned to inert atmosphere, and increased to 180 °C. Simultaneously, a phosphorus solution was prepared with either 3 mL oleylamine in B) and C) or 2.25 mmol $ZnCl_2$ in 3 mL oleylamine in E) and F). These were then degassed for 30 min and put under inert atmosphere before being injected with 1.6 mmol $P(DEA)_3$. This phosphorus solution was allowed to stir for 30 min before increasing the temperature to 150 °C, adding 1 mL ODE, and loading the solution into a glass syringe. This phosphorus (or zinc-phosphorus) solution was then injected into their respective indium solutions to instigate nanoparticle growth. Aliquots of all solutions were then taken over time and final solutions were cleaned with toluene/ethanol precipitation. All samples were monitored with UV-Vis absorption spectroscopy as usual. Full synthetic details are available in Section 5.5.

Although ODE should not directly interact with these precursors, it can allow for some degree of ligand control. In the literature aminophosphine syntheses, such as with Figure 5.10A, using oleylamine as both ligand and solvent means there is always an excess of capping agent in solution. When this is restricted in the 2-pot reaction of Figure 5.10B, a systemic blue-shift in absorption features can be seen. This

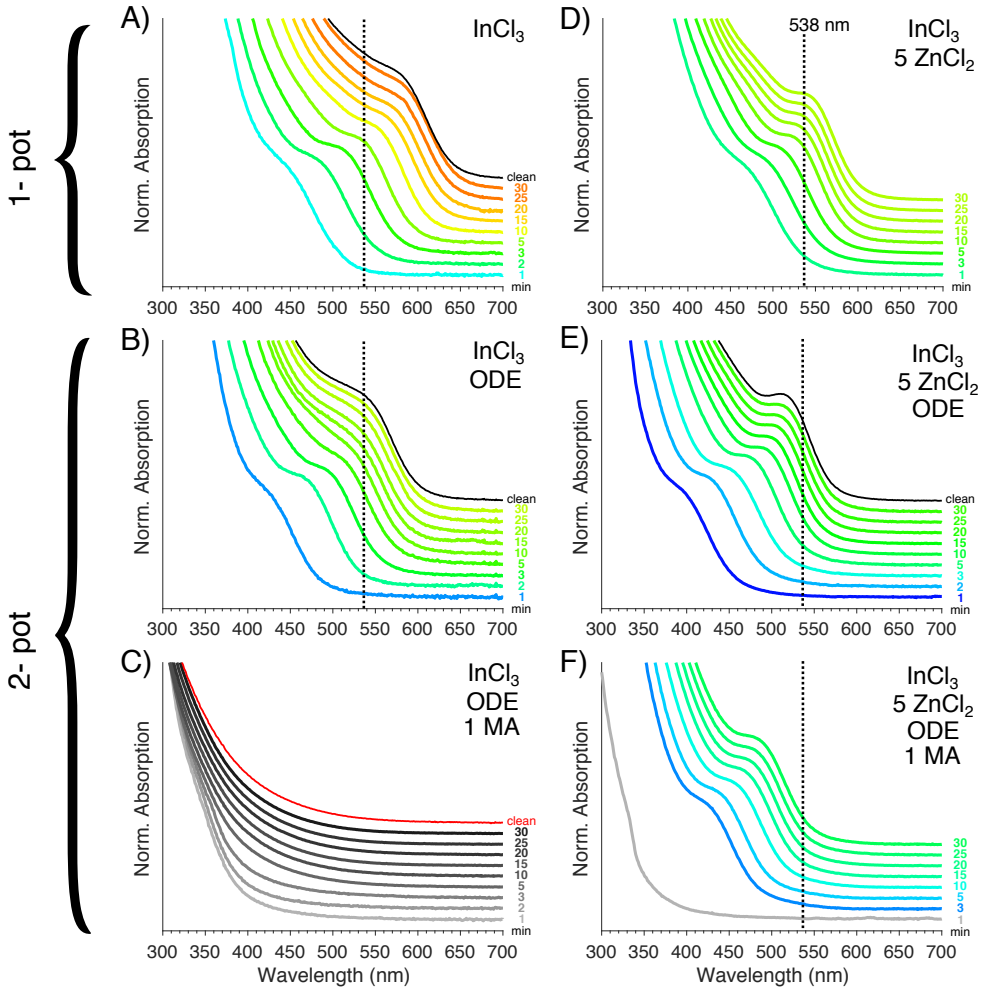

FIGURE 5.10: UV-Vis absorption traces of InP cores over time with A) 1-pot $InCl_3$, B) 2-pot $InCl_3$, C) 2-pot $InCl_3$ and 1 MA. These are compared to the same reactions with the addition of 5 $ZnCl_2$ in D)–E), respectively.

phenomenon is expected, as literature has noted several times that excess ligands generally lead to larger particles. Figures 5.10A and B then outline the maximum and minimum sizes that can be expected by adjusting ligand concentration, as they represent the 1:33 and 1:3 indium-oleylamine ratios, respectively.

Examining the peak maxima of the traces in Figures 5.10A and B also show a steady red-shift over time. A broadening in absorption features accompanies these increases in mean size, which suggests the sample polydispersities are increasing. This effect is compounded by a slight blue-shift when comparing the cleaned samples to the traces at $t = 30$ min, which indicates that the minimal precipitation removed some larger, bulk-like species from the solutions. All of these observations are consistent with ripening-based growth, which is typical as $t \to \infty$ for most nanoparticle syntheses.

With that in mind, Figures 5.10D and E are then atypical as they mostly maintain a constant peak size and shape for $t > 15$ min. This is similar to results seen throughout this thesis with ZnX_2 are involved, but the comparison to 5.10A and B

should highlight how unusual it is. The consistency of this effect across many reaction designs and mechanisms suggests that ZnX_2 may be capping these quantum dots as they reach the midpoint of the reactions. While this could limit their ability to ripen and would preserve size distributions as seen here, proving this is notoriously difficult and would at least require solid-state ^{31}P-NMR spectroscopy to verify.

Comparing the $ZnCl_2$ reactions of Figure 5.10D and E to each other shows again a blue-shift when reducing the concentration of oleylamine. Notably, however, the early times of Figure 5.10D show a red-shift when compared to Figure 5.10A. This is contrary to the 2-pot reactions, which show a blue shift for their initial aliquots, and is more consistent with the logic of decreased ligand yields smaller sizes.

The larger nuclei in $t = 1$ of Figure 5.10D may instead be a factor of an artificially decreased phosphorus concentration. While total phosphorus concentrations are the same in each reaction, the synthesis in Figure 5.10D is the only one with the potential to form two different phosphorus species. Recalling the discussions from the DFT calculations, $P(NEt_2)_3$ could form either $P(NHR)_3$ or Zn-$P(NHR)_3$ in a solution containing both oleylamine and zinc halides. As these have significantly different reactivities, a portion of the phosphorus population will not be available to generate particles, regardless of which species is responsible for forming them. This division of resources could yield an apparent low initial concentration of reactive phosphorus, which would result in fewer nuclei, and therefore larger particles when the remaining phosphorus is consumed.[7, 8]

Figure 5.10F is similar to Figure 5.10E in that they have the same total concentration of ligands, but one third of those in the ODE-1MA synthesis are stronger. Interestingly, we know from Figure 3.19 that even if all 3 eq. are myristic acid, a similar equilibrium size is reached, which suggests that the final sizes are more dependent on surface energies than kinetics. This supposition also matches the zinc-capping hypothesis as well as the dependence halide concentration. However, attempts to manipulate this further by varying the ligand chain length or binding moiety have not been met with any success.

Finally, the ODE-1MA control without zinc in Figure 5.10C shows that no particles can be grown in this reaction. The lack of absorption features or precipitate implies that no nucleation occurred, not even unstable particles that aggregated to bulk. Instead, the presence of a small number of fatty acid ligands appeared to be enough to interfere with the reaction, likely by preventing the In$\cdots$P ligand exchange from occurring. Because this is not the case in Figure 5.10F, it can be determined that the activation by zinc is responsible for strengthening the aminophosphine and allowing it to form an In–P bond. In the reactions without myristic acid, the ligands are likely weak enough to be displaced by the aminophosphine on its own and allow the disproportionation to instigate nucleation.

5.4 Conclusions

Several new syntheses with aminophosphines were designed to control halide concentrations. Using oleylammonium halides were found to be interesting for their ability to convert useless $In(OAc)_3$ precursors into reactive $InCl_3$ species. When present in extreme excess, they were also found to switch particle growth to a more rapid, H_3P-like syntheses. This spike in nucleation and growth is likely due to the excess RNH_4^+ species, which could convert $P(NEt_2)_3$ into a more reactive precursor than $P(NHR)_3$. Unfortunately, identifying this mechanism is dependent on producing RNH_4Cl *ex situ*, which was found to be extremely time consuming and low yielding.

To avoid this challenging preparation, oleylammonium halides were generated *in situ* instead. Although these syntheses could approximate the mean particle sizes from the *ex situ* preparations, they were shown to be limited in their ability to produce particles outside of a 1 In : 3 Cl^- regime. Additionally, controls with acetic acid showed that oleylamine is quite capable of forming an RNH_4OAc adduct as well as it forms RNH_4Cl. This complication implies that any acetate ions introduced to the solution could negatively impact the reaction. While this could be avoided by using $InCl_3$ as the indium source, the presence of ethanol and water could both similarly form adducts with the excess oleylamine solvent and affect the synthesis. Until this problem can be eliminated, further work with oleylammonium halides would be suspect, as proving the origin of spectral differences would be near impossible.

Commercial cetyltrimethylammonium halides were then used to circumvent both of these problems. However, introducing the strong $RNMe_3^+$ cation was systemically found to produce very small InP cores. While this made comparisons to previous syntheses difficult, it does allow for unique sizes to be accessed. Interestingly, both core and core/shell materials made in this manner appeared invariant to temperature, which is highly unusual for quantum dot syntheses. While the absorption profiles broadened from the presence of non-emissive states, the excitation spectra showed narrow excitonic features suggesting tight particle size distributions. The use of an elevated temperature then allowed for PLQY >70% to be produced.

These emission yields are the best values reported in this thesis and the use of a 2 hr degassing time may account for a portion of the improvements. Due to the high humidity ubiquitous to New Zealand indoor environments, the use of hygroscopic precursors frequently present problems with water contamination. The first year of synthesis was plagued by these issues when previously good reaction schemes suddenly only produced materials with <30% PLQY. After a barrage of controls, it was determined that ambient moisture was the issue and that greater care needed to be taken to keep the desiccators with the halides in inert atmosphere and with fresh desiccant. While this saw a routine increase in PLQY, achieving >50% was still difficult. Thus, the syntheses of Chapter 3 became publication-worthy when this barrier was overcome.

The more recent revelation from Figure 5.6 then highlighted the importance of having a long degassing stage when moisture is a problem. The work of this Chapter showed that routine >50% PLQY is possible, so this has now become a standard pre-reaction phase in order to maximize results for all materials. Since this implementation, several standard reactions such as 1-pot $InCl_3/ZnCl_2$ in oleylamine have demonstrated 50-55% PLQY, where previously it produced a maximum of 39% (Figure 3.18A). However, this effect seems to be particularly useful in non-coordinating solvents, as a 2-pot ODE-1MA $InCl_3/ZnBr_2$ synthesis (like Figure 3.20) produced materials with PLQY = 84%. This significant improvement is likely due to the inability of water to form an adduct such as RNH_4OH, so much more is removed during the extended vacuum heating. Unfortunately, there was not the time to uniformly apply this change to affect all of the results in this thesis, so the data from the other Chapters are left with their 1 hour vacuum times for consistency.

5.5 Experimental Details

List of Chemicals Indium chloride (Sigma-Aldrich, anhydrous 99.999%), zinc chloride (Sigma-Aldrich, anhydrous 97%), zinc bromide (Sigma-Aldrich, anhydrous 98%), and zinc iodide (Sigma-Aldrich, 98%) were stored in a common desiccator under inert atmosphere. Tris-(diethylamino) phosphine (Sigma-Aldrich, 97%) and trioctylphosphine (Sigma-Aldrich, 97%) were stored under nitrogen with septa and accessed with Schlenk techniques. Oleylamine (Acros Orgamics, 80-90%), 1-octadecene (Sigma-Aldrich, 90%), myristic acid (Merck, 98%), zinc undecylenate (Merck), sulfur (BDA, sublimed), hydrochloric acid (PureScience, 37%), glacial acetic acid, (Fisher, geq99.7%), toluene (ROMIL, 99.9%), and ethanol (Fisher, 99.99%) were used as received and stored under ambient conditions.

Preparation of oleylammonium halides

Oleylammonium halides were prepared according to a literature procedure.[2] 100 mL ethanol and 12.5 mL (0.038 mol) of oleylamine were combined in a 250 mL 2-neck flask and vigorously stirred. The reaction mixture was cooled in an ice-water bath and HX (0.076 mol, HCl $\geq$37% or HBr 48%) was added. The reaction mixture was left to react overnight under N_2 flow. Then the solid was collected with vacuum filtration and the obtained product was purified by rinsing multiple times with diethylether. The product was left under vacuum overnight resulting in a white powder.

Standard 1-pot synthesis of $InCl_3$ InP cores (Figures 5.1A and 5.10A)

Nanoparticles were synthesized using a modification of literature methods.[9] Typically, 100 mg (0.45 mmol) $InCl_3$ and 5.0 mL (15 mmol) of oleylamine were degassed at 120 °C under vacuum for 1 hour before flushed with nitrogen atmosphere and heated to 180 °C. 0.45 mL (1.6 mmol) tris(diethylamino)phosphine was injected and allowed to stir for 30 minutes before rapidly cooling to 70 °C.

Standard 1-pot synthesis of $InCl_3$–$ZnCl_2$ InP cores (Figures 5.1C and 5.10D)

Nanoparticles were synthesized using a modification of literature methods.[9] Typically, 100 mg (0.45 mmol) $InCl_3$, 300 mg (2.2 mmol) $ZnCl_2$, and 5.0 mL (15 mmol) of oleylamine were degassed at 120 °C under vacuum for 1 hour before flushed with nitrogen atmosphere and heated to 180 °C. 0.45 mL (1.6 mmol) tris(diethylamino)phosphine was injected and allowed to stir for 30 minutes before rapidly cooling to 70 °C.

1-pot synthesis of InP cores with 3 or 13 OAmCl *ex situ* (Figures 5.1B and D)

Typically, 131 mg (0.45 mmol) $In(OAc)_3$, 410 mg (1.35 mmol) or 1.78 g (5.85 mmol) OAmCl, and 4.5 or 3.1 mL of oleylamine were degassed at 120 °C under vacuum for 1 hour before flushed with nitrogen atmosphere and heated to 180 °C. 0.45 mL (1.6 mmol) tris(diethylamino)phosphine was injected and allowed to stir for 30 minutes before rapidly cooling to 70 °C.

1-pot synthesis of InP cores with $3-6$ OAmCl *in situ*(Figures 5.2B –E)

Typically, $0.113-0.226$ mL 37% HCl was added to 1 mL ethanol and swirled to mix. This was added to 5 mL oleylamine and allowed to stir for 1 hr. Then 131 mg

(0.45 mmol) $In(OAc)_3$ was added and the solution was degassed at 120 °C under vacuum for 2 hours before flushed with nitrogen atmosphere and heated to 180 °C. 0.45 mL (1.6 mmol) tris(diethylamino)phosphine was injected and allowed to stir for 30 minutes before rapidly cooling to 70 °C.

1-pot synthesis of InP cores with 5 OAmCl *in situ* and 1 $Zn(OAc)_2$(Figure 5.2F)

Typically, 0.188 mL 37% HCl was added to 1 mL ethanol and swirled to mix. This was added to 5 mL oleylamine and allowed to stir for 1 hr. Then 131 mg (0.45 mmol) $In(OAc)_3$ and 98.8 mg $Zn(OAc)_2 \cdot 2\ H_2O$ were added and the solution was degassed at 120 °C under vacuum for 2 hours before flushed with nitrogen atmosphere and heated to 180 °C. 0.45 mL (1.6 mmol) tris(diethylamino)phosphine was injected and allowed to stir for 30 minutes before rapidly cooling to 70 °C.

1-pot synthesis of InP cores with 3 OAmOAc *in situ*(Figure 5.3)

0.077 mL glacial acetic acid was added to 1 mL ethanol and swirled to mix. This was added to 5 mL oleylamine and allowed to stir for 1 hr. Then 100 mg (0.45 mmol) $InCl_3$ was added and the solution was degassed at 120 °C under vacuum for 2 hours before flushed with nitrogen atmosphere and heated to 180 °C. 0.45 mL (1.6 mmol) tris(diethylamino)phosphine was injected and allowed to stir for 30 minutes before rapidly cooling to 70 °C.

1-pot synthesis of InP cores with 3 CTAC or CTAB (Figures 5.5A–D)

Typically, 131 mg (0.45 mmol) $In(OAc)_3$ and 420 mg CTAC or 492 mg CTAB (1.35 mmol) were combined in 5 mL of oleylamine and degassed at 120 °C under vacuum for 1 hour before flushed with nitrogen atmosphere and heated to 180 °C. 0.45 mL (1.6 mmol) tris(diethylamino)phosphine was injected and allowed to stir for 30 minutes before rapidly cooling to 70 °C. For synthesis with ZnX_2, 300 mg $ZnCl_2$ or 495 mg $ZnBr_2$ were added in the beginning as well.

Temperature dependent 1-pot synthesis of InP cores with 3 CTAB and 5 $ZnBr_2$ (Figures 5.7A–C)

Typically, 131 mg (0.45 mmol) $In(OAc)_3$, 492 mg CTAB (1.35 mmol), and 495 mg $ZnBr_2$ were combined in 5 mL of oleylamine and degassed at 120 °C under vacuum for 2 hour before flushed with nitrogen atmosphere and heated to 180, 220, or 260 °C. 0.45 mL (1.6 mmol) tris(diethylamino)phosphine was injected and allowed to stir for 30 minutes before rapidly cooling to 70 °C.

Temperature dependent 1-pot synthesis of InP/ZnS materials with 3 CTAB and 5 $ZnBr_2$ (Figures 5.8A–C)

A modified literature method was used to grow a shell of zinc sulfide in situ.[9, 10] The core syntheses were carried out as above, however after 20 minutes of core growth, 1 mL saturated TOP-S (2.2 M) was slowly injected into the reaction solution. At 120 minutes, 2.55 g of zinc $(undecylenate)_2$ in 1.5 mL TOP and 4.5 mL ODE was slowly injected. After, the temperature was set to 260 °C and a further 1 mL 2.2 M TOP-S was slowly injected as it heated. At 240 minutes, the reaction was rapidly cooled to 70 °C.

2-pot synthesis of InP cores in ODE (no MA) (Figures 5.10B and E)

100 mg (0.45 mmol) $InCl_3$, 0.45 mL (1.35 mmol) oleylamine, and 10.0 mL (31 mmol) of 1-octadecene (ODE) were degassed at 120 °C under vacuum for 1 hr before being put under nitrogen atmosphere and raised to 180 °C. Separately, 3 mL oleylamine or 2.2 mmol of zinc halide and 3 mL oleylamine were degassed at 120 °C under vacuum for 30 min. The zinc solution was put under nitrogen atmosphere and the temperature increased to 150 °C. 0.45 mL (1.6 mmol) tris(diethylamino)phosphine was injected and the solution was stirred for 30 minutes. 1.0 mL (3.1 mmol) of additional ODE was introduced and briefly allowed to mix before loading the zinc-phosphorus solution into a syringe and quickly injecting into the hot In-ODE solution. The reaction was allowed to react for 30 minutes before rapidly cooling to 70 °C.

2-pot synthesis of ODE-1MA InP cores (Figures 5.10C and F)

100 mg (0.45 mmol) $InCl_3$, 0.3 mL (0.9 mmol) oleylamine, 113 mg (0.45 mmol) myristic acid, and 10.0 mL (31 mmol) of 1-octadecene (ODE) were degassed at 120 °C under vacuum for 1 hr before being put under nitrogen atmosphere and raised to 180 °C. Separately, 3 mL oleylamine or 2.2 mmol of zinc halide and 3 mL oleylamine were degassed at 120 °C under vacuum for 30 min. The zinc solution was put under nitrogen atmosphere and the temperature increased to 150 °C. 0.45 mL (1.6 mmol) tris(diethylamino)phosphine was injected and the solution was stirred for 30 minutes. 1.0 mL (3.1 mmol) of additional ODE was introduced and briefly allowed to mix before loading the zinc-phosphorus solution into a syringe and quickly injecting into the hot In-ODE solution. The reaction was allowed to react for 30 minutes before rapidly cooling to 70 °C.

Sample cleaning and analysis

$\sim$0.1 mL aliquots were removed at various times and quenched in $\sim$0.5 mL toluene before centrifugation and UV-Vis analysis. The reaction solution was diluted with toluene and centrifuged (5 min, 10,000 rpm) to separate any solid precipitate. The supernatant was cleaned once with toluene/ethanol precipitation and centrifugation (10 min, 10,000 rpm). The resulting nanoparticle precipitate was dispersed in toluene for further analysis. Sample absorption and emission spectroscopy were analyzed with the same methods and equipment in Section 3.5.

Bibliography

[1] D. Zhang, Y. Yang, Y. Bekenstein, Y. Yu, N. A. Gibson, A. B. Wong, S. W. Eaton, N. Kornienko, Q. Kong, M. Lai, A. P. Alivisatos, S. R. Leone, and P. Yang, "Synthesis of Composition Tunable and Highly Luminescent Cesium Lead Halide Nanowires through Anion-Exchange Reactions," *Journal of the American Chemical Society*, vol. 138, no. 23, pp. 7236–7239, 2016.

[2] G. Nedelcu, L. Protesescu, S. Yakunin, M. I. Bodnarchuk, M. J. Grotevent, and M. V. Kovalenko, "Fast Anion-Exchange in Highly Luminescent Nanocrystals of Cesium Lead Halide Perovskites ($CsPbX_3$, X = Cl, Br, I)," *Nano Letters*, vol. 15, no. 8, pp. 5635–5640, 2015.

[3] L. Xie, Q. Zhao, K. F. Jensen, and H. J. Kulik, "Direct Observation of Early-Stage Quantum Dot Growth Mechanisms with High-Temperature Ab Initio Molecular Dynamics," *The Journal of Physical Chemistry C*, vol. 120, no. 4, pp. 2472–2483, 2016.

[4] M. R. Dewi, G. Laufersky, and T. Nann, "A highly efficient ligand exchange reaction on gold nanoparticles: preserving their size, shape and colloidal stability," *RSC Advances*, vol. 4, no. 64, pp. 34217–34220, 2014.

[5] W. Silke and F. Claus, "Microemulsions: Options To Expand the Synthesis of Inorganic Nanoparticles," *Angewandte Chemie International Edition*, vol. 55, no. 51, pp. 15728–15752, 2016.

[6] M. B. Yue, W. Q. Jiao, Y. M. Wang, and M.-Y. He, "CTAB-directed synthesis of mesoporous γ-alumina promoted by hydroxy polyacids," *Microporous and Mesoporous Materials*, vol. 132, no. 1, pp. 226–231, 2010.

[7] S. Abe, R. K. Čapek, B. De Geyter, and Z. Hens, "Tuning the Postfocused Size of Colloidal Nanocrystals by the Reaction Rate: From Theory to Application," *ACS Nano*, vol. 6, no. 1, pp. 42–53, 2012.

[8] C. R. Bullen and P. Mulvaney, "Nucleation and Growth Kinetics of CdSe Nanocrystals in Octadecene," *Nano Letters*, vol. 4, no. 12, pp. 2303–2307, 2004.

[9] M. D. Tessier, D. Dupont, K. De Nolf, J. De Roo, and Z. Hens, "Economic and Size-Tunable Synthesis of InP/ZnE (E = S, Se) Colloidal Quantum Dots," *Chemistry of Materials*, vol. 27, no. 13, pp. 4893–4898, 2015.

[10] V. Chandrasekaran, M. D. Tessier, D. Dupont, P. Geiregat, Z. Hens, and E. Brainis, "Nearly Blinking-Free, High-Purity Single-Photon Emission by Colloidal InP/ZnSe Quantum Dots," *Nano Letters*, 2017.

Chapter 6

Conclusions

The insatiable desire for nanomaterials in today's day and age has spurred countless research endeavors into understanding how they are formed and designing better ways of producing them. With more and more of these nanotechnologies ending up in the hands of the public, there is a similarly increasing need for safer, less-toxic methods and materials that accomplish the same results. For decades, indium phosphide has stood poised to supplant the more popular Cd- and Pb-based nanoparticles as the chief quantum dot material, but the reliance of syntheses on TMS_3P presents a technical and safety barrier that is difficult to overcome. Aminophosphines then present safer to make and easier alternatives for InP QDs, but they are not easily controlled due to the lack of understanding of their mechanism.

This thesis strove to shine a light on the conversion of aminophosphines and to produce indium phosphide materials in a more accessible, safer way. The interplay between theory and experiment was a huge driving force for this work, as no Chapter was without inspiration or motivation from material presented in another. Being able to concertedly probe both fields to understand the dynamics of this aminophosphine reaction has fostered a greater knowledge than either could produce independently. This Chapter highlights what this thesis contributed to the field and identifies some of the problems, old and new, that deserve to be explored in the future.

6.1 Mechanistic Matters

Identifying the prevalence of zinc in the indium-aminophosphine reaction mechanism is undoubtedly the keystone of this work. While other groups have shown similar effects of zinc salts on TMS_3P,[1] our publication[2] was the first to suggest it occurs with these $P(NR_2)_3$ precursors as well. The interaction was broken down into stages of activation by zinc, indium ligand exchange, and aminophosphine disproportionation, with a logical progression throughout. Although the final phosphorus-phosphorus redox reaction presented high energetic barriers, it was by far the most likely interaction examined in this work. While the inclusion of zinc did not overtly alter any of the processes, its presence significantly stabilized both the transition states and products of each reaction. Without it, the reactions have large, positive ΔG that result in poor equilibria.

This three-step mechanism was expanded in Chapter 4 by describing the differences that larger halides imposed on the various structures and their energies in this reaction. While the impact on the $\Delta G_g^{\ddagger}$ of the ligand exchanges was varied, the disproportionations displayed a systemic increase in activation energy when the bromides or iodides were used. This relationship appeared to be strongly impacted by the interplay of the Zn-P-P distances and also appeared to have influence regardless if InX_3 or ZnX_2 were adjusted in the calculations.

The ΔG_g of the activated disproportionation products had some interesting deviations but were all very stable (< -3.00 kcal/mol) regardless of their halide content.

Instead, the ligand exchange may be the most responsible for the various differences in quality seen with the choice in precursor salts. In Figure 4.15, it can be clearly seen that the free energies of the $\mathbf{9_{II}}$ geometries are very good for the bromides and very bad for the iodides, which trends well with our knowledge of size distributions, PLQY, and defects in these systems. As this reaction has to occur before the disproportionation, its degree of stability for a given precursor set is highly suggestive as a reason for final particle quality.

6.2 Synthetic Summary

As evident from Chapter 3, the identification of this mechanism led directly to advances in nanoparticle synthesis. Specifically, the development of Equation 3.3 helped to explain why a 2-pot oleylamine synthesis was worse than the 1-pot reaction and inspired solutions to solve the issue. This analysis then led to the introduction of ODE and fatty acid ligands to these syntheses, which greatly improved PLQY and allowed new, smaller sizes of materials to be accessed. The development of a 2-pot method also went further to support the zinc-based mechanism, as comparing the syntheses of Figure 5.10C and F show that in some cases, a zinc-aminophosphine interaction is explicitly necessary to grow InP nanoparticles.

Together, the spectra of Figure 5.10 did much to identify the contributions of the various components in the 2-pot syntheses. What is more interesting from a practical view, however, is that they also expanded the list of accessible, quality nanoparticle sizes that can be produced. Although the aminophosphine syntheses were previously restricted to four sizes, applying the various combinations of precursors to the setups in Figures 5.10D–F yields a dozen total permutations.[†] While this is still not a continuously tunable system, increasing the available choices can be an effective mimic in the interim.

In order to address the issue of tunability, several sources of compatible halides were implemented to adjust the $[X^-]$ in the reactions. Despite its issues in preparation, the use of oleylammonium chloride with indium acetate was revealed to be a suitable replacement for $InCl_3$. Additionally, the large excess of OAmCl in solution was found to significantly impact the behaviors of the precursors and produced particles. The evidence in Figure 5.1 points to the presence of a much more reactive phosphine species than $P(NHR)_3$, but this conclusion will be difficult to prove, and even more difficult to exploit.

The OAmCl syntheses were made more useful by preparing the adduct *in situ*. These reactions were found to behave similarly to those using the pre-made compound but avoided the hassle of its isolation. Unfortunately, these methods also produced several new complications by exposing the solutions to water and ethanol.

[†]The syntheses with InI_3 and ZnI_2 are left out as the former is not accessible (cheap) while the latter is not quality (narrow emission, good PLQY). If they are included, the permutations increase from 9 before this thesis to 27 after.

An indication of trace acetate anions also meant more synthetic control was needed before pursuing this work further.

Finally, cetyltrimethylammonium halides were introduced to combat the problems of both uses of OAmCl. While they were able to produce interesting core sizes, the emissions of their InP/ZnS structures were unable to be tuned by either concentration or temperature. However, at the expense of linewidth broadening, the PLQY were able to be improved to >70% with elevated temperatures. Therefore, this could indicate a route towards more preserved particle sizes during the high-temperature shelling and annealing steps that are often necessary for emission in InP-based products.

6.3 Future Work

As with most multi-year efforts, this thesis produced many unanswered questions in pursuit of its original goals. While forming an exhaustive list of topics is likely impossible, this section presents some preliminary areas of investigation directly related to the work of the previous chapters. Perhaps unsurprisingly at this point, subjects relating to both experiment and computation have some interesting aspects of discussion and will be addressed below.

6.3.1 Experimental Prospects

There still exists a desire to tune the products of these aminophosphine reactions by one easily controllable handle. While many paths towards this have been explored in this work, the best that could be achieved was increasing the number of discrete sizes that can be produced. Although the zinc-free reactions have poorer size distributions, they do appear to have continuously growing particles. If zinc salts or some other capping agent could be added midway through such a synthesis, they may be able to trap and refine sizes other than the equilibrium ones presented here.

In order to remove the effects of contaminants from the OAmCl reactions, the solvent could be changed to something non-coordinating like ODE. This alteration should reduce the ability of water or ethanol to form an adduct with oleylamine and improve the quality of those syntheses. However, this solvent comes with its own problems, as neither $InCl_3$ nor $In(OAc)_3$ are soluble in ODE on their own. Therefore, ligands need to be added that will help to disperse the indium salts while not allowing the contaminants the ability to coordinate. Tertiary amines such as trioctylamine may be the best suited, but even these will likely change the particle growth as its ability to bind to InP surfaces is different from oleylamine. In any case, a large number of controls need to be performed to ensure the full removal of water, ethanol, and acetate ions from the solution.

Similarly, new halide sources may help this tunability as well as be a better probe for affecting halide concentrations. Compounds such as TMS-Cl and other organic

sources of halides may offer more control over [X^-], but they usually require glove-box conditions or significant synthesis to be produced. Both of these requirements make them challenging to use in general but are particularly detrimental for any large scale applications.

The evolution of the position and shape of absorption characteristics have been used throughout this work as a stand-in for particle size and size distributions. As such, loose arguments about reaction kinetics have also been made based on how these change for different reactions. However, rigorous kinetic data is necessary to more accurately describe these and to make stronger correlations to the calculated rates of reaction. Unfortunately, the studies required for this information are notoriously challenging for nanoparticle syntheses. Identifying the rate of precursor consumption, the total number of particles, and the size of the particles over time are all necessary to paint a clear picture of the reaction events, and not one of those is remotely easy for InP syntheses.

6.3.2 Theoretical Avenues

One of the reasons kinetic information would be useful is to help pinpoint the limiting process in these systems. A case in point is that the change in disproportionation $\Delta G_g^{\ddagger}$ of the zinc-activate structures trends in the opposite direction one would expect for it to be the determining factor. From Figure 6.1A it can be seen that if the rate of nucleation is dependent on the rate of disproportionation, it should reduce in the order $InCl_3$ > $InBr_3$ > InI_3 > $ZnBr_2$ > ZnI_2, which would then result in particles with larger sizes moving from left to right in that list. Instead, examining Figure 6.1B and C shows that list order is correlated with decreasing particle size if emission peak maxima can be roughly correlated to particle volume.

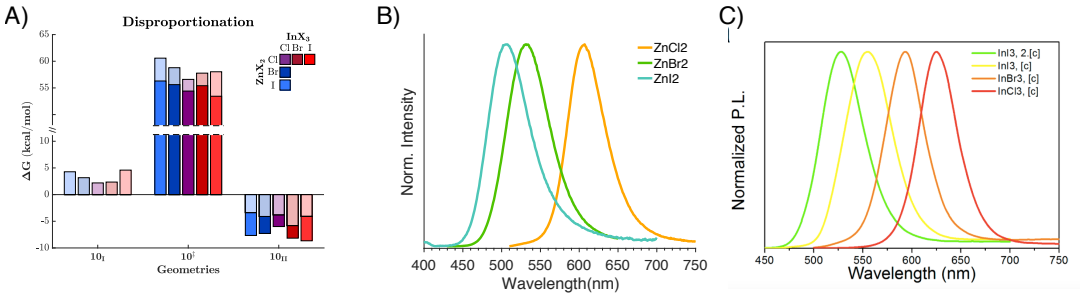

FIGURE 6.1: A comparison of the A) free energy of the disproportonation reaction from Figure 4.15, B) emission of InP/ZnS particles from syntheses with different ZnX_2 from Figure 3.18A, and C) emission of InP/ZnS particles from syntheses with different InX_3, awhich was adapted with permission from Tessier *et al.*[3] Copyright 2015 American Chemical Society.

A reason for this contradiction could be that the disproportionation mechanism is wrong. A disadvantage of time-independent calculations is that they are highly impacted by what input is used. Despite the large number of controls that have been run for the calculations presented in this work, the strongest conclusion that can be made is "for the structures examined, the proposed mechanism is the most likely."

Therefore, there may exist another reaction pathway that has more realistic $\Delta G_g^{\ddagger}$ and does not follow the trends observed in Chapters 3 or 4.

However, there is much higher confidence in the likelihood of the $\mathbf{9_{II}}$ structures existing, as the activation and ligand exchange processes are much less tenuous. Because most of the differences in energies could be tied to the In–X or Zn–P interactions, the trends of the disproportionation are not likely to change. The ease of the electron transfer may be increased by excess solvent molecules or by partially reduced phosphines, but the effect each metal halide salt has on the reaction should still be proportionally similar.

A way to investigate the precursor interactions without relying on specific input geometries is to use a computational method that observes compounds over time. *Ab initio* molecular dynamics is a technique that calculates the energies and structures of molecules, but uses the force information to build trajectories of the atoms instead of finding a minimum. By iteratively calculating energy then using the trajectory to find a new geometry, this process can offer a way to examine snapshots of a simulated reaction and can provide evidence for mechanisms. A paper using this technique was able to show, for example, that instead of $In(OAc)_3$ and TMS_3P precursors reacting to form InP monomers, they preferred to form In_4P-based clusters first.[4] While this is a potentially powerful tool, it has its own set of limitations such as the number and frequency of the "frames" during which information is collected. If the data is not sampled frequently enough or if the interaction takes a long time to occur, then a similar needle-in-a-haystack search can occur.

If the reduction mechanism proposed in this thesis is not wrong, then another reason for the contradiction could be that these precursors do not obey traditional nucleation and growth mechanics. The calculations and experiments only disagree because it is assumed that the slowest reaction determines the number of nuclei formed and the remaining precursors are then consumed to grow the nuclei. When this is the case, faster nucleation rates produce more, smaller nuclei while slower rates produce fewer, larger particles. If something else is more limiting than the disproportionation or interferes with the growth process, then the typical, reaction-controlled processes do not occur.

An example of this could be that something such as X^- or ZnX_2 caps the crystals and inhibits further growth. Contributing to this would be one part surface energy passivation and one part kinetic hindrance, the effect of either could be determined with plane-wave DFT calculations on InP surfaces, the former being more straightforward than the latter. If instead the reaction is controlled by the slow diffusion of a material (perhaps $\mathbf{10_{II}}$) to the particle surface, then diffusion-limited regimes take over. This would then imply that different diffusion rates of the various species would determine particle growth, which would be challenging to calculate either experimentally or theoretically.

6.4 Final Thoughts

It has now been shown that quality indium phosphide quantum dots can be made with simple Schlenk techniques and basic considerations for ambient moisture. Understanding the activation by zinc salts has dramatically altered the perception of their role and allowed for improved reaction designs. Due to the development of more reaction schemes, this has also expanded the range of available material sizes. While the syntheses with OAmX are still being improved, the use of simple acids and indium acetate compounds shows promise for a water-insensitive reaction. A deeper understanding of the various halide relationships was also revealed and will aid future endeavors for optimization. These mechanistic and synthetic improvements will allow these syntheses to be accessed by a broader range of researchers and will lead to further improvements not only with indium phosphide materials, but with indium arsenide and antimonide syntheses as well.

Bibliography

[1] S. Koh, T. Eom, W. D. Kim, K. Lee, D. Lee, Y. K. Lee, H. Kim, W. K. Bae, and D. C. Lee, "Zinc–Phosphorus Complex Working as an Atomic Valve for Colloidal Growth of Monodisperse Indium Phosphide Quantum Dots," *Chemistry of Materials*, vol. 29, no. 15, pp. 6346–6355, 2017.

[2] G. Laufersky, S. Bradley, E. Frécaut, M. Lein, and T. Nann, "Unraveling aminophosphine redox mechanisms for glovebox-free InP quantum dot syntheses," *Nanoscale*, vol. 10, no. 18, pp. 8752–8762, 2018.

[3] M. D. Tessier, D. Dupont, K. De Nolf, J. De Roo, and Z. Hens, "Economic and Size-Tunable Synthesis of InP/ZnE (E = S, Se) Colloidal Quantum Dots," *Chemistry of Materials*, vol. 27, no. 13, pp. 4893–4898, 2015.

[4] L. Xie, Q. Zhao, K. F. Jensen, and H. J. Kulik, "Direct Observation of Early-Stage Quantum Dot Growth Mechanisms with High-Temperature Ab Initio Molecular Dynamics," *The Journal of Physical Chemistry C*, vol. 120, no. 4, pp. 2472–2483, 2016.

Appendices

Appendix A

Discussions and Derivations

Full-Width at Half-Maximum Discussion

As many nanoparticles have size-dependent properties, the profile of particle diameters, edge lengths, facet shapes, and the like are often of chief importance when having discussions about their usefulness. While electron microscopy is typically held as the gold standard for acquiring these profiles, the relatively insignificant number of sampled particles[†] makes it easy for these to be misrepresenting. Instead, a more ensemble-based measurement would be better, but analyzing individual nanoparticles in a high throughput way is challenging. As such, a variety of solutions-based spectroscopic techniques, such as dynamic light scattering, absorption, and emission, are frequently used as proxies for size distributions. While these techniques measure many more particles than possible with microscopy, their ability to yield size profile information is limited by the understanding of the size-dependent relationship as well as the assumptions made about the data.

In most cases, the fundamental nature of the size dependence is more or less understood, especially if the field has progressed to the point where many researchers report spectroscopy over microscopy. However, what is less well-developed and most often overlooked are the assumptions a researcher has to make in order to use these methods as a stand-in for concrete size information. For quantum dots, this is a slippery slope where emission profiles are occasionally used to justify characteristics about the particle shapes and sizes, which is a tenuous justification at best. While size does determine quantum dot absorption profiles, which do determine emission behaviors, there are several other factors in each of those steps that influence the outcome. Different sized particles do have different degrees of exciton confinement that result in different absorption energies, but so too do different shapes and different surface ligand interactions. Similarly, the presence of different kinds of excited electrons and holes (light hole/heavy hole) result in different absorption phenomena for the same sized particles. And while emission is a function of absorption, it is also affected by other things such as different radiative and non-radiative decay pathways, the presence of electron or hole traps, and the likelihood of multiple exciton

[†]A good study will count $\sim 10^3 - 10^4$ particles, but a small batch synthesis can make anywhere between $10^{16} - 10^{20}$ particles.

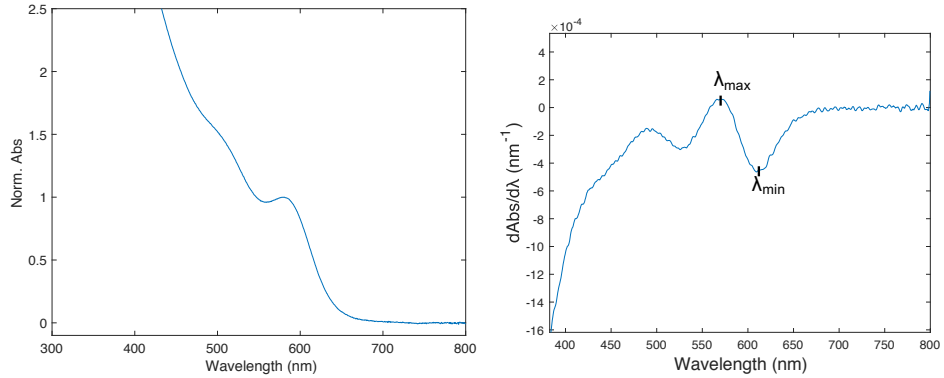

FIGURE A.1: (Left) A typical absorption profile of an InP quantum dot sample and (Right) the first derivative of this spectrum with the exciton maximum (λ_{max}) and minimum (λ_{min}) labelled.

generation.

Although it's clear that emission profiles shouldn't be used as a proxy for size distributions, how bad is it to use absorption? Again, this depends on the assumptions a researcher uses. The first one is that the exciton energy has a Gaussian distribution. This is not a bad assumption, as it is a "normal" variable and can be expected to have a matching profile. As such, the full-width at half-maximum (FWHM) of this peak could be used as an acceptable measure of size distributions. However, there are two issues that complicate this matter: the assumption of the shape of the background signals and the energy scale used.

As seen in Figure A.1 (left), quantum dots by their nature have continuous absorption at energies larger than those associated with their exciton (lowest energy peak). It is clear that the researcher must decide on a background contribution to isolate a Gaussian profile, however it is less obvious what that contribution should look like. While it is tempting to use a number of other Gaussian functions to draw this background, the complex nature of the reaction solutions combined with the relatively unknown higher-order excitation behaviors makes this very suspect. Without concrete physical reasons for assigning a Gaussian peak position and intensity, it is very easy to get a range of exciton "profiles" based on how you draw the background curves. To accommodate this, some researchers have begun looking at the derivatives of the absorption profiles as a workaround to deciding on the shape of the background.[1] The logic behind this is that as long as the background is linear, it comes out as a constant and the extrema of the derivative can be used to calculate FWHM according to Equation A.1. While assuming the background is linear is not anything approaching rigorous, the extrema of this peak should be the least affected by the background curves, as they are the lowest energy features of this exciton peak.

$$FWHM = \sqrt{2\,ln(2)}\,|\lambda_{max} - \lambda_{min}| \tag{A.1}$$

While identifying the FWHM from an absorption profile is problematic, what is more concerning is the blasé nature with which researchers choose the units of

their x-axes. Typically, UV-Vis absorption is reported in wavelength and has units of nanometers (nm). However, the relationship between nanoparticle size and the position of the exciton feature is dependent on energy, usually with units of electron volts (eV).

$$E = \frac{hc}{\lambda} \tag{A.2}$$

$$E * \lambda = 1240 \text{ eV-nm} \tag{A.3}$$

While translating between eV and nm is trivial by using Equation A.3, the inverse nature of the relationship means that two peaks centered around different wavelengths with the same FWHM measured in nm translate to different FWHM in eV.

$$FWHM_{600nm} = |620 \text{ nm} - 580 \text{ nm}| = 40 \text{ nm} \tag{A.4}$$

$$FWHM_{400nm} = |420 \text{ nm} - 380 \text{ nm}| = 40 \text{ nm} \tag{A.5}$$

$$600 \text{ nm} = 2.07 \text{ eV} \text{ ; } 400 \text{ nm} = 3.10 \text{ eV} \tag{A.6}$$

$$FWHM_{2.07eV} = |2.00 \text{ eV} - 2.14 \text{ eV}| = 0.14 \text{ eV} \tag{A.7}$$

$$FWHM_{3.10eV} = |2.88 \text{ eV} - 3.26 \text{ eV}| = 0.38 \text{ eV} \tag{A.8}$$

This discrepancy can lead to researchers to choose the axis that makes their data look the best. But which representation is correct? This question is compounded by the fact that the size-exciton relationship is dependent on energy, generally described in eV. For a tetrahedral InP particle, this has been experimentally determined[2] to follow Equation A.9, where the energy of the exciton (E_{ex}) is dependent on the sum of the bulk band gap (1.35 eV) and a relationship with the particle edge length (A).

$$E_{ex} = \frac{4.25}{A^{0.96}} + 1.35 \text{ eV} \tag{A.9}$$

Figure A.2 shows that this relationship, when converted into nm, is of the opposite trend as the wavelength-energy one, which significantly complicates this matter.

The intersection of these two curves suggests that perhaps some sort of cancellation of errors can be taken advantage of in this situation. If we examine the 400 nm case from Equations A.4 - A.8 and input them into Equation A.9, we can get some notion of the spread of sizes given by a 40 nm absorption FWHM.

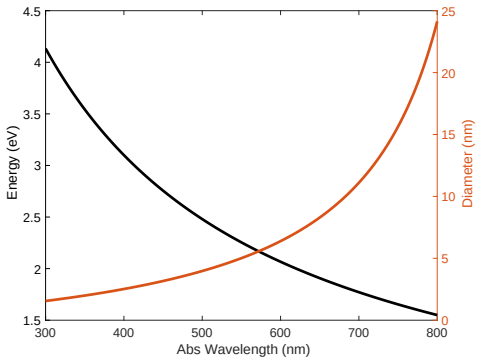

FIGURE A.2: A graph of the relationship between wavelength and energy in general (black, left) and the wavelength of an exciton in confined InP and the size of the confining nanoparticle (right).

$$\lambda_1 = 380 \text{ nm} = 2.88 \text{ eV} \Rightarrow A_1 = 2.76 \text{ nm} \tag{A.10}$$

$$\lambda_\mu = 400 \text{ nm} = 3.10 \text{ eV} \Rightarrow A_\mu = 2.52 \text{ nm} \tag{A.11}$$

$$\lambda_2 = 420 \text{ nm} = 3.26 \text{ eV} \Rightarrow A_2 = 2.30 \text{ nm} \tag{A.12}$$

$$\frac{|A_1 - A_2|}{A_\mu} * 100\% \tag{A.13}$$

So a peak centered at 400 nm with a FWHM of 40 nm yields a spread of edge lengths of ~18.5%. If a similar treatment is done across the UV-Vis range, but keeping the 40 nm FWHM the same, we can get an idea for how a theoretical FHWM would represent particle sizes.

Interestingly, in Figure A.3 there appears to be a window from ~370–540 nm where the same FWHM profile results in similar $\%A$ values. This window was found to be constant regardless of FWHM value chosen. Because this relationship is dependent on the degree of confinement (Equation A.9), this was affected by the assumptions of particle shape. Figure A.4 shows the same kind of curve, but with the addition of a spherical particle assumption. Here, L and $\%L$ are used, where L = D (diameter) or A (edge length) of the particle respectively.

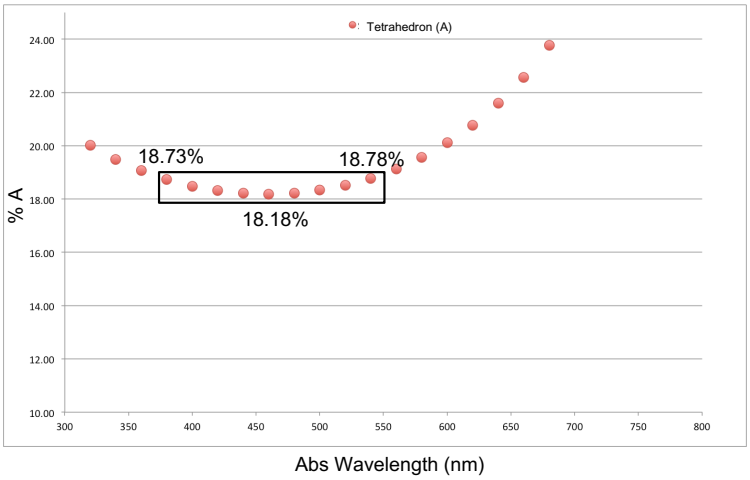

FIGURE A.3: Spread of edge lengths of InP QDs calculated by Equation A.13 for peaks with 40 nm FWHM centered at different wavelengths. Samples in the black box represent those with "consistent" values.

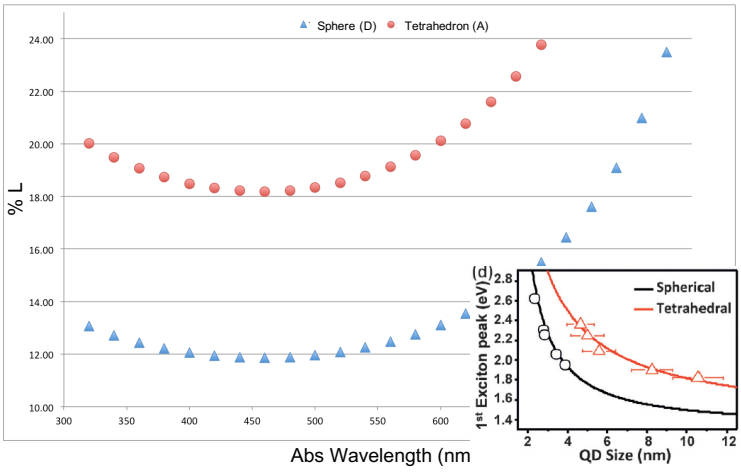

FIGURE A.4: Spread of lengths of InP QDs, L = diameters (D) or edge lengths (A), calculated by Equation A.13 for peaks with 40 nm FWHM centered at different wavelengths.

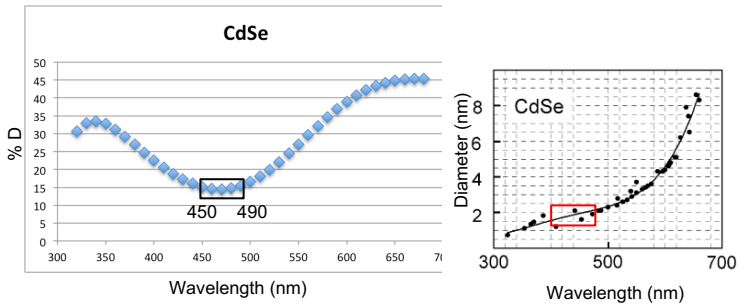

FIGURE A.5: (Left) Spread of diameters of CdSe QDs calculated by Equation A.13 for peaks with 40 nm FWHM centered at different wavelengths using an experimental fit from literature.[3] Samples in the black box represent those with "consistent" values. (Right) Polynomial fit of CdSe particle size and exciton energy based on a variety of experimental data. Red box corresponds to the wavelengths identified by the black box in the left image. Adapted with permissions from Leatherdale *et al.*[3] Copyright 2002 American Chemical Society

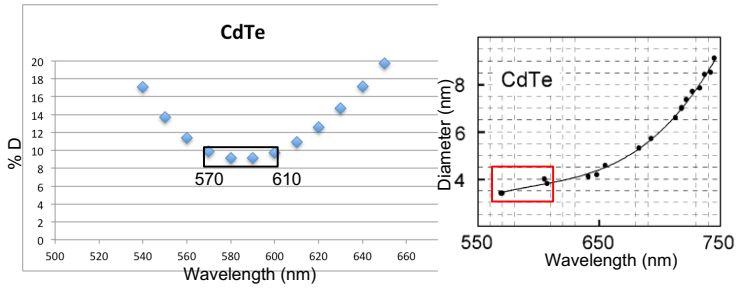

FIGURE A.6: (Left) Spread of diameters of CdTe QDs calculated by Equation A.13 for peaks with 40 nm FWHM centered at different wavelengths using an experimental fit from literature.[3] Samples in the black box represent those with "consistent" values. (Right) Polynomial fit of CdTe particle size and exciton energy based on a variety of experimental data. Red box corresponds to the wavelengths identified by the black box in the left image. Adapted with permissions from Leatherdale *et al.*[3] Copyright 2002 American Chemical Society

Thankfully, the assumption of spherical particle shape seems to broaden out the window of applicability for these samples. This wide window in both of these cases is likely a function the large exciton Bohr radii in III-V materials (Section 2.4). As such, the II-VI materials with much smaller r_{Bohr} were similarly examined for theoretical 40 nm absorption FWHM.

Figures A.5 and A.6 show that this window of reliability is much smaller with CdSe and CdTe materials. In addition, examining where this window exists compared to where literature publishes particle size and emission data shows that the majority of works exist outside of this window. That means that researchers should be very careful about using wavelength to describe sizes in Cd-based materials. Even while using eV, this issue becomes complicated again because the cancellation from Equation A.3 is removed and a 0.1 eV FWHM results in different particle size ranges at different peak centers (%A at 3.2 eV = 6% vs. 12% at 2.2 eV for InP tetrahedrons).

Finally, because the values deemed "comparable" in Figure A.3 themselves have

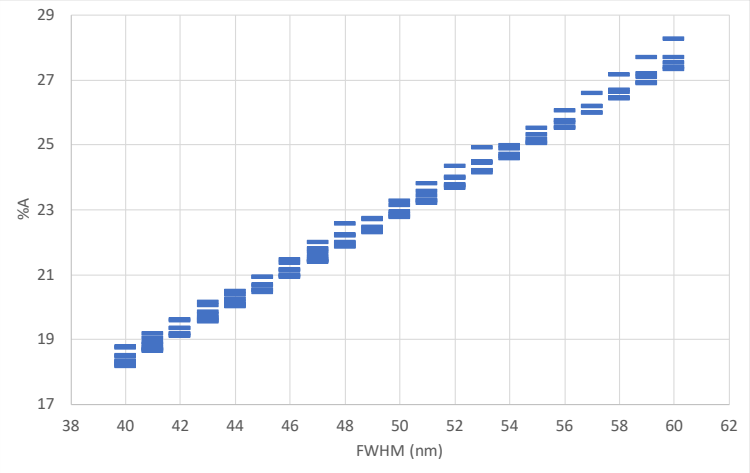

FIGURE A.7: The comparisons of Figure A.3 were performed with different values of FWHM. The points in the black box (from 370-540 nm) were then presented together as bars.

a range of values, the effect of different FWHM on this representation was examined. Figure A.7 shows the each of the points in that box from 370-540 nm but as calculated with different FWHM in nm. As can be seen, there is some overlap in directly adjacent values, i.e. both FWHM vales of 45 nm and 46 nm could yield a %A value of 21%. Therefore, only differences of more than 2 nm in FWHM should be considered significant.

Taken all together, this Appendix should highly caution the reader against making assumptions that proxy measurements (like UV-Vis absorption) can be readily used to discuss nanoparticle sizes. The nature of nanoparticle-spectroscopic trends as well as the function of wavelength vs. energy of the light used should be taken in consideration before this can occur. For the work in this Thesis, the properties of InP confinement appear to cancel out some of these trends in the wavelength region of interest, which is a fortunate coincidence. While these are basically back-of-the-envelope calculations, they quiet more fears than they generate for this system.

And as a last note, although emission profiles should not be used to justify different size characteristics on their own, many researchers care solely about emission linewidth so are not bothered by these concerns. In applications such as lasing or LED fabrication, the control of size matters less than control of color, so many works minimally characterize the physical aspects of the solutions and jump straight to their photophysical or more "useful" characteristics. While I am of the firm believe that size and shape considerations are the key to controlling such characteristics, sometimes the utility of a material matters more.

Bibliography

[1] M. D. Tessier, D. Dupont, K. De Nolf, J. De Roo, and Z. Hens, "Economic and Size-Tunable Synthesis of InP/ZnE (E = S, Se) Colloidal Quantum Dots," *Chemistry of Materials*, vol. 27, no. 13, pp. 4893–4898, 2015.

[2] K. Kim, D. Yoo, H. Choi, S. Tamang, J.-H. Ko, S. Kim, Y.-H. Kim, and S. Jeong, "Halide–Amine Co-Passivated Indium Phosphide Colloidal Quantum Dots in Tetrahedral Shape," *Angewandte Chemie*, vol. 128, no. 11, pp. 3778–3782, 2016.

[3] C. A. Leatherdale, W. K. Woo, F. V. Mikulec, and M. G. Bawendi, "On the Absorption Cross Section of CdSe Nanocrystal Quantum Dots," *The Journal of Physical Chemistry B*, vol. 106, no. 31, pp. 7619–7622, 2002.

Rate Derivations

$$k^{\ddagger} = \frac{k_b T}{h} e^{-\Delta G^{\ddagger}/RT} \tag{A.14}$$

$$\frac{k_2^{\ddagger}}{k_1^{\ddagger}} = e^{\frac{\Delta G_1^{\ddagger} - \Delta G_2^{\ddagger}}{RT}} \tag{A.15}$$

$$\text{let } \Delta(\Delta G^{\ddagger}) = \Delta G_1^{\ddagger} - \Delta G_2^{\ddagger} \tag{A.16}$$

$$\ln\left(\frac{k_2^{\ddagger}}{k_1^{\ddagger}}\right) = \Delta(\Delta G^{\ddagger})/RT \tag{A.17}$$

$$\ln(10)\log\left(\frac{k_2^{\ddagger}}{k_1^{\ddagger}}\right) = \frac{\Delta(\Delta G^{\ddagger})}{RT} \tag{A.18}$$

$$\log\left(\frac{k_2^{\ddagger}}{k_1^{\ddagger}}\right) = \frac{\Delta(\Delta G^{\ddagger})}{\ln(10)\, RT} \tag{A.19}$$

$$\text{for } T = 435.15\ K: \tag{A.20}$$

$$\approx \frac{\Delta(\Delta G^{\ddagger})}{2.07} \tag{A.21}$$

$$k_2^{\ddagger} = k_1^{\ddagger} * 10\text{^}\left(\frac{\Delta G_1^{\ddagger} - \Delta G_2^{\ddagger}}{2.07}\right) \tag{A.22}$$

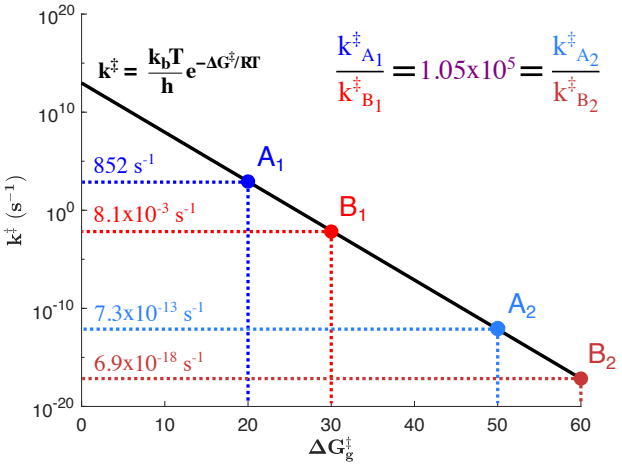

FIGURE A.8: Graph depicting the equivalence of relative transition rates across various ΔG_g, provided $\Delta(\Delta G_g)$ remains the same.

Appendix B

Gas Phase Energy Comparisons

$InCl_3$ – NoZinc

	PBE0-D3/def2-TZVP/PCM_{OAm}				PBE0-D3/def2-TZVP			
	ΔE	ΔU	ΔH	ΔG	ΔE	ΔU	ΔH	ΔG
1	0.00	0.00	0.00	0.00	0.00	0.00	0.00	0.00
$\mathbf{1_a}$	68.07	63.78	66.48	15.90	65.60	61.19	63.90	14.54
$\mathbf{1_b}$	33.20	29.53	31.33	-0.94	32.89	29.94	31.74	-1.75
$\mathbf{1_c}$	20.93	19.44	20.34	3.41	22.10	20.70	21.60	4.30
$\mathbf{1_d}$	11.55	10.16	11.06	-6.70	9.61	8.21	9.11	-8.36
$\mathbf{1_e}$	3.93	3.72	3.72	4.88	5.15	5.10	5.10	5.16
$\mathbf{1_f}$	17.00	18.70	17.80	32.78	15.50	17.28	16.38	31.19
$\mathbf{1_g}$	-10.30	-8.73	-9.63	6.28	-12.11	-10.63	-11.53	5.30
3	0.00	0.00	0.00	0.00	0.00	0.00	0.00	0.00
$\mathbf{3_a}$	0.42	0.28	0.28	0.71	1.09	0.88	0.88	1.52
$\mathbf{3_b}$	4.10	3.49	3.49	5.40	2.59	1.99	1.99	3.76
$\mathbf{3_c}$	7.63	7.03	7.04	9.06	7.01	6.62	6.62	7.48
$\mathbf{4_I}$	0.00	0.00	0.00	0.00	0.00	0.00	0.00	0.00
$\mathbf{4}^{\ddagger}$	14.26	13.37	13.36	19.99	12.39	11.45	11.45	16.93
$\mathbf{4_{II}}$	-1.18	-1.09	-1.09	1.86	-3.47	-3.34	-3.34	-3.34
$\mathbf{4_{aI}}$	-0.08	-0.34	-0.34	1.86	-0.98	-1.20	-1.20	-0.51
$\mathbf{4}^{\ddagger}_{\mathbf{a,1}}$	5.84	5.43	5.43	7.31	3.35	2.88	2.88	4.22
$\mathbf{4_{a,2}}$	2.91	2.99	2.99	4.00	-0.50	-0.44	-0.44	-0.49
$\mathbf{4}^{\ddagger}_{\mathbf{a,3}}$	5.53	4.90	4.90	8.10	2.73	2.14	2.14	4.05
$\mathbf{4_{aII}}$	-0.24	-0.23	-0.23	3.60	-0.57	-0.48	-0.48	0.75
$\mathbf{5_I}$	0.00	0.00	0.00	0.00	0.00	0.00	0.00	0.00
$\mathbf{5}^{\ddagger}$	61.50	61.21	61.21	64.01	62.85	62.29	62.29	67.05
$\mathbf{5_{II}}$	0.01	-0.61	-0.61	3.60	0.93	0.41	0.41	3.98

TABLE B.1: Comparisons of the electronic, internal, enthalpic, and free energy differences (in kcal/mol) of the zinc-free structures presented in Chapter 3 with and without the use of the PCM.

$InCl_3 - ZnCl_2$

	PBE0-D3/def2-TZVP/PCM_{OAm}				PBE0-D3/def2-TZVP			
	ΔE	ΔU	ΔH	ΔG	ΔE	ΔU	ΔH	ΔG
6	0.00	0.00	0.00	0.00	0.00	0.00	0.00	0.00
$\mathbf{6_a}$	42.92	39.90	41.70	14.25	49.01	46.05	47.85	19.01
$\mathbf{6_b}$	20.54	18.98	19.88	5.27	23.06	21.61	22.51	5.48
$\mathbf{6_c}$	-9.49	-8.00	-8.90	7.73	-12.06	-10.46	-11.36	3.53
$\mathbf{6_d}$	-10.53	-9.00	-9.90	6.71	-12.62	-11.11	-12.01	3.88
$\mathbf{6_e}$	-17.81	-14.79	-16.59	18.77	-21.81	-18.59	-20.39	12.88
$\mathbf{7_a}$	0.00	0.00	0.00	0.00	0.00	0.00	0.00	0.00
$\mathbf{7_b^‡}$	0.88	0.14	0.14	4.25	2.91	2.85	2.85	3.69
$\mathbf{7_c}$	0.62	0.66	0.66	1.16	-2.09	-1.48	-1.48	-1.79
$\mathbf{7_d^‡}$	1.05	0.47	0.47	3.10	-0.66	-0.41	-0.41	-1.17
$\mathbf{7_e}$	1.06	0.88	0.88	4.25	-2.17	-1.19	-1.19	-5.51
$\mathbf{7_f^‡}$	3.39	2.35	2.35	8.37	-	-	-	-
$\mathbf{7_g}$	0.80	0.55	0.55	2.62	-	-	-	-
$\mathbf{7_h^‡}$	0.82	-0.17	-0.17	5.95	-	-	-	-
$\mathbf{7_i}$	-0.44	-0.66	-0.66	2.74	-	-	-	-
$\mathbf{7_j^‡}$	1.66	1.12	1.12	4.14	-	-	-	-
$\mathbf{7_k}$	-0.71	-0.48	-0.48	-0.11	-	-	-	-
8	0.00	0.00	0.00	0.00	0.00	0.00	0.00	0.00
$\mathbf{8_a}$	3.64	3.54	3.54	2.56	5.23	5.20	5.20	3.88
$\mathbf{8_b}$	6.87	6.72	6.72	7.30	7.31	7.17	7.17	7.55
$\mathbf{8_c}$	6.57	6.24	6.24	7.53	4.66	4.30	4.30	5.63
$\mathbf{9_I}$	0.00	0.00	0.00	0.00	0.00	0.00	0.00	0.00
$\mathbf{9^‡}$	15.02	14.78	14.78	16.37	10.96	10.55	10.55	13.93
$\mathbf{9_{II}}$	-3.29	-2.90	-2.90	-3.97	-7.75	-7.57	-7.57	-7.17
$\mathbf{10_I}$	0.00	0.00	0.00	0.00	0.00	0.00	0.00	0.00
$\mathbf{10^‡}$	52.56	51.95	51.96	55.13	52.18	51.85	51.85	53.52
$\mathbf{10_{II}}$	-8.43	-8.47	-8.47	-9.03	-7.79	-7.89	-7.89	-6.64

TABLE B.2: Comparisons of the electronic, internal, enthalpic, and free energy differences (in kcal/mol) of the zinc-activated structures presented in Chapter 3 with and without the use of the PCM.

	$InBr_3$ − NoZinc				InI_3 − NoZinc			
	ΔE	ΔU	ΔH	ΔG	ΔE	ΔU	ΔH	ΔG
1	0.00	0.00	0.00	0.00	0.00	0.00	0.00	0.00
$\mathbf{1_a}$	63.37	58.95	61.65	11.77	57.42	52.99	55.69	5.51
$\mathbf{1_b}$	31.88	28.99	30.79	-4.11	28.43	25.51	27.31	-6.95
$\mathbf{1_c}$	22.07	20.67	21.57	4.21	20.57	19.13	20.03	3.19
$\mathbf{1_d}$	9.83	8.42	9.32	-7.83	8.89	7.46	8.36	-8.65
$\mathbf{1_e}$	7.59	7.72	7.72	7.30	7.21	7.26	7.26	7.77
$\mathbf{1_f}$	17.37	19.19	18.29	33.66	22.61	24.88	23.98	35.61
$\mathbf{1_g}$	-11.66	-10.19	-11.09	5.48	-11.48	-10.06	-10.96	6.57
3	0.00	0.00	0.00	0.00	0.00	0.00	0.00	0.00
$\mathbf{3_a}$	0.67	0.31	0.31	3.20	2.12	2.37	2.37	-0.08
$\mathbf{3_b}$	3.80	3.24	3.24	5.45	6.61	6.42	6.42	5.98
$\mathbf{3_c}$	6.61	5.89	5.89	8.99	9.59	9.39	9.39	8.36
$\mathbf{4_I}$	0.00	0.00	0.00	0.00	0.00	0.00	0.00	0.00
$\mathbf{4}^{\ddagger}$	13.30	12.42	12.42	18.02	15.11	14.05	14.05	21.71
$\mathbf{4_{II}}$	-3.39	-3.03	-3.03	-4.87	-1.78	-1.56	-1.56	-2.05
$\mathbf{4_{aI}}$	0.00	0.00	0.00	0.00	0.00	0.00	0.00	0.00
$\mathbf{4}^{\ddagger}_{\mathbf{a,1}}$	4.59	4.26	4.26	4.56	*	*	*	*
$\mathbf{4_{a,2}}$	0.81	1.05	1.05	-0.01	0.28	0.42	0.42	0.80
$\mathbf{4}^{\ddagger}_{\mathbf{a,3}}$	3.74	3.51	3.51	3.50	3.38	3.02	3.02	4.61
$\mathbf{4_{aII}}$	-0.39	0.11	0.11	-1.55	-0.18	0.22	0.22	-0.16
$\mathbf{5_I}$	0.00	0.00	0.00	0.00	0.00	0.00	0.00	0.00
$\mathbf{5}^{\ddagger}$	62.51	62.07	62.07	66.14	60.56	60.04	60.04	63.13
$\mathbf{5_{II}}$	2.36	1.98	1.98	5.68	-2.15	-2.42	-2.42	-0.01

	$InBr_3$ − $ZnCl_2$				InI_3 − $ZnCl_2$			
	ΔE	ΔU	ΔH	ΔG	ΔE	ΔU	ΔH	ΔG
8	0.00	0.00	0.00	0.00	0.00	0.00	0.00	0.00
$\mathbf{8_a}$	3.82	3.69	3.69	4.03	3.05	2.73	2.73	1.93
$\mathbf{8_b}$	7.74	7.37	7.37	8.68	3.12	2.96	2.96	3.32
$\mathbf{8_c}$	3.90	3.57	3.57	4.49	6.58	6.17	6.17	7.83
$\mathbf{9_I}$	0.00	0.00	0.00	0.00	0.00	0.00	0.00	0.00
$\mathbf{9}^{\ddagger}$	12.05	11.59	11.59	14.70	13.48	13.08	13.08	15.92
$\mathbf{9_{II}}$	-7.48	-7.03	-7.03	-8.46	-4.49	-4.62	-4.62	-1.63
$\mathbf{10_I}$	0.00	0.00	0.00	0.00	0.00	0.00	0.00	0.00
$\mathbf{10}^{\ddagger}$	51.74	51.07	51.07	55.42	50.88	50.33	50.33	53.44
$\mathbf{10_{II}}$	-8.51	-8.52	-8.52	-8.17	-9.31	-9.29	-9.29	-8.66

TABLE B.3: Comparisons of the electronic, internal, enthalpic, and free energy differences (in kcal/mol) of the structures with varying indium halides. Geometries marked with (*) were unable to be obtained.

	$\mathbf{InCl_3 - ZnBr_2}$				$\mathbf{InCl_3 - ZnI_2}$			
	ΔE	ΔU	ΔH	ΔG	ΔE	ΔU	ΔH	ΔG
6	0.00	0.00	0.00	0.00	0.00	0.00	0.00	0.00
$\mathbf{6_a}$	49.84	46.89	48.69	19.10	48.92	45.95	47.75	17.82
$\mathbf{6_b}$	23.65	22.18	23.08	6.45	23.41	21.95	22.85	5.95
$\mathbf{6_c}$	-11.87	-10.23	-11.13	3.36	-11.54	-9.96	-10.86	3.91
$\mathbf{6_d}$	-13.78	-12.29	-13.19	1.87	-14.06	-12.67	-13.57	1.41
$\mathbf{6_e}$	-22.90	-19.83	-21.63	12.76	-23.21	-20.35	-22.15	13.21
$\mathbf{7_a}$	0.00	0.00	0.00	0.00	0.00	0.00	0.00	0.00
$\mathbf{7_b}^{\ddagger}$	5.01	4.19	4.19	8.37	5.54	4.83	4.83	7.87
$\mathbf{7_c}$	-0.10	-0.21	-0.21	2.45	0.76	0.83	0.83	1.97
$\mathbf{7_d}^{\ddagger}$	1.44	0.98	0.99	3.15	1.79	1.54	1.54	1.57
$\mathbf{7_e}$	-0.32	-0.06	-0.06	-0.88	-0.23	0.18	0.18	-2.14
8	0.00	0.00	0.00	0.00	0.00	0.00	0.00	0.00
$\mathbf{8_a}$	5.85	5.55	5.55	5.28	5.87	5.54	5.54	6.02
$\mathbf{8_b}$	8.12	7.72	7.72	9.33	8.33	8.10	8.10	9.07
$\mathbf{8_c}$	0.99	0.62	0.62	2.08	5.32	4.91	4.91	6.92
$\mathbf{9_I}$	0.00	0.00	0.00	0.00	0.00	0.00	0.00	0.00
$\mathbf{9}^{\ddagger}$	13.52	13.28	13.28	15.08	12.79	12.36	12.36	16.13
$\mathbf{9_{II}}$	-6.98	-6.71	-6.71	-6.21	-6.14	-5.82	-5.82	-5.63
$\mathbf{10_I}$	0.00	0.00	0.00	0.00	0.00	0.00	0.00	0.00
$\mathbf{10}^{\ddagger}$	52.01	51.33	51.33	55.62	51.76	51.04	51.04	56.30
$\mathbf{10_{II}}$	-8.23	-8.37	-8.37	-7.28	-8.83	-8.80	-8.80	-7.66

TABLE B.4: Comparisons of the electronic, internal, enthalpic, and free energy differences (in kcal/mol) of the structures with varying zinc halides.

Appendix C

Halide Energy Comparisons

$InCl_3$ – NoZinc

	ΔE	ΔU	ΔH	ΔG	ΔE_g	ΔU_g	ΔH_g	ΔG_g
$\mathbf{4_I}$	0.00	0.00	0.00	0.00	-16.88	-15.51	-16.41	4.59
$4^{\ddagger}$	12.38	11.45	11.45	16.93	-4.50	-4.06	-4.96	21.52
$\mathbf{4_{II}}$	-3.47	-3.34	-3.34	-3.34	-20.35	-18.85	-19.75	1.25
$\mathbf{4_{aI}}$	0.00	0.00	0.00	0.00	-17.88	-16.73	-17.63	4.06
$\mathbf{4^{\ddagger}_{a,1}}$	4.40	4.15	4.15	4.81	-13.48	-12.58	-13.48	8.87
$\mathbf{4_{a,2}}$	0.48	0.78	0.78	0.03	-17.40	-15.95	-16.85	4.09
$\mathbf{4^{\ddagger}_{a,3}}$	3.77	3.40	3.40	4.64	-14.11	-13.33	-14.23	8.70
$\mathbf{4_{aII}}$	0.41	0.73	0.73	1.29	-17.47	-16.00	-16.90	5.35
$\mathbf{5_I}$	0.00	0.00	0.00	0.00	-24.92	-23.68	-24.58	0.23
$\mathbf{5}^{\ddagger}$	62.85	62.28	62.28	67.05	37.93	38.60	37.70	67.28
$\mathbf{5_{II}}$	0.93	0.40	0.40	3.98	-23.99	-23.28	-24.18	4.21

$InCl_3$ – $ZnCl_2$

	ΔE	ΔU	ΔH	ΔG	ΔE_g	ΔU_g	ΔH_g	ΔG_g
$\mathbf{7_a}$	0.00	0.00	0.00	0.00	-19.51	-19.26	-20.16	4.15
$\mathbf{7_b}^{\ddagger}$	2.91	2.85	2.85	3.69	-16.60	-16.41	-17.31	7.84
$\mathbf{7_c}$	-2.09	-1.49	-1.49	-1.79	-21.60	-20.75	-21.65	2.36
$\mathbf{7_d}^{\ddagger}$	-0.66	-0.42	-0.42	-1.17	-20.17	-19.68	-20.58	2.98
$\mathbf{7_e}$	-2.17	-1.20	-1.20	-5.51	-21.68	-20.46	-21.36	-1.36
$\mathbf{9_I}$	0.00	0.00	0.00	0.00	-24.00	-23.31	-24.21	6.29
$\mathbf{9}^{\ddagger}$	10.96	10.54	10.54	13.93	-13.04	-12.77	-13.67	20.22
$\mathbf{9_{II}}$	-7.75	-7.58	-7.58	-7.17	-31.75	-30.89	-31.79	-0.88
$\mathbf{10_I}$	0.00	0.00	0.00	0.00	-32.07	-31.21	-32.11	2.19
$\mathbf{10}^{\ddagger}$	52.18	51.73	51.72	54.41	20.11	20.52	19.61	56.60
$\mathbf{10_{II}}$	-7.79	-7.91	-7.91	-5.99	-39.86	-39.12	-40.02	-3.80

TABLE C.1: Comparisons of the electronic, internal, enthalpic, and free energy differences (in kcal/mol) of the $InCl_3$-based structures calculated with two different methods.

$InBr_3$ – NoZinc

	ΔE	ΔU	ΔH	ΔG	ΔE_g	ΔU_g	ΔH_g	ΔG_g
$\mathbf{4_I}$	0.00	0.00	0.00	0.00	-16.56	-15.35	-16.25	6.44
$\mathbf{4}^{\ddagger}$	13.30	12.42	12.42	18.02	-3.26	-2.93	-3.83	24.46
$\mathbf{4_{II}}$	-3.39	-3.03	-3.03	-4.87	-19.95	-18.39	-19.29	1.57
$\mathbf{4_{aI}}$	0.00	0.00	0.00	0.00	-17.87	-16.59	-17.49	4.18
$\mathbf{4}^{\ddagger}_{\mathbf{a,1}}$	4.59	4.26	4.26	4.56	-13.29	-12.33	-13.23	8.74
$\mathbf{4_{a,2}}$	0.81	1.05	1.05	-0.01	-17.06	-15.54	-16.44	4.17
$\mathbf{4}^{\ddagger}_{\mathbf{a,3}}$	3.74	3.51	3.51	3.50	-14.13	-13.08	-13.98	7.69
$\mathbf{4_{aII}}$	-0.39	0.11	0.11	-1.55	-18.26	-16.48	-17.38	2.63
$\mathbf{5_I}$	0.00	0.00	0.00	0.00	-26.40	-25.33	-26.23	-0.38
$\mathbf{5}^{\ddagger}$	62.51	62.07	62.07	66.14	36.11	36.74	35.84	65.76
$\mathbf{5_{II}}$	2.36	1.98	1.98	5.68	-24.04	-23.35	-24.25	5.30

$InBr_3$ – $ZnCl_2$

	ΔE	ΔU	ΔH	ΔG	ΔE_g	ΔU_g	ΔH_g	ΔG_g
$\mathbf{7_a}$	0.00	0.00	0.00	0.00	-19.51	-19.26	-20.16	4.15
$\mathbf{7_b}^{\ddagger}$	2.91	2.85	2.85	3.69	-16.60	-16.41	-17.31	7.84
$\mathbf{7_c}$	-2.09	-1.48	-1.48	-1.79	-21.60	-20.75	-21.65	2.36
$\mathbf{7_d}^{\ddagger}$	-0.66	-0.41	-0.41	-1.17	-20.17	-19.68	-20.58	2.98
$\mathbf{7_e}$	-2.17	-1.19	-1.19	-5.51	-21.68	-20.46	-21.36	-1.36
$\mathbf{9_I}$	0.00	0.00	0.00	0.00	-23.31	-22.51	-23.41	7.23
$\mathbf{9}^{\ddagger}$	12.05	11.59	11.59	14.70	-11.26	-10.93	-11.83	21.93
$\mathbf{9_{II}}$	-7.48	-7.03	-7.03	-8.46	-30.78	-29.55	-30.45	-1.24
$\mathbf{10_I}$	0.00	0.00	0.00	0.00	-31.66	-30.68	-31.58	2.35
$\mathbf{10}^{\ddagger}$	51.74	51.07	51.07	55.42	20.07	20.39	19.48	57.77
$\mathbf{10_{II}}$	-8.51	-8.52	-8.52	-8.17	-40.17	-39.20	-40.10	-5.81

TABLE C.2: Comparisons of the electronic, internal, enthalpic, and free energy differences (in kcal/mol) of the $InBr_3$-based structures calculated with two different methods.

InI_3 – NoZinc

	ΔE	ΔU	ΔH	ΔG	ΔE_g	ΔU_g	ΔH_g	ΔG_g
$\mathbf{4_I}$	0.00	0.00	0.00	0.00	-17.11	-15.73	-16.63	4.35
$\mathbf{4}^{\ddagger}$	15.11	14.05	14.05	21.70	-2.00	-1.68	-2.58	26.05
$\mathbf{4_{II}}$	-1.78	-1.56	-1.56	-2.06	-18.89	-17.29	-18.19	2.29
$\mathbf{4_{aI}}$	0.00	0.00	0.00	0.00	-17.36	-16.03	-16.93	4.11
$\mathbf{4}^{\ddagger}_{\mathbf{a,1}}$	*	*	*	*	*	*	*	*
$\mathbf{4_{a,2}}$	0.28	0.42	0.42	0.80	-17.08	-15.61	-16.51	4.91
$\mathbf{4}^{\ddagger}_{\mathbf{a,3}}$	3.38	3.02	3.02	4.61	-13.98	-13.01	-13.91	8.72
$\mathbf{4_{aII}}$	-0.18	0.23	0.23	-0.16	-17.54	-15.80	-16.70	3.95
$\mathbf{5_I}$	0.00	0.00	0.00	0.00	-27.00	-25.85	-26.75	-1.30
$\mathbf{5}^{\ddagger}$	60.55	60.04	60.04	63.13	33.55	34.19	33.29	61.83
$\mathbf{5_{II}}$	-2.16	-2.42	-2.42	-0.01	-29.16	-28.27	-29.17	-1.31

InI_3 – $ZnCl_2$

	ΔE	ΔU	ΔH	ΔG	ΔE_g	ΔU_g	ΔH_g	ΔG_g
$\mathbf{7_a}$	0.00	0.00	0.00	0.00	-19.51	-19.26	-20.16	4.15
$\mathbf{7_b}^{\ddagger}$	2.91	2.85	2.85	3.69	-16.60	-16.41	-17.31	7.84
$\mathbf{7_c}$	-2.09	-1.49	-1.49	-1.79	-21.60	-20.75	-21.65	2.36
$\mathbf{7_d}^{\ddagger}$	-0.66	-0.42	-0.42	-1.17	-20.17	-19.68	-20.58	2.98
$\mathbf{7_e}$	-2.17	-1.20	-1.20	-5.51	-21.68	-20.46	-21.36	-1.36
$\mathbf{9_I}$	0.00	0.00	0.00	0.00	-23.91	-22.78	-23.68	4.55
$\mathbf{9}^{\ddagger}$	13.48	13.09	13.09	15.92	-10.43	-9.69	-10.59	20.47
$\mathbf{9_{II}}$	-4.48	-4.62	-4.62	-1.63	-28.39	-27.40	-28.30	2.92
$\mathbf{10_I}$	0.00	0.00	0.00	0.00	-30.37	-29.46	-30.36	4.59
$\mathbf{10}^{\ddagger}$	50.88	50.33	50.33	53.44	20.51	20.87	19.97	58.03
$\mathbf{10_{II}}$	-9.31	-9.30	-9.30	-8.66	-39.68	-38.76	-39.66	-4.07

TABLE C.3: Comparisons of the electronic, internal, enthalpic, and free energy differences (in kcal/mol) of the InI_3-based structures calculated with two different methods. Geometries marked with (*) were unable to be obtained.

$InCl_3 - ZnBr_2$

	ΔE	ΔU	ΔH	ΔG	ΔE_g	ΔU_g	ΔH_g	ΔG_g
$\mathbf{7_a}$	0.00	0.00	0.00	0.00	-20.99	-19.95	-20.85	0.29
$\mathbf{7_b}^{\ddagger}$	5.01	4.18	4.18	8.37	-15.98	-15.77	-16.67	8.66
$\mathbf{7_c}$	-0.10	-0.21	-0.21	2.45	-21.09	-20.16	-21.06	2.74
$\mathbf{7_d}^{\ddagger}$	1.44	0.98	0.98	3.15	-19.55	-18.97	-19.87	3.44
$\mathbf{7_e}$	-0.32	-0.06	-0.06	-0.88	-21.31	-20.01	-20.91	-0.59
$\mathbf{9_I}$	0.00	0.00	0.00	0.00	-24.09	-23.20	-24.10	4.63
$\mathbf{9}^{\ddagger}$	13.53	13.27	13.27	15.08	-10.56	-9.93	-10.83	19.71
$\mathbf{9_{II}}$	-6.97	-6.72	-6.72	-6.21	-31.06	-29.92	-30.82	-1.58
$\mathbf{10_I}$	0.00	0.00	0.00	0.00	-30.93	-29.93	-30.83	3.17
$\mathbf{10}^{\ddagger}$	52.01	51.33	51.33	55.62	21.08	21.40	20.50	58.79
$\mathbf{10_{II}}$	-8.22	-8.36	-8.36	-7.27	-39.15	-38.29	-39.19	-4.10

$InCl_3 - ZnI_2$

	ΔE	ΔU	ΔH	ΔG	ΔE_g	ΔU_g	ΔH_g	ΔG_g
$\mathbf{7_a}$	0.00	0.00	0.00	0.00	-20.29	-19.38	-20.28	2.00
$\mathbf{7_b}^{\ddagger}$	5.53	4.83	4.83	7.87	-14.76	-14.55	-15.45	9.87
$\mathbf{7_c}$	0.76	0.84	0.84	1.97	-19.53	-18.54	-19.44	3.97
$\mathbf{7_d}^{\ddagger}$	1.78	1.55	1.55	1.57	-18.51	-17.83	-18.73	3.57
$\mathbf{7_e}$	-0.23	0.18	0.18	-2.14	-20.52	-19.20	-20.10	-0.14
$\mathbf{9_I}$	0.00	0.00	0.00	0.00	-23.39	-22.64	-23.54	6.42
$\mathbf{9}^{\ddagger}$	12.78	12.35	12.35	16.13	-10.61	-10.29	-11.19	22.55
$\mathbf{9_{II}}$	-6.15	-5.82	-5.82	-5.63	-29.54	-28.46	-29.36	0.79
$\mathbf{10_I}$	0.00	0.00	0.00	0.00	-29.18	-28.13	-29.03	4.28
$\mathbf{10}^{\ddagger}$	51.76	51.04	51.04	56.30	22.58	22.91	22.01	60.58
$\mathbf{10_{II}}$	-8.83	-8.81	-8.81	-7.66	-38.01	-36.94	-37.84	-3.38

TABLE C.4: Comparisons of the electronic, internal, enthalpic, and free energy differences (in kcal/mol) of the $ZnBr_2$- and ZnI_2-based structures calculated with two different methods.

	In–X (Å)	In–N (Å)	In–P (Å)	Dipole (D)	$D_{I\vec{n}X}$ (%)	$D_{I\vec{n}P}$ (%)
$\mathbf{1}-InCl_3$	2.455	2.342	-	2.83	99.5	-
$\mathbf{1}-InBr_3$	2.616	2.343	-	2.87	95.8	-
$\mathbf{1}-InI_3$	2.834	2.361	-	2.86	65.4	-
$\mathbf{4_I}- InCl_3$	2.469	2.323	4.719	3.89	-89.7	56.6
$\mathbf{4_I}- InBr_3$	2.627	2.327	4.793	4.08	-97.9	85.1
$\mathbf{4_I}- InI_3$	2.848	2.337	4.838	4.08	-91.6	87.8
$\mathbf{4}^{\ddagger}-InCl_3$	2.484	2.556	2.866	3.45	-93.7	47.6
$\mathbf{4}^{\ddagger}-InBr_3$	2.649	2.573	2.874	3.75	-97.3	85.7
$\mathbf{4}^{\ddagger}-InI_3$	2.873	2.602	2.912	4.14	-91.1	87.7
$\mathbf{4_{II}}- InCl_3$	2.495	2.365	2.651	2.37	-94.6	42.6
$\mathbf{4_{II}}- InBr_3$	2.662	2.366	2.661	2.61	-97.4	85.8
$\mathbf{4_{II}}- InI_3$	2.892	2.379	2.687	2.78	-90.9	87.7

TABLE C.5: Comparisons of select bond distances, the molecular dipole, and the percentages of the dipole in the In–X and In–P directions of the zinc-free indium halide ligand exchange calculations.

	In–X (Å)	In–N (Å)	In–P (Å)	Zn–P (Å)	Zn–$N_{(2)}$ (Å)	Zn–$N_{(3)}$ (Å)	Dipole (D)	$D_{\vec{InX}}$ (%)	$D_{\vec{InP}}$ (%)
$\mathbf{9_I}-InCl_3$	2.473	2.324	4.678	3.289	3.183	2.154	1.324	4.2	12.6
$\mathbf{9_I}-InBr_3$	2.635	2.327	4.755	3.296	3.178	2.155	1.204	4.5	29.8
$\mathbf{9_I}-InI_3$	2.856	2.332	4.866	3.322	3.185	2.158	0.955	19.7	41.2
$\mathbf{9}^{\ddagger}-InCl_3$	2.462	2.667	2.869	3.279	3.141	2.164	0.745	74.1	-66.7
$\mathbf{9}^{\ddagger}-InBr_3$	2.620	2.463	2.928	3.311	3.148	2.170	0.509	57.4	-75.8
$\mathbf{9}^{\ddagger}-InI_3$	2.805	2.401	3.350	3.284	3.122	2.146	1.471	44.0	-98.7
$\mathbf{9_{II}}-InCl_3$	2.490	2.349	2.664	3.290	3.147	2.179	1.821	35.8	-89.9
$\mathbf{9_{II}}-InBr_3$	2.653	2.355	2.673	3.306	3.151	2.183	1.509	31.0	-92.0
$\mathbf{9_{II}}-InI_3$	2.876	2.371	2.689	3.326	3.165	2.188	1.141	28.5	-90.5

TABLE C.6: Comparisons of select bond distances, the molecular dipole, and the percentages of the dipole in the In–X and In–P directions of the zinc-activated indium halide ligand exchange calculations.

		R	$\mathbf{7_e}$	L		D		
				Start	End	Start	End	
4/5	$InCl_3$	0%	–	0%	0%	0%	0%	$= 100\%$
	$InBr_3$	0%	–	0%	0%	0%	0%	
	InI_3	0%	–	0%	1%	0%	1%	
9/10	$InCl_3$	0%	0%	0%	0%	0%	8%	
	$InBr_3$	0%	0%	0%	0%	0%	77%	
	InI_3	0%	1%	0%	0%	0%	11%	

TABLE C.7: Proportions of the conformers that exist as the ligand exchange (L) and disproportionation (D) minima of each reaction path at equilibrium, as calculated by Equation 4.4 for all X geometries in the pathway.

	ΔG_g [a]	S [b]	α (°)	β (°)	$\alpha+\beta$ (°)	In–P (Å)	PP (Å)	ZnP (Å)	$PP+ZnP$ (Å)
$InCl_3/ZnI_2$	60.58	434.11	91.7	104.2	195.8	2.609	3.268	4.017	7.285
$InCl_3/ZnBr_2$	58.79	431.14	91.2	104.2	195.4	2.602	3.231	4.034	7.265
$InCl_3/ZnCl_2$	56.60	429.61	91.3	103.4	194.7	2.600	3.216	4.016	7.232
$InBr_3/ZnCl_2$	57.77	433.84	92.7	103.5	196.2	2.610	3.224	4.023	7.247
$InI_3/ZnCl_2$	58.03	439.54	94.5	103.9	198.4	2.630	3.233	4.040	7.273
[a] kcal/mol	R^2	0.0500	0.0173	0.7195	0.0087	0.0058	0.9123	0.0008	0.7928
[b] cal/mol-K	R^{2*}	0.4505	0.0023	0.7619	0.0270	0.2797	0.9184	0.0087	0.9924

TABLE C.8: Various bond lengths and angles of the zinc-activated disproportionation transition states, as depicted by Figure 4.16. Correlations to global free energy differences are also presented, with R^{2*} being calculated without the (*) geometry.

	R	$\mathbf{7_e}$	L		D		
			Start	End	Start	End	
$InCl_3/ZnI_2$	0%	0%	0%	0%	0%	4%	$= 100\%$
$InCl_3/ZnBr_2$	0%	0%	0%	1%	0%	10%	
$InCl_3/ZnCl_2$	0%	0%	0%	0%	0%	7%	
$InBr_3/ZnCl_2$	0%	0%	0%	0%	0%	66%	
$InI_3/ZnCl_2$	0%	0%	0%	0%	0%	10%	

TABLE C.9: Proportions of the conformers that exist as the ligand exchange (L) and disproportionation (D) minima of each zinc-activated reaction path at equilibrium, as calculated by Equation 4.4 for all X geometries in the pathway. Missing % arise from values <0.5%.